The Hamlyn Symposium on Medical Robotics
The Royal Geographical Society and Imperial College London, UK

12-15 July 2014

ISBN: 978-0-9563776-5-4

GZ Yang and A Darzi (Eds.)

Proceedings of the Hamlyn Symposium on Medical Robotics 2014

GZ Yang and A Darzi (Eds.)

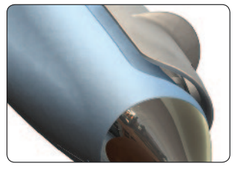

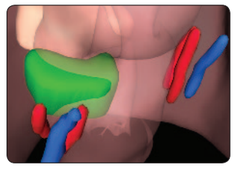

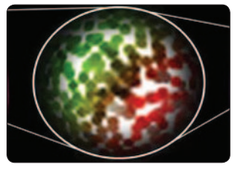

Proceedings

The Hamlyn Symposium on Medical Robotics

The Royal Geographical Society and Imperial College London, UK

12-15 July 2014

Proceedings

Guang-Zhong Yang and Ara Darzi (Eds.)

The Hamlyn Symposium on Medical Robotics

12-15 July 2014
Imperial College London, UK

Proceedings of
The Hamlyn Symposium on Medical Robotics
12-15 July 2014, Imperial College London
London, UK
ISBN: 978-0-9563776-5-4

Preface

With the UK government's announcement of robotics and autonomous systems (RAS) being one of the Eight Great Technologies that can potentially propel the nation's future growth, we have seen increasingly united effort across all disciplines underpinning the RAS research and development. With improved safety, efficacy and reduced costs, robotic platforms are approaching a tipping point, moving beyond early adopters to become standard surgical practice. Other drivers for healthcare robots are the aging population and the increasing importance of quality-of-life, independence and autonomy for those with chronic illnesses and disabilities.

The 7th Hamlyn Symposium on Medical Robotics was held at the Royal Geographical Society and the Hamlyn Centre for Robotic Surgery on 12th-15th July 2014. The theme for this year's symposium was *"Beyond Surgery - Independence and Quality of Life"* with an impressive line-up of leading scientists and engineers in collaborative robotics, navigation and image guidance, in particular, as invited speakers. The keynote lecture was delivered by Professor Toshio Fukuda of Nagoya University, who enlightened us on his experiences with Micro and Nano Robotics Systems; Professor Homayoon Kazerooni**,** University of California, Berkeley focused on developments on the lower extremity exoskeleton system; Professor Rajni Patel, Director of Engineering at CSTAR, shared his expertise and recent advances on haptics and teleoperation; Professor Robert Riener outlined the future steps for robots and their potential use in new therapies and treatment modalities. This year's Storz-Hopkins lecture was delivered by Professor Lee Swanstrom, who provided his insight and vision on the emerging technologies that might influence the future of surgery.

A total of 72 papers were submitted from 13 countries and 54 institutions, and after systematic peer review, 47 papers were selected for presentation at the Symposium. The topics covered ranged from Exo-Skeletons to Surgical Robots; Haptics and Teleoperation; Rehabilitation; Surgical Training; Micro, Nano and Flexible Access Robots; Image Guidance and Fusion; and Tracking, Navigation and Open Platforms.

We were delighted to see our workshop programs continue to grow and flourish, held on the days pre- and pro-ceding the Symposium. Topics covered included cognitive surgical robotics; MR-compatible robotics and interventions; paediatrics; imaging; flexible access surgery; open platforms for robotic surgery.

Unique to this year's symposium is the launch of the micro-robotics design challenge funded by the newly established Hamlyn Centre Micro-Engineering Facility as part of the EPSRC Capital for Great Technologies in RAS. This workshop brought together both clinicians and engineers for addressing the key challenges related to micro-robotics manufacturing, control and *in vivo* deployment. Participants will have 9 months to design, manufacture, and validate their proof-of-concept studies with support from the Hamlyn Centre. The winners will be announced in the next year's Hamlyn Symposium.

Two of the workshops were organised in conjunction with the new EPSRC-NIHR Healthcare Technology Co-operatives (HTC) Partnership Award on Devices for Surgery and Rehabilitation. In collaboration with the Trauma HTC at University Hospital Birmingham NHS Foundation Trust, the Wearable and Assistive Robots workshop had an impressive line-up of international leaders in the field. Wearable robots, actuated prostheses and exoskeletons have made significant inroads in recent years for functional rehabilitation, restoration of natural mobility and enhancing musculoskeletal strength and endurance. The workshop provided a forum to bring together researchers, engineers, and healthcare practitioners from a diverse range of disciplines to present the current state-of-the-art in wearable and assistive robots. It also covered some of the major technical challenges and unmet healthcare demands that can potentially reshape the future of wearable and assistive robots.

The Surgical Imaging Workshop was supported by the Enteric HTC at Barts Health NHS Trust and Queen Mary University of London, also with contribution from the EU FP7 FET-Open HELiCoiD project focussed on hyperspectral imaging for cancer detection. The workshop also brought strong industrial participation for addressing new ideas on the current state-of-the-art and future trends in surgical imaging techniques with a focus on robot assisted intervention.

We are particularly excited by the momentum exerted by the community in establishing open platforms for medical robots, with which the academic institutions and leading industrial players can work together to explore common problems and new research challenges in medical robotics. We are grateful to the strong support by Intuitive Surgical, Kuka Robotics, and Applied Dexterity for their help initiating and supporting this new venture. It is encouraging to see that many of these workshops have resulted in further on-going interactions among the participants and potential joint research grants or publications.

We would like to thank the International and Local Programme Committees, the Workshop Organising Committee and the Local Organising Committee for giving up their valuable time to ensure timely review of the submitted papers, to shape an excellent symposium programme.

We are also grateful to the team who have worked behind the scenes and for their continuous effort in managing all aspects of the Symposium organisation. In particular, thanks to Karen Kerr, Ruzanna Gulakyan, Su-Lin Lee, George Mylonas, Valentina Vitiello, Raphaele Raupp, Robert Merrifield, Charence Wong and Daniel Elson.

Lastly, special thanks go to Lady Hamlyn. This would not be possible without the generous philanthropic support from both the Helen Hamlyn Trust and Lady Hamlyn herself.

It was our great pleasure to welcome attendees to the 7th Hamlyn Symposium in London.

July 2014, London
Guang-Zhong Yang
Ara Darzi

Organisation

General and Programme Co-Chairs

Guang-Zhong Yang
Ara Darzi

International Programme Committee

Howie Choset	Carnegie Mellon University, USA
Kevin Cleary	The Sheikh Zayed Institute, Washington, USA
Paolo Dario	Scuola Superiore Sant'Anna, Pisa, Italy
Simon DiMaio	Intuitive Surgical Inc, USA
Pierre Dupont	Children's Hospital Boston, USA
Hubertus Feussner	Technical University Munich, Germany
Gabor Fichtinger	Queen's University, Canada
Dennis Fowler	Columbia University, USA
Blake Hannaford	University of Washington, USA
Leo Joskowicz	The Hebrew University of Jerusalem, Israel
Jacques Marescaux	University Hospital Strasbourg, France
Bradley Nelson	ETH Zürich, Switzerland
Vipul Patel	Global Robotics Institute, USA
Cameron Riviere	Carnegie Mellon University, USA
Rick Satava	University of Washington, USA
Ichiro Sakuma	University of Tokyo, Japan
Lee Swanstrom	University of Oregon, USA
Mark Talamini	University of California, San Diego, USA
Russ Taylor	Johns Hopkins University, USA
Ashutosh Tewari	Weill Cornell Medical College, USA

Local Programme Committee

Kaspar Althoefer	King's College London, UK
Thanos Athanasiou	Imperial College London, UK
Colin Bicknell	Imperial College London, UK
Nicholas Cheshire	Imperial College London, UK
Daniel Elson	Imperial College London, UK
Leonard Fass	GE Healthcare, UK
Mohamad Hamady	Imperial College London, UK
Andreas Melzer	Dundee University, UK
Azad Najmaldin	St James University Hospital, Leeds, UK
Geoff Pegman	RU Robotics, UK
Ferdinando Rodriguez y Baena	Imperial College London, UK
Julian Teare	Imperial College London, UK
Justin Vale	Imperial College London, UK

Table of Contents

Micro, Nano and Flexible Access Robots

Image Guidance and Fusion

Tracking, Navigation and Open Platforms

Poster Presentations

Quantifying Innovation in Robotic Surgery

A. Hughes-Hallett[1], E. Mayer[1], P. Pratt[2], J. Vale[1], A. Darzi[1,2]

[1]*Department of Surgery and Cancer, Imperial College London, UK*
[2]*The Hamlyn Centre, Institute of Global Health Innovation, Imperial College London, UK*

a.hughes-hallett@imperial.ac.uk

INTRODUCTION

Since the first robot-assisted procedure in 1992 [1], robotic surgery has significantly altered the landscape of surgical practice and has been identified as an area of growing innovation [2]. Patents and publications represent easily accessible and well validated measures for innovation diffusion [2,3]. In this article we utilise these tools to quantify the areas of greatest innovation in robot assisted surgery, in addition to this we aim to offer a prediction of the important robotic surgical innovations of the future.

METHODS

The methodology in this paper follows that in our recent publication 'Quantifying Innovation in Surgery'[2]. All patent and publications numbers were corrected for the overall exponential growth in patenting and publication over time prior to analysis utilising our previously published formula [2].

The DOCBD patent database was searched using the Boolean search strategy: (*surgeon* or *surgery* or *surgical*) and (*robot* or *robotic* or *davinci* or "*da vinci*"). In order to extract the areas of greatest technological innovation the top performing patent codes, by number, were extracted and sorted into well-defined technology clusters. A further Boolean search of the DOCBD database was then performed specific to each cluster in order to capture patents not identified within the top 30 codes.

Table 1. Top performing innovation clusters in robotic surgery since 1980. All p values were < 0.0001

Innovation Cluster	No. Patents	Growth Curve	r_s
Manipulators	1461	**Exp**	0.98
Master Slave	540	**Exp**	0.91
Endoscopes/Camera	298	**Sig**	0.95
Flexible Robots	294	**Exp**	0.85
Tendon drives	292	**Sig**	0.81
Haptics	249	**Exp**	0.94
Image guidance	242	**Exp**	0.92
Simulation/Planning	127	**Exp**	0.94
Automation	76	**Exp/Sig**	0.94

Exp = Exponential Sig = Sigmoidal

Growth curves for patents and publications were then plotted for these clusters in addition to robotic surgery as a whole. Spearman's rank correlation coefficient r_s was calculated between patent and publication number for each of the technology clusters.

RESULTS

Overall, robotic surgery has demonstrated exponential growth over the time period examined (Figure 1) with high correlation seen between patents and publications ($r_s = 0.96$, $p < 0.0001$).

When examining the top performing technology clusters we see two distinct patterns of growth (Table 1): exponential and sigmoidal. Strong correlation was seen across all of the clusters examined with all having r_s values greater than 0.8.

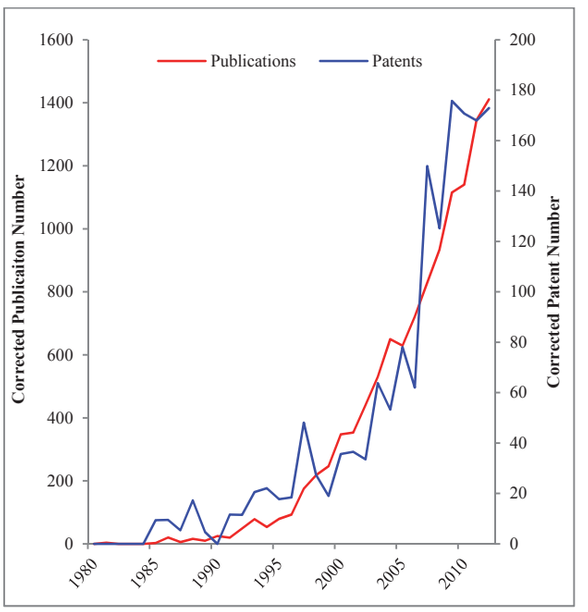

Fig. 1. Graph elucidating the innovation growth within robotic surgical technology

DISCUSSION

In this study we have objectively assessed and quantified innovation in robotic surgery both macroscopically and with greater granularity, scrutinising the technology clusters that have accounted for the bulk of innovation in robotic surgery.

The *exponential growth* in publications and patents seen within robotic surgery as a whole suggests that it is currently within a phase of *maximal innovation* [2]. This exponential growth reflects a period of symbiosis between industry and academia with each party driving the other to increasing levels of innovation [2,4].

Although the paper highlights the innovation surrounding robotic surgery the metrics of patent and publication are not without their respective limitations. Firstly, patent numbers seems to begin to plateau in 2010. There are two possible explanations for this. First, that innovation in surgery is currently in a state of *lapsed activity,* perhaps as a consequence of the recent global economic crisis. The second, and possibly more likely explanation is that this downturn in patenting is a result of the *delay* between a patent being applied for and it being granted. This trend has been observed across multiple datasets in the field of surgery [2]. This lag also applies to peer reviewed publication, although the delay is shorter.

Secondly, and specific to the publication metric, much of the literature published has been low quality small volume case series, and as such does not directly represent innovation. This said it does represent the diffusion of the technology through the target population and as such is likely to be a proxy measure of innovation in this community, with the high level of correlation between patent and publication numbers strengthens this hypothesis.

When looking to the future of robotic surgery the data presented suggests that robotic surgery continues to be the subject of increasing research and innovation, existing in a state of exponential growth. When looking at areas of contemporary innovation, of particular interest are flexible and haptic-enabled robotic platforms. Although these technologies are not currently commercially available, the exponential growth in these two clusters adds weight, and objective data, to the previously subjective claims that they represent a significant part of the future of robot-assisted surgery.

REFERENCES

[1] Moustris GP, Hiridis SC, Deliparaschos KM, Konstantinidis KM. Evolution of autonomous and semi-autonomous robotic surgical systems: A review of the literature. Int J Med Robot Comput Assist Surg 2011;7:375–92.

[2] Hughes-Hallett A, Mayer E, Marcus HJ, et al. Quantifying Innovation in Surgery. Ann Surg 2014. [Epub ahead of print]

[3] Daim TU, Rueda G, Martin H, Gerdsri P. Forecasting emerging technologies: Use of bibliometrics and patent analysis. Technol Forecast Soc Chang 2006;73:981–1012.

[4] Bengisu M, Nekhili R. Forecasting emerging technologies with the aid of science and technology databases. Technol Forecast Soc Chang 2006;73:835–44.

[5] Rogers E. Diffusion of Innovations. 5th ed. New York: Free Press; 1962.

Identification of Non-technical Roadblocks in Cognitive Robotic Surgery

E. Berges[1], A. Casals[1,2]

[1]*Institute for Bioengineering of Catalonia, IBEC, Spain*

[2]*Technical University of Catalonia, Barcelona Tech, UPC, Spain*
eberges@ibecbarcelona.edu

INTRODUCTION

Many challenges are still to be overcome, before European robotic community reaches full clearance on how to commercialize surgical robots, even more if they are endowed with some cognitive features. Besides the technical difficulties of developing such devices from the engineering and medical point of view, firm obstacles are also present regarding the social, legal and ethical implications that will arise, once this technology is available and ready to use for surgical purposes. This presents the results reached by the coordinated action Eurosurge to face non-technical roadblocks foreseen in future robotic surgery, including recommendations for the robotic, legal and medical communities involved in this field.

MATERIALS AND METHODS

The objective of Eurosurge is to describe a feasible roadmap for cognitive robotic surgery in Europe to be developed and put into service. One of associated work packages was specific for the obstacles that are not directly linked to the design of the devices, but to legal and ethical aspects associated. Concretely, it focused on three main subjects: the difficulties of dealing with intellectual property (patents), the needs of European rules and regulations to fit and manage devices endowed with cognition and finally, the ethical practice of such robots in the operating room, provided the patients give their consent after being fully informed. Being different the methods used for the analysis in each case, the chapter is divided into three parts.

Analysis of patents

The risks of patent infringement, as well as the strategy to protect one's invention demand a hard bibliographic evaluation task, which is in most cases out of the scope of researchers and developers. Researchers may spend excessive resources by searching; collecting and managing documents without feeling they obtain solid conclusions. Definitely, a patents database specific for surgical robots would facilitate the hard tasks above cited, reducing time consuming efforts. Moreover, making this database available for robotic community, the validity of existing patents could be widely discussed.

An exhaustive search of existing software for patents management has been done, realizing that free license products are not operative to generate a subdatabase, but only expensive commercial products allow it. For this reason, it was decided to create a tailored tool, developed by our own team, which could extract information from a patents free source, according to users' desired queries. The software will be required to search patents and tag them, so that users will be able to classify the documents and build up their own database.

Survey on legal aspects

Due to the nature of the tasks expected to be carried out by cognitive surgical robots, the evaluation of risks is critical and, in case of injury during the clinical procedure, civil liability has to be deeply examined, considering that robots are expected to behave with a certain form of autonomy. In order to foresee the way that laws, rules and regulations will have to contemplate this situation, the current body of European, Italian and Spanish laws referring to surgical robotics has been disseminated. In order to foresee the applicability of current laws in the event that robots are cognitive, a practical case of liability assignment was performed with present legal framework, where potential failures of a cognitive system where identified. The setup used to simulate the scenarios is described in [2], the methodology follows the guidelines of [3] and the result of this study highlighted some valuable considerations to prevent researchers' responsibilities when designing future cognitive systems.

Analysis on ethical aspects

The informed consent process needs to be updated together with technology advances in surgery. Robots endowed with cognitive features will bring more complex forms of autonomy and patients shall be properly informed about the circumstances. The risks and benefits of using such devices ought to be explained with necessary details, but not exceeding to an unnecessary level that might bring confusion to patients. Since there are no referents of cognitive surgical robots yet, the project focused on the informed consent today, by means of bibliographic research; the analysis of written informed consent templates and personal interviews with surgeons and experts in robotics. After evaluating which are the key points of the process, it was considered when, where and how the information should change in case that the robot used in the surgery was cognitive.

RESULTS

Following the structure of the chapter above, the results of the project will also be shown case by case.

Results of the analysis of patents

The first obstacle to develop the patents search and classify tool was to find the source from which the documents would be extracted. It was solved by accessing to MAREC's database [1], which includes 19 million worldwide patents. An interface was developed and integrated in a portal created by Eurosurge. It allows the user to search by keywords and refine the queries by means of Boolean operators, wildcards and constraining words proximity. The results are returned in order of relevance and the user has the chance to select and tag the ones desired. Tags can be introduced by the user or chosen from the list of concepts available in the same webpage. These concepts are validated by expert users in a wiki mode, according to one of the objectives of Eurosurge which is not subject of this paper.

Results of the survey on legal aspects

Apparently, European directives and Spanish or Italian laws present very little differences regarding robotic surgery. Indeed, the terms cognition and autonomy applied to machines do not appear in any text, thus no specific treatment for civil liability in this kind of devices. Applying laws may vary depending on whether the product is defective (manufacturer's liability) or the service (surgeon/hospital's liability).

The first conclusion obtained by the study case is that surgical robots, whatever the level of autonomy they dispose of, need mechanisms for the surgeon to assume the control at any time. Depending on the availability of these mechanisms, civil liability will fall on the manufacturer or on the surgeon. Nevertheless, it will be important in the future to define the autonomy level of the robot and distinguish the applicable law accordingly. The Sheridan's autonomy scale could be a good basis to work with.

On the other hand, it was noticed that European directives concerning robotic surgery (i.e. Directive 93/42/EEC concerning medical devices, or 85/374/EEC on product liability) and recent advances are out of phase. It is obvious that science runs faster than laws are updated. One of the recommendations from Eurosurge is the use of "soft" laws (i. e. ISO rules), which are more dynamic and its geographical applicability is more feasible than harmonizing national laws.

From the regulatory point of view, the only autonomous device currently working in dynamic scenarios, which can be taken as reference is Google's driverless car. Its approval process, though only recognized in three American states, indicate that the best way to demonstrate the product's safety when behaving autonomously is by means of experience. Cognitive surgical robots will need to proof their reliability and, also depending on the level of autonomy they are endowed with, the number of controlled interventions or working hours supervised before they can be considered operative will have to be regulated.

Results of the analysis on ethical aspects

This section summarises the most relevant conclusions from the analysis on the informed consent, considering that the total number of templates analyzed was 87, from 19 different sources, five countries and 38 different surgical specialties. These conclusions also take into consideration the comments received from four surgeons and ten experts in robotics and are divided into three groups, depending on whether the recommendations refer to general aspects of the informed consent process, additional information that should be included or the relationship between patients and the physicians.

The first group remarks the need to include some critical information in the written informed consent, which was not always found explicit along the reviewed templates (i.e. specific risks and benefits, alternative treatment). It is also proposed a modular document, which fits better the level of information that patients request. It consists of a main document with unavoidable information and other annexes, which patients may wish (not) to consult.

The second recommendations group explicitly suggests what kind of information could be included in the modules above mentioned, the availability of which should be expressly stated in the core document: statistics concerning the success rate of cognitive robotic surgery; explanation graphics; associated costs compared to alternative treatments and autonomy limits of the robot, etc.

Finally, almost like a reminder, the report highlights the origin of the informed consent, which is based on human relationship and doctor-patient confidence. The aim is to establish a difference between what is strictly legal and what is ethical in providing information about a new technology.

DISCUSSION

Although significant subjects of cognitive robotic surgery have been deeply analyzed, legal and ethical considerations or even social reactions on autonomous machines in clinical environments are not yet very predictable. Technologically, robotic surgeons are still far from been designed, hence little scientific steps should be progressively considered by the non-technical environments. Probably, one of the most difficult challenges to handle will come from the ethical implications of robots taking their own decisions in critical situations, which have repercussion in humans' life.

REFERENCES

[1] I. R. Facility. [On line]. Available: http://www.ir-facility.org. [Last access: 2012].

[2] R. Muradore, D. Bresolin, L. Geretti, P. Fiorini i T. Villa, «Robotic Surgery,» *IEEE Robotics & Automation Magazine,* vol. 18, núm. 3, pp. 24-32, 2011.

A Framework for Multilateral Manipulation in Surgical Tasks

K. A. Nichols, A. M. Okamura

Department of Mechanical Engineering, Stanford University, USA
{kirk.nichols,aokamura}@stanford.edu

INTRODUCTION

In robot-assisted surgery, exploration and manipulation tasks can be achieved through collaboration among robotic and human agents. Collaboration models employed by current surgical robots vary from pure teleoperation (e.g., the da Vinci Surgical System [1]) to cooperative models where the human and robot perform tasks independently but in parallel [2]. Collaboration models can potentially include multiple robotic and human agents working towards a shared objective – a scenario that we call *multilateral manipulation*.

We present a multilateral manipulation software framework capable of supporting development and testing of different collaboration models between robotic and human agents. We describe three possible collaboration models, and demonstrate the effectiveness of the framework experimentally by employing each model in a palpation task.

MATERIALS AND METHODS

Our exemplar task is palpation, where the goal is to physically explore a planar surface of simulated tissue in order to segment—that is, define the boundary of—an embedded, relatively stiff inclusion. This is representative of surgical tasks that aim to eliminate positive surgical margins after excision of tumors [3]. Three human-robot collaboration models were considered: full robot autonomy, bilateral teleoperation, and guided palpation with shared control. As described in the following sections, our framework allows the embodiment of each of these models.

Software Framework

Figure 1 graphically illustrates the class structure of our multimodal manipulation framework, extended to the inclusion segmentation task. (In the following, class names within the framework are italicized.)

Surgical tasks are implemented by extending five base classes (*Manager*, *Robot*, *Virtual Environment*, *File I/O*, and *Operator*), to make them task specific. Extensions of two of the five base classes are pictured in Figure 1. The extended classes are further extended into sub-classes that implement various features of the specific surgical task. An *Operator* uses the *Robot* instances assigned to it by the *Manager* to carry out the surgical task, potentially in collaboration with a human agent. Accumulated information is relayed to the *File I/O Manager* and *Virtual Environment* for storage and rendering. The extensions to the task-specific *Operator* implement different collaboration models. For example, the *Inclusion Segmentation Operator* in Figure 1 has three extended classes: *Bilateral Teleoperation, Guided, and Fully Autonomous*.

Extensions of the task-specific *Robot* class are tools that different extended operator classes can use to implement collaboration models. In the *Inclusion Segmentation Robot*, these are *Palpation Inclusion Segmentation Robot*, a fully autonomous robot, and *Human Interface Inclusion Segmentation Robot*, which allows human input via a master device.

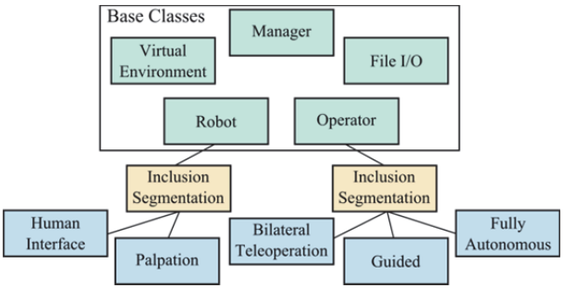

Fig. 1. Class hierarchy diagram. All base-level classes (green) are extended for the specific task (here, the inclusion segmentation task, shown in yellow). Two such extensions are pictured. Sub-classes for task extensions are in blue. Lines between classes indicate an extended class relationship.

Multilateral Manipulation Models

Using this framework, we consider three different collaboration models: full robot autonomy, bilateral teleoperation, and guided palpation.

Full Robot Autonomy: In this (non-)collaboration model, the slave robot operates autonomously, palpating points across the surface of the tissue. The palpation actions in our implementation are force controlled, to limit stress on the tissue. Force and displacement data from the downward palpation stroke are recorded and analyzed to estimate local stiffness at the palpated point. The *Fully Autonomous Inclusion Segmentation Operator* (i.e., the extended class) uses machine learning algorithms to segment the stiff inclusion from the surrounding soft tissue [4]. A stiffness classifier is used to label points as stiff or soft. If a palpated point is sufficiently stiff, its neighborhood is explored. The stiffness classifier is improved during successive iterations of a machine learning algorithm; converging to the value appropriate to classify the inclusion separate from its surrounding soft tissue. Between iterations of the machine learning algorithm, the union of the neighborhoods of points theorized to belong to the boundary of the inclusion are explored. Once the classifier has converged, a negative surgical margin boundary for the inclusion is calculated.

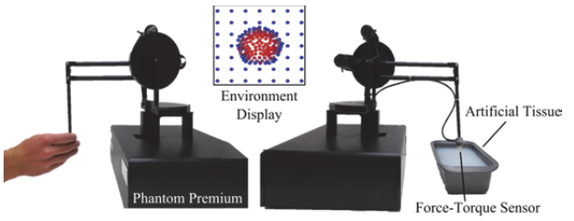

Fig. 2. Teleoperation scheme. A human operator (left) sends commands to the slave robot (right) that is positioned to palpate an artificial tissue with an embedded stiff inclusion. A virtual environment displays the collected data.

Bilateral Teleoperation: In this collaboration model, the slave and master robots are connected by a virtual spring and damper. Force feedback provides the operator with information from the remote environment. The experiment ends once the user indicates that he or she has collected enough data to feel confident in the estimate of the boundary of the inclusion.

Guided Palpation: In this collaboration model, the control is the same as in the full robot autonomy case, except that it uses bilateral teleoperation in the palpating (vertical) degree of freedom for safety. When a palpation force threshold is reached, the slave robot proceeds autonomously to the next point.

Experimental Setup

In our preliminary experiments, two Phantom Premium 1.5A haptic devices (Geomagic) were employed (Figure 2). The slave device was used to palpate the artificial tissue, and the master robot was used to receive human input. The artificial tissue was a slab of medium-stiffness silicone with a circular inclusion of stiffer silicone at the center. A Nano-17 force/torque sensor (ATI Industrial Automation) was mounted to the terminal link of the slave robot. Palpation data were visualized graphically in the virtual environment. After a point is palpated, it was added to the virtual environment; color indicated the estimated stiffness.

Evaluation Metrics

For each of the three tested collaboration models, the actual location of the stiff inclusion was compared to the estimated location to generate sensitivity and specificity metrics; a higher sensitivity decreasing the likelihood that any tumorous cells would be left behind after excision [3]. Additional data gathered during testing for each collaboration model included the number of palpations, maximum force exerted during experimentation, and duration of experiment. The duration of the experiment was measured from the moment the *Palpation Inclusion Segmentation Robot* received its first command to when the inclusion was segmented.

RESULTS

Figure 3 graphically depicts inclusion segmentation results using full robot autonomy. Similar tests were conducted using the bilateral teleoperation and guided palpation collaboration models. Performance metrics for all models are shown in Table 1.

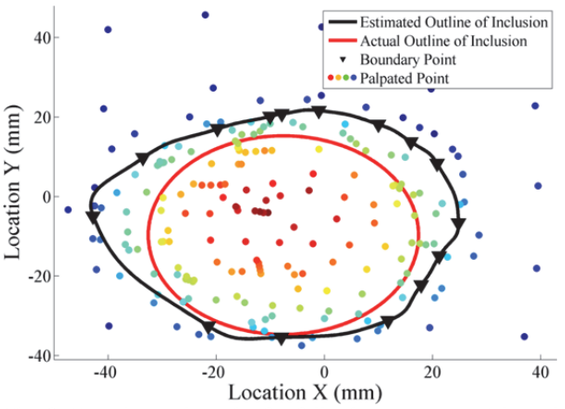

Fig. 3. Experimental results for full robot autonomy. The red line interpolates through the boundary points in black and forms the estimated boundary of the inclusion. The black circle is the actual boundary of the inclusion. Stiffness values are represented by colors ranging from stiffest (red) to least stiff (blue).

Table 1. Experimental results for all collaboration models.

Collaboration Model	*Sensi-tivity*	*Speci-ficity*	*Max Force (N)*	*Data Samples*	*Duration (s)*
Full Robot Autonomy	1.00	0.85	1.86	215	626.72
Bilateral Teleoperation	0.64	1.00	2.11	144	274.43
Guided Palpation	1.00	0.81	1.84	168	465.85

DISCUSSION

As shown in Table 1, full robot autonomy resulted in a higher sensitivity while palpating the tissue with a lower maximum force compared to bilateral teleoperation. However, bilateral teleoperation required less time and fewer palpations. Guided palpation had similar performance to full robot autonomy, which is expected since both collaboration models use the same inclusion segmentation algorithm.

We have described a multilateral manipulation software framework with the flexibility to implement multiple collaboration models, and demonstrated that it enables completion of a robot-assisted medical task. In the future, this framework will be applied to more complex surgical tasks, such as robotic suturing, potentially involving several robotic and human agents collaborating together.

This work was supported by NSF grant 1227406.

REFERENCES

[1] C. Freschi, et al, Technical Review of the Da Vinci Surgical Telemanipulator. Int'l J. of Medical Robotics and Computer Assisted Surgery. 2013; 9(4): 396-406.

[2] P. T. Rose, and B. Nusbaum. Robotic Hair Restoration. Dermatologic clinics. 2014; 32(1):97-107.

[3] S. B. Williams, et al. Radical Retropubic Prostatectomy and Robotic-Assisted Laparoscopic Prostatectomy: Likelihood of Positive Surgical Margin(s). Urology. 2010; 76(3):1097–1101.

[4] K. A. Nichols, A. M. Okamura. Autonomous Robotic Palpation: Machine Learning Techniques to Identify Hard Inclusions in Soft Tissue. IEEE Int'l. Conf. on Robotics and Automation. 2013; pp. 4369-4374.

Realisation of Robotics in Spinal Surgery

M. Shoham

Robotic Laboratory, Technion-Israel Institute of Technology
Mazor Robotics, Caesarea, Israel
moshe.shoham@gmail.com

ABSTRACT

The increasing incidence of instrumented spinal surgeries has set the stage for development and integration of surgical robots designed to overcome the limitations of minimally invasive procedures, enhance open surgery performance and reduce occupational risk. Renaissance™ Surgical Guidance Robot (Mazor Robotics Ltd., Caesarea, Israel), a next generation application of the company's SpineAssist®, upgraded to expand its indications and performance.

The FDA-cleared and CE-marked cylindrical semi-active robotic guidance unit measures 50X90 mm, weighs 300 grams and features six degrees-of-freedom through parallel robot kinematic design. The mechanical system design offers accuracy greater than 0.3 mm and resolution greater than 0.03 mm with overall positional accuracy that includes the entire error chain including CT scan, registration etc. of better than 1.5 mm. The platform software enables off-line planning for optimisation of implant dimensions and trajectories. The robotic guidance system is mounted onto the bony anatomy, enabling maintained positional accuracy, insusceptible to the patient's respiratory activity and minor movements. Automatic, image-based registration is then performed to spatially align the surgical blueprint with the mounting platform and the patient's spine.

Both Renaissance and SpineAssist are in routine use in over 60 medical centers worldwide and have been applied in over 5,000 cases, involving over 45,000 implants, in a broad range of spinal applications, including spinal fusion surgeries, correction of spinal deformities, biopsy collections, tumor excisions and cement augmentations.

To date, no reports of permanent robotically-related neurological deficits have been made, in sharp contrast to the 0.6-2% typically reported in the scientific literature for pedicle screw insertions. System performance has been clinically validated, with a successful implementation rate of >89.9%. Several studies report clinically acceptable implantation accuracy of about 98-99%, even when involving significant numbers of percutaneously inserted implants and spinal deformities. Moreover, fewer adverse events and a 48.9% decrease in opiod usage during the perioperative period, as well as a 24.7% shortening of hospitalization periods were associated with Renaissance/SpineAssist employment when compared to patients treated with a conventional, open approach. Comparing fluoroscopy time, SpineAssist reportedly involves less radiation exposure with up to 4-fold shorter time when freehand percutaneouse surgeries.

Complementation of current spine surgery approaches with SpineAssist and Renaissance show advantageous particularly in complex deformity cases which lack coherent anatomical landmarks.

REFERENCES

[1] Barzilay Y, Schroeder J, Hiller N, Singer G, Hasharoni A, Safran O, Liebergall M, Itshayek E, Kaplan L. Robotic assisted vertebral body augmentation – a radiation reduction tool. Spine Journal, 2013. Web.

[2] Hu X, Ohnmeiss D. Lieberman,I. Robotic-assisted pedicle screw placement: lessons learned from the first 102 patients. Eur Spine J., 2013.

[3] Kantelhardt SR, Martinez R, Baerwinkel S, Burger R, Giese A, Rohde V. Perioperative course and accuracy of screw positioning in conventional, open robotic-guided and percutaneous robotic-guided, pedicle screw placement. Eur Spine J., 2011.

[4] Devito DP, Kaplan L, Dietl R, Silberstein, et al. Clinical acceptance and accuracy assessment of spinal implants guided with SpineAssist surgical robot: retrospective study. Spine, 2010.

[5] Pechlivanis I, Kiriyanthan G, Engelhardt M, et al. Percutaneous placement of pedicle screws in the lumbar spine using a bone mounted miniature robotic system, first experiences and accuracy of screw placement. Spine, 2009.

[6] Shoham, M, Burman, M, Zehavi, E, Joskowicz, L, Batkilin, E, Kunicher Y. Bone mounted miniature robot for surgical procedures: concept and clinical applications. IEEE Transactions on Robotics and Automation, 2003.

Multi-Fingered Palpation using Pseudo-Haptic Feedback

M. Li[1], S. Sareh[1], M. Ridzuan[1], L. D. Seneviratne[1], P. Dasgupta[2], H. A. Wurdemann[1], K. Althoefer[1]

[1]*Centre for Robotics Research, Department of Informatics, King's College London, UK*

[2]*MRC Centre for Transplantation, DTIMB and NIHR BRC, King's College London, UK*

k.althoefer@kcl.ac.uk

INTRODUCTION

The inclusion of haptic palpation in training simulators is beneficial for the acquisition of practical experience. Pseudo-haptic feedback, which creates an illusion of force and haptic feedback using only visual information, can replace expensive haptic devices [1]. In this paper, a multi-fingered palpation simulation using pseudo-haptic feedback with three indenter avatars is introduced and evaluated to prove the hypothesis that multi-fingered palpation is more time-efficient than single-fingered palpation. Multi-fingered palpation is more common than single-fingered palpation in real practice when attempting to detect differences in stiffness in the examined tissue [2]. With multiple indenter avatars, a wider tissue area can be investigated in one go instead of only one spot when using a single indenter avatar. Moreover, the user can conveniently compare the stiffness values at different locations by observing the differences of indentation depths of those separate indenter avatars.

MATERIALS AND METHODS

Our pseudo-haptic-based feedback approach utilizes a cursor speed-changing strategy. The trace of the cursor movement at the same time intervals is shown in Fig. 1. When the cursor (indenter avatar) slides over a tissue area whose stiffness value is higher than the surrounding tissues, reduced indentation depth and tissue surface deformations are displayed. To simulate multi-fingered palpation, three indenter avatars are aligned in a triangular-shape during the operation. Thus, users can explore 3 neighbouring tissue areas simultaneously as if they were using three fingers to palpate (see Fig. 2).

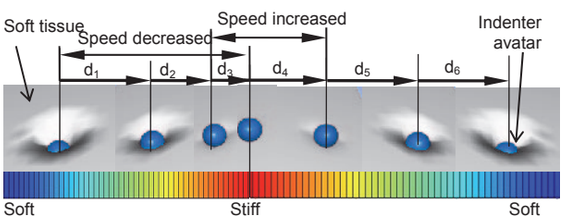

Fig. 1. Pseudo-haptic feedback: modification of the cursor speed when passing over a hard nodule ($d_1>d_2>d_3$, $d_3<d_4$).

Two types of tablet computers are used in this study – Samsung Galaxy Note 10.1 (using an S-pen input) and Motorola Xoom (using the user's bare finger input). A virtual model of a tissue block with a flat surface is displayed on a graphical interface. The stiffness information of the tissue model is described by reaction force matrices acquired from rolling indentation tests [1, 3, 4].

The coordinates of the program window are linearly mapped to the tissue surface. The user moves a force-sensitive pen or their bare finger over the surface of a tablet computer tangentially providing 2-DOF movement kinematics and a normal force as inputs. The outputs are the normal reaction force from the tablet computer, the virtual resistance along the movement direction generated by using pseudo-haptic feedback, and the soft object deformation shown on the graphical interface.

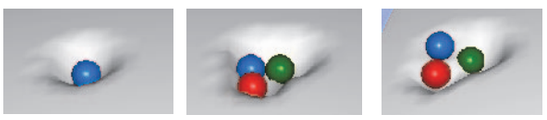

Fig. 2. (a) A single indenter avatar represents one finger; (b) three indenter avatars, representatives of three fingers, are at the same height indicating no abnormalities; (c) avatars are at different heights indicating possible tissue abnormalities.

The Samsung Note (using a Wacom S-pen) is force-sensitive and has 1024 levels of pressure sensitivity. The force level-force value relationship is described as

$$f_n = 0.1008\ e^{4.2081\ f_l}, \quad (1)$$

where f_l is the force level reading from Android SDK and f_n is the corresponding normal force values. The Motorola Xoom tablet senses the area of touch: when the touched area is broader, it recognizes the applied force as larger. The force level-force value relationship is described as

$$f_n = 0.0772\ e^{3.0727\ f_l}. \quad (2)$$

The modification of the indenter avatar speed is achieved by adding a time delay to the rendering task of the indenter avatar when it is approaching a stiffer area. If the indenter passes over the stiffer area, the indenter avatar continues to follow the contact point. The delay time is expressed as

$$t_d = \Delta f_t \cdot m, \quad (3)$$

where the value of the tangent reaction force f_t is acquired from the reaction force matrices formed during the rolling indentation; Δf_t is the reaction force difference ($\Delta f_t = f_t - f_{tl}$); f_{tl} is the tangent reaction force value at the last avatar position; m is a scalar value set to be 500 in this study.

In order to validate the proposed multi-fingered palpation using pseudo-haptic feedback, four evaluation tests were conducted: 1) single-fingered pseudo-haptic

palpation using a tablet and S-pen as input devices, 2) multi-fingered pseudo-haptic palpation using a tablet and S-pen as input devices, 3) single-fingered pseudo-haptic palpation using a table and a bare finger of the user as input devices, 4) multi-fingered pseudo-haptic palpation using a table and a bare finger of the user as input devices. Twenty right-handed participants, who have normal or corrected vision, participated in this empirical study. Firstly, participants were asked to do a practice run with known tumour locations. Then, they were asked to manipulate the input device to "palpate" the virtual soft object and observe the change of the ratio between the indenter avatar displacement distance and their input. When they found hard inclusions, they reported their locations. The researchers recorded the nodule detection rates and the time consumed. The order of tests was pseudo-random and during all those tests, the same stiffness distribution was used, but the orientation of the soft object was different from test to test. So the participants would not know the nodules' locations from the earlier tests. Fig. 3 shows the user interfaces of the pseudo-haptic soft tissue stiffness simulation using the two tablet computers.

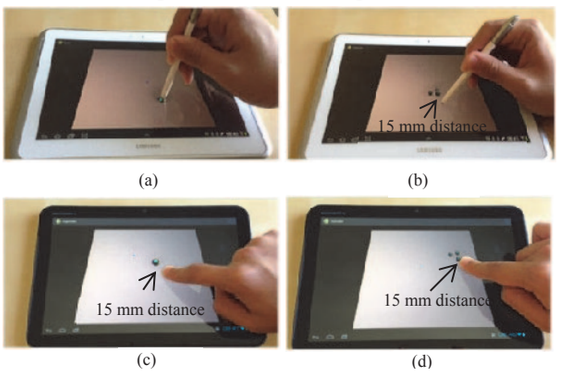

Fig. 3. Pseudo-haptic palpation: (a) single-fingered palpation using a tablet and an S-pen; (b) multi-fingered palpation using a tablet and an S-pen; (c) single-fingered palpation using a tablet and a bare finger; (d) multi-fingered palpation using a tablet and a bare finger.

RESULTS

Fig. 4 presents the nodule detection sensitivity *Se* [5] that is the measure of the test's ability to identify positive results. It is defined as sum over all *n* trials of the true positives divided by the sum of false negatives and true positives. Fig. 5 presents the consumed time for nodule detection. Wilcoxon signed-rank test [6] is used to compare the time consumed in pairs.

DISCUSSION

The user study results show good performance of nodule detection sensitivities during pseudo-haptic palpation and there was no significant difference between single-fingered and three-fingered pseudo-haptic palpation. The multi-fingered pseudo-haptic palpation either using an S-pen or a bare finger input consumed significantly less time than single-fingered pseudo-haptic palpation. We could show that multi-fingered pseudo-haptic palpation is more time-efficient than single-fingered pseudo-haptic palpation.

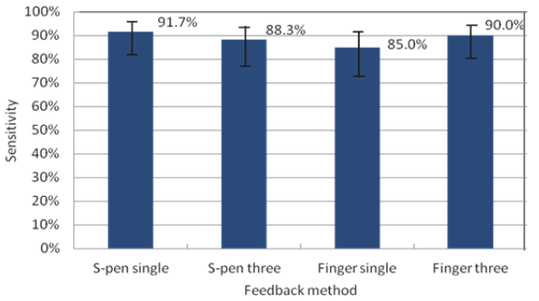

Fig. 4. Nodule detection sensitivities with Wilson score intervals [7] at a 95% confidence level.

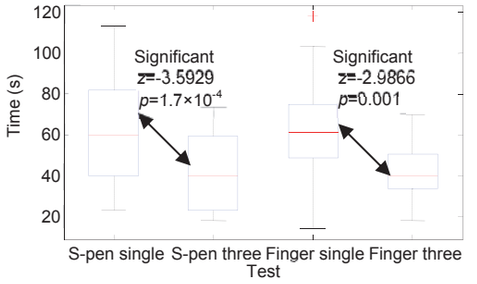

Fig. 5. The consumed time of single-fingered and multi-fingered palpation using pseudo-haptic feedback.

ACKNOWLEDGMENT

The research was partially funded by the GSTT Charity and the Vattikuti Foundation, the European Commission's Seventh Framework Programme under grant agreement 287728 in the framework of EU project STIFF-FLOP, and the China Scholarship Council.

REFERENCES

[1] Li M, Liu H, Seneviratne LD, Althoefer K. Tissue stiffness simulation and abnormality localization using pseudo-haptic feedback, in *IEEE International Conference on Robotics and Automation*, 2012, pp. 5359–5364.

[2] Dinsmore M, Langrana N, Burdea G, Ladeji J. Virtual reality training simulation for palpation of subsurface tumors, in *IEEE Virtual Reality Annual International Symposium*, 1997, pp. 54–60.

[3] Sangpradit K, Liu H, Seneviratne LD, and Althoefer K, Tissue identification using inverse finite element analysis of rolling indentationof Rolling Indentation, in *IEEE International conference on Robotics and Automation ICRA*, 2009, pp. 1250–1255.

[4] Liu H, Li J, Song X, Seneviratne LD, Althoefer K. Rolling indentation probe for tissue abnormality identification during minimally invasive surgery, *IEEE Trans Robot.* 2011 27 (3): 450–460.

[5] Altman D, Bland J. Diagnostic test 1: Sensitivity and specificity," *BMJ*, 1994 308:1552.

[6] Wilcoxon F. Individual comparisons of grouped data by ranking methods.," *J Econ Entomol.* 1946 39: 269, 1946.

[7] Wilson EB, Probable inference, the law of succession, and statistical inference, *J Am Stat Assoc.* 1927 22:209–212.

Development of a force-sensing system for endoscopic submucosal dissection

K. Naito[1], T. Ando[1], J. Wang[1], H. Kiyomatsu[2],
E. Kobayashi[1], M. Fujishiro[2], I. Sakuma[1]

[1]*Graduate School of Engineering, The University of Tokyo, Japan*
[2]*The University of Tokyo Hospital, Japan*
naito@bmpe.t.u-tokyo.ac.jp

INTRODUCTION

Flexible endoscopy is commonly used for the diagnosis of endoluminal lesions as well as for the treatment of early stage cancer. Endoscopic submucosal dissection (ESD) is an effective technique for the removal of tumours; however, doctors who can operate ESD are limited because of the difficulty of the procedures. Although the flexible endoscope has a camera and a device, they are fixed to the same direction. Thus, doctors must operate ESD in a limited degree of freedom. Furthermore, the operator cannot feel the reaction force of the instruments because the flexible endoscope is driven by long wires, which have considerable friction and compliance. Some groups have developed an endoscopic manipulator and a navigation system to improve the operability of the endoscope [1, 2]; however, force feedback is not equipped in those systems. Because dissection under endoscope requires delicate skills, the implementation of a force-feedback system can improve the safety of the operation.

In this study, we proposed a novel force-sensing system for endoscopic operations considering the temperature compensation. Although there have been many trials for measuring the force of laparoscopic instruments [3], to the best of our knowledge, the force of endoscopic instruments have never been measured. Our system can be applied to endoscopic instruments, leading to safer endoscopic operations.

MATERIALS AND METHODS

In this research, we focused on a dissection procedure in ESD. Because the monopolar knife used in ESD cuts tissues laterally, a bending force is applied to the instrument. Therefore, we aimed to measure the bending force applied to the monopolar knife. To measure the bending force, we used customized-fibre Bragg grating (FBG) sensors whose centre wavelength is 1545nm (Neolux Inc., Germany). Although the FBG sensor can measure only the longitudinal distortion of the fibre, the force can be measured by calibration between the force and the distortion of the fibre. Figure 1a illustrates the sensor configuration. Four FBG sensors (ϕ 0.15 mm) were attached to the edge of the knife 90° apart from each other in a circle for measuring the bending force from an arbitrary direction. The outer diameter of the knife after FBGs were attached was 2.9 mm, which was thin enough to pass the channel of the colonoscope. The monopolar knife was covered with a thermal shrinkage tube to protect fibres and drawn markers (Figure 1b).

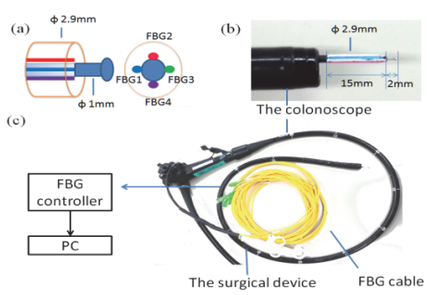

Fig. 1 (a) FBG sensors attached to the edge of the knife; **(b)** Surgical knife with markers in the endoscopic channel; **(c)** Whole system for force sensing.

Figure 1c shows the whole system. The monopolar knife equipped with FBG sensors is inserted into the channel of the colonoscope. FBG sensors were connected to a controller (AWE-8-CCD, Neolux Inc., Germany) and the distortion of axial direction was measured using a computer.

Although the FBG sensor can measure very small distortions, the measurement results were largely affected by temperature. Furthermore, the sensitivity of the sensor varied with the attachment conditions of FBG sensors to the knife. Therefore, we proposed a novel calculation technique to compensate temperature changes and sensitivity variations.

In this system, the distortion of FBGs depends on two elements; strength and direction of force. The distortion measured by each sensor is proportional to the strength of the force when the direction of the force is constant [4], and the angular dependence of the distortion can be approximated as a sine curve when the strength of the force is kept constant. Furthermore, the variation of the sensitivity of each sensor can be approximated as the amplitude of each sine curve. To calculate the bending force compensating the change of temperature, the approximate sine curves of the diagonal sensors (FBG1 and FBG3, FBG2 and FBG4) were subtracted:

$$f_{ij}(x,\theta) = A\cos(\theta - \psi_i) - \alpha B\cos(\theta - \psi_j) = C\cos(\theta - \phi_{ij})$$

Here θ shows the angle based on fixed angle [degree] and x shows the strength of the force [mN]. Alpha was defined by the ratio of the sensitivities of two sensors.

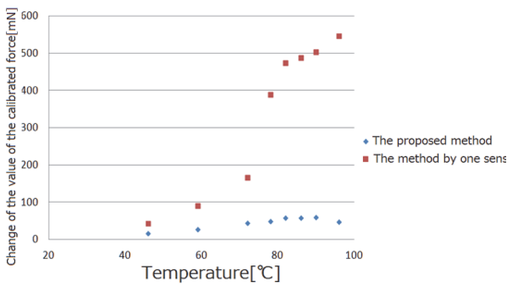

Fig.2 Calculated force shift at different temperatures.

Hence, the direction of the force can be determined uniquely by the ratio of the subtracted curves, and the strength of the force can be given by the magnification of the subtracted curves. Therefore, the strength and the direction of the force can be estimated by substituting the measured value in the calculated curves.

The calibration was performed using a rotational stage, a *z*-axis stage and an electric balance. Sixteen data sets (two kinds of strengths of force with 45° intervals for 360°) were used for the calibration, and the results were averaged for five times. According to this, $A, B, \psi_i, \psi_j, C,$ and ϕ_{ij} were determined.

RESULTS

Error evaluation

To evaluate the measurement accuracy, forces of arbitrary strength and direction were applied to the instrument, and the error between the true value and the estimated value was calculated. As a result, the error of the strength of the force was -29.6 ± 30.9 [mN] and that of the direction of force was -3.79 ± 8.23 [°].

We also evaluated the effect of temperature compensation. The device was heated from 26°C to 100°C by a heat gun while applying a constant force (250 mN). The temperature was monitored by a thermocouple attached at the tip of the device. When the direction of the force was constant, the strength of the force could also be calculated by only one FBG sensor, which did not compensate the temperature. We compared the force calculated by the proposed method with that calculated by only one sensor. Figure 2 shows how the calculated value changed while the temperature rose. When the temperature reached 100 °C, an error of 550 mN was measured in the method in the absence of temperature compensation. On the contrary, the proposed method achieved an error of less than 50 mN. This result shows that the proposed method enables us to compensate for the thermal effects.

Ex vivo experiment

We performed *ex vivo* experiments to simulate ESD using cattle rectum and calculated the strength of the force (Figures 3, 4). We synchronized the measurement of FBG to the endoscopic image before the operation. A doctor specialized in endoscopic therapy performed the whole ESD procedure, during which the bending force was measured. The FBG sensor monitor was set at 100 Hz. We found that most of the force was

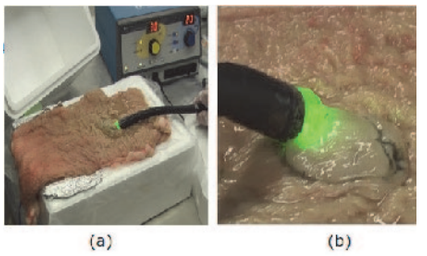

Fig.3 (a) Set-up of the *ex vivo* experiment; **(b)** State of the cutting surrounding the lesion.

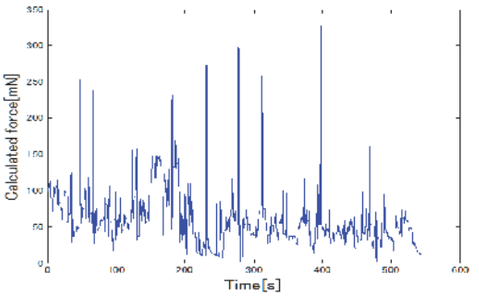

Fig.4 Force calculated during the experiment.

approximately from 50 mN to 150 mN. However, some values exceeded 200 mN when the instrument was clogged by the tissue in the endoscopic image.

DISCUSSION

In this study, we successfully measured the force during an ESD procedure and revealed that it almost ranged from 50 mN to 150 mN. It has a novelty to measure the force which the device of the flexible endoscopic surgery was given. The instrument developed in this study cannot measure the longitudinal force compensating temperature changes; however, the measurement of the longitudinal force with temperature compensation could be achieved by adding an extra FBG sensor. Moreover, the errors in the calculated force are mainly caused by the estimation error of the approximate curves. Therefore, the measurement accuracy can be improved by using more data sets at the calibration.

Although the direction of the force is not indicated in this study, our device has the potential to measure it. The coordinates of the device can be transformed to those of the endoscopic images by observing the marker on the device. Moreover, this system can help doctors' surgical skills to evaluate them objectively and numerically. Therefore, our technique can be used as a force-feedback system for endoscopic instruments in the near future.

REFERENCES

[1] C.A. Peters, et al., "Navigated endoscopy: prototype system for robotically assisted ureteroscopy," *Hamlyn Symposium on Medical Robotics*, 2012, pp.73-74.

[2] J. Ruiter, et al., "Robotic Control of a Traditional Flexible Endoscope," *Hamlyn Symposium on Medical Robotics*, 2012, pp.25-26.

[3] X. He, et al., "Force sensing micro-forceps with integrated fiber Bragg grating for vitreoretinal surgery," *SPIE BiOS*. International Society for Optics and Photonics, 2012.

[4] J. Arata, et al., "Fiber optic force sensor for medical applications within a backbone-shape structure," *Procedia CIRP*, 2013, Vol.5, pp.66-69.

Demonstration of Autonomous Atraumatic Cochleostomy by Combined Advanced Surgical Robot Systems

S. Weber [1], B. Bell [1], N. Gerber[1], T. Williamson[1], P. Brett[2], X. Du [2], M. Caversaccio[3], D. Proops[4], C. Coulson[4], A. Reid[4]

[1]*ARTORG Center, University of Bern, Switzerland*
[2]*Brunel Institute for Bioengineering, Brunel University, UK*
[3]*Department of ENT, Head and Neck Surgery, Bern University Hospital, Switzerland*
[4]*Department of Otolaryngology, Queen Elizabeth Hospital, UK*
xinli.du@brunel.ac.uk

INTRODUCTION

Surgery on the lateral skull base provides an ideal environment for the integration of surgical robotics and computer assisted surgical techniques due to the relative rigidity of anatomical structures and the desire for high precision and accuracy. Recent work at the University of Bern has seen the realization of a robotic system designed specifically for minimally invasive cochlear implantation. The system enables significantly reduced invasiveness by removing the need for a mastoidectomy, replacing this with a direct tunnel approach known as direct cochlear access (DCA) [1, 2]. Typically, a DCA trajectory will pass from the mastoid through the facial recess (formed by the divergence of the facial nerve and chorda tympani) to the round window. Meanwhile, work at Brunel University has focused on improving the safety and accuracy of inner ear access through the cochleostomy. The formation of the cochleostomy is thought to be one of the key components in preserving hearing [3]. The reduction of initial trauma due to the creation of a cochleostomy, or extension of the round window through the use of robotics has also been a subject of interest.

This work describes both systems and the preliminary work on the combination of a high accuracy robotic system, designed specifically for minimally invasive access to the cochlear through a facial recess approach, and a robotic smart drilling system designed for the completion of a safe, minimally invasive cochleostomy.

MATERIALS AND METHODS

A robotic system was designed specifically for minimally invasive cochlear implantation procedures (Fig. 1). The lightweight (5.5 kg), 5 degree of freedom robotic arm can be mounted directly to the side rails of a standard OR table with a dedicated robot mount, which includes a non-invasive patient fixation mechanism for minimization of patient movement. A force torque sensor is fitted at the robot wrist, enabling haptic control, semi-automatic registration and measurement of drilling process variables.

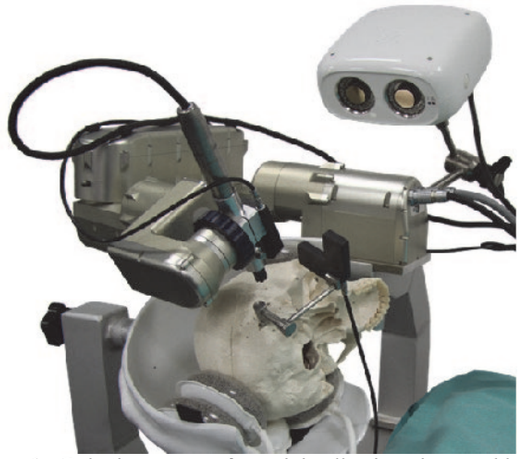

Fig. 1. Robotic system for minimally invasive cochlear access.

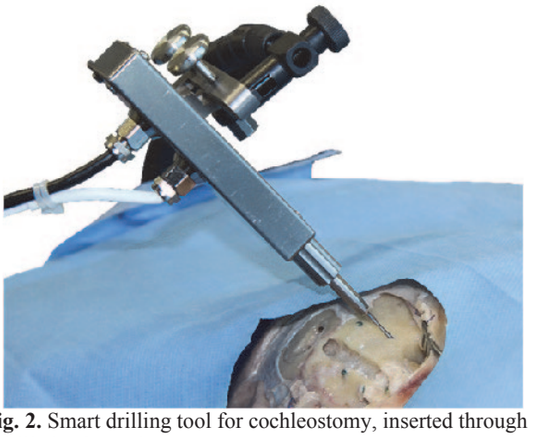

Fig. 2. Smart drilling tool for cochleostomy, inserted through a drilled DCA trajectory.

The smart drilling system with the ability to discriminate tissue and changes in tissue composition ahead on the drilling trajectory was developed for the completion of cochleostomy procedures [4-5]. The system consists of linear and rotational drives to feed and rotate standard surgical burrs. This system is attached to a flex lock arm, permitting free movement and stabilization of the drill, and was placed through the DCA trajectory (Fig. 2). The drilling is entirely controlled through a hardwired control unit with the surgeon retaining executive control. Autonomous perception of critical phenomena and structures is completed using the coupled force and torque drilling

transients in real-time. This enables automated selection of appropriate control strategies to achieve a precise and consistent result with respect to the flexible tissues. The most important responsibility of the system is to prepare the window on the endosteum without penetration.

RESULTS

The minimally invasive robotic system allowed minimally invasive inner ear access without damage to surrounding anatomy in all cases. An accuracy of 0.08 ± 0.05 mm was observed at the surface of the mastoid; an accuracy of 0.15 ± 0.08 mm was observed at the planned target. Full electrode insertion through the round window approach was achieved in seven of eight cases: in a single case two electrode pairs remained outside of the cochlea. The setup of the robotic system took on average 7.1 minutes; positioning of the patient and fixation of the reference tracking marker an average of 4.6 minutes; patient to image registration approximately 3 minutes. The drilling, performed in 3 stages, required an average of 6 minutes to complete. The total procedure took, on average, approximately 21 minutes. Anatomy segmentation and trajectory planning was completed in less than 20 minutes in all cases.

The smart drilling system allows information about the state of the drilling process to be extracted from observed force and torque data; subsequently drill breakthrough can be predicted and controlled, minimizing trauma to the inner ear. Laboratory investigations confirmed robustness of the techniques to different angles of incidence with tissue interfaces and tissue thickness [5]. Laser vibrometer measurements during cochleostomy demonstrated that the robotic approach produced only 1% of the peak disturbance amplitude of manual drilling [6]. It was also shown that cochleostomies were uniform and that the endosteum remained intact. The results indicate that using the robotic drill reduces trauma within the cochlea and that the approach for detection is robust and consistent when subjected to a wide variation of operating and tissue conditions.

DISCUSSION

Comprehensive pre-clinical validation of the image guided robotic system for minimally invasive cochlear access has established an overall accuracy sufficient for the safe completion of the procedure. In addition to being highly accurate, the system has been designed with eventual clinical integration in mind. Additionally, novel safety features based on alternative sensor sources provide an additional level of safety on top of the high accuracy workflow. The autonomous system for cochleostomy is able to penetrate the cochlear while leaving the endosteal membrane intact, thus maintaining sterility and avoiding the influx of debris. A decrease in complications, as well as increased retention of residual hearing, is expected as a result of this approach compared with conventional methods

Recent debate about the best route for cochlear electrode insertion (round window or cochleostomy) stems mostly from the desire for clinicians to retain residual hearing loss by minimizing intra-cochlear damage during the insertion process. Most literature advocates a round window approach when possible due to the increased trauma associated with the manual drilling process [7-8]. The robotic systems described within have proven successful in allowing both minimally invasive access to the cochlea and trauma free cochleostomy for electrode insertion. The combination of these two complimentary approaches will allow safe and reliable execution of the cochleostomy procedure, as well as highly accurate placement of the cochleostomy site, potentially leading to decreased trauma during insertion retention of residual hearing.

REFERENCES

[1] R.F. Labadie, R. Balachandran, J.H. Noble, G.S. Blachon, J.E. Mitchell, F.A Reda, B.M. Dawant and J.M. Fitzpatrick, “Minimally invasive image-guided cochlear implantation surgery: First report of clinical implementation.” Laryngoscope, 2013 Nov 22.

[2] B. Bell, N. Gerber, T. Williamson, K. A. Gavaghan, W. Wimmer, M. Caversaccio, and S. Weber, “In Vitro Accuracy Evaluation of Image-Guided Robot System for Direct Cochlear Access.” Otology & Neurotology 34(7):1284-90, 2013.

[3] Lehnhardt E. “Intracochlear placement of cochlear implant electrodes in soft surgery technique.” HNO, 41(7):356-359, 1993

[4] Taylor, R.P., Du, X., Proops, D.W., Reid, A.P., Coulson, C., Brett, P.N. “A sensory-guided surgical micro-drill.” Proceedings of the Institution of Mechanical Engineers, Part C: Journal of Mechanical Engineering Science, 224(7): 1531-1537, 2010

[5] Du, X., Zoka Assadi, M., Jowitt, F., Brett, P.N., Henshaw, S., Dalton J., Proops, D.W., Coulson, C., Reid, A.P. “Robustness analysis of a smart surgical drill for cochleostomy. ” The International Journal of Medical Robotics and Computer Assisted Surgery, 9(1):119-26, 2013

[6] C. Coulson, M.Z. Assadi, X. Du, P.N. Brett, and D.Proops, “Smart micro-drill for cochleostomy formation: A comparison of cochlear disturbances with manual drilling and a human trial.” Cochlear Implants International, 14(2): 98-106, 2013.

[7] S. Havenith, M.J Lammers, R.A. Tange, F. Trabalzini, A. Della Volpe, G.J. van der Heijden, “Hearing preservation surgery: cochleostomy or round window approach? A systematic review.” Otology & Neurotology, 34(4):667-74, 2013.

[8] C. Richard, J.N. Fayad, J. Doherty, F.H. Linthicum Jr., “Round window versus cochleostomy technique in cochlear implantation: histologic findings.,” Otology & Neurotology, 33(7):1181-7, 2012.

Robotic versus Non-Robotic Instruments for Minimally Invasive Surgery in Spatially Constrained Operative Workspaces

T. P. Cundy[1], H. J. Marcus[1], A. Hughes-Hallett[1], T. MacKinnon[1], K. Shetty[1], A. S. Najmaldin[2], G.-Z.Yang[1], A. Darzi[1]

[1]*The Hamlyn Centre, Institute of Global Health Innovation, Imperial College London, UK*
[2]*Department of Paediatric Surgery, Leeds General Infirmary, Leeds, UK*
t.cundy@imperial.ac.uk

INTRODUCTION

Fields of highest uptake and potential growth in robotic surgery include those involving pelvic, trans-oral, retroperitoneal, and paediatric procedures. Common features of these clinical application areas are spatially confined operative environments with limited access [1]. Instinctively, smaller instruments are better suited in these settings, however balance exists in miniaturisation of instruments as smaller calibre risks compromise in structural rigidity, durability and concentration of force over tip surface area. As scalability limits are reached, focus shifts to design and control mechanism solutions for optimizing performance capabilities. These technical goals are best achieved with robotic technology.

Despite anecdotal opinion that robot-assistance is well-suited for complex surgical tasks in diminutive workspaces, this remains unsupported by empirical evidence and thresholds are poorly defined. The aim of this study was to compare 7-degrees-of-freedom (DOF) robotic instruments with conventional 4-DOF non-robotic instruments, and to investigate the influence of workspace size and instrument characteristics on task performance.

MATERIALS AND METHODS

Three pairs of needle driver instruments were compared; 3mm non-robotic mini-laparoscopy instruments (Karl Storz), 5mm robotic instruments and 8mm robotic instruments (Intuitive Surgical) (Figure 1). Participants performed single intra-corporeal sutures with each of the 3 instrument pairs within each of 3 workspace sizes (Figure 2). The task was assembled within a modified Pediatric Laparoscopic Surgery (PLS) simulator such that it could be interchanged between 3 different sized cylindrical workspaces with diameters of 4cm, 6cm and 8cm respectively and a constant height of 4cm. The task was positioned at the cylinder base. The optical-axis-to-target angle was perpendicular. The cylinders were formed by wire frame mesh coated with elastic foam medical tape. The instrument manipulation angle was 35 degrees and distance from the port sites to task position site was 16 cm. The suture material used was 4/0 monofilament pre-cut to 8cm. Port placement was configured according to the PLS manual, separated by a distance of 9.5cm [2]. All tasks were undertaken with 2-D standard definition optics to standardise visual quality.

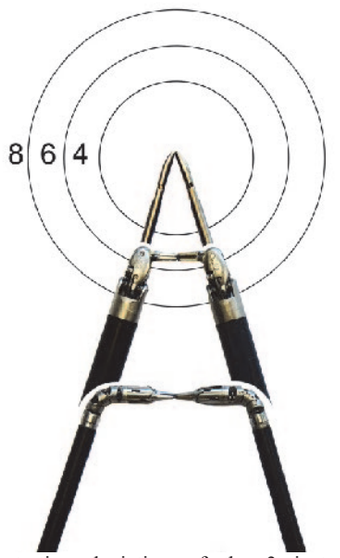

Fig. 1. Illustrative depiction of the 3 instrument pairs investigated (3mm non-robotic, 8mm robotic, and 5mm robotic positioned top, middle, and bottom respectively) in maximum positions of distal angulation. The 3 workspace diameter sizes (8cm, 6cm, and 4cm diameter) are infraposed and drawn to scale with respect to the instruments.

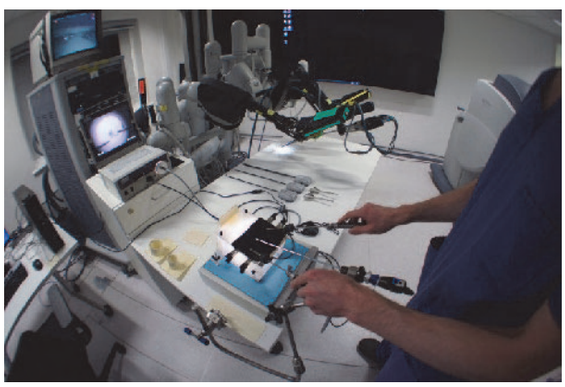

Fig. 2. Overview of the experimental set-up demonstrating a participant engaged with the non-robotic instrument task (foreground) and also the un-docked slave component of the robot (background).

Participants were surgeons recruited from one university hospital trust. A minimum proficiency standard of 200 seconds for both laparoscopic and robotic tasks was set for participants to be eligible for study inclusion. A randomised double-crossover study design was

implemented with 3 randomisation sequences run for each participant to determine order of robotic or non-robotic instruments, order of robotic instruments, and order of workspace sizes. Primary outcomes were validated objective task performance scores [2] and instrument workspace breaches. Workspace breach counts were regarded as the number of times that the instrument made contact with the internal surface of the cylinder. Secondary outcomes included assessment of perceived task workload using the NASA Task Load Index (NASA-TLX) and subjective impressions. One-way ANOVA was used to compare outcomes between instruments and workspace sizes. Statistical analysis was undertaken using SPSS version 21.0 (IBM Corp).

RESULTS

A total of 20 surgeons performed 180 suture task repetitions. All tasks were able to be completed successfully. Task performance scores decreased when spatial constraints were imposed by smaller workspace sizes. Scores were highest (best) for 3mm non-robotic instruments, and lowest for 8mm robotic instruments. A borderline significant difference was observed between instruments for task scores in the smallest workspace size (Figure 3a, $P = 0.052$). An indirect relationship was seen between workspace boundary breaches and workspace size. A higher number of workspace breaches occurred with robotic instruments compared to non-robotic instruments across all workspace sizes, and this was statistically significant for the smallest size (Figure 3b, $P = 0.007$). There was no significant difference between NASA-TLX ratings for instruments amongst each workspace size, although higher perceived task workload was observed for both smaller workspace sizes and robotic instrument use. When asked to select one instrument pair for preferred clinical use, 3mm instruments (45%) were the most favoured, and 5mm instruments were the least favoured (15%).

DISCUSSION

Our findings identify a workspace threshold of between 4cm and 6cm diameter (or between 50cm^3 and 113cm^3) for which robotic instruments do not confer an objective or subjective advantage over 3mm mini-laparoscopy instruments for a complex bimanual reconstructive task. These spatial dimensions are clinically relevant for a variety of anatomical locations in which feasibility of robotic surgery is currently being assessed; such as the oropharynx, rectum, mediastinum, paediatric retroperitoneal space, infant thorax, and anterior neck for endoscopic thyroid surgery. The longer curve radius of the 5mm instrument continuum wrist design likely accounts for higher workspace breach counts compared to 8mm instruments that possess a compact EndoWrist®.

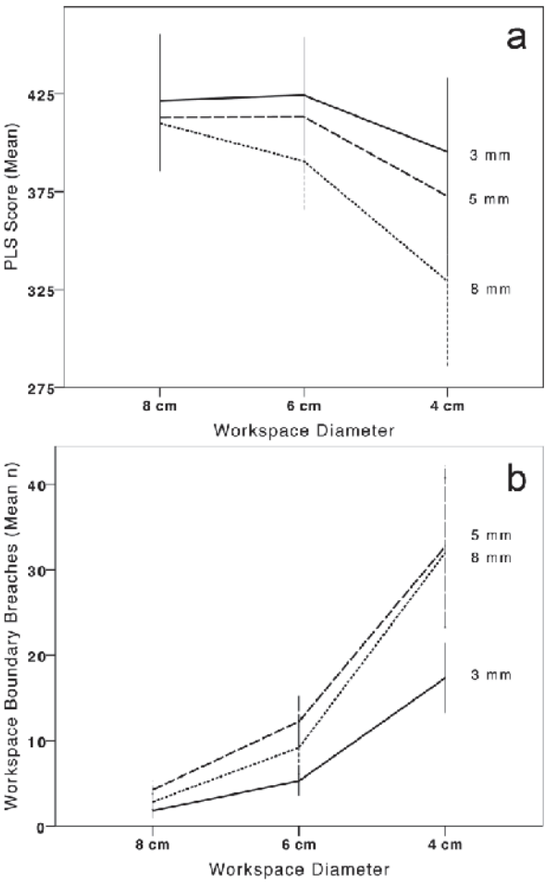

Fig. 3. (a) Objective task scores (higher score = superior performance) and (b) workspace breach counts for instrument pairs amongst the workspace sizes investigated (95% CI).

There are countless variations of ergonomic settings for the experimental set-up used in this study. Although our arrangement was felt to be representative of optimum set-up [3], variations in factors such as port positioning, distance to target site and robot docking might yield differences in outcomes.

Future challenges for enhanced robotic instrument design in this setting will include miniaturisation, shortened articulating segment curve radius, improved control interfaces, and limiting DOF redundancy.

REFERENCES

[1] Berlinger NT. Robotic surgery - squeezing into tight places. NEJM. 2006 May;354(20):2099-101.

[2] Azzie G, Gerstle JT, Nasr A, Lasko D, Green J, Henao O, et al. Development and validation of a pediatric laparoscopic surgery simulator. J Pediatr Surg. 2011 May;46(5):897-903.

[3] Hanna GB, Shimi S, Cushieri A. Influence of direction of view, target-to-endoscopic distances and manipulation angle on endoscopic knot tying. Br J Surg. 1997 Oct;84(10):1460-4.

A Haptic Simulator for Upper Gastrointestinal Endoscopy

S. Chakravarthy, A. M. Rao, G. K. Ananthasuresh

Mechanical Engineering, Indian Institute of Science, Bangalore, India

{sc, ashwinmr, suresh}@mecheng.iisc.ernet.in

INTRODUCTION

We present a haptic simulator for upper gastrointestinal (GI) endoscopy. It consists of a novel three Degree-of-Freedom (DoF) haptic device together with visualization and a model for computing forces. Endoscopy is a minimally invasive procedure where a flexible tube is inserted through the digestive tract for medical examination and, in recent years, for surgical procedures too. Endoscopists ought to have high degree of hand-eye coordination and experience gained from large variety of cases. This requirement can be best addressed by Virtual Reality (VR) based training simulators whose benefits include versatility in creating disease scenarios, quantitative evaluation of trainee's skills, and low cost of training [1]. However, for the training to be effective, the VR simulators should have a haptic device for realistic force feedback. This paper presents our efforts towards the development of such a device and its integration with a control system and graphical visualization.

BACKGROUND AND MOTIVATION

Two commercial endoscopy training devices from Immersion Corporation (http://www.immersion.com) and Simbionix (http://www.simbionix.com) exist in the market. They focus primarily on visualization and test cases. Many developmental efforts on haptic interfaces for endoscopy are reported in the literature. Ikuta et al. [2] developed an endoscopic training system with force feedback through a ball driven by four motors. Yi et al. [3] built a two-DoF colonoscopy simulator with folding guides and a belt drive. Recently, researchers from Ecole Polytechnique Fédérale de Lausanne (EPFL) designed a compact haptic interface for colonoscopy using V-type friction rollers and customized brakes [4].

We aim to overcome the following limitations of existing devices.

- Brake-like force feedback with limited active force control.
- Fewer DoF and/or DoF coupled to one another.
- Use of gears and belt drives, which cannot reproduce forces with high fidelity in haptics.

Unlike regular haptic devices, in which maximizing forces and/or torques are of prime importance, here it is important to have a device that can reflect back small forces and torques with high fidelity. These requirements call for special care in design of the haptic device. We use capstan drives with pre-tensioned wires that provide cogless backdrivable transmission. We also reduce inertia by placing one of the actuators at the base. In addition to translational and rotational DoF, we also introduce an additional DoF in the radial direction. This additional DoF can simulate the passage through the critical junction seperating the esophagus (food-pipe) and the trachea (wind-pipe). Like a few reported simulators, ours too permits the use of an actual endoscope and thus it enhances the realiasm in training.

DESIGN CONSIDERATIONS

The simulator consists of two parts: a haptic device and virtual reality visualization environment. The former is an impedance-type haptic device consisting of actuators and sensors for imparting kinesthetic force sensations to the user. The latter consists of interactive graphical rendering and force-computation model. Our physics-based computation model gives reaction forces and global deformation using real-time Finite Element Analysis (FEA). Currently a 2D linear FEA is implemented. The two systems communicate with each other through a serial port.

Manoeuvres carried out by an endoscopist can be categorised into three essential DoF: longitudinal, radial and rotational. Furthermore, the kinematics of the haptic interface should be similar to the actual endoscopy procedure. Rotational DoF is one of the important DoF, which some doctors use to rotate the scope by twisting his/her torso. To cater to this need, the haptic interface is required to have infinite rotational capability. Most upper GI endoscopy procedures end at the duodenum, which is located at ~0.7-0.8 m from the mouth. This establishes the workspace requirement for the longitudinal DoF. In addition, provision should be made for easy removal and re-insertion of the endoscope. The novel DoF of radial motion of the endoscope and its importance were noted above. The ranges of force and torque are consistent with those in [4].

DESIGN AND VALIDATION

As shown in Fig. 1, we use a circumferentially actuated mechanism [5] to provide the radial DoF. The mechanism consists of eight triangular elements that fold radially inwards applying radial forces on the endoscope. It is driven by a capstan drive that applies a torque of 1.17 N-m. The longitudinal DoF is achieved by a carriage moving on a 1 m-long rail guide. The carriage is actuated by a capstan drive whose maximum speed is set at 4 m/s and maximum force at 3.5 N on the carriage. The motor on the carriage provides independent unlimited rotary motion to simulate torque on the endoscope. Latching of the endoscope to the carriage is achieved using a specially designed snap-fit

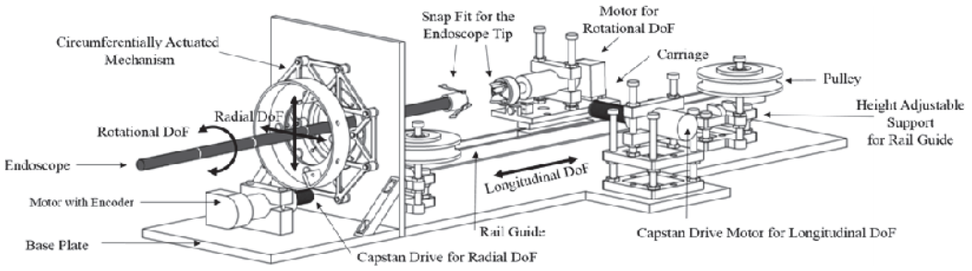

Fig. 1. Schematic of an endoscopic haptic display system.

mechanism attached to the tip of the endoscope. The force for snap-fit is designed to be less than 0.5 N on the endoscope. When the endoscope is pulled out, the latch releases naturally and thus simulating the real scenario.

Maxon DC motors with a maximum torque of 176 mN-m are used as actuators. Sensing of the displacement is through encoders with 1000 counts per revolution. This corresponds to 0.047 mm resolution in the longitudinal direction. Driver circuits are used to supply controlled current to the motors. A proportional-derivative (PD) controller is implemented for all three motors. In the current prototype, all the force controllers run on the dSPACE 1103 DSP. The visualization and force model runs on a regular work-station.

Figure 2 shows the endoscopic simulator system developed in our lab. Experiments were carried out to test the haptic device with the FEA model. Figure 3(a) shows a real-time 2D FEA model of the flexible stomach and Fig. 3(b) shows the force characteristics for an arbitrary exploration of the model by a user. Figure 4 shows the displacement vs. force characteristic for a virtual-wall experiment. The stiffness of the virtual

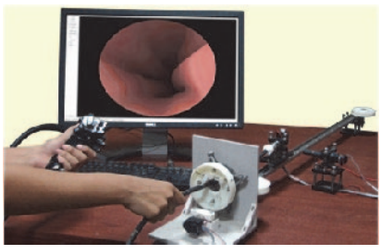

Fig. 2. Prototype of the endoscopic simulator.

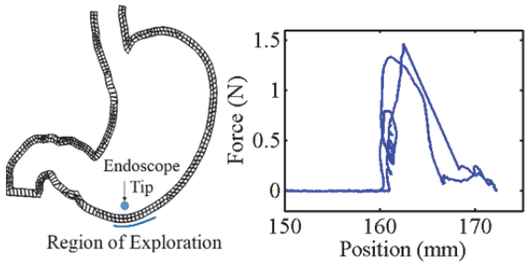

Fig. 3. (a) 2D FEA model of stomach (b) measured force characteristics with the stomach model for region of exploration shown in (a).

wall was set to 500 N/m. These experiments showed that the haptic device and virtual environment work seamlessly to provide accurate force feedback based on the force model.

CLOSURE

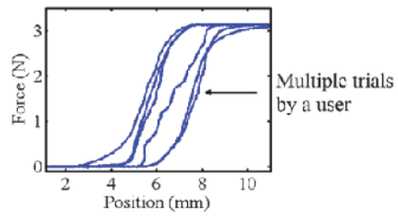

Fig. 4. Displacement vs. force characteristic for virtual wall test.

A three-DoF endoscopic simulator is presented. The haptic device is designed to reflect forces with high fidelity. Ongoing and future work includes: accounting for damping, inertia, and nonlinear stiffness into the FEA model; adopting dynamics-based controller; incorporating ergonomics into the embodiment; and improving visualization with disease scenarios.

ACKNOWLEDGEMENT

This work is supported by the Robert Bosch Centre for Cyber Physical Systems (RBCCPS) at the Indian Institute of Science (IISc), Bangalore.

REFERENCES

[1] S. Haque and S. Srinivasan, "A meta-analysis of the training effectiveness of virtual reality surgical simulators," IEEE Transactions on Information Technology in Biomedicine. 2006; vol. 10, pp. 51-58.

[2] K. Ikuta, M. Takeichi, and T. Namiki, "Virtual endoscope system with force sensation," in Medical Image Computing and Computer-Assisted Interventation—MICCAI'98, ed: Springer. 1998; pp. 293-304,.

[3] S. Yi, H. Woo, W. Ahn, J. Kwon, and D. Lee, "New colonoscopy simulator with improved haptic fidelity," Advanced Robotics, 2006; vol. 20, pp. 349-365.

[4] E. Samur, L. Flaction, and H. Bleuler, "Design and evaluation of a novel haptic interface for endoscopic simulation," IEEE Transactions on Haptics, 2012; vol. 5, pp. 301-311.

[5] J. Patel and G. Ananthasuresh, "A kinematic theory for radially foldable planar linkages," International journal of solids and structures, 2007; vol. 44, pp. 6279-6298.

Computational Simulations of Airflow in Tracheal Compression due to Retrosternal Goitre

R. Cetto[1, 2], A. J. Bates[1], A. P. Comerford[1], G. Madani[3], D. J. Doorly[1], N. S. Tolley[2]

[1]*Department of Aeronautics, Imperial College London, UK*
[2]*Deparment of Endocrine Surgery, Imperial College NHS Healthcare Trust, UK*
[3]*Department of Clinical Radiology, Imperial College NHS Healthcare Trust, UK*
raul.cetto10@imperial.ac.uk

INTRODUCTION

Compressive symptoms from a retro-sternal goitre (RSG) are a common clinical problem which may present with choking, dyspnoea and rarely dysphagia [1]. The correlation between the Radiological finding of constriction and airflow however is poorly understood [2]. The current method of analysing respiratory function is forced spirometry, this method is more specific to lower lung disease and does not always correlate with the degree of tracheal constriction or severity of symptoms[2].

Computed Tomography (CT) is routinely used to assess retrosternal extension of goitres and a constriction of >35% on a single axial slide is considered an indication for surgical intervention [3].

Although routine axial CT images may suffice for evaluating some airway abnormalities, several limitations are associated with single plane images especially when displaying complex 3D relationships [4]. 3D reconstructed images from the original axial CT data sets can help overcome the limitations of axial images by providing a more anatomically meaningful display of complex structures. Computational Fluid dynamics a (CFD) can help understand how tracheal deformations affect airflow and local pressures drops within the trachea [5].

METHODS

Thirteen CT scans of the thorax of patients with retrosternal goitre were obtained retrospectively, of which one was reported as normal. The tracheal lumen within the scan field of view was reconstructed in 3D using Amira Visage 5.2.2. Geometric analysis of the lumen was performed to derive metrics such as the minimum inscribed sphere radius (MISR). Further work will report on morphological classification applied to the data.

The effect of the RSG on tracheal flow resistance is variable; both constriction length and severity are parameters likely to increase tracheal flow resistance. Using a scatter plot of the proportional length of the constriction versus MISR (figure 1) it can be seen that the impact of retrosternal goitre on flow resistance is variable. Quantifying the impact of RSG on flow resistance is difficult from a purely geometric analysis. CFD on the other hand allows precise evaluation under modelling assumptions such as a rigid wall and constant geometry. Work is currently underway to apply this technique to all of the data set.

CT scan data was available for one subject (G13), circled in figure 1, before and after total thyroidectomy. Quasi-steady simulations were performed on both pre and post-operative geometries for normal breathing using the large eddy simulation technique incorporated in the Star-CCM+ package and the results were analysed using MATLAB.

RESULTS

Mean velocity and pressure were studied in both pre- and post-operative CT scans. The pre-operative scan showed a significant constriction along the upper third of the trachea caused by compression of the thyroid gland (figure 2). This causes a large drop in pressure (figure 3) and a high tracheal resistance. In the post-operative case, this constriction is significantly reduced (figure 2) and the resulting flow field resembles that of a normal trachea (with no jet formation in the middle tracheal region - note the threefold reduction in velocity scale). The tracheal resistance is reduced by approximately 90% compared with the pre-operative scan.

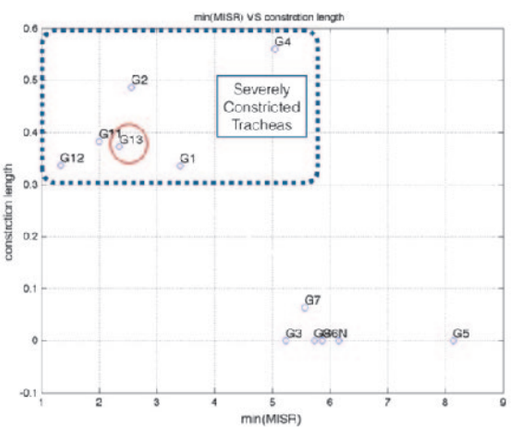

Fig. 1. Shows the relationship of constriction length of the pre-operative geometry (G13) between the minimum MISR and the nature of constriction.

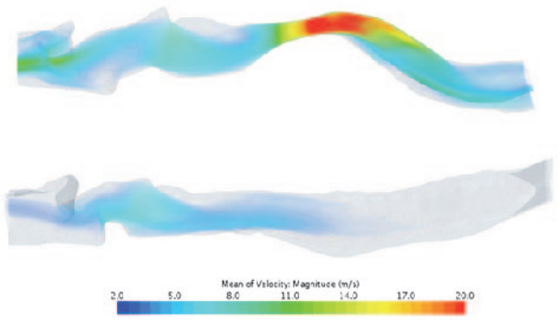

Fig. 2. Sagittal cross section with superimposed computation of airflow velocity on a surface through the centreline in the same patient, comparing pre-operative trachea (Top) and post-operative trachea (Bottom). In the pre-operative CT the constriction leads to a high velocity jet forming in the middle trachea. Images correspond to peak flow during normal ventilation (sinusoidal flow with a 7.5 L respiratory minute volume).

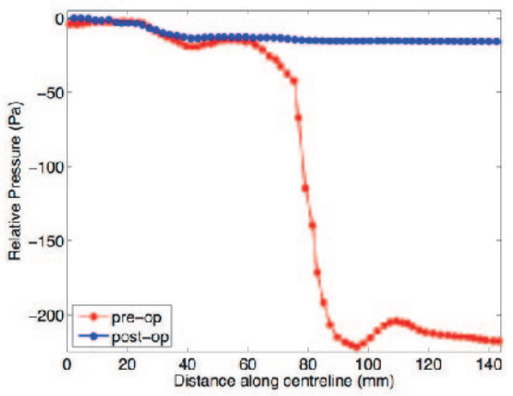

Fig. 3. Relative total pressure ($P\text{-}P_{REF}$), cross-sectionally averaged, plotted along the centreline for both pre and post-operative tracheas demonstrating a large drop through the narrowest point of the pre-operative trachea.

DISCUSSION

Patient specific simulation geometrical analyses with CFD provides an objective method to evaluate the severity of symptoms and surgical outcomes of patients with tracheal compression. This provides a tool for quantitative evaluation of airflow within the large airways, delivering objective outcomes, which can aid patient selection and surgical planning.

A 3D reconstructed trachea from a CT scan provides detailed information about constrictions along the length of the trachea and not only on a single cross sectional plane. This facilitates a correlation between tracheal geometrical measurements and function.

REFERENCES

[1] Chen, Amy, et al. "American thyroid association statement on optimal surgical management of goiter." Thyroid ja (2013).

[2] Albareda, Mercè, et al. "Upper airway obstruction in patients with endothoracic goiter enlargement: no relationship between flow-volume loops and radiological tests." European Journal of Endocrinology 163.4 (2010): 665-669.

[3] Stang, Michael T., et al. "Positional dyspnea and tracheal compression as indications for goiter resection." Archives of Surgery 147.7 (2012): 621-626.

[4] Boiselle, Phillip M., Kevin F. Reynolds, and Armin Ernst. "Multiplanar and three-dimensional imaging of the central airways with multidetector CT." American Journal of Roentgenology 179.2 (2002): 301-308.

[5] Mylavarapu, Goutham, et al. "Validation of computational fluid dynamics methodology used for human upper airway flow simulations." Journal of biomechanics 42.10 (2009): 1553-1559.

Development of a Dynamic Soft Tissue Phantom for Cooperative Control Testing in Robotic Surgery

M. Cattilino[1], R. Secoli[2], S. Galvan[2], A. E. Forte[2], D. Dini[2], F. Rodriguez y Baena[2]

[1]*Department of Mechanical and Aerospace Engineering, Polytechnic of Turin, Italy*
[2]*Department of Mechanical Engineering, Imperial College London, UK*
f.rodriguez@imperial.ac.uk

INTRODUCTION

Tissue motion is a relevant source of error in image guided surgery, which is usually based on pre-operative scans of the area of interest. For instance, during neurosurgical procedures, respiration and cardiac pulsation cause movement and the deformation of the brain tissue. As reported by Felblinger et al. [1], the overall translation and deformation in neurosurgery can be assumed to be in the range of 0.1-0.5 mm toward the caudal direction [2]. Also, the displacement of the brain is affected by a slower deformation, known as "brain shift", which occurs in the first few hours after the opening of the skull and is assumed to be in the range of 0.3-17.4 mm [3,4].

Since 2011, the ACTIVE European research consortium has been working on the design and development of an integrated redundant robotic platform for neurosurgery (www.active-fp7.eu). The project aims to enhance the cooperation between the surgeon and the robot by means of "*Dynamic Active Constraints",* which are a supervised robot control scheme that limits and directs the motion, force and speed of surgical tools: they prevent damage to important areas, as defined on realistic tissue models which are updated intra-operatively on the basis of sensors information [5]. The dynamic brain phantom described here was developed to provide a robust testing platform for the ACTIVE integrated system, and to act as a realistic benchmark to assess overall performance.

In the literature, anthropomorphic dynamic brain phantoms exist, but are mostly static or slow moving, as their main purpose is to provide gold standard measurements for image processing algorithms, where volumetric and/or surface features are used to register the position of the anatomy in the operating theatre. Some of these also reproduce brain shift with the inflation of one or more balloon catheters, positioned inside the phantom, by a controlled volume of liquid (water or air) (e.g. [6-7]), but a quantitative mechanical characterisation of a suitable synthetic analogue to brain tissue, coupled with periodic pulsation and higher frequency deformations, does not appear to have been considered yet.

In this work we present a phantom brain which mimics the displacement of the brain defined as the sum of a semi-radial expansion of the brain surface (e.g. due to pulsatile forces and/or brain shift) and an additional translation of the skull along the caudal direction. This latter translational movement has been incorporated into the design to test the robustness of the ACTIVE project control strategy in the presence of significant skull displacement (e.g. due to respiration or a seizure), which is likely to occur since the test scenario for the project revolves around awake epilepsy surgery with an only partially constrained skull.

MATERIALS AND METHODS

As shown in Fig.1, the system is composed of a translating platform (2) that moves along the normal direction, referred to as the base platform (1), by means of a cam mechanism driven by a stepper motor. By changing the eccentricity of the cam, it is possible to achieve different amplitudes of translation, while predefined frequencies are obtained by varying the speed of the motor. The phantom brain is fixed on top of the moving platform inside a *Polylactic Acid* (PLA) skull, manufactured using a 3D printer (Ultimaker2, Ultimaker inc.).

Segmentation of a human Magnetic Resonance Imaging (MRI) dataset obtained from an open-source database (MIDAS/NAMIC dataset 01017) was performed to generate a realistic volumetric model, which was subsequently used to rapid prototype the shape of the skull support (in blue, Fig. 1). A second model was printed out of the brain shape and used to create a silicone mould for the phantom (Fig. 2, right). The phantom model used in these tests is composed of PVAc, with a 6% solution of PVA powder in distilled water. Freeze/thaw cycling was carried out to empirically obtain viable properties for the final phantom.

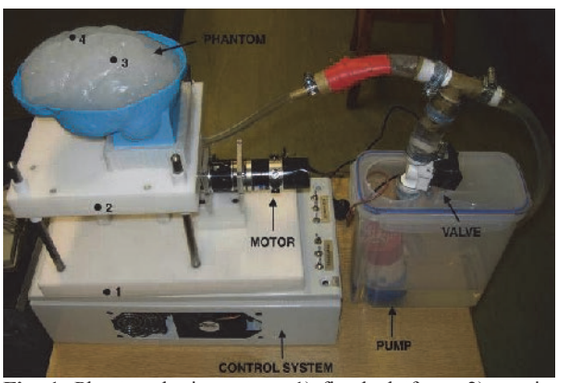

Fig. 1. Phantom brain system: 1) fixed platform, 2) moving platform, 3) silicone phantom brain, including actuation box with water pump and tank used to fill and deform the brain.

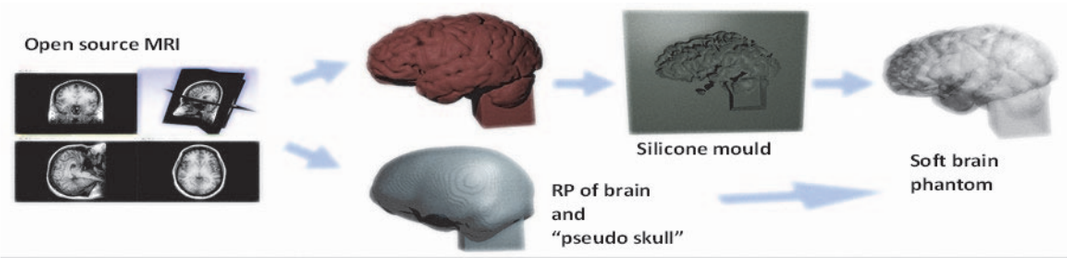

Fig. 2. Brain phantom development workflow: from brain MRI scan segmentation (left) to final soft phantom manufacture (right).

The deformation of the phantom brain is controlled by a hydraulic system composed of an inflatable balloon inserted inside the phantom and a pump/valve system that regulates the flux of water. A microcontroller (Arduino Uno©) is used to control the stepper motor as well as the hydraulic system. The latter is used to perform a change of inflation/deformation of the balloon in a range of amplitudes and frequencies which are multiples of the minimum physiological deformation. The controller is driven by a switch panel that allows changing the deformation among 8 preselected configurations. The overall system was sealed in order to prevent possible water leakage.

CALIBRATION AND VALIDATION

To avoid modelling complexities, the phantom brain and the hydraulic system were treated as "black boxes", meaning that the system was calibrated via an iterative method. A motion capture system (Optotrack© Certus, Northern Digital Inc.), with active markers evenly distributed over the exposed surface of the phantom brain (Fig.1, 3-4), was used to record the deformation and fine tune the synchronization of the hydraulics.

RESULTS

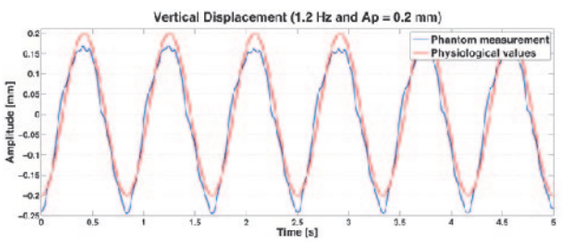

Fig. 3. Theoretical displacement obtained with the physiological values of the movement (red) compared with the function obtained from the recorded data (blue).

As shown in Fig. 3, a caudal deformation of the phantom brain corresponding to the mean physiological frequency of a pulsating heart (1.2 Hz [8], with amplitudes within the range described in [1]) was achieved by the system, after iterative calibrations of the reference signals for the pump and the valve.
Subsequently, tests with the system running for an average of 60 sec. were carried out in order to test the phantom's ability to provide any selected amplitude and frequency, with results reported in the Table 1.
Finally, a test was performed to measure the highest frequency achievable for the maximum deformation obtained with the phantom: 0.05 Hz for a peak amplitude of 0.74 mm.

Table 1. Mean values (and standard deviation) for the recorded data, compared to the corresponding physiological measurements associated with brain motion.

	Amplitude (mm)	Frequency (Hz)
Physiological	0.1-0.5	1.2
Recorded	0.2157 (A_P)	1.1333
ST Dev.	0.0137	0.1155

DISCUSSION

The majority of brain phantom applications available in the literature relates to static or slows moving benchmark imaging systems. In this work, we presented a new dynamic phantom built to test aspects of the EU FP7 ACTIVE robotic neurosurgical suite, which is able to generate physiological deformations and translations in the range of frequencies (0.05-1.2 Hz) and amplitudes (0.22-0.74 mm) associated with brain surgery. Ongoing work is now focussing on the tuning of a novel, hydrogel-based material blend for the phantom, which will help the dynamic system to more closely reflect the physiological measurements associated with brain shift. Additionally, future work will aim to increase the range of amplitudes and frequencies which the hardware can replicate and to design a deformation model which will help to improve the system controller.

REFERENCES

[1] J. Felblinger et al., "Effects of physiologic motion […]", NMR Biomed 11, 107–114 (1998).
[2] D. Greitz et al., "Pulsatile brain movement and associated hydrodynamics […]", Neuroradiology (1992) 34:370-380.
[3] P. Hastreiter et al., "Strategies for brain shift evaluation", Med. Image Anal. 8 (2004) 447–464
[4] M. Oskar et al., "Real Time 3D Shift […]", IPMI'99, LNCS 1613, pp. 42-55, 1999.
[5] Bowyer, S.A. et al., "Active Constraints/Virtual Fixtures: A Survey", Robotics, IEEE Transactions on, Vol. 30, no.1, pp.138,157, Feb. 2014
[6] S. Chen et al., "An Anthropomorphic Polyvinyl Alcohol Triple-Modality Brain […]", MICCAI 2010, Part II, LNCS 6362, pp. 92–100, 2010.
[7] I. Reinertsen et al., "A realistic phantom […]", Med. Phys. 33 (9), September 2006".
[8] E. Marieb, "Human anatomy and physiology" Sixth edition, Benjamin Cummings, Pearson Ed.

Trainee Learning Curve for Transoral Surgery with a Novel Flexible Endoscopic Surgery System

D. Clayburgh[1], N. Godse[1], H. Choset[2], U. Duvvuri[1]

[1]*Veterans Affairs Pittsburgh Health System, Department of Otolaryngology, University of Pittsburgh Medical Center, USA*

[2]*Biorobotics Laboratory, Carnegie Mellon University, USA*

duvvuriu@upmc.edu

ABSTRACT

Transoral robotic surgery (TORS) has revolutionized treatment of oropharyngeal tumors. However, TORS may not be feasible with current robotic surgical systems in all patients due to poor exposure. Recently, the Medrobotics Flex® System, a computer-assisted flexible endoscope, has been developed specifically for transoral applications. This consists of a computer-driven flexible endoscope with a HD digital camera and attached instrument channels that allows for transoral visualization and access to the oropharynx and larynx. As with any technology, the learning curve needs to be evaluated to faciliate adoption [1,2]. The aim of this study was to assess the learning curve and ease of use for new users of the Flex® System.

METHODS:

Residents and fellows were recruited as study subjects. After an introduction to the Flex® System, subjects were asked to perform four tasks with the Flex® System on an anatomic model head. The tasks included: 1) exposure of the right tonsil, grasping the anterior tonsillar pillar, and tracing a tonsillectomy incision; 2) exposing the epiglottis, grasping the epiglottis, and touching an electrocautery instrument to the tip; 3) exposing the glottis and touching the bilateral vocal processes; and 4) exposing the glottis, grasping the interarytenoid area, and touching an electrocautery instrument to this. Time to completion of each task was recorded, and the movement of the Flex® Scope was monitored using an electromagnetic spatial tracking system. The subjects performed these tasks 4 times over the course of a week to establish a learning curve for proficiency at these surgical tasks.

RESULTS:

Thirteen (13) subjects were recruited for the study. These subjects were classified as junior residents (within the first 3 years of PG training), senior residents (PG 4-5) and Fellows (PG 6-7). While there was considerable variability on the first round of tasks, all subjects demonstrated rapid improvement with all tasks. For example, the time to completion of the task involving driving the system to the larynx decreased from a mean of 184sec initially (range 60 to 596) to 65sec (range 49 to 92) by the fourth round (p=0.01). Mean distance travelled by the tip of the Flex® Scope to visualize the glottis decreased from 27.1cm (range 11.4 to 85.5) to 12.6cm (range 8.3 to 19.7) by the fourth round (p=0.04). Similar significant improvements were noted with the other two tasks as well.

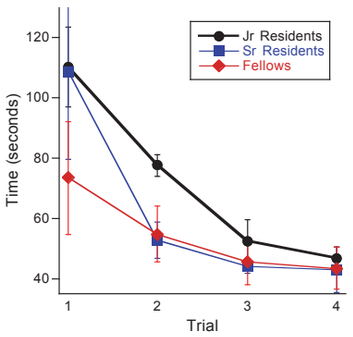

Fig. 1. The learning curve to drive the Flex® System to the epiglottis in a training mannequin. All subjects improved to a baseline proficiency in 4 trials. The learning curve was less steep for Fellows and Senior Residents.

CONCLUSION:

Novice users of the Flex® System rapidly gain proficiency with driving this computer assisted flexible endoscope with simple surgical tasks within the oropharynx and larynx. While further study of actual surgical procedures within cadaveric specimens will be needed to provide data that is more applicable to clinical situations, this study suggests that proficiency with the Flex® System may be gained quickly. This system may provide a useful tool for the head and neck surgeon to visualize and access the oropharynx and larynx for tumor resection.

REFERENCES

[1] Nelson EC, Gottleib AH et al. Robotic cholecystectomy and resident education- UC Davis experience. Int J Med Robot. 1013 Dec 4; doi: 10.1002/rcs.1554.

[2] Leonardis RL, Duvvuri U, Mehta D. TransoralmRobotic-assisted lingual tonsillectomy in the pediatric population. JAMA Oto HNS. 2013;139(10):1032-36.

Concentric Tube Robots for Transurethral Prostate Surgery: Matching the Workspace to the Endoscopic Field of View

R. J. Hendrick[1], C. R. Mitchell[2], S. D. Herrell[2], R. J. Webster III[1]

[1]*Deparment of Mechanical Engineering, Vanderbilt University, USA*

[2]*Department of Urologic Surgery, Vanderbilt Medical Center, USA*

{richard.j.hendrick, christopher.r.mitchell, duke.herrell, robert.webster}@vanderbilt.edu

INTRODUCTION

Transurethral laser surgery using a flexible multi-backbone robot was recently demonstrated by Simaan et al. for bladder resection [1]. For transurethral prostate resection, thinner flexible manipulators are desirable. We have developed a hand-held system that transurethrally deploys two concentric tube robots through an 8.3 mm diameter rigid endoscope [2], as shown in Figs. 1 and 2. The purpose of this system is to facilitate Holmium Laser Enucleation of the Prostate (HoLEP), a surgery that is rarely used despite its demonstrated clinical benefits, because it is so challenging for the surgeon to perform [3]. The objective of the surgery is to remove prostate tissue transurethrally with a laser, and the challenge arises from the need to angulate the entire endoscope (impeded by a great deal of soft tissue) to aim the laser. Our system assists by providing one manipulator to aim the laser and a second to retract tissue, exposing desired targets to the laser.

The purpose of this paper is to explore optimal design of the concentric tube manipulators. We define an optimal design as one in which there is maximal overlap between the workspace of the manipulator and the space viewable by the endoscope. Here, we restrict our attention to the special case in which the concentric tube robot consists of two tubes, where the outer tube is straight and the inner tube is circularly curved. We note that more complex concentric tube manipulators are possible, such as the three tube robot shown in Fig. 2, but leave more complex cases to future work. Based on this, our objective is to choose (1) the curvature of the inner tube, and (2) the distance behind the camera lens inside the endoscope where the base of the workspace should occur.

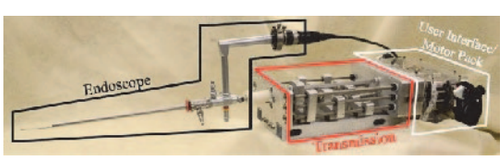

Fig. 1. This system is made up of three sections: a rigid endoscope that the manipulators pass through, a transmission where rotation and translation are applied to tube bases, and a user interface enabling the surgeon to control the endoscope and both manipulators. See [2] for a detailed description of this robot.

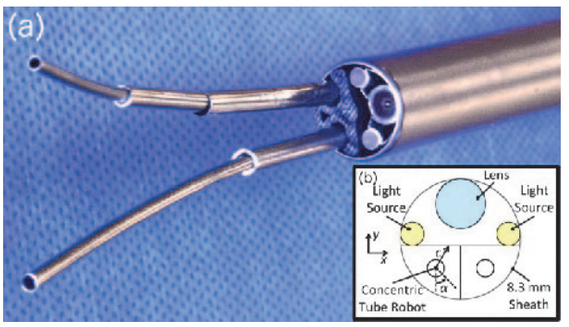

Fig. 2. (a) Two concentric tube manipulators are deployed through the 8.3 mm endoscope. One aims the laser fiber, and the other retracts tissue. (b) A cross section of the endoscope.

MATERIALS AND METHODS

The rigid endoscope mounted to our robotic system (Storz, Inc. 27292 AMA) delivers a camera lens and two fiber optic light sources through an 8.3 mm outer diameter sheath, with cross section illustrated in Fig. 2. This endoscope has a 6° angle of view, 103° field of view, 30 mm depth of view, and the lens is located 1.2 mm from the tip of the endoscope. Based on these specifications, the visualization volume is modeled as a cone with its vertex at the lens as shown in Fig. 3.

The manipulator that guides the laser fiber is currently the two-tube, 3-DOF robot. It has a straight, rigid stainless steel outer tube that can translate axially, and an elastic, curved nitinol inner tube that can both translate and rotate axially. The forward kinematics for this simple manipulator can be computed analytically [2], and the workspace can be analytically described by a revolved circular arc with a cylinder appended (here we assume maximum arc length is limited to an arc that sweeps 90° and that the outer tube is perfectly rigid).

For the optimization, we place the robot exit point at the position within the endoscope cross section shown in Fig. 2. We note that this is not the only possible exit point (the tool channels shown in Fig. 2 are a design choice, not part of the endoscope), but it is roughly equidistant from the boundary defined by the endoscope sheath, a line tangent to the light sources, and the midline of the endoscope between the two manipulators. We denote the absolute tube rotation with α, the distance from the tube axis to the boundary with $c(\alpha)$, the radius of the inner tube with r (assumed to be 0.5

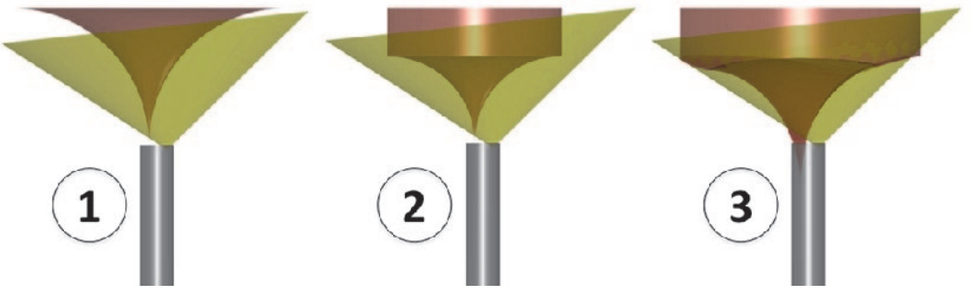

Fig. 3. Manipulator workspace (red) overlaid on visualization volume (yellow) for: (1) tube design (κ =30.1 m^{-1}, coverage=8.9%) in [2], (2) optimal design (κ =47.8 m^{-1}, coverage=29.5%) with workspace beginning at endoscope tip, and (3) optimal design (κ =34.6 m^{-1}, coverage=64.9%) when the workspace begins a short distance inside the endoscope.

mm here), the curvature of the inner tube with κ, the angle subtended by the curved portion of the inner tube with θ, and the critical angle at which the inner tube collides with the boundary as θ_c. This angle and the distance behind the tip of the endoscope where the straight tube should end to achieve it, d, are given by:

$$\theta_c = \cos^{-1}\left(\frac{c\kappa - 1}{r\kappa - 1}\right)$$
$$d = \kappa^{-1}\sin(\theta_c).$$

From this, the trumpet-like workspace boundary, $\boldsymbol{b}$, can be shown to be

$$\boldsymbol{b} = \begin{pmatrix} -\kappa^{-1}\sin(\alpha)(\cos(\theta) - 1) \\ \kappa^{-1}\cos(\alpha)(\cos(\theta) - 1) \\ \kappa^{-1}\sin(\theta) - d \end{pmatrix},$$

where $\alpha \in [0\ 2\pi)$, $\theta \in [0\ \pi/2]$. The closed curve defined at $\theta = 90°$ forms the bottom of a cylinder which extends out axially and forms the remainder of the workspace boundary (the cylindrical space can be accessed by extending both tubes simultaneously).

RESULTS

To choose the optimal curvature for the curved tube within a range of 20 to 70 m^{-1} we began by discretizing this range into 100 evenly spaced values. For each, the workspace was computed and the percentage of the visualization volume covered was determined. This was done by discretizing the visualization cone into 0.5 mm isotropic voxels, and counting as "covered" those voxels whose centers were inside the manipulator's workspace. Three different example cases of overlaid workspace and view volume are shown in Fig. 3 and view volume coverage as a function of curvature is shown in Fig. 4.

DISCUSSION

The value of optimizing tube design is illustrated by the ability to access a greater percentage of the endoscope visualization volume than the initial tubes in [2] could achieve. The most noteworthy result from this study is that placing the base of the workspace a short distance inside the endoscope is useful for reaching the maximum percentage of the visualization volume. To extend this design framework, one could consider also optimizing the exit location in the endoscope cross

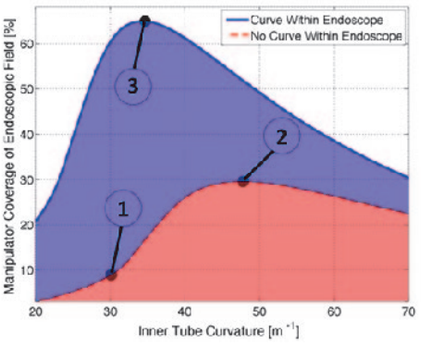

Fig. 4. Manipulator coverage as curvature is varied. The labeled points correspond to the cases illustrated in Fig. 3.

section, adding additional curved tubes to the end of the manipulator, or using curves beyond 90°. One could also consider using an endoscope with a different angle of view.

Before studying these additional parameters, however, we intend to rigorously test the system in bench-top and cadaver experiments, to determine whether additional optimization variables are needed, and whether 3 DOF manipulators are sufficient to accomplish the surgery effectively and easily.

REFERENCES

[1] R. E. Goldman, A. Bajo, L. S. MacLachlan, R. Pickens, S. D. Herrell, and N. Simaan. Design and Performance Evaluation of a Minimally Invasive Telerobotic Platform for Transurethral Surveillance and Intervention. IEEE Transactions on Biomedical Engineering. 2013;60(4):918-25.

[2] R. J. Hendrick, S. D. Herrell, and R. J. Webster III. A Multi-Arm Hand-Held Robotic System for Transurethral Laser Prostate Surgery (in-press). IEEE International Conference on Robotics and Automation. 2014.

[3] J. E. Lingeman. Holmium laser enucleation of the prostate - if not now, when? The Journal of Urology. 2011;186(5):1762-63.

Acknowledgements: This work was funded in part by the National Science Foundation (NSF) under IIS-105433, in part by the National Institutes of Health (NIH) under R01 EB017467, and in part by the Vanderbilt Initiative in Surgery and Engineering. The content is solely the responsibility of the authors and does not necessarily represent the official views of the NSF or NIH.

Design and Evaluation of a Concentric Tube Robot for Minimally-Invasive Endoscopic Paediatric Neurosurgery

V. Bodani[1,2], H. Azimian[1], T. Looi[1], J. M. Drake[1,2]

[1]*Center for Image Guided Intervention and Therapeutic Innovation, The Hospital for Sick Children, Canada*
[2]*Department of Neurosurgery, University of Toronto, Canada*
vivek.bodani@utoronto.ca

INTRODUCTION

Neuroendoscopy is a minimally-invasive surgical technique that has played an increasingly important role in the treatment of neurosurgical disease [1]. This modern technique has provided neurosurgeons with improved access to and visualization of deep-seated lesions within the ventricles of the brain while causing minimal approach-related trauma to critical anatomical structures. As a result, the morbidity, mortality, and cost associated with open transcranial approaches have been greatly reduced [1]. Despite this progress, current endoscopic instruments still lack the required size, accuracy, dexterity, and reachability to address more complex neurosurgical pathology [1-2]. In such cases, neuroendoscopic procedures remain technically challenging and time consuming leading to increased surgeon fatigue, errors and complications [3].

Concentric tube continuum robots consist of telescoping, precurved, superelastic tubes [4]. When the tubes are rotated and translated relative to each other, robot shape and tip position and orientation can be precisely controlled. Such robots may be able to reach deep-seated targets within small, complex environments of the brain (i.e. ventricles), while avoiding adjacent neuroanatomical structures. The added dexterity and reachability has the potential to overcome the limitations of standard neuroendoscopic techniques and expand their scope to more complex and comprehensive intraventricular procedures. We have developed a miniaturized, teleoperated, concentric tube robot for intraventricular neuroendoscopy. This paper presents an overview of the system design, performance, and its ability to perform an endoscopic third ventriculostomy (ETV) in a phantom hydrocephalus brain model.

MATERIALS AND METHODS

This dextrous suction/irrigation tool to clear blood products, aspirate cyst contents, and dissect soft tissues is conceived as an independent tool, or used in combination with other dextrous tools within the same endoscopic portal. All instruments and a stereo-endoscope (VisionSense VSII) pass into the ventricles via a stainless steel trocar. The suction/irrigation tool consists of two telescoping Nitinol tubes. The inner tube is straight (length, L=254 mm; inner diameter, ID=1.57 mm; outer diameter, OD= 1.92 mm) and the outer tube has straight (L=159.5 mm, ID=2.25 mm, OD=2.48 mm) and curved sections (L=34.5 mm, curvature=0.027 m^{-1}). The resultant curvature of the overlapping segment of the manipulator (curved segment of outer tube and straight inner tube) is 0.012 m^{-1}. This simplified design has three advantages: 1) it eliminates torsional interactions which can lead to undesirable snap-through effects (seen with 2 curved tubes), 2) it has a closed-form solution to the forward and inverse kinematics, and 3) it is able to reach points along the robot's centerline (z-axis), which is not possible with 2 curved tubes within small workspaces because of torsion. The resultant workspace is an inverted cone with a base diameter of 18.4 mm and height of 40 mm (Figure 1).

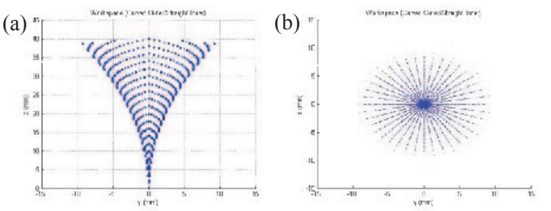

Fig. 1. Reachable workspace of micromanipulator, (a) cross-sectional view at x = 0, and (b) top-view.

The actuation unit is assembled on an aluminum mount and consists of a stepper motor (NMB PG25L-D24-HHC1) that rotates the outer tube and two linear actuators (Firgelli L12, 50 mm stroke) that provides tube translation. Rotary position feedback is obtained using a 2-phase resistive position sensor (ALPS RDC80). The linear actuators have built-in potentiometers for linear position feedback. The actuation unit is powered by a Dell power supply unit. Real-time position control is implemented in MATLAB/Simulink 2013a running on an Intel i7, 2.94 GHz processor with a Windows 7 operating system. The controller interfaces with the motor drivers via a National Instruments PCI-6224 data acquisition card.

RESULTS

To evaluate position accuracy, the robot was instructed to move in a specific sequence between 5 positions within a 10 mm cube for 30 cycles. Front and side views of the robot's motion were captured using two Logitech C615 cameras and position extracted using ImageJ. The Euclidean norm between the instructed position and the barycenter of achieved positions was calculated. The

average tip position error was 0.99 mm. The robot accurately followed a vertical line and circular-path trajectory (Figure 2). Sources of error include tube dimension measurements, manipulator assembly (tubes not concentric), position measurement/image calibration, modeling (friction, motor dynamics), and motor errors (resolution, gear backlash).

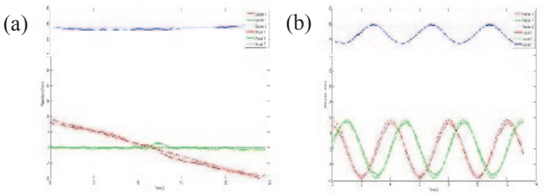

Fig. 2. Robot path accuracy, (a) following vertical line trajectory, and (b) following circular trajectory. Dashed line: desired trajectory, solid line: actual trajectory, red: x-coordinate, green: y-coordinate, blue: z-coordinate.

The robot successfully performed an ETV in a patient-specific silicone brain phantom with realistic intraventricular anatomy and a thinned-out third ventricular floor (Figure 3). Via a transcortical approach, the robot and stereoendoscope were successfully inserted through a trocar into the right lateral ventricle. Using a Novint Falcon master, the manipulator was steered from the trocar into the right lateral ventricle, through the foramen of Munro, and to the third ventricle without touching the surrounding neuroanatomy (fornix, choroid plexus, and veins). The robot was steered to the floor of the third ventricle between the infundibular recess and mammillary bodies. The tip of the inner tube was used to bluntly perforate the floor. By controlling the manipulator's depth of insertion through the floor and moving the tip in different directions, the ventriculostomy was widened. The manipulator was then retracted into the trocar, which was then advanced to the prepontine cistern to visualize the basilar artery and rule out persistent membranes. We were able to manually irrigate and aspirate fluid from the ventricles via the lumen of the manipulator using a syringe. Performance was limited by significant time delay between the master and slave systems, and the lack of an active repositioning system for the trocar/endoscope.

DISCUSSION

We have successfully developed a miniaturized, teleoperated, 3-DOF concentric tube robot for pediatric neuroendoscopy. The accuracy, dexterity, and reachability of the instrument were sufficient to successfully perform an ETV in a brain phantom. Future work will focus on additional phantom and animal testing, including other neuroendoscopic procedures (aqueductoplasty, choroid plexus cauterization, intraventricular cyst/tumor resection, lamina terminalis fenestration), improvements in positioning accuracy, system responsiveness (Jacobian-based controller), and workspace (higher outer tube curvature), and the development of automated irrigation/suction and trocar/endoscope repositioning systems.

REFERENCES

[1] Chowdhry S, Cohen AR. Intraventricular neuroendoscopy: complication avoidance and management. World Neurosurg 2013;79(Suppl 2):S15.e1–10.

[2] Marcus HJ, Seneci CA, Payne CJ, Nandi D, Darzi A, Yang GZ. Robotics in keyhole transcranial endoscope-assisted microsurgery: a critical review of existing systems and proposed specifications for new robotic platforms. Neurosurgery 2014;10(Suppl 1):84–96.

[3] Souweidane MM. Endoscopic surgery for intraventricular brain tumors in patients without hydrocephalus. Neurosurgery 2005;57(Suppl 4):312–8.

[4] Dupont PE, Lock J, Itkowitz B, Butler E. Design and control of concentric-tube robots. IEEE Trans. Robot. 2010;26:209–25

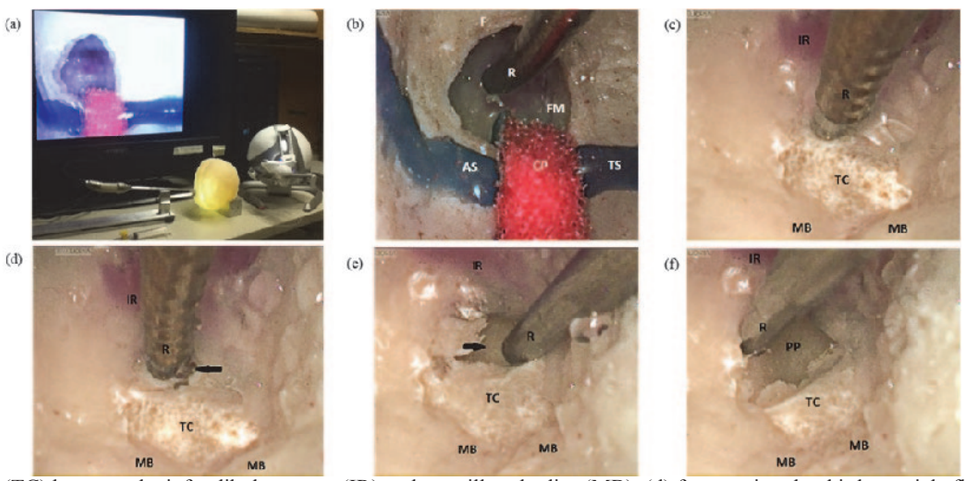

Fig. 3. Robotic endoscopic third ventriculostomy on a phantom brain model, (a) experimental setup, (b) robot (R) steered from the right lateral ventricle, through the foramen of Munro (FM) into the third ventricle, avoiding the fornix (F), choroid plexus (CP), anterior septal (AS) and thalamostriate (TS) veins, (c) navigating to the third ventricle floor/tuber cinereum (TC) between the infundibular recess (IR) and mamillary bodies (MB), (d) fenestrating the third ventricle floor (arrow), (e) widening the ventriculostomy (arrow), and (f) visualizing the prepontine cistern (PP) and clivus below the floo

A Master Slave Y-type Single Port Laparoscopic Surgery Robot with High Force Transmission and Large Workspace

S. Shim[1], D. Ji[1], J. Arata[2], M. Hashizume[2], J. Hong[1]

[1]*Department of Robotics Engineering, DGIST, Daegu, Republic of Korea*

[2]*Faculty of Medical Sciences, Kyushu University, Fukuoka, Japan*

jhong@dgist.ac.kr

INTRODUCTION

Single Port Laparoscopic surgery (SPLS) is an operation which makes use of the navel as an entry point of surgical tools. Due to making only one incision around the navel, SPLS offers for patients less post-operative scar, less post-operative pain, and faster recovery compared with traditional open surgeries and even multi-port laparoscopic ones. However, as the surgical instruments are intersected through the navel, the operation is counter-intuitive for surgeons [1]. Therefore, SPLS prompts surgeons not only to have experienced delicate operating skills, but also to spend a great deal of operating time.

In order to address this problem, diverse master-slave robots for SPLS have been developed. In case of the slave robot, the types of robotic SPLS are mainly divided into X and Y type. The X type robot uses motorized laparoscopic forceps with intersection, a typical example of which is the da Vinci SI system [2]. Although the X-type SPLS robot provides enough force to conduct an operation, it has bulky structures including long and big arms in order that a laparoscope and two forceps should be attached to the three serial robots. The Y type robot has two phases in terms of its geometry which are 'I' and 'Y'. SPIDER surgical system (TransEnterix, Morrisville, NC, USA), and SPRINT [3] fall into this category. The initial phase, 'I' is for insertion of the robot into one small incision. After insertion, two forceps are spread to form 'Y' shape. In case of the Y-type robot, size is able to be reduced, since a laparoscope and two forceps don't need to be attached to the three serial robot.

In case of the master device, two types of the design exist; the first type only controls the tip of the robot by calculating the change of the rotation and translation [2] which is implemented in da Vinci system. The second type controls all joints of the robot separately by adopting joint to joint level control [4]. The method of the tip control helps surgeon to experience less fatigue. However, in case of the Y-type robotic SPLS where all joints of the robot are inserted into the abdominal space, surgeons should control all the joints to increase the safety of the surgery. Otherwise, some joint operations will not be under control and may damage tissues.

In this paper, we presents our prototype of the Y-type master slave robot for SPLS. The effectiveness of the system was also verified by experiments.

MATERIALS AND METHODS

1. Design of the Y-type slave robot

Conventional Y-type SPLS robots are not suitable for operations dealing with relatively large organs such as intestine and liver, since the starting point of two arms are fixed differ to manual SPLS and X-type SPLS robots. In order to slove this problem, six degrees of freedom (DOFs) robot for each arm was developed, which consist of two prismatic joints at joint 1 and 5, and four rotational joints at joint 2, 3, 4, and 6, as shown on Fig 1 [5]. The joint 1 provides a larger workspace by separating the starting division point of each arm. The most parts of the robot were made of stainless steel and the diameter of main stem is 33 mm.

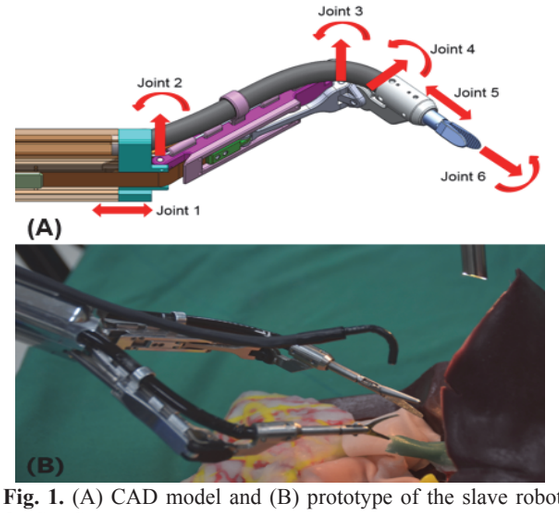

Fig. 1. (A) CAD model and (B) prototype of the slave robot for SPLS**.**

2. Design of the master device for Y-type robot

In order to control the aforementioned Y-type slave robot for SPLS, the master device should allow the surgeon to control all of the joints as well as the tip of the robot for the safety of the surgery.

The designed master device provides six DOFs of movements to manipulate the same DOFs of the slave robot. The CAD and kinematic model of the proposed master device are depicted on Fig 2 and the Denavit–Hartenberg parameters are given as shown on Table 1.

Each joint of the master device corresponds to each joint of human arm, enabling separate control of each joint. First, the joint 1 takes charge of the forward and backward motion of the whole arm. Second, the joint 2

and 3 are in charge of the motions of the shoulder and the elbow respectively. These two joints allow the slave robot to have triangulation. Third, joint 4 takes charge of the forward and backward motion of fingers. Last, joint 5 and 6 are used for flexion / extension and rotation of the wrist. This joint to joint correspondence enables the whole part of slave robot to move as desired.

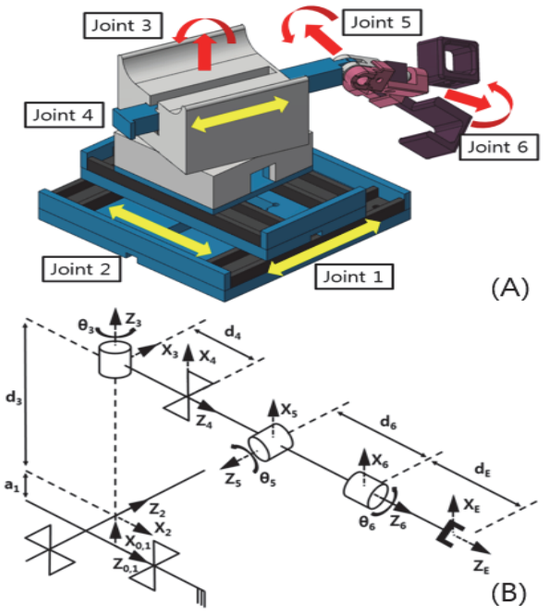

Fig. 2. (A) CAD and (B) kinematic model of the proposed master device for SPLS.

Table 1. D-H parameters of the master device

i	α_i	a_i	d_i	Θ_i
1	90	20	d_1	0
2	90	0	d_2	90
3	90	0	80	Θ_2+90
4	-90	0	d_4+35	90
5	90	0	0	Θ_5
6	0	0	80	Θ_6

RESULTS

The workspace of the slave robot was calculated as 3000cm^3 from the kinematic model. From this result, we confirmed the slave robot provides sufficient workspace for SPLS. High force transmission greater than 10 N were confirmed in the performace measurment test with varying loads. In the experiments, the robot could follow the tragectories with a payload up to 1.4 kg at the end effector. In addition, in the experiment of resecting the liver of a pig, it was verified that the slave robot is able to mimic the posture of the master device as shown on Fig 3.

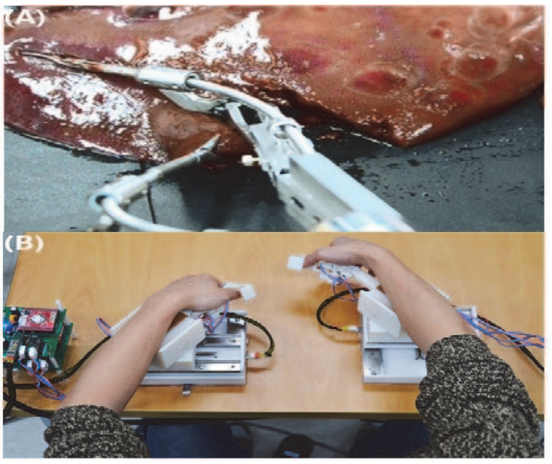

Fig. 3. Control of the Y-type master and slave robot.

DISCUSSION AND CONCLUSION

We proposed Y-type master slave robot for SPLS. The slave robot mimicked the posture of the operator's arm through the master device. Therefore, operators could control not only the position of the robot tip, but also the whole posture of the slave robot. We expect the proposed Y-type master slave robot can be applied in a wide range of abdominal surgeries with increased safety.

However, the slave robot requires providing a detachable structure to change the various surgical tools. Moreover, an endoscope required to be integrated in the slave robot. In the master part, more ergonomic design should be considered to reduce fatigue of the operator.

Acknowledgment

This work was supported by the Health and Medical R&D Program of the Ministry of Health and Welfare of Korea (HI13C1634) and by the R&D Program of the DGIST Convergence Science Center(12-BD-0402).

REFERENCES

[1] J. H. Kaouk, R. K. Goel, G. P. Haber, S. Crouzet and R. J. Stein. Robotic single-port transumbilical surgery in humans: initial report. British Journal of Urology International. 2009 Feb;103(3):366-369.

[2] R. Autorino, JH. Kaouk, JU. Stolzenburg, IS. Gill, A. Mottrie, A. Tewari and JA. Cadeddu. Current Status and Future Directions of Robotic Single-Site Surgery: A systematic Review. European Urology. 2013 Feb;63 (2):266-80.

[3] M. Piccigallo, U. Scarfogliero, C. Quaglia, G. Petroni, P. Valdastri, A. Menciassi and P. Dario. Design of a Novel Bimanual Robotic System for Single-Port Laparoscopy. IEEE/ASME Transaction on Mechatronics. 2010 Dec;15(6):871-878.

[4] K. Ikuta, T. Hasegawa and S. Daifu. Hyper redundant miniature manipulator "hyper finger" for remote minimally invasive surgery in deep area. International Conference on Robotics & Automation. 2003 Sep;1098-1102.

[5] B. Cheon, E. Gezgin, D. Ji, M. Tomikawa, M. Hashizume, H. Kim and J. Hong. A single port laparoscopic surgery robot with high force transmission and a large workspace. Surgical Endoscopy. 2014 Mar; DOI 10.1007.

Augmented Instrument Control for the CYCLOPS Robotic System

V. Vitiello, T. P. Cundy, A. Darzi, G.-Z. Yang, G. P. Mylonas

The Hamlyn Centre, Institute of Global Health Innovation, Imperial College London, UK

v.vitiello@imperial.ac.uk

INTRODUCTION

Surgical innovators are currently pursuing a second renaissance in minimally invasive surgery (MIS) techniques. The first-generation of MIS was defined by a paradigm shift from traditional large open surgical incisions to multiple small 'key-hole' incisions. This transition inferred many patient benefits, contributing to the acceptance of MIS as standard surgical care in many settings. Today, there is growing momentum towards further minimizing access trauma such that many procedures may be essentially 'scarless' when performed via single-incision laparoscopic surgery (SILS), natural orifice endoluminal surgery (NOES) and natural orifice transluminal endoscopic surgery (NOTES) techniques. With the exception of improved image quality and minor adjustments in scalability, the laparoscope and flexible endoscope are items of surgical technology that remain essentially undisturbed since they were first introduced several decades ago and still are the default platforms for SILS, NOES and NOTES. There is currently a variety of prototype platforms developed worldwide by a number of academic groups. Most of them remain in the pre-clinical phase with only a small number having reported feasibility *in vivo*. The most notable ones are discussed by Vitiello *et al* in [1]. Major limitations of these prototypes are universally shared and pertain to adequate triangulation, force delivery, stability and control.

The CYCLOPS system introduced by Mylonas *et al* [2], can overcome the above limitations by addressing bimanual instrument triangulation and force-delivery over a large workspace via a highly original design based on the concept of tendon-driven parallel robots. This involves lateral tendons introduced through small openings/fulcrums on a deployable structure resembling an open-ended bulb and then attached on a pair of overtubes as shown in Fig. 1B. Six tendons are attached on each of the overtubes. By appropriately controlling the length of the tendons using motor actuation, each overtube can be dexterously controlled in 5 degrees of freedom (DoF) as shown in Fig. 1C.

Standard small diameter flexible endoscopic instruments can be inserted through the endoscope available channels and robotically controlled by the accommodating overtubes, as shown in Fig. 1A. The system is adaptive to any existing laparoscope or flexible endoscope, while the stability and the navigational control of these existing instruments are preserved. This novel design gives the CYCLOPS a number of unique features including unparalleled force exertion capabilities of up to 65N, large and adjustable workspace and dexterous instrument control. In [2], the system has been successfully used in a peg-transfer task (Fig. 1A) by allowing robotic control of conventional flexible endoscopic instruments. Since its introduction, a fully functional bimanual CYCLOPS has been implemented, as show in Fig. 1B, which in addition to the aforementioned characteristics also allows for bimanual tissue triangulation. We are also exploring different approaches for the design of the deployable structure, such as an inflatable scaffold.

Due to the unilateral property of tendons (*e.g.,* they can only pull and not push), N number of tendons will allow the actuation of the overtube at $N-1$ DoF [3]. For the CYCLOPS, six tendons are used per overtube, permitting a maximum of 5 DoF actuation. Specifically, this configuration does not allow axial rotation. This abstract proposes a novel strategy for achieving axial rotation without the need of modifying the existing tendon arrangement. This is implemented by introducing a simple torque transmission and tendon alignment mechanism described in the next sections.

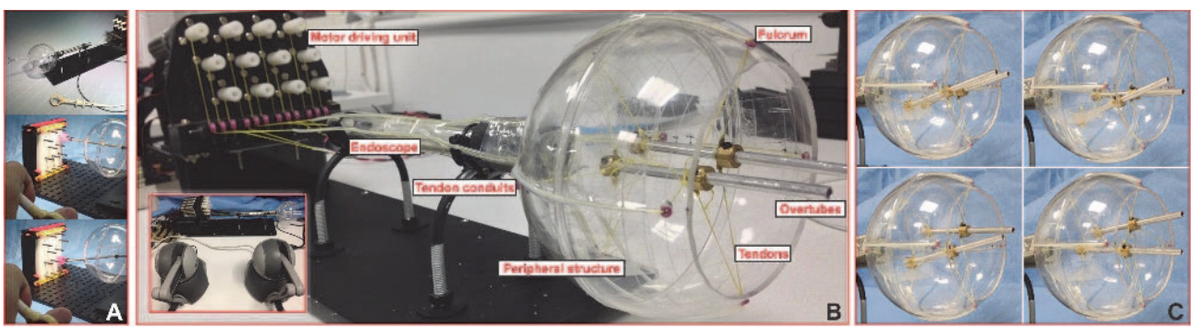

Fig. 1. (A) The original CYCLOPS system used in a peg-transfer task. (B) The functional prototype of the bimanual CYCLOPS. Motor controlled tendons are introduced through fulcrum points and are used to dexterously control two overtubes inside a deployable peripheral structure. The overtubes can accommodate and subsequently control any introduced standard flexible endoscopic instruments. (C) Typical configurations of the controlled overtubes in 5 DoF each.

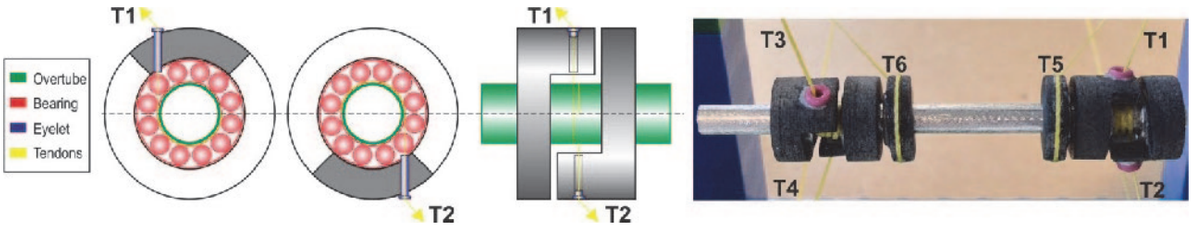

Fig. 2. On the left, a schematic of the torque transmission and tendon alignment mechanism is shown for T1-T2 but the same concept is mirrored for T3-T4. On the right, the actual mechanism is shown, with all tendons T1-T6 wrapped around the overtube.

PROPOSED FRAMEWORK

The proposed tendon alignment and torque transmission mechanism is shown in Fig. 2. Firstly, tendons T1 to T4 are wrapped around the overtube so that the resulting tension is always directed tangentially to its radius, thus generating the maximum torque at any pose. In particular, counterclockwise rotation can be achieved by pulling on tendons T1 and T2, while pulling on tendons T3 and T4 generates a clockwise axial rotation of the overtube. Subsequently, each tendon passes through a hole on a supporting bearing mechanism, thus generating a fulcrum point for the application of tension forces on the overtube. The fulcrum points are positioned so that the resulting pairs of tendon forces act antagonistically on the overtube when the system is under tension. Finally, the tendons are connected to the corresponding motors after passing through specific feeding points on the peripheral scaffold. With regards to tendons T5 and T6, these are attached on the outer surface of two freely rotating bearing mechanisms, so that the resulting tension forces on the overtube are always intersecting its main axis independently of the amount of axial rotation.

In our previous paper [2], the controllable workspace of the CYCLOPS was determined by modelling each overtube as a cable-driven parallel mechanism following the approach in [3]. This model can now be modified to take into account the effect of the above described mechanism on the system behaviour. Specifically, the bearing can be considered as a supporting structure with larger diameter than the overtube. The resulting motion of the overtube is therefore equivalent to the one of the supporting structure for all DoF except the rotation around the overtube axis. This is partially decoupled from the others thanks to the proposed mechanism.

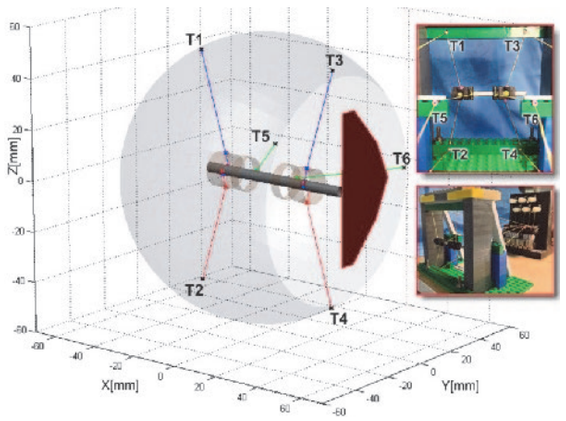

Fig. 3. The system controllable workspace (red patch). The insets show the experimental rig and the tendon arrangement.

As shown in Fig. 3, the tendons controlling the supporting structure are arranged in the same way as the ones controlling the original CYCLOPS overtubes. Its kinematics can therefore be modelled following the same procedure used in [2]. Assuming that the centre of mass of the overtube coincides with this of the supporting structure, the structure matrix for the two systems will also coincide. This is true except for the fourth row of the matrix, which determines the torque τ_x generated by the tendons around the axis of the overtube. In fact, the resulting τ_x for the supporting structure is always null, due to the specific tendon configuration, while it is maximized for the overtube, as described above. The controllable workspace of the overtube can therefore be calculated using the same procedure presented in [2] on the basis of its modified structure matrix and can be seen in Fig. 3. As shown in the figure, the in-and-out motion of the overtube is impaired because the axial rotation can only be stabilized when tendons T1 to T4 have the same orientation with respect to the overtube. However, in-and-out motion of the flexible endoscopic instrument can still be manually achieved by externally translating it inside the CYCLOPS overtube.

DISCUSSION

In this abstract, the CYCLOPS bimanual system has been presented, together with a novel concept for achieving axial rotation of its overtubes. The feasibility of the proposed mechanism has been demonstrated through a theoretical model and an experimental rig has been built. Further studies have to be carried out to assess the efficacy of the system for controlling flexible endoscopic instruments to perform a bimanual task.

Aspects of this research have been supported by the National Institute for Health Research (NIHR) Biomedical Research Centre at Imperial College Healthcare NHS Trust and Imperial College London. Patent application **GB1316333.2** has been filed for the system.

REFERENCES

[1] V. Vitiello, S.-L. Lee, T.P. Cundy, G.-Z. Yang, "Emerging Robotic Platforms for Minimally Invasive Surgery," IEEE Reviews in Biomedical Engineering, vol. 6, pp. 111-126, 2013.

[2] G. Mylonas, V. Vitiello, T. Cundy, A. Darzi, G.-Z. Yang, "CYCLOPS: A Versatile Robotic Tool for Bimanual Single-Access and Natural-Orifice Endoscopic Surgery," in ICRA, 2014 (to appear).

[3] M. Hiller, S. Fang, S. Mielczarek, R. Verhoeven, D. Franitza, "Design, analysis and realization of tendon-based parallel manipulators," Mechanism and Machine Theory, vol. 40, pp. 429-445, 2005.

Accuracy Evaluation of Interventional Nuclear Tomographic Reconstruction using Mini Gamma Cameras

P. Matthies[1], J. Gardiazabal[1,2], A. Okur[1, 2], T. Lasser[1], N. Navab[1]

[1]*Computer Aided Medical Procedures (CAMP), Technische Universität München,*

[2]*Department of Nuclear Medicine, Klinikum Rechts der Isar, Technische Universität München*

matthies@in.tum.de

INTRODUCTION

Advanced 3D functional imaging modalities like PET or SPECT play a crucial role in today's healthcare, providing accurate, patient-specific information for diagnosis and treatment planning. However, the scanners are very bulky, limiting their use in interventional scenarios. Wendler et al. have introduced an interventional technique called 'Freehand SPECT' [1], and presented a first clinical setup [2].

Using a tracked radioactivity detector, counts from known, well-distributed perspectives around the phantom are acquired and reconstructed using tomographic solution techniques. Based on such three-dimensional activity maps, interesting hot spots can then be identified and localized interventionally.

In order to improve the interventional imaging, newly developed, miniaturized gamma cameras for nuclear tomographic imaging have been introduced recently [3]. Using a mini gamma camera held by a robot arm, tremendously improved intra-operative SPECT-like reconstructions compared to acquisitions using only a single detector have been demonstrated.

In [4], we elaborated on this earlier work, in particular using an improved detection model of the mini gamma camera. We conducted a series of experiments on a hot spot phantom, showing that high accuracy can be reached reproducibly with radically shortened acquisition times of only 15s. In this paper we further evaluate the reconstruction errors of the proposed method.

MATERIALS AND METHODS

The imaging setup consists of three parts: the mini gamma camera, the robot arm and the optical tracking system, see Fig. 1. The mini gamma camera acquires the radiation emitted from the radionuclide, the robot arm is used for moving the gamma camera, and the optical tracking system is used for spatial localization of the mini gamma camera and the hot spot phantom.

Hardware setup

The mini gamma camera (CrystalCam, Crystal Photonics, Germany) uses a 4x4cm^2 CdZnTe crystal that has 16x16 pixels and a parallel-hole collimator measuring 11.15mm in length and containing square holes with a side length of 2.16mm. A tracking target with retro-reflective markers is attached to the camera for tracking by an optical tracking system (Polaris Spectra, Northern Digital Inc., Canada). An additional tracking target, attached to the phantom, is used to define the reconstruction volume *V*. A computer is used to control and read out all the hardware.

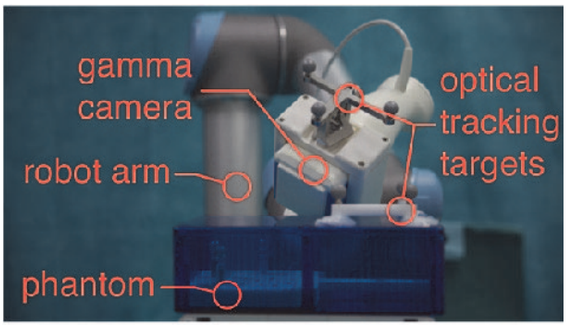

Fig. 1. Setup with the robot arm, the mini gamma camera and the phantom. Both the gamma camera and the phantom are attached with optical tracking targets.

Phantom

A phantom containing three hollow spheres, each with a volume of 0.25ml and inner diameter of 8.6mm, was created to mimic scenarios found in sentinel lymph node biopsy procedures [5]. The three spheres are filled with a ^{99m}Tc solution, 1.2MBq in sphere (1), 0.5MBq in sphere (2) and 1.4MBq in sphere (3), cf. Fig. 2.

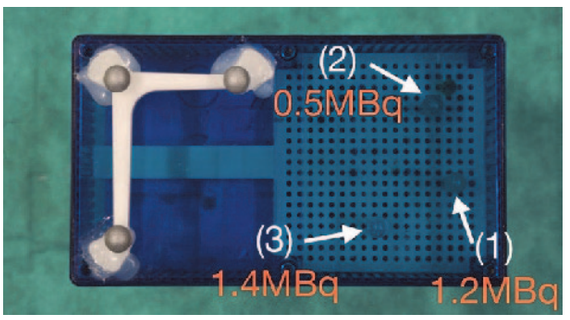

Fig. 2. Photograph of the box phantom, showing the three spheres containing radioactive ^{99m}Tc solution. The spheres are marked with their respective number (white) and ground truth activity (orange).

Model of the gamma camera

The gamma camera model needed for the 3D reconstructions, a high-resolution lookup table, was obtained in a long-term experiment by rasterizing a 150x150x150mm^3 volume in front of the gamma camera with a ^{57}Co source. More details can be found in [3].

Experiment design

The robot arm with the gamma camera acquires data from up to 21 poses around the phantom that we divide in 6 sets of poses. For brevity, we denote these pose sets as 1S (one side), 1SD (one side with diagonals), 2S (two sides), 2SD (two sides with diagonals), 3S (three sides), and 3SD (three sides with diagonals). Coverage of one side refers to orthogonal poses and ±45° to that direction. Diagonal poses cover the whole volume from three directions tilted 45° against all three orthogonal directions. The robot arm stopped at each pose for 10s while the gamma camera integrated the detected events.

Tomographic reconstruction

By moving the camera along the acquisition trajectory, we are collecting gamma events caused by emission from the radiotracer. To perform the reconstruction of the SPECT image, we consider the Poisson-distribution of the measured values *mj*, and compute the maximum-likelihood estimate

$$\arg\max_{\mathbf{x}} \left(\sum_{j=1}^{m} m_j \log(\overline{m}_j(\mathbf{x})) - \overline{m}_j \right)$$

where $\overline{m}_j(x)$ denotes the expected measurement given a reconstruction **x**. To find a solution to this optimization problem, we apply Maximum Likelihood Expectation Maximization (MLEM) as suggested by Shepp and Vardi [6], using the gamma camera model described above.

Evaluation of reconstruction accuracy

To evaluate the accuracy of the reconstructed images, all the sets of poses were repeated five times, and the average localization error and the standard deviation **σ** were calculated. The localization error is defined as the distance between the center of mass of the reconstructed sphere and its corresponding ground truth position in the phantom. The images were reconstructed with a voxel size of $1mm^3$.

RESULTS

We repeated the acquisitions and reconstructions five times and evaluated the reconstruction accuracy. The localization error was consistent across the different views, as shown by sub-millimeter values of **σ** in Tab. 1. At the same time, the localization error was very small in the views covering all three sides.

DISCUSSION

As seen in Tab. 1, the selection of the poses used for the reconstruction has a great impact on the localization error of the spheres. The configurations including the diagonal poses show that it is also possible to improve the localization, even if not all sides are accessible, a common problem during many surgeries. Scanning from only one side (1S) is very error prone, since the reconstruction problem is heavily ill-posed.

Table 1. Average localization errors and their standard deviations of the radioactive spheres, for each set of poses.

Set of poses	Average error [mm]	σ [mm]
1S	24.6	0.57
1SD	1.7	0.05
2S	5.6	0.26
2SD	1.3	0.06
3S	1.2	0.01
3SD	1.0	0.04

The low standard deviation **σ** shows that our results are highly repeatable, an expected result given that the robot is moving the camera in a very consistent and precise way. In summary, this evaluation proves the feasibility of acquiring interventional SPECT images with a constant image quality.

REFERENCES

[1] Wendler, T., Hartl, A., Lasser, T., Traub, J., Daghighian, F., Ziegler, S.I., Navab, N.: Towards Intra-operative 3D Nuclear Imaging: Reconstruction of 3D Radioactive Distributions Using Tracked Gamma Probes. In: Ayache, N., Ourselin, S., Maeder, A. (eds.) MICCAI 2007, Part II. LNCS, vol. 4792, pp. 909–917. Springer, Heidelberg (2007)

[2] Wendler, T., Herrmann, K., Schnelzer, A., Lasser, T., Traub, J., Kutter, O., Ehlerding, A., Scheidhauer, K., Schuster, T., Kiechle, M., Schwaiger, M., Navab, N., Ziegler, S.I., Buck, A.K.: First Demonstration of 3-D Lymphatic Mapping in Breast Cancer Using Freehand SPECT. Eur. J. Nucl. Med. 37(8), 1452–1461 (2010)

[3] Matthies, P., Sharma, K., Okur, A., Gardiazabal, J., Vogel, J., Lasser, T., Navab, N.: First Use of Mini Gamma Cameras for Intra-operative Robotic SPECT Reconstruction, in: Springer LNCS 8149 (MICCAI), pp. 163-170 (2013).

[4] Matthies, P., Gardiazabal, J., Okur, A., Vogel, J., Lasser, T., Navab, N.: Mini Gamma Cameras for Intra-operative Nuclear Tomographic Reconstruction. Medical Image Analysis, accepted, in press (2014)

[5] Kuehn, T., Bembenek, A., Decker, T., Munz, D.L., Sautter-Bihl, M.L., Untch, M., Wallwiener, D.: A concept for the clinical implementation of sentinel lymph node biopsy in patients with breast carcinoma with special regard to quality assurance. Cancer 103, 451–461 (2005).

[6] Shepp, L.A., Vardi, Y.: Maximum Likelihood Reconstruction for Emission Tomography. Transactions on Medical Imaging MI-1(2), 113–122 (1982).

A Pilot Study of Augmented Reality from Intraoperative CBCT for Image-Guided Thoracic Robotic Surgery

W. P. Liu[1], M. Azizian[2], J. M. Sorger[2], B. Mungo[3], O. J. Wagner[2]
D. Molena[3], R. H. Taylor[1]
[1]*Computer Science, Johns Hopkins University, Baltimore, USA*
[2]*Intuitive Surgical Inc., Sunnyvale, USA*
[3]*Robotic and Minimally Invasive Thoracic Surgery, Johns Hopkins Hospital, USA*
wen.p.liu@jhu.edu

INTRODUCTION

Minimally-invasive robotic-assisted surgery is an increasingly popular surgical approach. Its utilization in thoracic surgery has been shown to lead to comparable outcomes to Video-Assisted Thoracoscopic Surgery (VATS) [1]. The tele-robotic approach, available with a *daVinci* system (Intuitive Surgical Inc., Sunnyvale, CA) offers notable advantages for enhanced visualization and delicate dissection required for mediastinal lymphadenectomy, pulmonary resection, or other interventions within the thoracic cavity. Initial studies have shown promising results in regards to improved short-term outcome, when compared to open thoracotomy. In fact, several articles [2] show the feasibility, efficacy and safety of robotic pulmonary applications including lobectomy, segmentectomy, or wedge resections.

Surgical approaches to resect lung tumor within a wedge, segment or lobe are derived from preoperative volumetric data (i.e. computed tomography (CT)). In a standard clinical setting the image data is obtained with the lung inflated, ideally in end-inspiratory hold, and the patient in a supine position. Intraoperatively, the patient is rotated laterally and the lung is collapsed in order to create a suitable surgical workspace in the thoracic cavity. Correlating information from preoperative datasets to the surgical scene is currently a mental exercise; thus the accuracy of these practices is not only a function of the surgeon's experience but subject to inconsistencies.

This paper presents an initial pilot study to evaluate the applicability of augmented reality using intraoperative cone-beam CT (CBCT) with the *da Vinci® Si* system for a pulmonary wedge resection. Augmentation of thoracoscopic video with planning data defining the target and critical structures offers the potential to provide initial localization of the pulmonary segment of interest. Although collapsing the lung deforms the bronchi and parenchyma, we explored whether relative deformation of select mediastinal structures may still provide adequate intraoperative overlay. Using a porcine model, we measured deformation from intraoperative deflation and patient position. Furthermore, using an in-vivo ovine model, we tested the proposed image-guidance system by conducting a robotic wedge resection, guided by video augmentation from intraoperative CBCT.

MATERIALS AND METHODS

I. Evaluation of Lung Deformation

In standard clinical practice a preoperative CT is acquired with the patient supine and lungs inflated. Intraoperatively, the patient is rotated laterally (surgical side up) and the lung is collapsed. An imaging study was performed on a live pig in order to estimate lung deformation from both intraoperative deflation and patient rotation. Three mock tumors were created with urethane, medium durometer spherical medical balloons (10 mm diameter) and filled with 0.5 ml of rigid polyurethane foam, and 0.3 ml of acrylic paint. The tumor targets, along with a peri-tumor metal fiducial (52100 Chromium 1 mm diameter spheres), were placed in the animal's left lung using a radiopaque FEP I.V. catheter (Abbocath®-T 14G x140 mm). We imaged the porcine thorax using a volumetric CBCT (Siemens syngo DynaCT, 90 kVp, 290 mA, 0.48x0.48x0.48 mm^3 voxel size) in the following four positions: *1). Supine, Inflated (SI) 2). Supine Collapsed (SC) 3). Lateral Inflated (LI) 4). Lateral Collapsed (LC).* We segmented the three peri-tumor fiducials, pulmonary bifurcation and hemiazygos vein (proximal to the medial tumor) in each of the four data sets as targets. We compute the vector of each target created from inflated to collapsed. In the same patient position (Supine/Lateral) we measured the absolute value of the vector,. however, for data differing in rotation we compared their L2-norm.

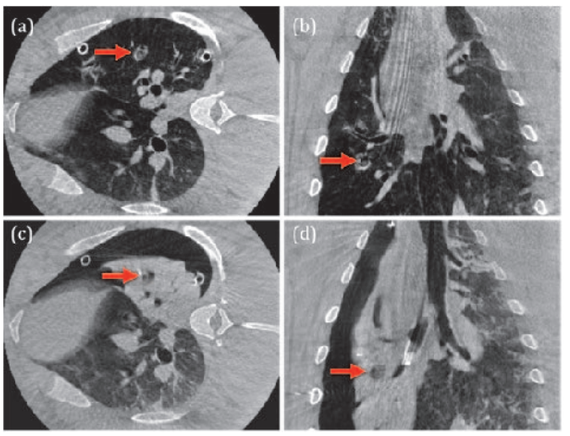

Fig. 1. (a) Axial and (b) coronal slice of lateral, inflated lung (c) Axial and (d) coronal slice of lateral, collapsed lung with a medial mock tumor marked in red.

II. In-Vivo Robotic Experiment

A robotic wedge resection in an ovine model was conducted to evaluate the feasibility and clinical

workflow required for augmented reality from intraoperative CBCT. A mock tumor and a peri-tumor fiducial were placed in the left upper lobe using the same protocol as above. The sheep was placed in a right lateral position. We then collapsed the lung and used manual laparoscopy to suture five plastic registration fiducials onto the abdominal wall before re-inflation. A CBCT acquired at this step not only captured intraoperative patient position, but also imaged the current physiology and anatomy, which may differ from preoperative scans obtained in clinic. Next, segmentation of the critical anatomy of interest (i.e. tumor, pulmonary artery, hemiazygos vein) and registration fiducials is completed manually (Fig. 2c). Automatic segmentation in medical imaging is an extensive field of research, but is beyond the scope of the work described. The segmented critical anatomy is registered to the stereo endoscopy using the 3D interface of the video augmentation software by manually aligning the registration fiducials and adjusting with visible anatomical landmarks (Fig. 2a). This augmentation system, described in detail elsewhere [3], is implemented by extending *cisst*/*SAW* [4], open source libraries supported by the ERC/LCSR center at the Johns Hopkins University. The augmented scene overlaid the tumor, pulmonary artery and hemiazygos vein onto the stereo endoscopic images (Fig. 2a, b, c). A fellowship-trained cardiothoracic surgeon, expert in minimally invasive interventions, was tasked to remove the synthetic tumor with a wedge resection (Fig. 2d).

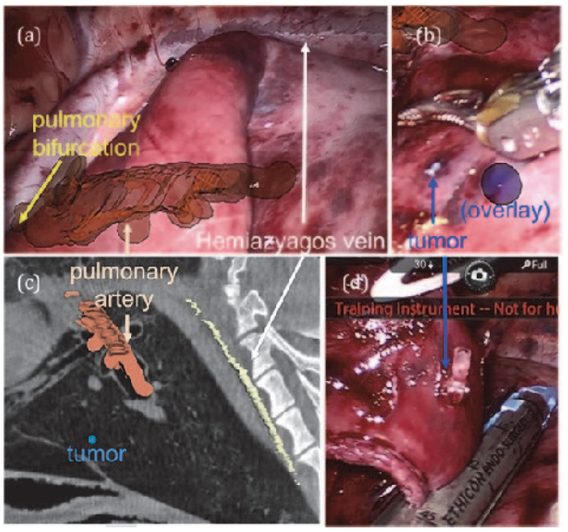

Fig. 2. (a,b) Overlays from anatomic registration (c) Segmentation of critical structures in CBCT (sagittal slice of lateral, inflated data) (d) Wedge resection.

RESULTS

Differences of vector norm between targets from standard preoperative image acquisition (SI) to intraoperative setup (LC Fig. 1c, d) was measured at 19.6 ± 11.4 mm while changes from a lateral rotation averaged 9.0 ± 8.9 mm. Deformation solely from lung deflation was measured at 20.1 ± 9.2 mm and 13.9 ± 7.3 mm for supine and lateral, respectively. Other studies [5] tracking surface points (compared to our targets embedded in parenchyma) have reported lung (porcine) deflation displacement ~48-63 mm. In fact, the displacement from deflation of natural landmarks used in registration (i.e. pulmonary bifurcation and hemiazygos vein) measured 3.3±1.4 mm. From postoperative analysis of recorded video**,** augmentation of the tumor (LI) was optically measured at ~25 mm away from actual target. The robotic experiment successfully removed the entire tumor within a wedge resection, with results confirmed visually through post-experimental dissection of the resected specimen, as well as fluoroscopically using an x-ray indicting the presence of the metal peri-tumor fiducial within the wedge.

DISCUSSION

Experimental results from an in-vivo ovine pilot study demonstrated the capability of augmented reality with intraoperative CBCT to provide initial localization for thoracic robotic wedge resection. A 3.3 mm deformation for mediastinal structures was adequate for registration purposes. Overlays of embedded parenchyma targets from inflated acquisitions onto collapsed lung may be displaced ≥ 20 mm, but can still provide navigational value, especially for inexperienced surgeons. For other thoracic interventions involving vascular dissection (i.e. lobectomy and segmentectomies) systematic accuracy must be improved. This was an initial pilot studies and further, studies are needed to evaluate quantitative outcomes. Future work will explore overlays from multi-modal preoperative volumetric data, the precedence of natural landmarks and deformable intraoperative registration.

ACKNOWLEDGEMENTS

This research is supported by Intuitive Surgical Inc., Johns Hopkins internal funds, Swirnow Family Foundation and NIH-R01-CA-127444, NSF EEC9731748.

REFERENCES

[1] Farivar, A. S., Cerfelio, R.J., Vallieres, E., Knight, A.W., Bryant, A., Lingala, V., Aye, R. W., Louie, B.E.: Comparing robotic lung resection with thoracotomy and video-assisted thoracoscopic surgery cases entered into the society of thoracic surgeons database. Innovations (Phila) 9, 10-5, (2014)

[2] Park, B.J.: Robotic lobectomy for non-small cell lung cancer (NSCLC): Multi-center registry study of long-term oncologic results. Annals of cardiothoracic surgery 1, 24-26 (2012)

[3] Liu, W.P., Reaungamornrat, S., A., D., Sorger, J.M., Siewerdsen, J.H., Richmon, J.D., Taylor, R.H.: Toward Intraoperative Image-Guided Transoral Robotic Surgery. Robotic Surgery 7, 217-225 (2013)

[4] Deguet, A., Kumar, R., Taylor, R.H., Kazanzides, P.: The cisst libraries for computer assisted intervention systems. MICCAI Workshop https://trac.lcsr.jhu.edu/cisst/, (2008)

[5] Katsuyama, Y., Yamazaki, N., Kobayashi, Y., Hoshi, T., Miyashita, T.: A study on estimation of the deformation behavior in the collapse process of lung. Conf Proc IEEE Eng Med Biol Soc 2012, 2817-2822 (2012)

Intraoperative 3D Fusion of Microscopic and Endoscopic Images in Transanal Endoscopic Microsurgery

P. Giataganas, C. Bergeles, P. Pratt, M. Hughes, A. Darzi, G.-Z. Yang

The Hamlyn Centre, Institute of Global Health Innovation, Imperial College London, UK

c.bergeles@imperial.ac.uk

INTRODUCTION

Colorectal cancer is among the most significant health problems worldwide and one of the highly prevalent forms of the disease. Early diagnosis and the improvement of excision techniques have reduced the mortality rate. Most procedures, however, involve the radical excision of the tumour through anterior bowel resections. Transanal Endoscopic Microsurgery (TEM), *i.e.* the bimanual excision of early stage carcinomas in the insufflated rectum using binocular magnified vision (see Fig. 1), achieves equivalent results with more rapid recovery times [1]. To improve the outcomes of TEM further, this paper proposes a method for augmented reality visualisation to fuse high resolution microscopic images of the cancerous region, acquired intraoperatively, with the endoscopic views in a three-dimensional representation of the surgical field. This augmented reality approach can assist in tumour margin identification, whose misidentification is the strongest cause of malignancy recurrence rates [2].

MATERIALS AND METHODS

Endoscope

A Wolf stereo endoscope (Richard Wolf, Germany) is used for imaging. The endoscope has a tilted lens and observes the surgical field at an angle of 50°. A custom bracket secures two Storz HD (1920x1080i) camera heads (Karl Storz, Germany) on the endoscope. Thus, during endoscope manipulation, the relative camera positions and the stereo baseline are held constant. The long length of the endoscope allows operations in the majority of the lower rectum. Together with the instruments, it is inserted through a Wolf TEM rectoscope tube and faceplate (Richard Wolf, Germany). In this study, the endoscopic images are subsampled by a factor of four to achieve real-time performance.

Endomicroscopy probe

Microscopic images are captured using a widefield optical microscopy probe of an established design [6]. A royal blue LED (M455L3, Thorlabs, New Jersey), low pass filtered by a 450 nm excitation filter (FES0450, Thorlabs), is directed to a leached fibre bundle (#1251343, Schott, New York) via a dichroic mirror (DMLP505R, Thorlabs), a x10 microscope objective and imaged onto a monochrome CCD camera (DCU 223, Thorlabs) via the dichroic, an emission filter (FEL0500, Thorlabs) and a 5 cm focal length tube lens.

The distal end of the probe provides a fixing mechanism for the optic fibre tip and the latter is positioned in contact with the tissue until a desired microscopic image is presented. A total of 17,000 fibre cores spaced at 8 µm provide a resolution of 16 µm and a usable field-of-view of 970 µm. The length of the fibre bundle is 80 cm, with an outer diameter of 1.3 mm. The outer diameter of the probe is 8 mm. The probe is actuated under robotic control for large-area scanning. Two brushless DC-servomotors (0620C-006-B, Faulhaber, Germany) operated through a C++ interface, control the insertion and rotation of the probe. Scanning velocities of 1 mm/s are achieved.

A checkerboard pattern (KeyDot®, Key Surgical, Minnesota) is statically attached at the distal end of the endomicroscopy probe, thus having a fixed, known relationship between the imaging tip and the probe shaft. The marker is constantly visible in the stereo endoscopic images during scanning (see Fig. 2a).

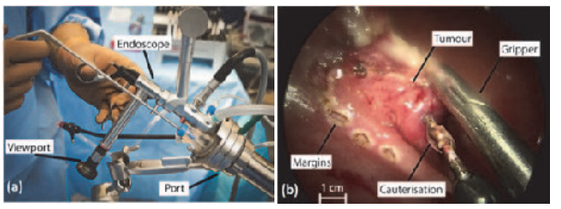

Fig. 1. (a) TEM port and instrumentation. (b) Endoscopic images provide no pathological information that can assist in tumour margin identification.

Image acquisition and processing

The workflow of the algorithm is as follows. First, camera calibration is performed offline [3]. Online, the stereo images are rectified based on the calibration parameters. Subsequently, stereo reconstruction using semi-global block matching [4], as implemented in Matlab® (Mathworks, Massachusetts) is carried out to extract the three-dimensional structure of the field-of-view. Semi-global block matching enforces consistent disparities among neighbouring pixels in the scene [4], alleviating several of the problems encountered due to a lack of high frequency texture in endorectal images. The endomicroscopy probe is actuated and the images that it acquires are processed offline using, initially, an approach similar to Le Gouahler *et al.* [5] to remove the honeycomb pattern due to the fibre-bundle cores, and then the images are mosaicked, *i.e.* stitched together, using a methodology adapted from confocal endomicroscopy based on a simple normalised cross correlation algorithm.

During scanning, the checkerboard marker at the distal end of the probe is tracked in the stereo images using a checkerboard pattern detection algorithm based on corner extraction [8]. The calculated disparity, back-projection, and triangulation, result in localisation of the probe in the three-dimensional field-of-view [9]. The relative pose of the probe's tip to its calibration pattern is known from the CAD models of the components and is fixed throughout the experiments. Also, the camera pose is fixed during both the reconstruction and tracking phases. Hence, tracking and localizing the checkerboard pattern relates the microscopic image and the mosaic to the three-dimensional reconstructed field-of-view. Finally, the mosaicked images are warped on the 3D reconstruction according to the results of probe localisation.

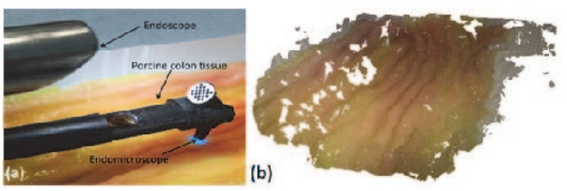

Fig. 2. (a) Relative positions of endoscope, checkerboard pattern, and endomicroscopy probe. (b) Three-dimensional reconstruction of the field-of-view.

RESULTS

The system and algorithm are evaluated on *ex vivo* tissue, specifically a porcine colon tissue specimen that gives rise to clinically relevant endoscopic and microscopic images. The tissue sample is brought to room temperature prior to experimentation, and is stained with proflavine fluorescent contrast agent. To simulate physiological curvature, the tissue is placed in a curved plastic container. Fig. 2a shows the distal side of the experimental apparatus.

The three-dimensional field-of-view is reconstructed, and, as shown in Fig. 2b, the curvature of the tissue is captured. The probe is actuated while keeping contact with the tissue to cover a linear region of approximately 10 mm. Tracking results and triangulation relate the microscopic views to the global coordinate frame of the 3D reconstruction allowing the fusion of the created mosaic with the coarse reconstructed anatomy. Hence, the presented three-dimensional map may provide information on multiple scales, ranging from high-level anatomy to the microscopic level, and allows closer identification of tumour margins and tissue characteristics (Fig. 3).

DISCUSSION

Transanal Endoscopic Microsurgery (TEM) is characterised by significant requirements in terms of dexterity, but is furthered challenged by the limited amount of subcutaneous tissue-level information that is provided solely by the endoscopic images. The highest post-surgical recurrence rate is related to erroneous tumour margin selection, and suboptimal excision. This work presents the integration of 3D endoscopic imaging with automated robotically controlled microscopic scanning to provide tissue-level information registered on the 3D intraoperative field-of-view. The recorded data (surface, images and positions) build up a virtual map of the diseased area for reference later in the procedure. *Ex vivo* experiments demonstrate that this technique can supply clinically relevant multiscale information, and support further investigation into both robotically assisted large-scale endomicroscopy mosaics and advanced TEM navigation.

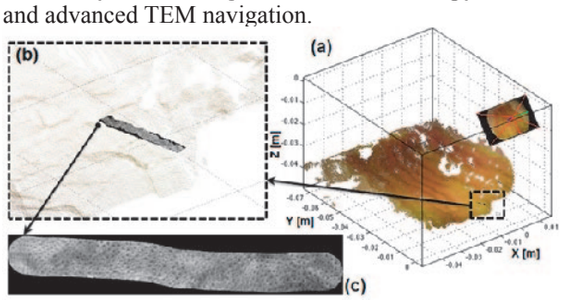

Fig. 3. (a) Field-of-view in the global coordinate frame of the endoscope, (b) overlay of the microscopic images on the reconstructed field-of-view, and (c) endoscopic mosaic rendered in 3D based on tracking.

ACKNOWLEDGMENTS

This research is conducted with support from the Dep. of Health and Wellcome Trust through the Health Innovation Challenge Fund (HICF-T4-299) and the EPSRC Grant EP/I027769/1: SMART Endomicroscopy.

REFERENCES

[1] Cataldo, P. and Buess, G.: Transanal endoscopic microsurgery: principles and techniques. Springer (2009).

[2] McCloud, J. M., Waymont, N., Pahwa, N. Varghese, P. Richards, C. Jameson, J. S., and Scott A. N. D.: Factors predicting early recurrence after transanal endoscopic microsurgery excision for rectal adenoma. Colorectal Disease, 8: 581-585 (2006).

[3] Zhang, Z.: A flexible new technique for camera calibration. IEEE Trans. Pattern Analysis and Machine Intelligence, 22(11): 1330-1334 (2000).

[4] Hirchmuller, H.: Stereo processing by semi-global block matching and mutual information. IEEE Trans. Pattern Analysis and Machine Intelligence,30(2):328-341 (2008).

[5] Le Goualher, G. Perchant, A. Genet, M. Cav, C. Viellerobe, B. Abrat, B., Ayace, N. Cave, C. and Berier, F.: Towards optical biopsies with an integrated fibered confocal fluorescence microscope. *In Proc.* Medical Image Computing and Computer-Assisted Intervention: 761-768 (2004).

[6] Pierce, M., Yu, D. and Richards-Kortum, R.: High-resolution fiber-optic microendoscopy for *in situ* cellular imaging. J. Visualized Experiments, 47 (2011).

[8] Bradski, G. and Kaehler, A.: Learning OpenCV: Computer vision with the OpenCV library. O'Reilly Media, Inc. (2008).

[9] Hartley, R. and Zisserman, A.: Multiple view geometry. Cambridge University Press (2003).

Robotic Image-guidance of an MR-compatible Catheter for Left Atrium Ablation with Flattened Maps for Procedure Planning

R. Karim[1], A. Ataollahi[2], S. Wang[1], J. Back[2], H. Liu[2], R. Razavi[1], K. Althoefer[2], T. Schaeffter[1], K. Rhode[1]

[1]*Division of Imaging Sciences and Biomedical Engineering, Kings College London, UK*

[2]*Centre for Robotics Research, Department of Informatics, King's College London, UK*
rashed.karim@kcl.ac.uk

INTRODUCTION

Minimally-invasive catheter-based interventions are widely used to treat patients with complex cardiac arrhythmias. Traditionally, these procedures have used fluoroscopic imaging with resultant long procedure times and associated radiation exposure. In recent times, magnetic resonance imaging (MRI) has been utilized extensively for non-invasively imaging the heart. It provides excellent soft-tissue contrast for both ventricular and atrial myocardium. Using MRI for guiding cardiac catheterization procedures necessitates the use of MR-compatible devices. In previous work [1], it was shown that a novel MR-compatible catheter steering mechanism was able to attain good steerability. In this work, the MR-compatible catheter is integrated as part of a robotic system which is controlled using image-guided feedback. The system also utilizes 2D planar maps of the target chamber for planning the procedure. In particular, flattened or planar maps of the left atrium (LA) are demonstrated here for planning ablation procedures.

MATERIALS AND METHODS

CATHETER STEERING MECHANISM

The MR-compatible catheter has 3 degrees of freedom (DOF) and is made of multiple segments stacked together to shape a long steerable catheter tip (see Fig. 1). It is designed to fit inside a 9-10 Fr sheath inserted into the femoral vein. Each segment is helical having a length of 9 mm and outer diameter of 3 mm with an inside lumen 1.7 mm in diameter allowing the insertion of optional elements. These helical segments are deflectable and this is achieved through tendons. The tendons run along the catheter's longitudinal axis though four guiding channels with a diameter of only 250 µm. The four tendons individually allow the catheter to deflect in a spring-like fashion. To allow a variable deflection curvature radius, a sliding carbon fibre rod through the central lumen of the catheter (see Fig. 1) is also employed. This blocks a number of the helical segments from being deflected, thus constraining and allowing the curvature of deflection to be controlled. All materials employed are MR-compatible.

In the prototype used in this work, the catheter had fourteen helical segments stacked together with their tendon guiding channels perfectly aligned. This created a steerable tip of 112 mm in length. The prototype is connected to a robotic actuation device with four stepper motors. The motors are attached to a gear which fits into the catheter's spool pulley for providing the 2-DOF tendon actuation. A linear stepper motor is employed to actuate the third axis by linearly moving the carbon fibre tube in and out of the central lumen. A second linear stepper motor allows the catheter to translate along a fixed axis. Overall, this gives the catheter a full 3D workspace.

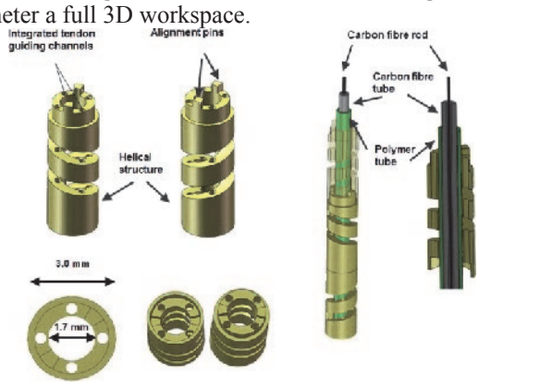

Fig. 1. Schematic view of the catheter design showing helical segments of the catheter (left) and through a cross-section (right)

IMAGE GUIDANCE USING PLANAR MAPS OF THE HEART

The catheter is guided using custom-made image guidance software. The software and the catheter steering mechanism is set up as a master/slave configuration (see Fig. 2). The catheter's robotic actuation device is run by a motion controller which interfaces with custom-made controller software. This acts as the slave to the image guidance unit. Commands between master/slave are sent via the Ethernet using TCP/IP. This allows the robotic steering mechanism to be remotely controlled.

The image guidance software includes a 3D and 2D visualization section (see Fig 3). A 3D mesh is extracted from pre-operative MRI/CT images of the LA of the heart and surrounding chambers. The 2D planar representation of the 3D LA is computed by employing surface parameterization [2]. Two cost functions are derived quantifying distortions in angles and areas when 3D meshes are flattened onto a 2D square. These are defined over a 3D mesh vertex's immediate neighbourhood. The cost function is optimized and a compromise between angle and area preservation during the flattening process is achieved. The boundary of the 3D LA (mitral valve annulus) is matched to the border of the mapped 2D square border setting the boundary

conditions of the optimization process. Optimization is achieved using the iterative conjugate gradient method

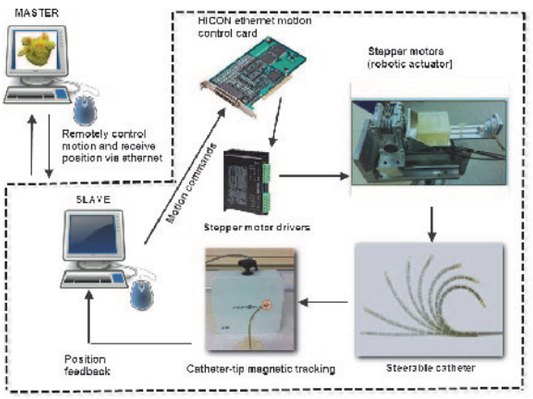

Fig. 2. Schematic showing master-slave configuration setup of the robotic steering mechanism (slave) controlled using the image guidance system (master)

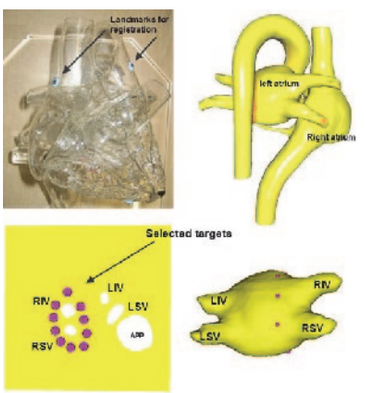

Fig. 3. Glass-heart phantom (top left) with its CT reconstructed 3D mesh (top right). Planar map of the LA (bottom left) and selected targets chosen circumferentially. Targets selected on the planar mapped back to the 3D mesh using 2D-3D mapping (bottom right).

In this work, the system is evaluated inside a glass-heart phantom (Farlow's Scientific Glassblowing, Grass Valley, CA, USA). The phantom consists of all chambers of the heart (Fig. 3). The phantom was scanned by a 512 × 512 × 384 voxel CT scan with 0.68 mm × 0.68 × 1.00 mm voxel resolution (Brilliance iCT, Philips healthcare, The Netherlands). It consisted of lead balls situated on the glass surface as landmarks as shown in Fig. 3. The image-guidance software reconstructed the 3D mesh from the CT scan. A planar 2D map of the LA was computed. The catheter was placed inside the glass-heart. A commercial magnetic coil tracking system (NDI Aurora® EM) with a 5-DOF coil was used to measure the position of the catheter tip in the experimental setup (see Fig 2). This was possible due to a sensor placed on the catheter tip. Registration between the co-ordinate systems of the catheter tip in physical space and in CT image space was solved using the absolute orientation method [3]. A rigid registration matrix was computed allowing the catheter tip to be displayed in real-time on the image guidance software's 3D model, with positions exchanged over the Ethernet between a multi-threaded master/slave configuration. In instances when the catheter came in contact with the 3D model's surface, it could also be displayed on the 2D planar map.

Furthermore, the catheter was tested for MR-compatibility using the MR scanner. Several experiments to test its steering were performed and no noticeable RF-induced heating was observed.

RESULTS

To evaluate the system, 2D planar maps of the LA was used to select target sites. The robotic catheter was guided using image guidance to reach each target location. The final distance to target was measured in mm with spatial position feedback information from the catheter-tip magnetic tracker. A total of fifty target locations were selected on the planar map. Results were plotted in the histogram shown in Fig. 4. The mean distance to selected targets achieved was 11.0 ± 8.2 mm. Ideally accuracy of less than 5 mm is desirable in such applications. Accuracy limitations are primarily due to errors in the catheter-tip magnetic tracking device feeding position information to image guidance software.

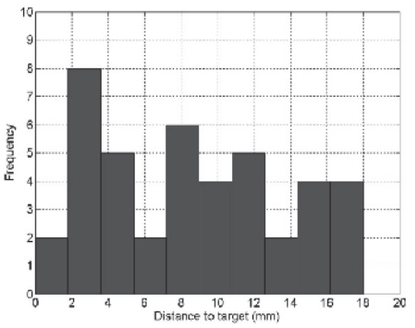

Fig. 4. Plotting the accuracy (distance to target in mm) of the robotic catheter using image guidance for 50 target locations.

CONCLUSIONS

The work presents an MR-compatible catheter steering mechanism controlled using image guidance. Procedure planning and selection of targets was performed on planar maps. It is envisaged that the use of planar maps for LA ablation planning will lower the complexity of visualizing variable LA 3D anatomy. 3D models require constant interaction during procedures for viewing anterior and posterior ends of the LA. Planar maps provide simultaneous view of the anterior and posterior sides of the LA, reducing operator interactivity.

REFERENCES

[1] A. Ataollahi, R. Karim, et al. 3-DOF MR-Compatible Multi-Segment Cardiac Catheter Steering Mechanism IEEE Transactions on Biomedical Engineering (In Press), 2013.

[2] R. Karim, et al. Surface Flattening of the Human Left Atrium and Proof-of-Concept Clinical Applications in Computerized Medical Imaging and Graphics, (In Press), 2014

[3] K. Berthold and P. Horn, Closed-form solution of absolute orientation using unit quaternions. Journal of Optical Society of America 4(4), pp 229-642, 1987.

Real-Time Electromagnetic Navigation for Breast Tumor Resection: Proof of Concept

G. Gauvin[1], C. T. Yeo[2], T. Ungi[2], G. Fichtinger[2], J. Rudan[1], C. J. Engel[1]
[1]*Department of Surgery, Queen's University, Canada*
[2]*School of Computing, Queen's University, Canada*
Jay.Engel@krcc.on.ca

INTRODUCTION

Breast cancer, the most common cancer in women, is ideally treated by breast-conserving surgery during its early stage. Current strategies, including the gold-standard method of wire-localization, have positive margin rates as high as 47% at initial excision [1]. The presence of a positive margin is a strong predictor for local recurrence despite adjuvant radiotherapy, and therefore leads to the patient requiring additional surgeries and treatment [2].The balance between adequate surgical margins and cosmesis is an additional challenge. Precise delineation of the tumor margins is difficult as lesion margins are commonly not physically palpable or well defined, and breast tissue moves and deforms during the procedure. The method proposed in this study utilizes real-time electromagnetic (EM) tracking to three-dimensionally delineate and track the tumor resection volume, allowing the surgeon to navigate around the tumor and improve the precision of the resection.

MATERIALS AND METHODS

System and Workflow Design

This proposal builds on the current gold-standard wire-localization method. One EM sensor is attached externally to the patient to create a global frame of reference and one EM sensor is attached to the wire-localization needle to account for local deformation and movement of the breast tissue. An EM tracked ultrasound (US) probe is used intra-operatively to identify and register the tumor location and delineate the desired resection volume. A final sensor is attached to the cautery device to allow real-time visualization of the surgical tool relative to the planned resection volume.

The wire-localization needle is placed within the tumor, creating a locally rigid region immediately surrounding the tumor. The needle is anchored in place using the deployment of dual-hooks at the needle tip. Intraoperatively, the EM sensor is attached to the needle hub and calibrated to the tip. As the needle and tissue in the vicinity of the tumor is manipulated during surgery, the EM transmitter is able to continuously track the location of the tumor based on its relationship to the needle. Intraoperative tracked US is used to register the tumor resection volume by placing 6 fiducial points at the desired resection margin. A model of the resected volume is created in the navigation screen.

Figure 1 shows a schematic of the sensor placement and registration workflow. Figure 2 illustrates the overall navigation system. We used a SonixGPS Tablet (Ultrasonix, Vancouver, CA) ultrasound with built-in EM tracker and multiple sensor ports. The scanner and tracker broadcast their data through the open-source PLUS toolkit (www.plustoolkit.org) to the SlicerIGT navigation software (www.SlicerIGT.org) [3], providing real-time registration and visualization of the resection volume and tool position w.r.t. the reference sensor.

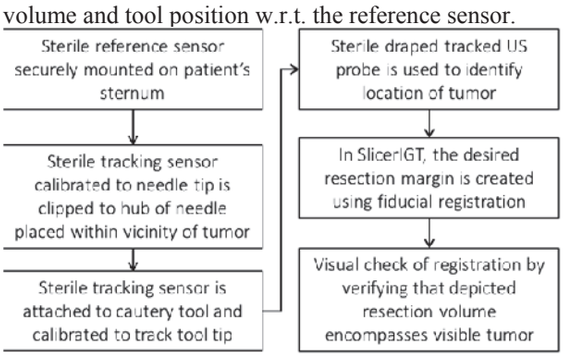

Fig. 1. Schematic workflow of sensor placement and registration process.

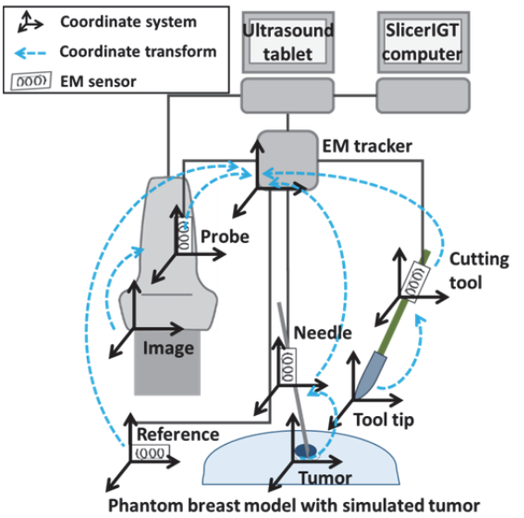

Fig. 2. EM navigation system setup.

Experimental Design

Figures 3a and 3b demonstrate the experimental setup. Phantom breast models of varying sizes were created with PVC plastic made to simulate breast tissue density and deformability. The models were created with consistently sized PVC tumors that were not physically differentiable from the surrounding tissue. Tumors were visible only in US and under fluorescent lighting for 'pathology' analysis. Wires were inserted under US guidance prior to volume registration. 8 surgical trainees and 2 staff breast surgeons were recruited to resect a total of 42 synthetic tumors, 21 using wire-localization alone (control method), and 21 using EM-augmented-wire-localization (EM method). Participants resected an equal number of tumors using each method.

Participants were instructed to raise a mock skin flap and to resect down to 'chest wall' as per standard of practice for both methods. For the control method, participants were instructed to use the standard procedure for wire-localized resection. For the EM method, participants were given instructions on how to utilize the navigation system to visualize their surgical instrument in relation to the resection volume. Resected volumes were analyzed in a blinded fashion for presence of tumor at the edge of the resection in all 6 planes, and size and weight of resected volume in relation to the breast model. Participants were asked to give feedback on the ease of using EM navigation.

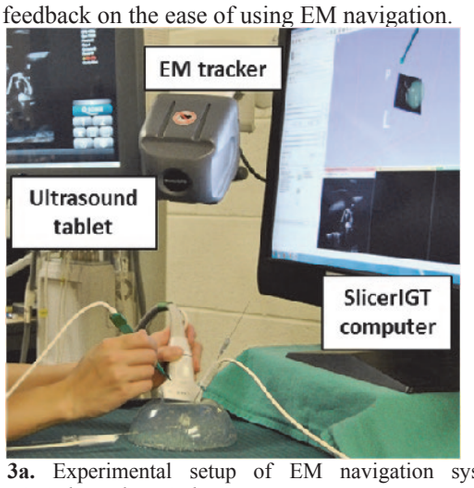

Fig. 3a. Experimental setup of EM navigation system demonstrated on a breast phantom.

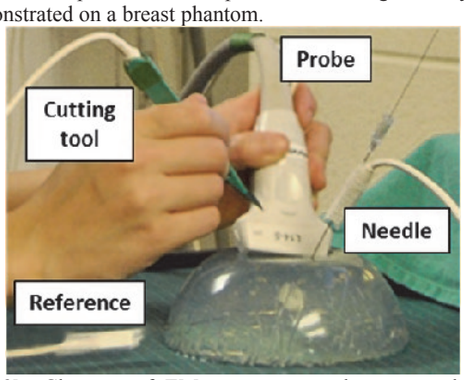

Fig. 3b. Close-up of EM sensor setup demonstrated on a breast phantom. For the purpose of demonstration, the target is visible in this figure; however phantoms used for the experiments had non-palpable, non-visible tumors.

RESULTS

The positive margin rate for the control method was 42.9% (9 of 21), and the positive margin rate for the EM method was 19.0% (4 of 21). Although the data was not statistically strong (p=0.18) there is a trend toward significance. Difference in relative resected tissue size was not significant between the two groups (p=0.87, statistical power 0.84 at 2% effect size), and the EM method took an average of 2 additional minutes. Participant feedback stated that none found the EM sensors interfered with the surgical procedure, and that EM navigation was somewhat easy to use.

DISCUSSION

In this proof of concept study a reduction in positive margin rate from 42.9% using the standard procedure to 19.0% using the EM navigation procedure was seen. The positive margin rates for both groups may be higher than clinically reported due to fidelity limitations of the phantom model and setup. Although the data collected was not statistically strong, it does provide adequate precision of treatment effect to inform the next phase of research. The lack of significance may stem from the sample size calculation (n=42) for this study, which was calculated using a much larger effect size than was seen. However, due to the limited surgical fidelity of the phantom, a larger scale phantom study is not warranted. A qualitative study of the workflow is currently underway on cadaveric breast tissue, and will be followed by a clinical feasibility study and a pilot randomized control trial. Although there have been no noticeable tracking issues with the use of EM in the experimental setup, plans are underway to test accuracy of EM navigation using the proposed method.

One of the limitations of wire-localization is the issue of wire migration between placement in radiology and time of surgery. This limitation is overcome in our method by registering the tumor position in relation to the wire after the patient has been prepped and draped, thereby reducing migration potential.

The significance of simultaneously achieving adequate surgical margins and cosmesis cannot be overstated. It affects all women undergoing breast cancer surgery, especially breast conserving resection. Our method of surgical navigation has the potential to significantly reduce the incidence of positive margins during the first attempt at tumor resection in breast-conservation surgery. A decrease in positive margins translates to a direct decrease in patients requiring a second, and sometimes a third surgery to repeat the resection. It also reduces the risk of recurrence and spread of disease. Furthermore, EM navigation has the potential to decrease the amount of healthy tissue removed by improving the precision of the resection, thereby improving cosmetic outcome.

EM-based navigation technology has the potential to be adapted for a variety of other surgical procedures and minimally invasive interventions; not only in open surgical procedures, but in laparoscopic and percutaneous settings as well.

ACKNOWLEDGEMENTS

This work is funded as a Cancer Care Ontario Applied Cancer Research Unit. G. Fichtinger is supported as Cancer Care Ontario Research Chair

REFERENCES

[1] Ananthakrishnan, P., Balci, F. L., & Crowe, J. P. (2012). Optimizing surgical margins in breast conservation. *Int J Surg Onc*, 2012, Article ID 585670.

[2] Moran, M. S., Schnitt, S. J., Giuliano, A. E., Harris, J. R., Khan, S. A., Horton, J., ... & Morrow, M. (2014). Society of Surgical Oncology–American Society for radiation oncology consensus guideline on margins for breast-conserving surgery with whole-breast irradiation in stages I and II invasive breast cancer. *Int J Clin Onc,* 88(3), 553-564.

[3] Ungi, T., Abolmaesumi, P., Jalal, R., Welch, M., Ayukawa, I., Fichtinger, G.,... & Mousavi, P. (2012). Spinal needle navigation by tracked ultrasound snapshots. *IEEE Trans Biomed Eng., 59*(10), 2766-2772.

Boosted Hybrid EM-Video Endoscopic Navigation Using Organ Centerline Constraint and Structural Measure under Tissue Deformation

X. Luo, U. L. Jayarathne, T. M. Peters

Robarts Research Institute, Western University, London, Canada
{xluo, ujayarat, tpeters}@robarts.ca

INTRODUCTION

Many minimally-invasive procedures are performed using endoscopy to visually examine the interior of the organ cavity through a natural orifice or transcutaneous port. Recently navigation systems have been developed to guide the endoscope to the target, and provide the physicians with visual guidance information to assist the interventions. 3-D endoscope tracking is the key to these systems, performed using either electromagnetic (EM) tracking or using 2-D video images to perform 2-D/3-D registration to locate the endoscope in a reference frame defined by a pre-operative image (e.g., CT) [1].

Since each method has its limitations, a hybrid of EM and video-based tracking offers a promising solution for endoscopic navigation. Previous hybrid methods have employed either the current EM sensor measurement to initialize the optimizer directly in 2-D/3-D registration, or stochastic filtering to combine EM sensor outputs into video-based tracking [2-5]. However, these hybrid methods still remain susceptible to image artifacts and inaccurate EM sensor measurements, because of tissue deformation (e.g., respiratory motion) and magnetic field distortion associated with the EM system.

This work presents a new framework to combine EM sensor measurements and endoscopic video images for enhancing endoscopic navigation of tubular structures (bronchus, colon, nasal sinus) that incorporates two new principles. Based on the segmented information from the CT images, i.e., the centerline of the organ cavity, we constrain the current EM sensor output to be on this centerline. Such a constraint potentially keeps the EM sensor outputs inside the cavity interior under tissue deformation. We then use the centerline position corresponding to the current measured sensor position to initialize video-based tracking. On the other hand, in the optimization of the 2-D/3-D image registration, a structural measure may be employed to accurately characterize the similarity between the current video and the virtually rendering pre-operative images [6]. Such a measure is robust to image artifacts (e.g., motion blurring). Both the centerline constraint and the robust structural measure are shown to effectively address the problems introduced by image artifacts and inaccurate sensor outputs during tissue deformation, resulting in more accurate and stable endoscopic navigation.

MATERIALS AND METHODS

We use an EM tracker and an endoscope to acquire EM sensor measurements and video frames, respectively.

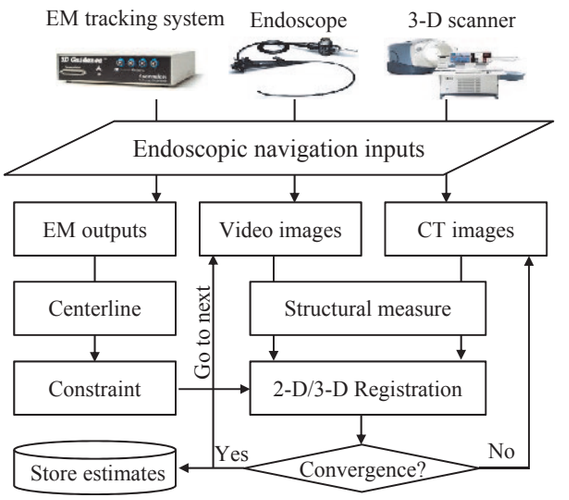

Fig. 1. Flowchart of our hybrid EM-video navigation

After obtaining the data, we constrain the EM sensor positions to the centerline and register the video images to CT on the basis of structural parameters (bifurcation position, branching angle and other salient features.) Fig. 1 illustrates the flowchart of our hybrid EM-video tracking, which consists of two principle components.

Centerline Constraint on Sensor Position: We align EM and CT spaces and transform the sensor measured position and orientation to the CT volume and obtain position $\mathbf{p}_i$ and orientation $\mathbf{o}_i$ at the time of frame *i*. By segmenting the CT images, we obtain the centerlines that are represented by $\mathcal{C} = \{\boldsymbol{\varphi}_m = \{\mathbf{c}_m^n\}_{n=1}^N)\}_{m=1}^M$. We assign the closest centerline to position $\mathbf{p}_i$ in terms of

$$\tilde{\boldsymbol{\varphi}}_* = \arg\min_{\boldsymbol{\varphi}_m \in \mathcal{C}} d(\tilde{\boldsymbol{\varphi}}_m, \mathbf{p}_i), \quad (1)$$

where $d(\tilde{\boldsymbol{\varphi}}_m, \mathbf{p}_i)$ is the distance between position $\mathbf{p}_i$ and line $\tilde{\boldsymbol{\varphi}}_m$ connecting the start and end points of $\boldsymbol{\varphi}_m$. We then determine the corresponding position $\tilde{\mathbf{c}}_*$ on the closest centerline $\boldsymbol{\varphi}_* = \{\mathbf{c}_*^n\}_{n=1}^N$ by the distance:

$$\tilde{\mathbf{c}}_* = \arg\min_{\mathbf{c}_*^n \in \boldsymbol{\varphi}_*} \|\mathbf{c}_*^n - \mathbf{p}_i\|, \quad (2)$$

where $\tilde{\mathbf{c}}_*$ is the output of the constraint step.

2-D/3-D Registration via Structural Measures: In this step, we define a structural measure to compute the similarity of the video and virtually rendering images:

$$S = \frac{1}{2}\left(1 + \frac{(2\xi_i\xi_r + C_1)(2\sigma_{i,r} + C_2)}{(\xi_i^2 + \xi_r^2 + C_1)(\sigma_i^2 + \sigma_r^2 + C_2)}\right), \quad (3)$$

where ξ_i and ξ_r are the average intensities of the current video image I_i and the virtually rendering image I_r, $\sigma_{i,r}$ is the correlation, and ξ_i and ξ_r are the variances.

The optimal position and orientation of the endoscope is determined by optimizing the similarity between the current video image I_i and the rendered image I_r:

$$(\mathbf{p}_i^*, \mathbf{o}_i^*) = \arg\max_{(\tilde{\mathbf{p}}_i, \tilde{\mathbf{o}}_i)} S\big(\mathrm{I}_i, \mathrm{I}_r(\tilde{\mathbf{p}}_i, \tilde{\mathbf{o}}_i)\big), \quad (4)$$

where the position and orientation are initialized by

$$\tilde{\mathbf{p}}_i = \tilde{\mathbf{c}}_*, \qquad \tilde{\mathbf{o}}_i = \mathbf{o}_i, \quad (5)$$

where $\tilde{\mathbf{p}}_i$ is set to the centerline constraint.

RESULTS

We manually generated five ground truth datasets comprising a total of 8319 frames. We compared three approaches: those of Mori et al. [2], Luo et al. [5], and our proposed method. The navigation accuracy, visual quality of virtually rendering images generated in terms of position and orientation estimates, and computational time are calculated to evaluate the tracking performance of using different methods for endoscopic navigation.

Table 1 summarises the position and orientation errors of different navigation approaches. The average tracking accuracy of our proposed method was 4.0 mm and 8.1 degrees, which were significantly enhanced, compared to previous methods that produced errors of at least 4.7 mm and 9.1 degrees. Fig. 2 plots the position and orientation accuracy in terms of Dataset 4 in Table 1. Fig. 3 shows the visual quality and the runtime. The visual quality on the basis of the similarity of the three methods were 0.67, 0.68, and 0.71 respectively. The runtime of ours was 0.50 seconds per frame, compared to the other two tested methods which required 0.38 and 1.23 seconds respectively. Fig. 4 proves our method which still works well in the presence of image artifacts.

Table. 1 Comparison of navigation accuracy (position, orientation) of using different methods (mm, degrees)

Data	Mori et al. [2]	Luo et al. [5]	Our method
1	(5.8, 10.0)	(5.8, 10.7)	(4.5, 8.9)
2	(5.9, 9.2)	(5.5, 10.2)	(4.8, 8.6)
3	(4.5, 8.1)	(4.2, 9.3)	(3.4, 7.5)
4	(5.0, 10.2)	(4.5, 11.6)	(3.6, 8.4)
5	(3.9, 8.2)	(3.5, 10.0)	(3.6, 7.0)
Ave.	**(5.0, 9.1)**	**(4.7, 10.4)**	**(4.0, 8.1)**

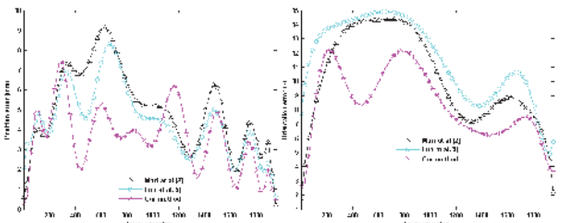

Fig. 2. Plotted navigation accuracy on Data 4

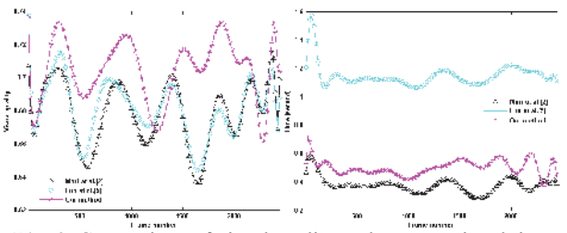

Fig. 3. Comparison of visual quality and computational time

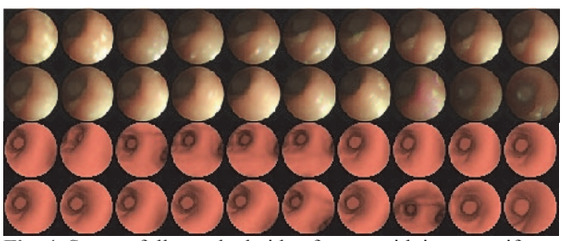

Fig. 4. Successfully tracked video frames with image artifacts: Rows 1-2 are continuous video images and other rows show virtually rendering images generated from the CT images.

DISCUSSION

Our proposed framework provides more accurate and robust endoscopic navigation than the two previous approaches, with the tracking accuracy being markedly improved without unduly sacrificing processing time. Such improvement results from two factors. In the presence of tissue deformation, the EM sensor can place the location of the endoscope outside the tubular structure. By initializing the 2-D/3-D registration with such EM measurements, the optimizer easily gets trapped in local minima. In our case, we constrain the sensor-measured position on the centerline, forcing the sensor position to be reported within the tubular structure, even in the presence of tissue deformation. From the interior positions, the optimizer is more easily able to search for the optimal solution. In addition, the structural measure is effective for characterizing the difference between video and virtually rendered images, since this measure has previously be shown to be robust to video image artifacts [6], possibly preventing the optimization from the premature convergence.

ACKNOWLEDGEMENTS

This work was supported by the Canadian Institutes for Health Research and JSPS.

REFERENCES

[1] T. Peters, K. Cleary, Image-guided interventions: Technology and applications, Springer, 2008.

[2] K. Mori, D. Deguchi, C. R. Maurer Jr., Y. Suenaga. Hybrid bronchoscope tracking using a magnetic tracking sensor and image registration. Med Image Comput Comput Assist Interv. 2005; 8(Pt 2): 543-50.

[3] T. D. Soper, D. R. Haynor, R. W. Glenny, and E. J. Seibel. In vivo validation of a hybrid tracking system for navigation of an ultrathin bronchoscope within peripheral airways. IEEE Trans Biomed Eng. 2010; 57(3):736-45.

[4] I. Gergel, J. Hering, R. Tetzlaff, H.-P. Meinzer, and I. Wegner. An electromagnetic navigation system for transbronchial interventions with a novel approach to respiratory motion compensation. Med Phys. 2011; 38(12), 6742-53.

[5] X. Luo, M. Feuerstein, T. Kitasaka, and K. Mori. Robust bronchoscope motion tracking using sequential Monte Carlo methods in navigated bronchoscopy: dynamic phantom and patient validation. Inter J Comp Assist Radio Surg. 2012; 7(3): 371-87.

[6] Z. Wang and A. C. Bovik. Modern Image Quality Assessment. Morgan & Claypool Publishers, 2006.

Implementation of a Motion Planning Framework for the daVinci Surgical System Research Kit

Z. Zhang, A. Munawar, G. S. Fischer

Automation and Interventional Medicine (AIM) Robotics Research Laboratory, Worcester Polytechnic Institute, Worcester, MA, USA
gfischer@wpi.edu

INTRODUCTION

Our goal is to extend the capabilities of robots used for laparoscopic surgeries, in particular the daVinci Surgical System (Intuitive Surgical). Primarily, we have integrated Robot Operating System (ROS) [1] as a middleware for the teleoperation control mode of the daVinci Research Kit (dVRK) [2]. This integration of ROS significantly enhances the ability to leverage the vast number of tools commonly used for robotics, to be employed to the dVRK.

In the traditional teleoperation mode, the Master Tool Manipulators (MTMs) interface with the Patient Side Manipulators (PSMs). Corresponding changes in the position and orientation of the MTM's grippers translate into corresponding actuation of the PSM's joints and correspondingly its end effector's pose. Integration of ROS as a middleware for data flow significantly enhances the ability to add computer intelligence to the surgical procedures. Within the described framework, kinematic and dynamic simulation models of the MTMs and PSMs have been developed. The framework is tightly integrated with *RViz*, a 3D visualization tool that is native to ROS and allows for tasks such as planning, manipulation and trajectory control.

For planning and manipulation tasks, it is necessary to have a 3D representation of the environment and obstacles. In order to generate 3D point clouds of the environment, we utilize a pair of compact stereo cameras. However, 3D volumes and point clouds from both live and registered preoperative imaging from various sources may be readily incorporated into the system. *In this paper, a system architecture and a method for a collision free motion planning is proposed from 3D streaming point clouds. The goal is to provide assistance to the surgeon by guiding a tool to follow an optimal path while avoiding sensitive anatomical features or other obstacles.*

ROBOT SIMULATION & CONTROL

The daVinci Surgical System consists of three primary components: MTMs (master manipulators), PSMs (slave arms) and High Resolution Stereo Viewer (HRSV). A developed ROS-based framework between MTMs and PSMs includes the following components:

Simulation: CAD models for the actual PSMs and MTMs have been developed (Fig. 2). These models have been used to define Unified Robot Description Format (URDF) files, which are compatible for simulation in ROS. These simulations may be run concurrently with actual teleoperation of the daVinci by mimicing the joint states and velocities of actual MTMs and PSMs in a live 3D rendering of the environment.

Teleoperation Interface: The teleoperation program provides a communication bridge over which ROS operates. This bridge is capable of reporting all joint positions, end-effectors cartesian pose, joint torques and current feedbacks of every MTM and PSM. Spontaneously the joint positions, end effector cartesian pose and joint torques can be set for any arm using standard ROS topics.

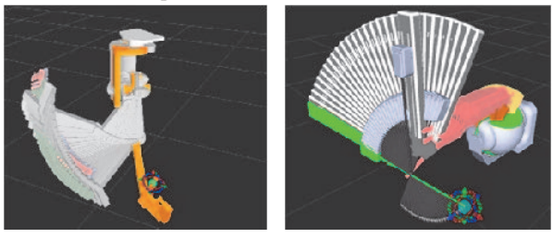

Fig. 1. Planned trajectory execution on both MTM and PSM.

Control: Controlling PSMs or MTMs directly from simulation is achieved by clicking the simulated PSMs or MTMs tip and dragging it in the dextrous workspace (Fig. 1). This simplification in control is possible only by efficient merging of low level libraries to the higher level graphical applications.

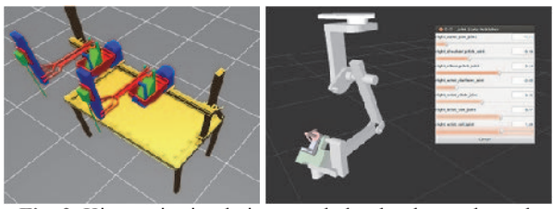

Fig. 2. Kinematic simulation coupled to hardware through ROS. PSMs (left) and MTM with slider control (right).

MOTION PLANING

In an effort to incorporate computer intelligence beyond the traditional teleoperation modality, the framework is configured to collect discrete points (6-DOF poses) in the operating space (OS) of the MTMs and generate a collision free path connecting those points for the PSMs in their OS. The points are selected using the MTMs pinch events as a trigger, which causes the current position and orientation of the corresponding MTM to be queued (Fig. 3). A proposed use case is where the surgeon's only visual access to the patient is via a stereoscopic viewer that is interfaced with stereo cameras near the PSMs. In cases where it is difficult to visualize the entire area that the surgeon is operating on, computer-guided path planning would allow specifying a set of guided points for a general surgical motion plan.

The desired path may be analyzed and improved by the planning and selection algorithms to generate an obstacle free path if one exists, or report failure otherwise.

PLANNING SETUP

A primary contribution of this work is the ability to leverage the vast array of existing tools into this framework for use with the dVRK. In particular, several popular motion planners are used including RRT, KPIECE, and SBL with their variants. All these planners are Random Time Planners and almost always produce a non-optimal path [3]. For this reason, one unique random time planner of particular interest for this paper is the RRT* planner, which guarantees an optimal path, if one exists. The planner searches for a path using traditional RRT algorithm and then improves upon the path produced incrementally as time progresses [3].

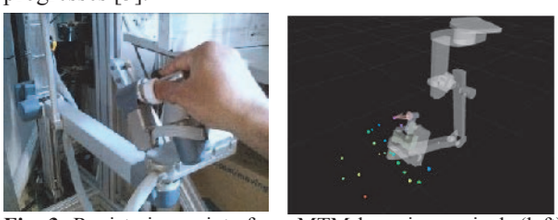

Fig. 3. Registering points from MTM by gripper pinch (left) and corresponding, registered points in simulation (right).

POINT CLOUD GENERATION & STREAMING

Visual feedback is essential for surgical teleoperation, especially under circumstances near sensitive or delicate structures. In order to render a 3D reconstruction of these structures and objects, we generate point clouds of the environment. To mimic a surgical system with stereo vision, two identical cameras are used (Microsoft LifeCam Cinema) are used to create the point clouds. The baseline between left and right camera is minimized to give a close range of depth information, maintaining a ratio of the focal distance to baseline depth that closely mimics that of the clinical daVinci stereo endoscope. The following ROS packages are used: *uvc_camera*, *camera_calibration*, and *stereo_image_proc* to provide camera drivers, camera calibration, stereo vision processing, disparity map generation and 3D point cloud generation. By tuning parameters for generating a disparity map in the range that needs to be detected, a high-quality point cloud is obtained [4]. An example of point cloud streaming is shown in Fig. 4.

POINT CLOUD BASED MOTION PLANNING

Prior to motion planning with the physical robot, accurate positioning of the point cloud with respect to the PSMs is essential. The 3D point cloud is first registered to the robot frame. *ar_pose*, a ROS wrapper for ARToolkit [5], is used to calculate the transformation between the camera frame and the PSMs. Markers are attached to camera, left PSM and right PSM respectively to provide their relative positions and orientation using *ar_tool*. The *Tf* ROS package provides a convenient way to manage all the frame transformations in the system. The transformation between any two frames can be obtained at any time by building a transformation tree. Utilizing the point cloud registration, motion planning and trajectory planning can be implemented in the real world corresponding to the simulation. The point cloud could be further registered to previously acquired anatomical or functional imaging, or a previously generated plan.

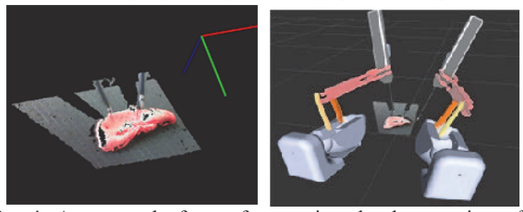

Fig. 4. An example frame from point cloud streaming of a liver phantom (left). Integration of the registered environment point cloud and the PSM robot model (right)**.**

DISCUSSION

The paper describes a framework that enables simulation and motion planning with the dVRK utilizing ROS-based tools, and a demonstration of example tasks that have been successfully implemented. Fig. 5 shows the outcome of a motion-planning problem for an anatomical target (a heart model in this case) that was identified as an obstacle. The PSM's start and goal pose are show in orange and green respectively, and the PSM follows a collision free path around the obstacle. The path is optimized using the RRT*, as can be seen, the path is smooth and tight around the anatomy.

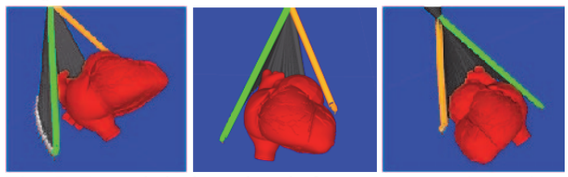

Fig. 5. Exampled planned path from start pose (orange) to goal pose (green) around a model of an anatomical obstacle.

We are currently working on more complex simulations based on registration of actual anatomical data to acquired point clouds. Further, we are working towards integration of force feedback on the MTMs based upon the virtual interactions with the 3D model so as to develop a sense of the forces being encountered at the PSMs. This requires the estimation/calculation of an accurate dynamical model of the MTM, another research area we are currently investigating as well.

REFERENCES

[1] http://www.ros.org/about-ros/

[2] Kazanzides P, Chen Z, Deguet A, Fischer GS, Taylor RH, DiMaio SP, An Open-Source Research Kit for the da Vinci Surgical System, ICRA, June 2014.

[3] Karaman, Sertac, and Emilio Frazzoli. "Sampling-based algorithms for optimal motion planning." The International Journal of Robotics Research 30.7 (2011): 846-894.

[4] http://wiki.ros.org/stereo_image_proc/Tutorials/ChoosingGoodStereoParameters

[5] Kato I, Billinghurst M, Poupyrev I, ARtoolkit user manual, version2.33, Human Interface Technology Lab, University of Washington, 2000.

da Vinci® Auxiliary Arm as a Robotic Surgical Assistant for Semi-Autonomous Ultrasound Guidance During Robot-Assisted Laparoscopic Surgery

O. Mohareri, S. E. Salcudean

Robotics and Control Laboratory, University of British Columbia, Canada
omidm, tims@ece.ubc.edu

INTRODUCTION

Robotic surgical systems enable surgeons to perform delicate and precise minimally invasive surgery. Currently, such systems are mostly controlled in a human-in-the-loop teleoperated framework. Introducing autonomy to some surgical sub-tasks has the potential to assist surgeons by decreasing their work-load, and also improving surgical navigation.

This paper describes a semi-autonomous robotic ultrasound guidance system for robot-assisted laparoscopic surgery, implemented on the *da Vinci*® surgical robot (Intuitive Surgical Inc.). The da Vinci auxiliary patient side manipulator (PSM) is introduced here as a robotic ultrasound surgical assistant (US-PSM). A robotic 'pick-up' ultrasound transducer [1] is rigidly grasped by the surgeon using the auxiliary PSM and the *ProGrasp*® instrument, and 3D ultrasound is registered to the tip of the other operating PSM's instrument performing tasks such as tumor resection. Solving a real-time inverse kinematics and ultrasound registration problem enables the auxiliary manipulator to autonomously track the surgical tool in a restricted workspace and provide real-time ultrasound guidance to the surgeon. The technique was implemented on the *da Vinci*® surgical system (classic version) for the first time using the da Vinci research kit (dVRK) controllers that enable complete access to all control levels of the da Vinci manipulators via custom mechatronics and open-source software.

MATERIALS AND METHODS

A. System overview

The mechanical hardware is the first generation da Vinci robot integrated with five controller packages (developed at Johns Hopkins University in collaboration with Intuitive Surgical Inc. [2]) each containing two pairs of custom designed boards (an IEEE-1394 FPGA Control board, and a Quad Linear Amplifier (QLA) board) and capable of closed-loop controlling up to eight servo motors. Each control box is responsible to control one da Vinci master or slave manipulator.

Software architecture is based on the centralized computation and distributed I/O architecture, in which high level control algorithms are implemented in a Linux PC, while high-speed I/O is performed through an IEEE-1394a serial network (as fast as 400 Mbits/sec). In order to establish a bimanual teleoperation system with two master-slave robot pairs, software modules for I/O level data read/write, joint level servo PID control and logical robot control have been defined and a custom teleoperation component based on kinematic correspondence with gravity compensation on the master devices has been implemented [3]. Furthermore, the bimanual teleoperation framework has been expanded to also include the control of the auxiliary PSM. The da Vinci foot pedal tray with five switches accessed using the foot, is employed in our custom control architecture as a user-controlled switch for different control modes between master-slave pairs.

B. 3D ultrasound registration for autonomous guidance using auxiliary manipulator

In our proposed method for control of the auxiliary PSM with ultrasound, the US imaging plane is automatically repositioned using the PSM wrist such that a 2D ultrasound image continuously contains the tip of a specified da Vinci surgical manipulator as shown in Figure 1.

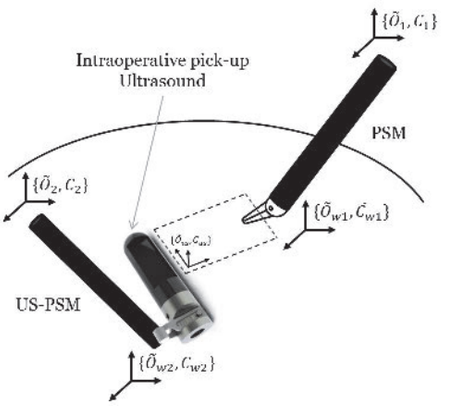

Fig. 1. Registration concept to enable the US-PSM to automatically reposition the ultrasound imaging plane to follow PSM tip point P. ($\{\tilde{O}_i, \underline{C}_i\}$ is located at each PSM's base and ($\{\tilde{O}_{wi}, \underline{C}_{wi}\}$ is located at each PSM's wrist base.

Surgeons can then elect to have a real-time ultrasound image that actively tracks their instruments as they work, allowing them to continuously monitor their position relative to sensitive anatomical structures, without pausing to reposition the ultrasound probe. Automatically tracking the tip of a da Vinci instrument with the ultrasound imaging plane requires that the position of the instrument tip relative to the US-PSM be known. Based on the coordinate frames introduced in Figure 1, we have:

$$^{US}P = {}^{\underline{C}_{US}}T_{\underline{C}_{w2}} \times {}^{\underline{C}_{w2}}T_{\underline{C}_2} \times {}^{\underline{C}_2}T_{\underline{C}_1} \times {}^{\underline{C}_1}T_{\underline{C}_{w1}} \times {}^{\underline{C}_{w1}}P \quad (1)$$

Using our established dVRK software platform, Cartesian position of the tip and wrist angles of the da

Vinci operating instruments are known in their corresponding coordinate frames ($\{\tilde{O}_2, \underline{C}_2\}$ and $(\{\tilde{O}_1, \underline{C}_1\})$, which are located at the base of each PSM as shown in Figure 1. Hence, ${}^{\underline{C}_{w1}}P$, ${}^{\underline{C}_1}T_{\underline{C}_{w1}}$ and ${}^{\underline{C}_{w2}}T_{\underline{C}_2}$ transformations are known in real-time. The ultrasound transducer used in this paper is custom-made to be picked up and manoeuvred by the ProGrasp instrument of the da Vinci [1]. Its unique design allows for it to be easily picked up in a repeatable manner such that the position of the ultrasound image, with respect to the da Vinci instrument can be pre-calibrated, hence ${}^{\underline{C}_{US}}T_{\underline{C}_{w2}}$ is also known. As a result, all that is required for tracking is a registration between the two PSM coordinate systems to calculate ${}^{\underline{C}_2}T_{\underline{C}_1}$.

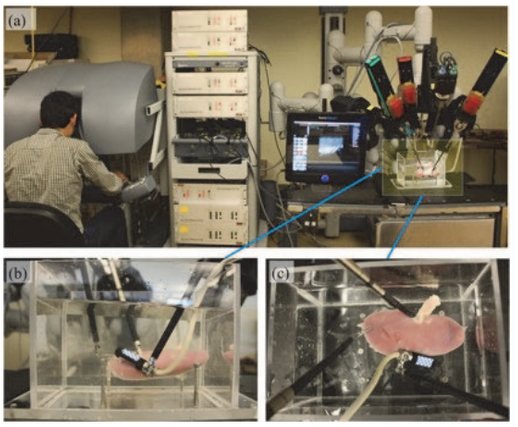

Fig. 2. (a) Overview of the da Vinci standard system with the dVRK platfrom in UBC RCL lab, (b) Experimental evaluation of the automatic tool tracking on a ex-vivo porcine kidney specimen. Two PSMs are used as operating arms and the third PSM is used as ultrasound surgical assistant.

The air-tissue boundary registration method presented in [4] is used here to compute this transformation intraoperatively. Once the transformation is found, solving the real-time inverse kinematics on the US-PSM enables the ultrasound imaging plane to automatically track the tip of the other instrument within its working space of the wrist which is 180 degrees (Yaw and Pitch) and 540 degree rotation (roll). Surgeons can also switch in and out of tracking mode, by activating the da Vinci surgeon console's clutch pedal, recognized by our software to change the control mode from automatic to manual surgeon-controlled.

Due to the redundancy in maintaining the PSM instrument tip within the imaging plane using the complete 6-DOF motion of the da Vinci PSM, in our implementation of this method, the US-PSM wrist base $(\tilde{O}_{w2}, \underline{C}_{w2})$ is placed in a fixed location by the user, and only the wrist is allowed to move and automatically track the other instrument's tip.

RESULTS

A series of *ex-vivo* registration experiments have been performed on the experimental setup shown in Figure 2 simulating the partial nephrectomy scenario, and mean target registration error of $1.44 \pm 0.4\,mm$ was achieved. In order to decompose this error, the relative motion accuracy of the used da Vinci instruments with respect to each arm's base coordinate frame is measured using the NDI OptoTrak Certus motion capture system. A custom-made 3D printed tool with 8 optical markers (shown in Figure 3a) was built so that it can be rigidly picked up and attached to the ProGrasp tool of the da Vinci and enable wrist motion accuracy measurements.

A custom-made stylus tool was also used to measure the Cartesian position accuracy of the instrument tip (Figure 3b). The mean Cartesian motion error was calculated to be $0.84 \pm 0.4\,mm$ and the mean wrist motion error is $2.62 \pm 1.2\,deg$. These values could vary from one instrument to the other and also in free versus in-contact situations, because of the errors caused by instrument aging, compliance in the cables and the bending deflection of the tools.

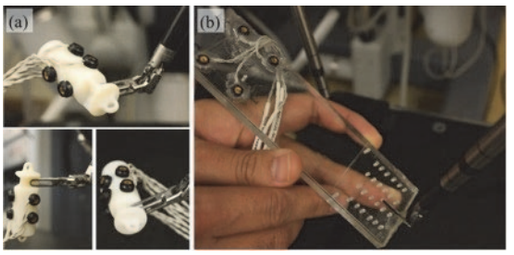

Fig. 3. (a) instrument wrist motion accuracy measurement using a custom-made tool, (b) instrument tip Cartesian position accuracy measurements.

DISCUSSION

The presented system is particularly applicable to the partial nephrectomy procedure, where the surgeon must resect a section of the kidney without leaving cancerous tissue behind. Having real-time ultrasound guidance at the time of resection could provide the surgeon with vital information to improve surgical margins and spare internal kidney anatomy. This has never been previously possible because the tumour resection requires the full attention of both operating arms and an external laparoscopic probe does not have the dexterity to show the surgeon useful information.

REFERENCES

[1] C. Schneider et al. "Intra-operative "Pick-Up" Ultrasound for Robot Assisted Surgery with Vessel Extraction and Registration: A Feasibility Study", in Proc. IPCAI 2011.

[2] P. Kazanzides, et al., "An open-source research kit for the da Vinci surgical robot," in Proc. ICRA'14.

[3] O. Mohareri et al. "Bimanual Telerobotic Surgery with Asymmetric Haptic Force Feedback: A daVinci surgical system implementation", in Proc. IROS 2014 (in review).

[4] T. Adebar et al. "Registration of 3D ultrasound through an air-tissue boundary", TMI, Vol. 31, No. 11, pp. 2133-2142, 2012.

ROS-Based GPU Acceleration Framework for Image Guided Surgery

F. Liu, G. Sison, F. Rodriguez y Baena

Mechanical Department, Imperial College London, UK

fangde.liu@imperial.ac.uk

INTRODUCTION

The breadth and heterogeneity of modern surgical robotic systems warrants a modular software architecture to reduce software development effort. Within this context, as the Robotic Operating System (ROS [1]) gains traction, the communication speed of its message passing mechanism becomes of increasing concern. Data transfer time in ROS increases linearly with size, which means it is negligible for light communication (e.g. homogenous transform data transfer), noticeable for e.g. two dimensional (2D) images, and prohibitively long for e.g. three-dimensional (3D) volumetric medical images. In Imagine Guided Surgery (IGS), different modules (which in ROS are called 'nodes') can be expected to exchange large data since, when operating on moving organs such as the heart, medical images have to be acquired intra-operatively on a regular basis and the surgical plan must be updated accordingly.

A specific example is illustrated in **Fig 1**, which depicts the graphical output of an IGS needle steering system for multi-target sampling of the liver. The "surgery planner" node computes an optimal needle insertion path through the liver without injuring the complex vasculature. In this process, an "image processor" labels all the vascular voxels in the medical images and a "path planner" ensures that none of the vasculature-related voxels intersect with the chosen path. As the liver moves and deforms during the needle insertion process, images of the liver must be aquired in real-time either by ultrasound or interventional Magnetic Resonance Imaging (MRI). However, IGS systems based on ROS and, for instance, the popular Image-Guided Surgery Toolkit (IGSTK) [2] struggle with the necessary processing speed due to lack of support for parallel processing and the limited bandwidth used for transferring large data.

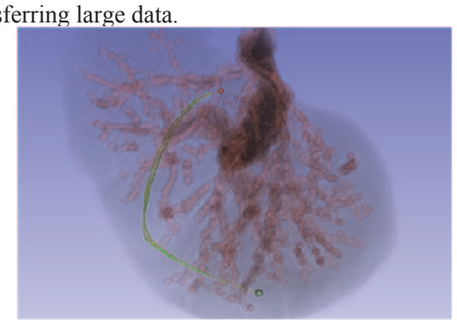

Fig. 1. Graphical output of an IGS system for needle steering. Collision-free paths (green) are shown against viable paths (yellow) which intersect the vasculature (red).

We propose an IGS framework that substantially improves upon the native data transfer speed of ROS, while maintaining its inherent modularity and scalability. A memory mapping mechanism is introduced to accelerate the exchange of large datasets between processes and a novel "closure transporting" architecture is proposed which significantly reduces the video memory transfer latency when parallel processing images with a graphics processing unit (GPU). This framework has been successfully applied in the context of a number of medical robot set-ups covering orthopaedics, neurosurgery and intra-vascular intervention, with excellent results pertaining to execution speed and data exchange time.

MATERIALS AND METHODS

Large Data Exchange with Memory Mapping

On modern operating systems, the most effective method for sharing large amounts of data across several processes is through the memory mapping facility.

In the proposed ROS-based architecture, ROS messages are used in conjunction with memory sharing to provide increased flexibility for data exchange. This is because, in ROS, message passing serves two purposes: (1) data exchange, which is replaced by memory sharing. (2) a mechanism for coordinating ROS nodes, which must be maintained to ensure ROS integrity.

When the exchange of large data is needed, messages are divided into two fields: the data descriptor and the raw data itself. Like for normal messages, a data descriptor is composed which includes information such as the time stamp, data size and application purpose. Within the data descriptor message, however, the actual image data is replaced by a handle which refers to a mapped memory region. The data descriptor is sent via the conventional message passing system, while the raw data is passed via memory mapping.

Closure Transporting for GPU Acceleration

Current IGS systems are increasingly leveraging the GPU to speed up many tasks, for instance image processing, simulation and visualization.

Data which is to be parallel processed by the GPU must reside in the on-board memory of the graphics card, since, as of today, there is no GPU memory sharing mechanism available on mainstream operating systems. When sharing data in video memory between ROS nodes, the 'publishing' node needs to copy the content

from the video memory to main memory and then the 'receiving' node copies the data back from main memory to video memory.

To reduce latency, our approach moves the processing logic around instead of the image data, a novel mechanism which we coined "Closure Transporting". Since, in IGS applications, the image data size is generally substantially larger than the code size of the processing logic, this transfer architecture can result in order of magnitude decreases in transfer times.

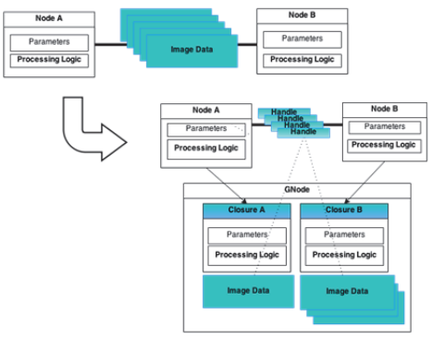

Fig. 2. Comparison of Typical ROS (upper left) with GPU-accelerated ROS (bottom right).

As shown Fig 2, an "intermediary" ROS node, GNode, is created for managing the GPU device, and is responsible for coordinating both computational and image data processes on the GPU. The work flow of a prototypical exchange can be summarised as follows:

- GNode communicates to the image device directly and places the image data in video memory;
- In the meantime, GNode publishes topics to notify the ROS node of the arrival of new image data.
- Each listening node submits its processing logic to the GNode, which will execute the commands and return the results.

As the memory sharing system presented in the previous section, closure transporting also builds on ROS without interfering with the ROS architecture. Thus, existing ROS nodes and modules can be easily integrated in this new ROS-based architecture without modification.

RESULTS

To illustrate the extent of speed improvement which can be achieved with the proposed architecture, the liver surgical planning task in **Fig 1** was implemented with and without accelerations, for comparison. The labelled liver data is ~64MB, with 512X512X256 voxels. The planning algorithm [3] first generates a large number of random paths, then checks for obstacles and constrains in a subsequent steps. In this specific scenario, the "surgery planner" produces ~70 obstacle-free paths after testing 10,000 arbitrary samples. On a test system running an Intel® Core™ i7-2600 CPU @ 3.40GHz, with 16GB of memory, equipped with an Nvidia GTX780 graphic card, the profiling results summarised in **Table 1** were obtained.

Table 1. Path Planning Profiling Results

CT Data Size (bytes)	67108864 (512x512 by256)
Planning Code Size (bytes)	5152
CPU Planning Time (μs)	8666700
GPU Planning Time (μs)	3525
CT ROS Messaging Time (μs)	3019900
Memory Mapping Time (μs)	800
GPU CT Copy Time (μs)	13055
Direct GPU Launch (μs)	14.3
Closure Evaluation (μs)	15.4

GPU planning was ~2,456 times faster, due to both the available computing unit and the texture cache system. The memory mapping system was ~3,700 times faster than the ROS messaging system for transporting CT images. With GPU and memory sharing, moving the data out and back into the GPU will require ~17,394 μs, while closure transporting will cost ~ 4,340.3 μs. With the GPU, the traditional ROS approach runs at about 0.3 frames per second, while our approach runs at ~200 fps, which is fast enough to track live tissue deformation.

DISCUSSION

The memory mapping and GPU closure transmission architectures proposed in this work can greatly reduce the message passing time in the presence of large data sets, with a consequent boost in the image processing performance achievable in IGS systems. Despite the necessary changes to the main message passing approach needed for these new transfer mechanisms to operate, the native ROS graph architecture is maintained and the user is still able to modify and reconfigure ROS nodes and connections at run time.

While these results have resulted in a marked improvement in performance for all of our systems, there are several avenues for future work. We are considering developing tools that automatically convert native ROS-based applications into our framework and a GUI is under development that will enable researchers to configure ROS nodes intuitively on the fly. Further extensions and a more aggressive optimization strategy are also being pursued.

REFERENCES

[1] M. Quigley, B. Gerkey, K. Conley, J. Faust, T. Foote, J. Leibs, E. Berger, R, Wheeler, and A. Ng, "ROS: An open-source robot operating system, "in Proc. Open-Source Software Workshop, ICRA 2009

[2] Gary K, Ibanez L, Aylward S, et al. IGSTK: an open source software toolkit for image-guided surgery[J]. Computer, 2006, 39(4): 46-53.

[3] F. Liu, C. Burrows, and F. Rodriguez, " Deformation As Control for a biological inspired steerable needle," in Proc. of IEEE (ROBIO 2013), Shenzhen,China, December 2013

Evaluation of a novel EM tracking system in a breathing lung model

K. O'Donoghue[1], A. Corvó[1], P. Nardelli[1], C. O' Shea[1], K. A. Khan[2], M. Kennedy[2], P. Cantillon-Murphy[1]

[1]*School of Engineering, University College Cork, Cork, Ireland*

[2]*Department of Pulmonology, Cork University Hospital, Cork, Ireland*

kilianod@rennes.ucc.ie

INTRODUCTION

Our prior work has demonstrated the design and operation of a novel EM tracking system in bench top tests with accuracy measured in an ideal environment [1]. Our end application is automated navigation and virtual endoscopy in the lung. For this purpose we have evaluated our system in a breathing lung phantom. By testing in an in-vitro scenario with the associated complications of breathing, registration errors and instrument distortion, the full capability of the system can be assessed.

MATERIALS AND METHODS

1. EM Tracker

The system uses planar magnetic coils transmitting low frequency magnetic fields (<30 kHz) and implemented on printed circuit board (PCBs), as well as a miniature pick-up coil sensors (8mm in length, 0.5mm diameter) placed at the distal end of a catheter. By measuring induced voltage in the pick-up coil caused by an array of magnetic sources emitting at various frequencies, position and orientation can be determined by solving a non-linear system of equations [1].

The sensor position is updated at a rate of approximately 25Hz. Commercially available sensors from NDI were used in this system. Having a fully custom EM tracking system allows for flexibility in its integration into the final system goal of automated airway navigation with virtual visualisation, as well as lower overall cost. Accuracy tests resulted in an overall RMS error of 1.2mm and an orientation error of 1° [1].

2. Emitter Board

The magnetic field emitter is a planar formation of PCB coils encapsulated in a 32cm×32cm×2cm Perspex. An approximate working volume of 30cm×30cm×30cm where the system operates to a high degree of accuracy exists on either side of the board.

3. Breathing lung model

A BioQuest Inflatable Lung kit (Nasco, Fort Atkinson, WI) was used as a phantom for evaluating the EM tracking system. The lungs are placed in a vacuum chamber, with the trachea connected to atmospheric pressure. When the chamber is evacuated, the pressure differential between the outside and the inside of the lungs causes them to inflate. Venting the chamber to the atmosphere equalises the pressure which causes the lungs to collapse to an uninflated equilibrium form (see Figures 1). Hence the lungs were made to inflate and deflate in a programmable way to simulate standard breathing patterns. An Arduino Uno microcontroller was used to enable a set of solenoid valves (AD612 by CS Fluid Power) to control the lung inflation level. One valve connects the vacuum pump, while another is used for venting the chamber. To set the breathing cycle, two dials are connected to the microcontroller. One sets the overall period of the cycle while a second sets the inflation time as a percentage of the period.

This simple and low cost solution proved very effective in simulating the human breathing pattern. A CT scan of the lungs in the inflated state was used to generate a 3D model [2] of the main airways which was then used to visualise the sensor's position in 3D.

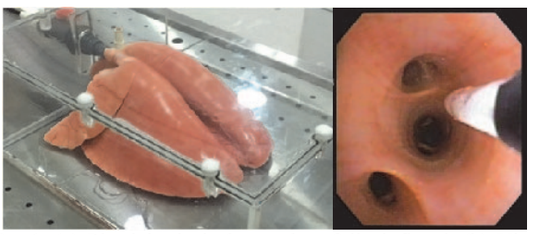

Fig. 1. (a) Plasticised pig lung when fully inflated. (b) View from the bronchoscope inside the phantom with the sensor extended out from the instrument port.

4. Bronchoscope

An Olympus 1T160 bronchoscope was used for the breathing lung tests. The unit has a 6mm OD with an instrument channel diameter of 2.8mm. The position tracking probe was inserted through the bronchoscopes instrument channel for the tests that follow.

5. Registration

A novel registration algorithm is used to register the sensor position to the coordinate frame of the lung model. The algorithm finds the transformation matrix $\mathbf{T}_m^e$ that minimizes the distance between a cloud of test points denoted by X_i distributed along the airway and the points that form the centre line of the airway Y_i (derived from CT segmentation). By calculating the mean of the minimum Euclidean distance between X_i and Y_i as a function of a transformation matrix $\mathbf{T}$, a non-linear 6 variable equation results (3 each for rotation and translation) where

$$\mathbf{T}_m^e = \min_{\mathbf{T}} \left| \mathbf{T} X_i - Y_i \right|$$

The Levenberg-Marquart method was used for this minimisation and was implemented in Matlab. Typical runtime was 1-2 minutes depending on the number of test points and the accuracy of the initial registration.

6. Breathing lung phantom tests

The system operation was accessed in the breathing lung phantom. Firstly the lung was fully inflated in order to match the 3D model derived from the CT scan. In this position, the bronchoscope was used to navigate the airways. The position sensor probe was inserted inside the instrument channel and extended beyond the scope as required. Position data was gathered during navigation and used to register the 3D model to the EM tracker frame of reference.

For the second test, cyclic breathing was enabled. The breathing cycle period was set to 5.3s, inhalation was enabled for 27% of this period, and exhalation occupied the remaining 73%. To assess the effect of breathing, the sensor was positioned in a number of points within the lung and its displacement versus time recorded.

RESULTS

1. Registration

When applied to real data acquired within the lung, our registration algorithm reached a result in 53s with 80 data-points. 78/80 of these points were found to be within the airway, with a mean distance between the points and the centreline of 2.1mm.

2. Navigation accuracy

Figure 2(a) shows a plot of data points recorded when the lung was fully inflated after they have been adjusted using the registration transformation. Clearly some recorded points diverge from the 3D model. The primary reason for this is misalignment of the lung model after its initial CT scan. This might be rectified with careful positioning of the lung in order to align it with the CT data. Other factors that affect accuracy are the level of inflation and general wear and tear of the model over time (CT data was acquired some time prior to the experiment). The errors associated with the EM tracker are small in comparison with the large divergence seen from the data. If we consider the data gathered along the main airways (Figure 2(a)) after registration, 89.3% of the points are found to be inside the lung model.

In order to visually confirm registration, the sensor position was displayed in real time on the 3D model alongside the view from the bronchoscope. After registration, the probe was navigated through the airways and the sensor could be seen to be invariably within the model boundary.

A video link to the navigation testing is available at http://youtu.be/wv1bwLzOxGc .

3. Breathing motion

Figure 2 (b) demonstrates position tracker displacement experienced at various points within the lung when a standard breathing cycle is implemented. As expected, the amplitude of displacement varies depending on the position of the lung. Maximum displacement was observed at points more central to the lung model, while distal points and smaller airways experienced less. The amplitude of the displacements recorded were found to range from a few mm to less than 10mm. This is in line with clinical test data from patients reported elsewhere [3], [4].

Methods exist for counteracting the effect of breathing displacements in position data [3] and future work will attempt to implement modelled displacements to account for these variations. This is required as typically only a static 3D model is available and breathing artefacts can affect registration and overall system accuracy.

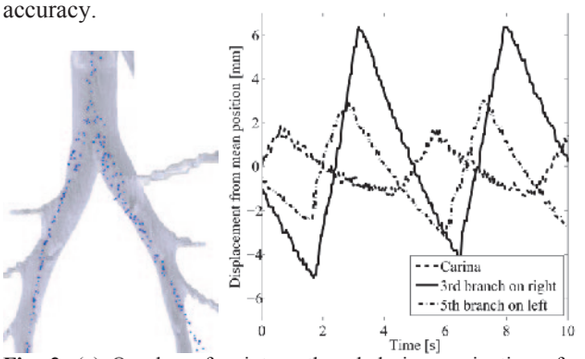

Fig. 2. (a) Overlay of points gathered during navigation of main airway after registration. (b) Displacement of sensor with time due to breathing cycle. The sensor was positioned in three positions, one at the carina, a second at a central location in the long and finally at a distal point. The max amplitude of displacement recorded was observed in the centre of the lung.

DISCUSSION

A highly accurate magnetic position tracking system has been presented and evaluated in a breathing lung model. After registration, the majority of recorded points were found to lie inside the boundaries of the 3D lung model. This was confirmed visually with real time display of the sensor probe position. This, in combination with the previously demonstrated accuracy of the system from bench-top tests effectively verifies the overall system operation in the in vitro setting. It was also observed that the close proximity of the probe to the bronchoscope had no observable effect on the system performance.

REFERENCES

[1] K. O'Donoghue, P. Cantillon Murphy, D. Eustace, J. Griffiths, H. Mansfield, T. Power, and M. O'Shea, "Catheter position tracking system using planar magnetics and closed loop current control," *IEEE Transactions on Magnetics*, vol. PP, no. 99, pp. 1–1, 2014.

[2] P. Nardelli, R. San Jose Estepar, and P. Cantillon-Murphy, "Semi-automated Airway Segmentation for Lung CT Datasets," in *27th International Congress and Exhibition in Computer Assisted Radiology and Surgery (CARS)*, 2013.

[3] D. Ruan, J. A. Fessler, and J. M. Balter, "Mean position tracking of respiratory motion.," *Medical physics*, vol. 35, no. 2, pp. 782–92, Feb. 2008.

[4] Y. Seppenwoolde, H. Shirato, K. Kitamura, S. Shimizu, M. van Herk, J. V. Lebesque, and K. Miyasaka, "Precise and real-time measurement of 3D tumor motion in lung due to breathing and heartbeat, measured during radiotherapy," *International Journal of Radiation Oncology*Biology*Physics*, vol. 53, no. 4, pp. 822–834, Jul. 2002.

The Face, Content and Construct Validity of a FAST Phantom

M. Chaudery[1], J. Clark[1], D. Apdafydd[2], J. Dunn[2], G.-Z. Yang[1], A. Darzi[1].

[1]*The Hamlyn Centre, Institute of Global Health Innovation, Imperial College London, UK*

[2]*St Mary's Hospital, Imperial College Healthcare NHS Trust, UK*

muzzafer.chaudery10@imperial.ac.uk

INTRODUCTION

One of the most significant reasons for trauma related mortality is uncontrollable haemorrhage from the torso[1]. Swift identification and control of bleeding, ideally in the pre-hospital setting, is of paramount importance. Focussed Assessment with Sonography in Trauma (FAST) offers a practical diagnostic modality for rapid identification of bleeding from the torso. It is quick, cheap, portable, effective in experienced hands with no radiation exposure to the patient [2]. However, utilisation of FAST in the pre-hospital setting has been slow due to extensive training necessary to gain the proficiency to recognise haemorrhage.

A high fidelity trauma phantom simulator could bridge the gap required to become competent in haemorrhage identification. Additionally consensus guidelines [3] state that validation of simulators is essential for future training and research. With no previous evidence available, this study aimed to develop a method to validate a FAST simulator from which future training systems could be guided.

MATERIALS AND METHODS

For construct validity a novice, intermediate and expert group performed a FAST scan on a phantom and were assessed in each area for the time taken to identify an abnormality (Time 1), time to freeze the pathology (Time 2) and total time to perform FAST (Time 3). Other metrics evaluated were errors made and missed targets. The accuracy of images obtained was verified by two independent expert radiologists who were blinded as to whether the subject was a novice/intermediate/expert. They scored the quality of the image on a scale of 1 to 4 (marks were awarded as follows e.g. for correct anatomy of Morison's pouch, liver=1, kidney=1, free fluid=1 and good image quality=1). Additionally, the expert group completed a face and content validity questionnaire.

The "FAST/ER FAN" ultrasound phantom built by Kyotokagaku Ltd was used in this study (Fig. 1).

The trauma pathology within the phantom that the subjects had to identify included fluid in Morison's pouch, spleno-renal angle, bilateral haemothorax, cardiac tamponade, pelvis and an abdominal aortic aneurysm(AAA). The study was conducted using the Zonare USS machine (Zonare Medical Systems, Inc. Mountain View CA, USA) with a C4-1 Curved array transducer which has a bandwidth of 1-4MHz and provides an 80 degree viewing angle. The ultrasound exam mode was set to FAST scan at a depth of 16cm, in a standard 2D Abdominal B-mode. This study had ethical approval obtained from the Imperial College Research Ethics Committee.

Fig. 1. The FAST/ER FAN Phantom

RESULTS

Of the 31 participants there were 11 experts, 10 intermediates and 10 novices. Experts had a mean of 5.68±4.8 years of ultrasound experience. The median number of ultrasound procedures previously performed by intermediates was 8±23 and experts 400±670 cases. The Face and content validity questionnaire (median score out of 5) highlighted that the phantom was easy to use (5±0.5), the anatomy (4±0), feel (4±1), pressure (4±0.5), angle of the probe (4±1.5) were considered lifelike and it was deemed as a useful training tool (5±1); with an overall realism mark (median score out of 10) of 8±1.5 on a Likert scale. There was a significant difference in Time 1, Time 3, missed targets, errors and accuracy of images across cohorts as well as in the inter-group analysis ($p<0.001$). Both the novices and intermediates were the slowest, least accurate and either missed or made the most errors in the region of lung bases, spleen and AAA (Fig. 2).

DISCUSSION

This study has demonstrated the validity of a leading FAST simulator as evidenced by high scores in the face-content validity questionnaire, as well as establishing construct validity. Of note, the novices and intermediates had the most difficulty scanning the lung bases, spleen and AAA. Subsequent training could focus on these areas in order to improve performance. Future research includes a longitudinal prospective

validity study to confirm the translational training capability of the simulator. Furthermore, an analysis of expert ultrasound probe motion during a FAST scan would yield valuable data which could be translated into an autonomous platform.

REFERENCES

[1] Kauvar DS, Lefering R, Wade CE. Impact of hemorrhage on trauma outcome: an overview of epidemiology, clinical presentations, and therapeutic considerations. J Trauma. 2006 Jun;60(6 Suppl):S3-11.

[2] Rippey JCR, Royse AG. Ultrasound in trauma. Best Practice & Research Clinical Anaesthesiology. 2009;23(3):343-62.

[3] Carter FJ, Schijven MP, Aggarwal R, Grantcharov T, Francis NK, Hanna GB, et al. Consensus guidelines for validation of virtual reality surgical simulators. Simul Healthc. 2006 Fall;1(3):171-9.

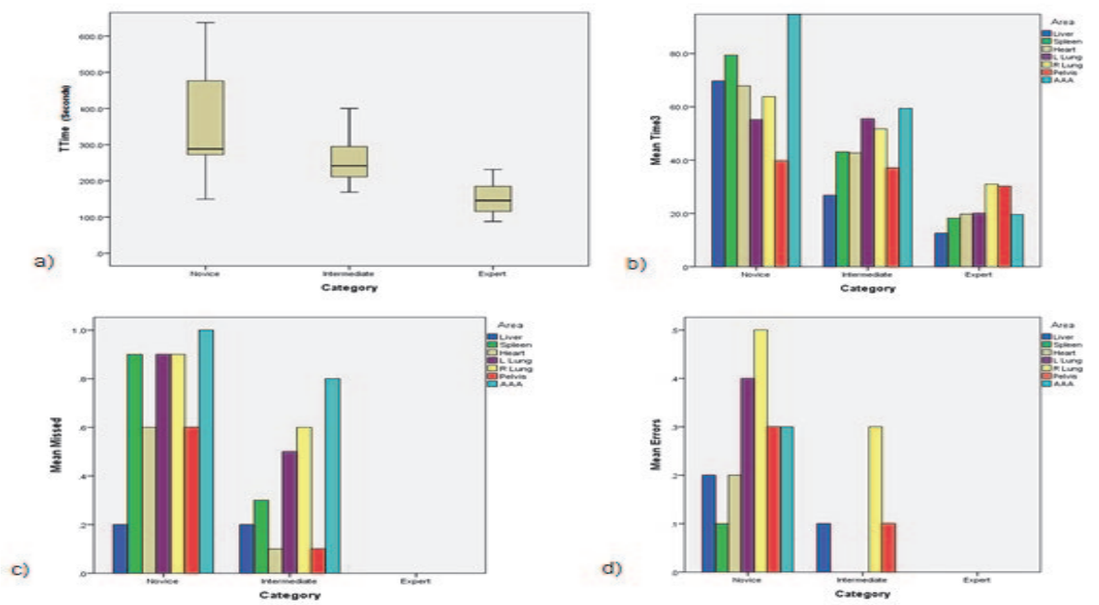

Fig. 2. a)Total Time to perform FAST scan between groups b) Mean time to perform FAST scan per Quadrant between groups c) Mean Missed Areas per Quadrant by Category d) Mean Errors Per Quadrant by Category

Prototype Design of Flexi-Hand for Single Incision Laparoscopic Surgery

G. K. Zhang, S. X. Wang, J. M. Lin, Y. Y. Sun, Y. Xing

Key Lab for Mechanism Theory and Equipment Design of Ministry of Education, Tianjin University, China

shuxinw@tju.edu.cn

INTRODUCTION

In single incision laparoscopic surgery (SILS), since the wholly rigid tools could not construct the necessary "operation triangle", flexible tool is the only choice. But it also faces up to the challenges of direct motion-mapping and enough applied force. Motion mapping could be carried out by the robotic technology that the motion of the tool's tip could be precisely calculated and well controlled depending on the motion modeling. Some single incision surgical robot could realize visual "motion mapping" now[1]. As for the operation force, many methods are proposed like layer jamming, welding flux, plasticization, force closure, etc[2,3]. This paper provides a systematically design method for an original flexible tool for single incision laparoscopic surgery based on classical surgical operation analysis. Different from the existing methods, phase-change material (PCM) is used to get variable stiffness of the tool. By this method, flexibility and rigidity of surgical tool would be adapted with material phase-change to satisfy the requirements 1) enter into body from single incision 2) implement the enough operation force.

MATERIALS AND METHODS

The tools for SILS get into the body via a single port. To construct the "operation angle", every tool involves an open joint, a triangle construction joint and an operation joint, then a flexible tool must has three movable joints at least. To improve the flexibility and get around the existed difficulties in control, four controllable joints would be an ideal solution. The necessary condition for precision control is that the number of activators equal to the DOFs of the instrument. Nevertheless, too many activators lead to larger volume. To reduce the system volume, four joints would be controlled by one activator, in which each joint must has the function of self-lock.

♦ Phase-Change Material (PCM)

PCM is a kind of martial which could change phases at hoped temperature. PCMs in common use are Paraffin, Salt hydrates, liquid metal and alloy. All of the PCMs could realize the motion in large scales in several DOFs by changing between solid and liquid. PCM has a good feature of stiffness-changeable, but large energy or strong filed would be needed to realize the change. Then it is very difficult to bring the PCM into the application of surgery. In this paper a kind of material, gallium base alloy, is adopted as inside material of a stiff-change joint. With melting point of 31.2 degree centigrade, its temperature change with phase change in a small scale will not do harm to human body. As alloy metal, it has good electrical conductivity for easy phase-change by electricity.

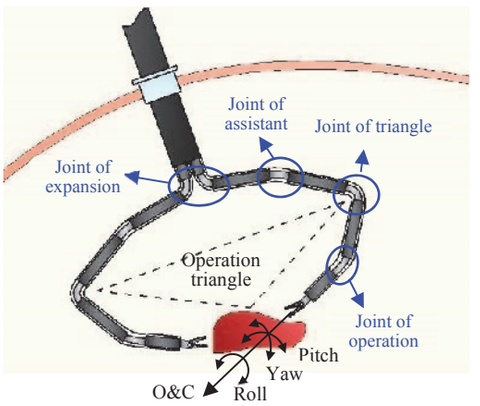

Fig. 1. Concept of Flexi-Hand

♦ Variable Stiffness Joint

The key to make Flexi-Hand available is a joint with changeable stiffness and multi-DOF. The joint owns rigid rod on both sides to connect to tool with PCM stored in the groove at the side of each rigid rod to improve joint rigidity at the phase of solid. In the middle of joint there is a Ni-Ti alloy pipe for connection and support. Then a soft axis could reach the end of Flexi-Hand through the pipe to control the DOF of O&C. To reduce energy loss by stiff-change, metal parts directly connecting to PCM would cover an insulating coat expect electrode.

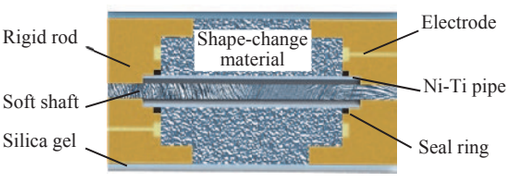

Fig. 2. Concept of Flexi-Hand

Since the operation joint has one more DOF of rotation than others, the Ni-Ti alloy pipe inside and the rigid rods could rotate relatively, not connected in other joints. The design that square terminal of the soft axis matches the square hole in tool terminal make the soft axis could active the tool switching and keep rotate along its own axis. To prevent leakage when material is

in liquid phase, the outside of joint is covered with high plastic silica gel. By motion and stiff separate control mode, the phase of material will be changed by inner electrode. Four driven tendons are distributed at the outside of joint to controlling the DOFs of swing and deflection.

♦ Shift of the Variable Stiffness Joint

Heat of fusion (HoF) is the change in enthalpy resulting from heating a given quantity of a substance to change its state from solid to liquid. Imported heat that is higher than its HoF is used to realize the joint from rigid to flexible. The resistance is very small and the average current is excessive, so a short circuit occurs if we take a normal power source. On the surface, such a large current is dangerous for patients. However, in fact, only a small voltage is needed to realize the shift of stiffness. Capacitor, an energy storage element, can also serve as power source under exceptional circumstances. What's more, the rate of its discharge is quite fast and we'll never need to worry about the short circuit. To allow for more than one shift, a super capacitor with a rated capacitance of 1800F and voltage of 2.5V is adopted. Given the voltage of the capacitor and the resistance of the joint, the discharge current vs. time is given by

$$I(t) = (U / R)\exp(-t / RC) \quad (1)$$

And the energy absorbed by PCM can be calculated as

$$w = \int_0^t RI^2(t)dt \quad (2)$$

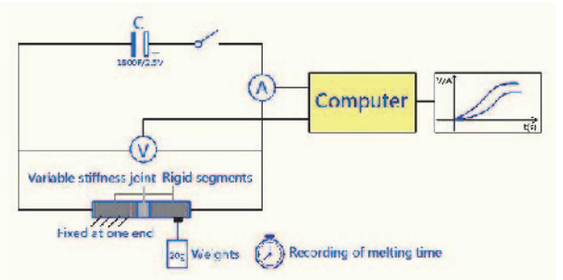

Fig. 3. Schematic diagram of melting time recording experiment

According to above derivation, the melting time at any voltage can be calculated. Besides the theoretical analysis, an experiment to measure the melting time is done as well. In the experiment, the variable stiffness joint is connected with a super capacitor of which the beginning voltage decreased from 2.5V to 0.5V by division into 5 times. The joint is rigid as a line before power on. One of two rigid rods is fixed and the other is hung with a weight. The drop times of the weight were recorded and compared with the theoretical data. The result shows that the recorded time is longer than the theoretical time. The reasons may be: 1) the system resistance cannot be measured accurately; 2) the recorder takes some response time. Although recording time is not in discipline, it helps us to correct the theoretical result.

RESULTS

On the basis of variable stiffness joint, a prototype of flexible surgical tool, Flexi-Hand, was developed originally. It composed of four joints and has an outer diameter of 6mm. The first-three joints are pose joints to reach the end of the lesion location. The last one is an operation joint to handle the effectors of the tool during operation. Each joint is able to rotate for 60 degrees. And locked position and orientation can be up to 180 degrees. The end of the tool has rotation DOF and O&C DOF. This prototype, realizing pitch, yaw and roll rotations, constitutes a line as manual operation habit. A tissue operation was performed with this prototype.

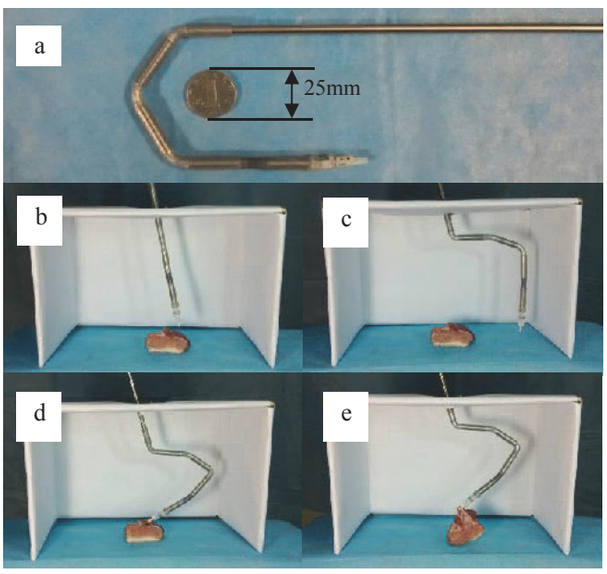

Fig. 4. a. Prototype of flexible tool for Flexi-Hand; b-e. An operaiong task under SILS condition using the prototype.

DISCUSSION

This paper presents the concept of Flexi-Hand, a surgical system for single incision laparoscopic surgery. And an initial experiment shows that it has both the flexibility to arrive the designed location and stiffness to perform the operation.

ACKNOWLEDGEMENT This work is supported by the Major Program of NSFC under grant No. 51290290.

REFERENCES

[1] Simaan N, Xu K, Kapoor A, *et al*. Design and Integration of a Telerobotic System for Minimally Invasive Surgery of the Throat. The International Journal of Robotics Research. 2009 Sep; 28(9): 1134-1153.

[2] Kim Y J, Cheng S, Kim S, and Iagnemma K. A Novel Layer Jamming Mechanism With Tunable Stiffness Capability for Minimally Invasive Surgery. IEEE Transactions on Robotics, 2013 Aug; 29(40): 1031-1042.

[3] Loeve A J, Bosma J H, Breedveld P, Dodou D, and Dankelman J. Polymer Rigidity Control for Endoscopic Shaft-Guide 'Plastolock'—A Feasibility Study. Journal of Medical Devices. 2010 Oct; 4(4): 045001.

Shedding Light on Surgeons' Cognitive Resilience: A Novel Method of Topological Analysis for Brain Networks

M. Kiani, J. Andreu-Perez, D. R. Leff, A. Darzi, G.-Z. Yang

[1]*The Hamlyn Centre, Institute of Global Health Innovation, Imperial College London, UK*

{m.kiani13, javier.andreu, d.leff, a.darzi, g.z.yang}@imperial.ac.uk

INTRODUCTION

The human brain performs as an extremely efficient and complex network [1]. Greater insights into the topology of human brain networks have been made possible through the emergence of complex system analysis. Theoretically, through repeated practice and learning related changes in synaptic function (i.e. neuroplasticity) expert surgeons may develop network architectures that are more stable and resilient when compared to those of novices. Whilst prior work has evaluated neuroplasticity associated with motor skills learning [2] [3] [4], there has been limited investigation of how experience in robotic minimally invasive surgery (MIS) influences the operator's network topology. One approach to compare network resilience during MIS tasks is to investigate how networks perform under computational attack.

The aim of this study is to investigate the hypothesis that through practice brain networks in experienced operators are optimized for performance and hence are more robust to attacks than novices. To this end computational attacks were used to investigate the resilience of brain networks in a group of surgeons, with varying experience of MIS, to appreciate the role of repeated practice on network resilience.

BACKGROUND

A number of studies have been conducted to analyze the topological resilience of complex networks For example, work by Joyce et al [5] and Alstott et al [6] focused on brain networks resilience against attacks whereas studies by Watts et al [7] and Albert et al [8] examine the resilience of social networks against attacks. However, none of these consider the role of optimization or evolution of a network in rendering it more robust to attack. This study is aimed at discerning the significance of experience in the adaptation of brain networks using computational attack as a surrogate.

METHODS

A total of 27 healthy participants took part in the study (9 novices, 10 trainees, and 8 experts, which require them to perform a set of laparoscopic procedures namely: needle insertion, double throw knot, and single throw knot). The subjects were asked to perform these tasks while a 44 channel (measuring point) - Optical Topography system positioned over the frontal lobes recorded their brain behavior. Light data was converted into oxygenated hemoglobin and deoxygenated - hemoglobin. In order to form adjacency matrices and to capture synergies between both hemoglobin species, standard correlation is not appropriate. Hence for the two-dimensional data obtained, RV-coefficients are calculated [9]. Here, for every subject performing a given task, an adjacency matrix of size 44x44 was calculated. In order to eliminate spurious data, averaging was used such that there is one adjacency matrix for a given group performing a given task. This computation produced a total of nine adjacency matrices (3 categories of MIS task, 3 experience groups).

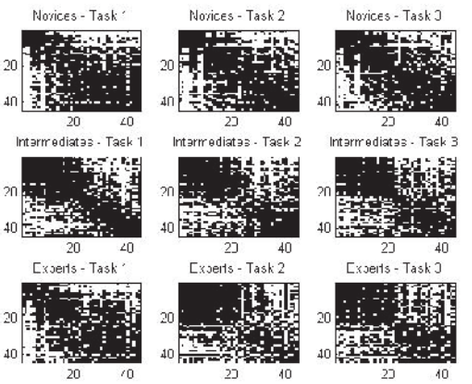

Fig. 1. The sampled adjacency matrices for all three experience groups performing three different motor learning tasks. A white pixel indicates connectivity between corresponding nodes.

After computing the nine adjacency matrices, pruning was performed for computational ease while ensuring that the ten strongest connections out of possible 44 connections of every node were retained. This resulted in a binary, asymmetrical matrix, which is then converted into a symmetrical matrix resulting in an average link density of 0.2273. Figure 1 illustrates the final adjacency matrices.

Pruning also resulted in disconnected networks. Thus, in order to regain connectivity, the strongest connection between the nodes of any two child components is restored till the entire network becomes reconnected.

The topological analysis was performed by removal of 11 (25%) random nodes sequentially. Figure 2 shows the final networks with the 20 highest degree nodes after random attack. Once a node is removed from the network, local metrics namely clustering coefficient and modularity are computed.

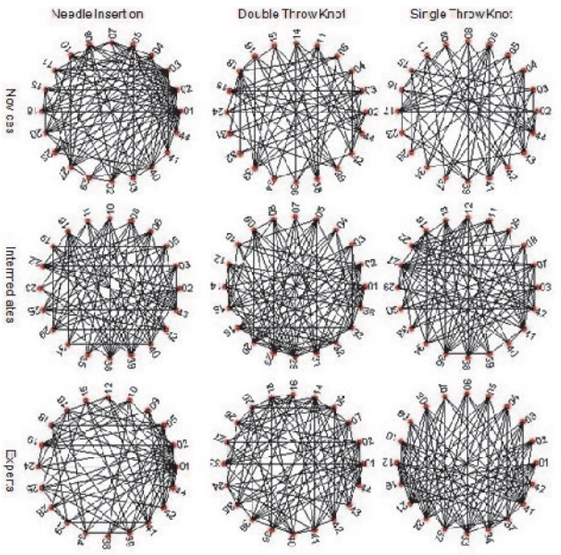

Fig. 2. Networks showing 20 highest degree nodes after random attack.

RESULTS

In order to quantitatively measure the resilience of functional brain networks against random attacks, clustering coefficient and modularity metrics are computed. The results obtained are preliminary.

As illustrated in Figure 3 experts have a lower clustering coefficient when compared with novices and intermediates for most number of nodes removed. This indicates that the brain networks of the experts is less clustered and more optimized rendering it more resilient to attacks.

The second metric, used for comparing the resilience of brain networks among subjects of different experience levels, is modularity. Figure 4 demonstrates that the more experienced the operator the lower the modularity emphasizing that expert brain networks are more tolerant to random node removals.

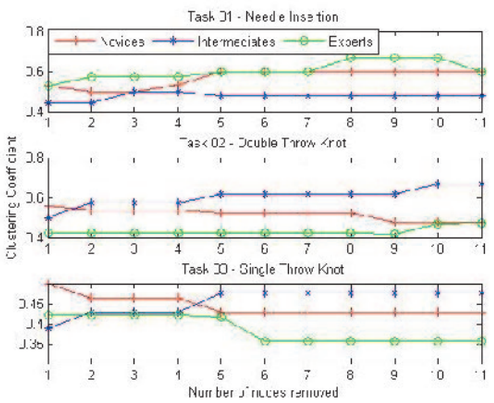

Fig. 3. Clustering coefficient values after every random node removal for novices, trainees and experts.

DISCUSSION

This study not only compares functional brain networks based on experience but also computationally quantifies their resilience against random topological attack. Overall, the results are intuitive and suggest that experience not only leads to refinements in motor technique but also impacts upon brain network resilience. Network performance degrades as networks nodes are progressively removed more so in novice operators. In contrast, expert brain networks are especially resilient for highly complex MIS tasks (e.g. knot-tying tasks). Critically, the current approach offers a new method for evaluating an operator's internal familiarity with robotic MIS.

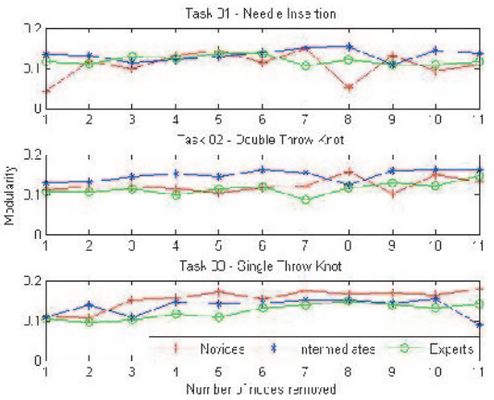

Fig. 4. Modularity values after every random node removal for novices, trainees and experts.

REFERENCES

[1] Bassett, D. S. *et al* .Small world brain networks. The Neuroscientist 2006; 12: 511-523

[2] Puttemans, V. *et al.* Changes in brain activation during the acquisition of a multifrequency bimanual coordination task: From the cognitive stage to advanced levels of automaticity. The Journal of Neuroscience 2005; 25: 4270-4278

[3] Zhu, F. F. *et al.* Implicit motor learning promotes neural efficiency during laparoscopy. Surg Endosc 2011; 25: 2950-2955

[4] Karni, A. *et al.* The acquisition of skilled motor performance: Fast and slow experience-driven changes in primary motor cortex. Proc Natl Acd Sci 1998; 95:861-868

[5] Joyce, K.E. *et al.* The human functional brain network demonstrates structural and dynamical resilience to targeted attacks. PLoS Computational Biology 2013; 9: e1002885

[6] Alstott J. *et al* .Modeling the impact of lesions in the human brain. PLoS Computational Biology 2009; 5: e1000408

[7] Watts D.J. A simple model of global cascades on random networks PNAS 2002; 9: 5766-5771

[8] Albert R. *et al.* Error and attack tolerance of complex networks 2000

[9] Robert, P. A unifying tool for linear multivariate statistical methods: the RV-coefficient. Applied Statistics 1976; 25: 257-265

Instrument-Based Registered Strain Imaging for Remote Palpation in Robot-Assisted Laparoscopic Surgery

O. Mohareri, C. Schneider, S. E. Salcudean

Robotics and Control Laboratory, University of British Columbia, Canada

{omidm,tims}@ece.ubc.edu

INTRODUCTION

Robotic surgical systems provide a platform for integrating surgical guidance with imaging and automation of particular tasks, while enhancing the ability of surgeons to perform delicate and precise minimally invasive surgery.

One limitation of many robotic surgical systems is the inability of the operating surgeon to feel the tissues on which they are operating. During open surgery, surgeons are able to physically palpate the tissue and feel for stiff tumours under the surface, which enables them to tailor their resection margins to remove only the cancerous tissue and preserve as much healthy tissue as possible.

Unfortunately, during robot-assisted operations, surgeons are only able to rely on visual cues for tissue characterization. This becomes particularly important for operations such as partial nephrectomy, during which the smallest amount of the kidney is removed while preserving surgical margins. Other operations such as radical prostatectomy could become less invasive if the precise location of tumors was known intraoperatively.

Previous work has used specialized da Vinci interfaces to create strain images by overlaying a sinusoidal motion over the surgeon's motion, but this cannot be easily transferred to a surgical environment [1].

In this paper, we propose a novel and straight forward method for creating high-quality real-time strain images using registered robotic ultrasound and manual surgical instrument indentation to provide subsurface images to the surgeon at the console.

MATERIALS AND METHODS

Two series of experiments were used to validate instrument-based strain imaging for robotic radical prostatectomy and partial nephrectomy using the *da Vinci*® surgical system (Intuitive Surgical Inc.). In both cases, the ultrasound transducers were robotically controlled and 3D ultrasound was registered to the da Vinci surgical instrument. In our proposed method for control of the robotic ultrasound [2, 3], the ultrasound imaging plane is automatically repositioned using the robot so that a 2D ultrasound image continuously contains the tip of a specified da Vinci surgical manipulatoras demonstrated in Figure 1. The automatic instrument tracking is achieved using an air-tissue boundary registration method for intraoperative registration of 3D ultrasound to an external coordinate system [2].

Mechanical excitation is applied to the tissue manually using the surgical instruments. A sequence of n_f frames of RF-data is acquired for each 2D plane by the ultrasound machine, and processed using a speckle tracking algorithm [4] to create a series of real-time displacements per pixel, and create strain images. The strain images are displayed to the surgeon within the console using the TilePro feature of the da Vinci Si surgical system to provide real time guidance.

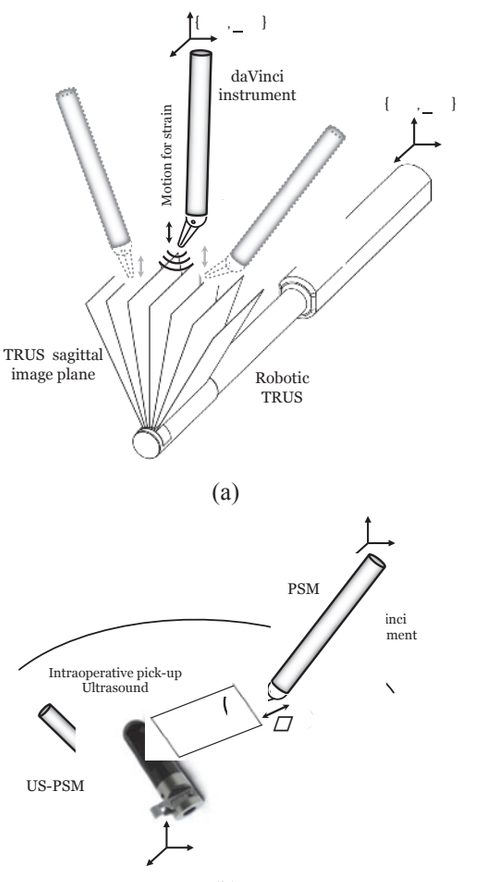

Fig. 1. (a) Instrument-based strain concept with robotic registered transrectal ultrasound for radical prostatectomy procedure, (b) Instrument-based strain concept with a pick-up ultrasound transducer grasped by the da Vinci auxiliary manipulator for partial nephrectomy procedure.

While it does not provide an absolute value of elasticity, strain imaging provides an idea of tissue compliance. If in response to an excitation, a certain region of interest

exhibits higher strain than the background, it is likely to be softer.

For validation of the method in the case of radical prostatectomy, a CIRS prostate phantom (Model 066) was used with a parasagittal/transverse biplane TRUS transducer shown in Fig. 2a. The *ProGrasp*® robotic instrument was used to touch the surface of the phantom gently. The prostate phantom contains several stiff inclusions as well as a simulated urethra.

When considering the case of partial nephrectomy, a different set-up was used. An ex-vivo kidney was implanted with stiff PVC inclusions. These inclusions were then imaged using a robotically held ultrasound transducer [5].

RESULTS

High-quality strain images were produced in the prostate phantom. The light pressure of the robotic tool was enough to create a strain image of the entire phantom. The lesions within the phantom can easily be located and other anatomical features, such as the simulated urethra can also be identified (Fig. 2).

Using an ex-vivo kidney, the lesions could also be seen on the strain and displacement images from the small intraoperative transducer. We touched several different locations around the transducer to estimate the effect on the strain image, but in all cases the strain image clearly depicted the imbedded stiffer region (Fig. 3).

DISCUSSION AND CONCLUSION

We have shown the feasibility of creating strain images with only the tools that would be normally available to a robotic surgeon. In the near future, we will be testing the method in real prostatectomy cases. This method is entirely feasible and easy to implement in a real surgical setting with a minimum of added equipment.

Although strain imaging is sensitive to boundary conditions and operator technique and, in the absence of measured forces, produces only relative measurements, it is a simple but highly effective method for determining the stiffness under the surgeon's tool. Because the proposed integration of strain imaging uses a tool tracking technique, the surgeon can easy and intuitively determine the stiffness directly in the area where they are going to work. This would potentially improve the surgical margins and allow for more precise dissections.

The proposed method in this work is an easy to integrate technique with promising results that justify further clinical studies to prove the real usefulness.

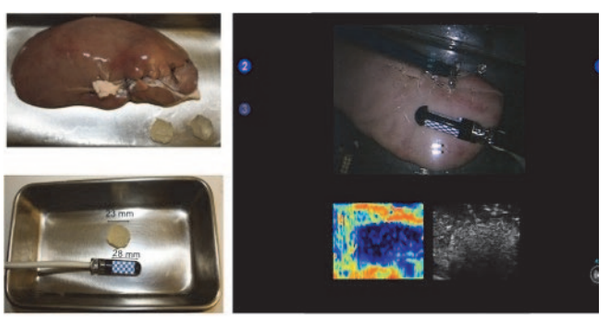

Fig. 3. (a) The porcine kidney specimen with implanted stiff PVC inclusions, (b) TilePro images from the da Vinci surgical console. Both strain and B-mode images could be provided to the surgeon at the console in real-time.

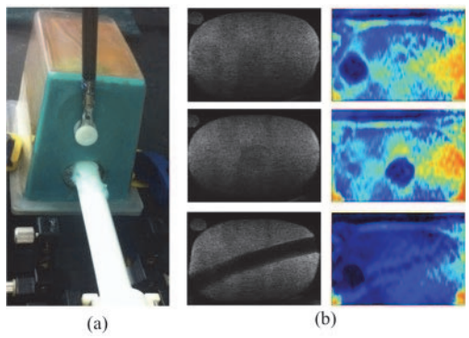

Fig. 2. (a) Experimental setup for imaging the CIRS prostate phantom using robotic TRUS and da Vinci ProGrasp instrument, (b) Real-time B-Mode and displacement images of the phantom's inclusions and urethra.

REFERENCES

[1] S. Billings et al. "System for Robot-assisted real-time laparoscopic ultrasound elastography", in Proc. SPIE 2012.

[2] T. Adebar et al. "Registration of 3D ultrasound through an air-tissue boundary", TMI, Vol. 31, No. 11, pp. 2133-2142, 2012.

[3] O. Mohareri et al. "*da Vinci*® auxiliary arm as a robotic surgical assistant for semi-autonomous ultrasound guidance during robot-assisted laparoscopic surgery", HSMR 2014, (in review).

[4] R. Zahiri-azar et al. "Motion estimation in ultrasound images using time domain cross correlation with prior estimates", TBME, Vol. 53, No. 10, pp. 1990-2000, 2006.

[5] C. Schneider et al. "Intra-operative 'Pick-Up' Ultrasound for Robot Assisted Surgery with Vessel Extraction and Registration: A Feasibility Study", in Proc. IPCAI 2011.

Why LopeRA failed to recruit? A qualitative study

R. Jalil[1], E. K. Mayer[1], N. Sevdalis[1], K. Kerr[1], J. S. Green[3], E. Hall[2], J. Vale[1], A. Darzi[1]

[1]*Division of Surgery, Imperial College London, UK*
[2]*Institute of Cancer Research- Clinical Trials and Statistics Unit, UK*
[3]*Barts Healthcare NHS Trust, UK*
r.jalil@imperial.ac.uk

INTRODUCTION

Empirically recruiting for randomised controlled trials (RCTs) is a challenging process [1-4] especially when competing biases impact on the ability of both patients and/or recruiter to truly accept clinical equipoise. LopeRA was a multi-centre randomised feasibility study for a phase III randomised controlled trial comparing laparoscopic, open and robot-assisted radical prostatectomy as treatment for prostate cancer.

The LopeRA study set out to recruit more than 100 patients in total within two years of the trial opening, with at least 75 patients being recruited within a 12-month period. In the first 15 months, however, only 29 patients were randomised representing 25% of eligible patients approached. Recruitment rates were below target and reported reasons for difficulty of recruitment included patient preference for robotics – primarily due to patients' independent research on the Internet and their preconception of wanting robotic prostatectomy.

The primary aim of this qualitative study was to identify factors that contributed to the lower than expected recruitment rate in LopeRA. The study would also assess whether adaptation of the recruitment process, by feedback to recruiters, can improve recruitment rates and information pertaining to recruitment to surgical RCTs in general will be obtained and subsequently the recommendations from this study can be extended to future surgical RCTs (secondary aims).

METHODS

This study considered the views of all parties involved in the LopeRA trial. Therefore patients, clinicians and research nurses were invited to take part in the qualitative study. To allow the barriers to randomisation to be explored in detail, semi-structured interviews were to be conducted with both recruiters and patients. These interviews would elicit key themes in the decision making process of both patients and also recruiters, which will be qualitatively compiled and compared. The main trial closed after completing the interviews with the recruiters therefore not allowing the patient interviews to be undertaken.

RESULTS

A total of 9 recruiters were interviewed (Surgeons=6, Research nurses=3). The number of robotic operations performed by the surgeons ranged from 15-150 per year. The number of open prostatectomies performed by surgeons ranged from 1-15 per year (the 15 was performed by a surgeon who has since moved away from prostate work). A single surgeon performed laparoscopic prostatectomy (approximately 90 per year).

The decision by patients to accept randomisation varied, according to recruiters' perspective, from 30%-90%. Reasons for patients declining randomisation, according to recruiters, were as shown in Table 1 below.

CONCLUSION

Evidence from the semi-structured interviews suggested that the recruiters had too much personal bias for one operation type over the others. In particular, those who conducted robotic surgery did not feel they could present all surgical options with equipoise.

There was also a quoted market-led bias with patients seeking out specific surgeons for specific surgery types. This could be impacted on by using advertising/marketing strategies for the clinical trial to improve the recruitment process.[5]

Confidence and trust is built up between a patient and their surgeon that can facilitate a truly balanced discussion when presenting multiple surgery options. The absence of a surgeon, within the trial, who could perform all three surgical techniques on offer prevented us from exploring this further.

The closure of the LopeRA trial meant we could not explore our secondary aims as intended, but a better understanding of barriers to recruitment general to all surgical RCTs could help inform a framework to screen future trials for likely success of recruitment.

Table 1. Illustrative verbatim quotes from the study recruiters provided as explanations for failure in randomisation.

- I think that many patients seek out a particular surgeon on the basis of reputation (6). "they would actually say…….Nurse, I can only enter into this trial if you promise me that, you know, Dr So and So is going to do my operation because he has done it for So and So and I know he turned out very well" (Research nurse from a laparoscopic site).
- The role of marketing/Google/family and friend factor (6). *" patient prefer robots what they have read and looked on the internet have coloured their judgment that robots are better"*
- *"The overwhelming reason for declining to take part was the patient was quite insistent that they have robotic surgery"* (1).
- They did not want open operation (2).
- They wanted to know the operating surgeon (5).
- Patients come and they know what they want (4).
- Most were happy to be randomised to lap or robotic but not open (1).
- Recruiter factor/bias (3) "*many centres bought the robot and wanted to feed the robot". "I have noticed that complicated cases are getting randomised while nice cases get to operated on by particular techniques".*
- Travel issue (3) *"however for a robotic operation they were ready to travel across the country"* (robotic surgeon).
- Some patients are referred from other centres to have robotic and have already offered lap and open in their centres (2).

REFERENCES

[1] Gul R.B, and Ali P.A, '- Clinical Trials: The Challenge of Recruitment and Retention of Participants', *Journal of Clinical Nursing,* 19 (2010), 227-33.

[2] Dear R.F, Barratt A.L, and Tattersall M.H.N, '- Barriers to Recruitment in Cancer Trials: No Longer Medical Oncologists' Attitudes', *Asia Pacific Journal of Clinical Oncology. Conference: 38th Annual Scientific Meeting of the Clinical Oncological Society of Australia, COSA,* 7 (2011).

[3] Kehoe S, Nankivell M, Cairns J, Qian W, and Swart A.M, '- Problems Recruiting to Surgical Trials: Examples from the Mrc/Nrci Chorus Randomised Clinical Trial', *International Journal of Gynecological Cancer. Conference: 17th International Meeting of the European Society of Gynaecological Oncology, ESGO,* 21 (2011).

[4] Treweek S, '- Recruitment to Trials - Why Is It Hard and How Might We Make It Less So?', *Trials. Conference: Clinical Trials Methodology Conference,* 20111004 (2011).

[5] McDonald A.M, Treweek S, Shakur H, Free C, Knight R, Speed C, and Campbell M.K, '- Using a Business Model Approach and Marketing Techniques for Recruitment to Clinical Trials', *Trials,* 12 (2011).

ACKNOWLEDGMENT

We are grateful to CRUK for funding this project. Jalil was also funded by the NIHR via the Imperial Patient Safety Translational Research Centre and Barts Healthcare NHS Trust.

A Study of Socially Acceptable Movement for Assistive Robots Concerning Personal and Group Workspaces

J. Correa, S. McKeague, J. Liu, G.-Z. Yang

The Hamlyn Centre, Institute of Global Health Innovation, Imperial College London, UK

{jc310, sjm05, jliu4, gzy}@imperial.ac.uk

INTRODUCTION

Human-friendly navigation is one of the key challenges that must be solved for a better acceptance of mobile assistive robots. A robot that moves too close to a person, or interrupts the activities of a person or a group of people will cause disruption and annoyance for the users. This is particularly critical when dealing with elderly people, for which most mobile assistive robot applications are targeted.

Socially acceptable navigation of mobile robots is a relatively new research area. Sisbot et al. [1] proposed a socially aware navigation method based on a social cost function. The definition of the cost function is related to the physical and mental safety of a person (the mental safety is understood as not scaring a person in the environment). People's attention is restricted to a binary value: looking towards the robot or looking away from the robot, as no means of detecting the gaze were introduced. Also, no information about groups of people is used. A different approach was presented by Rios-Martinez et al. [2]. Their approach uses a stochastic optimisation approach to find paths that respect a set of human comfort rules. A stochastic planner, such as the one used in their approach, will tend to produce bumpy trajectories, which is undesirable in many social situations.

This paper proposes a solution for socially acceptable mobile robot navigation in healthcare environments, by including two social requirements: do not disrupt a person's working area, and do not interrupt groups of people. People's position, gaze angle and velocity are initially detected and used to identify engaged groups. Then, by using the personal and group information available, social constraints are defined and applied to the robot navigation around the workspace of the person or group. Real world data is recorded and used to evaluate the behaviour of the proposed method. Results show the benefits of the solution over the classical method that does not take this social information into account.

METHOD

The first task in enabling a robot to navigate around people in a socially aware manner is to define which areas of the environment are socially acceptable. Any definition of socially acceptable areas will incorporate the position and gaze direction of people and groups in the environment. To detect people's gazes and groups of people, a method based on an active infrared camera was used [3]. With this information, and the definition of socially acceptable movement, the specifics of how the robot's motion should be altered must be defined.

Two important requirements for socially acceptable navigation can be defined. Firstly, a robot should leave a greater margin of distance when passing through a person's field of view than it would if it passed behind them. This is to reduce the amount of discomfort resulting from a robot traversing someone's personal space [2]. Secondly, if people have organised themselves into a group, the robot should not disturb this arrangement by passing through their "shared transactional space".

The first socially acceptable navigation requirement is modelled by an appropriate area around each person in an environment. This area has to be avoided by the robot whilst navigating. The shape is modelled by a summation of two stretched circles. One circle governs the greater distances in front of a person that a robot should leave free. The other circle should govern the smaller distances behind a person that a robot should leave free. The contour of the proposed shape is given by the following parametric equation:

$$\mathbf{x}(\mathbf{u}) = \left(\left[\frac{\mathbf{g}\cdot\mathbf{u} + 1}{2}\right]^{\mathrm{k}}(\mathrm{r_M} - \mathrm{r_m}) + \mathrm{r_m}\right)\mathbf{u} + \mathbf{x_p},$$

where $\mathbf{g}$ is the gaze direction, $\mathbf{u}$ is a unit vector, k is a parameter controlling how wide an area around a person's gaze direction the robot should avoid, r_M and r_m denote the maximum distance in front of, and behind a person, respectively, that a robot should avoid, and $\boldsymbol{x_p}$ is the position of the person in the map.

The second socially acceptable navigation constraint is not to pass through a group's "shared transactional space". To this end, an ellipse is used as the area to be avoided by the robot. The centre of the ellipse is set to the mean position of the people in the detected group. The semi-axis and semi-radii of the ellipse are chosen to be proportional the eigenvectors and eigenvalues of the position covariance matrix respectively. The proportional constant is chosen to be 3, equivalent to the well-known 3σ rule. To avoid ill-defined ellipses in cases of groups lying on a line, the minimum value a semi-radius can have is set to *30* cm. The resulting ellipse has the same inclination of the covariance of the people in the group.

With the areas of socially unacceptable movement defined, integrating them into the robot's path planning is done using the Robot Operating System (ROS) [4] navigation stack. Using a laser range sensor, the navigation stack detects and avoids static obstacles in the vicinity of the robot's path. People's legs are detected as static obstacles making the robot naturally

*** J. Correa and S. McKeague contributed equally to this work.**

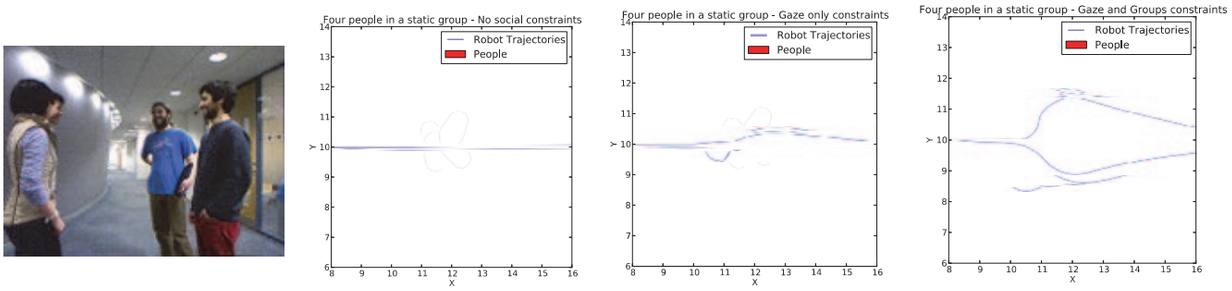

Fig. 1. Snapshot and resulting behaviour of the robot interacting in a four person scenario. In **(a)** a picture of the environment from the robot's perspective is shown. Subfigure **(b)** shows the resulting trajectories if no social requirements are enforced. In subfigure **(c)** the resulting trajectories when only the unacceptable gaze area is enforced. Finally, subfigure **(d)** shows the resulting trajectories when both, gaze direction and unacceptable group areas are enforced.

avoid moving too close to a person in the environment. This base navigation system is amended to ensure that planned robot movements lie outside socially unacceptable areas. To this end, a social cost-map is constructed which incorporates the previously defined unacceptable areas. The planner is modified to invalidate all trajectories that enter any unacceptable area. In this way, the robot can traverse healthcare environments, whilst minimising the interruptions to people within them.

RESULTS AND DISCUSSION

To evaluate the algorithm's effect on the robot's movement, multiple groups of varying size were recorded in a corridor environment. Data was subject to real sensor noise and natural variations in people's pose. For each scenario, the expected route taken by the robot was then simulated and analysed to see if it conforms to the two socially acceptable navigation requirements. The results from three navigation methods were compared. The unaltered ROS navigation stack was used as a base comparison algorithm. A second method, incorporating only the first social navigation requirement, was used to evaluate the sole impact of detected gaze direction on the robot's path planning. Finally, the complete algorithm, incorporating both navigation requirements, was tested. Datasets were recorded of groups composed of two, three and four people. Each algorithm was evaluated one hundred times for each group configuration. The percentage of resulting paths that correctly obeyed the social navigation requirements was recorded.

Figure 1 is an image from the robot's view for the four people scenario with the resulting paths generated by each algorithm. When navigating using only simple obstacle avoidance (b), it is clear that the robot has no incentive to avoid the group's "shared transactional space", as this is the most direct route to it's goal. When using only the first navigational requirement (c), at times the robot correctly avoids the group, but at other times the behaviour is similar to using only obstacle avoidance. Analysing the data, this is due to people closer to the robot occluding those behind them. An additional reason is head movements that cause the eyes to be occluded, which cause the gaze detector to fail. However, these limitations are overcome by incorporating the second social navigation requirement (d). With this, the robot's understanding of the group's space means that it correctly navigates around it almost every time. The exact percentage of correct navigation for each group configuration and algorithm is presented in Table 1.

Table 1. Percentage of agreement with the defined social requirements for the 3 different approaches.

	Two people	**Three people**	**Four people**
Base	15%	0%	0%
Gaze only	77%	27%	0%
Gaze and groups	100%	100%	99%

REFERENCES

[1] E.A. Sisbot, L.F. Marin-Urias, R. Alami, T. Simeon, "A Human Aware Mobile Robot Motion Planner," *Robotics, IEEE Transactions on* , vol.23, no.5, pp.874,883, Oct. 2007

[2] J. Rios-Martinez., A. Renzaglia, A. Spalanzani, A. Martinelli, C. Laugier, "Navigating between people: A stochastic optimization approach," *Robotics and Automation (ICRA), 2012 IEEE International Conference on* , vol., no., pp.2880,2885, 14-18 May 2012

[3] S. Mckeague, J. Correa, J. Liu, G.-Z. Yang, "Multi-Modal Gaze Based Group Detection for Mobile Assistive Robots", submitted to The Hamlyn Symposium 2014

[4] M. Quigley, K. Conley, B. Gerkey, J. Faust, T. Foote, J. Leibs, R. Wheeler, and A. Ng, "ROS: an open-source robot operating system," in *ICRA Workshop on Open Source Software*, 2009.

Paediatric Robot-Assisted Laparoscopic Heminephroureterectomy

S. P. Rowland[1], T. P. Cundy[1,2], J. A. Harikrishnan[1], A. S. Najmaldin[1]

[1]*Department of Paediatric Surgery, Leeds General Infirmary, Leeds*

[2]*The Hamlyn Centre, Institute of Global Health Innovation, Imperial College London, UK*

azad.najmaldin@leedsth.nhs.uk

INTRODUCTION

Robot-assisted minimally invasive surgery in children continues to be applied to an expanding range of childhood surgical conditions [1]. It may offer clinical, ergonomic, and economic benefits over traditional operative approaches. For many indications, robot-assistance is also seen as an enabling technology, facilitating a minimally invasive approach in circumstances when it otherwise might not be considered. Heminephroureterectomy in infants and children is a technically difficult procedure in which there is a promising role for a robot-assisted approach. We present the largest and the first European series of paediatric robot-assisted laparoscopic hemi-nephroureterectomy.

MATERIALS AND METHODS

Patient Selection

Consecutive infants and children who required heminephroureterectomy at our institution between July 2007 and February 2014 were included. All procedures were undertaken using the da Vinci® Surgical System (Intuitive Surgical). Indications for surgery were a non-functioning moiety associated with recurrent urinary infection, deterioration of dilatation on repeat imaging, symptomatic ureterocele, or wetting from an ectopic insertion of ureter.

Operative Procedure

Patients were positioned semi-lateral and maintained using adhesive strapping (Figure 1). Lateral flexion of spine was achieved using either appropriate padding under the contralateral 12th rib (infants) or a break in the table (children). Three robotic ports (12mm optical port, and either 5mm or 8mm working ports) were placed with positioning dependent on the site of relevant pathology (Figure 1). In the majority of cases a 3.5 or 5mm accessory laparoscopic assistant port was also placed for a retractor and suction probe. A transperitoneal approach was utilised in all cases, lateral to the hepatic or splenic flexure for right-sided and left-sided procedures respectively. Tissue dissection was performed using the plasma-kinetic (PK) dissector instrument, ultrasonic shears or scissors in order to expose the relevant anatomy. The abnormal ureter was transected just below the renal pelvis in order to provide access to the diseased moiety. Vessels were identified, secured and divided, and kidney transected at the demarcated level. The ureter was dissected distal to, or near the bladder wall, with care taken to avoid inadvertent injury to the normal moiety, vessels or ureter. The peritoneum was closed over the remaining moiety.

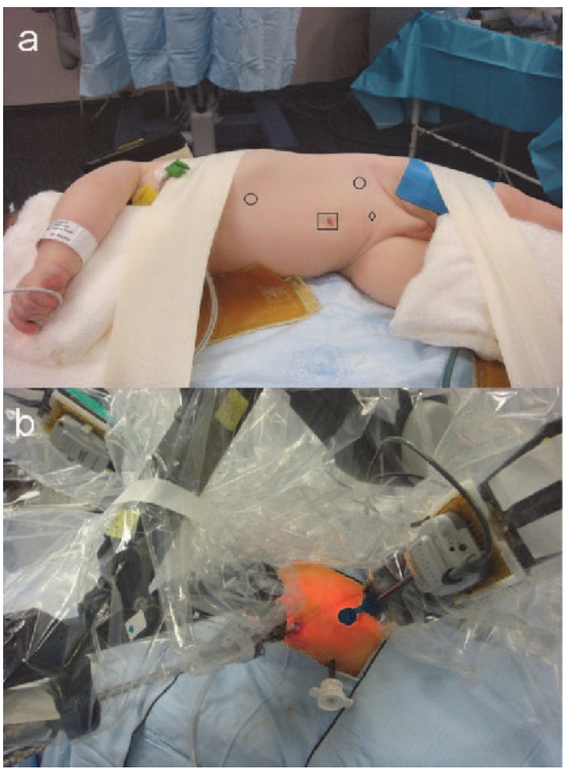

Fig. 1. Left heminephroureterectomy a) port site configuration and b) orientation of docked robotic arms.

Table. 1 Patient demographic details and clinical characteristics.

Total number of cases	24
Patient age (mean ± SD) (range)	6.7 ± 0.9 years (1.2 - 15.2 years)
Male:female	9:15
Associated morbidity	Urinary tract infection (58.3%)
Underlying pathology	Duplex system associated with; reflux (29.2%), ureterocele (58.3%), ectopic ureter (12.5%)

The excised renal tissue was extracted via the umbilical port site that occasionally needed to be extended as necessary. A drain was not routinely placed. The urethral catheter remained in-situ for 0 - 5 days depending on the underlying medical condition. Post-operatively oral and or intravenous opiate analgesia was offered and patients were discharged from the hospital within 1 - 2 days. Patients had regular outpatient clinic follow up and an ultrasound scan at both 1 month and 1 year. Subsequent investigations depended on clinical progress and the pre-existing associated anomalies. Data was collected prospectively in an electronic database.

RESULTS

A total of 24 children underwent right- (n = 17) or left (n = 7) procedures, with 84.2% involving the upper pole and 15.8% involving the lower pole. All procedures were completed using 3 robotic instruments without the need to convert to an open or conventional laparoscopic approach. There were no intra-operative complications encountered and estimated blood loss was minimal. Total operating time ranged from 112 - 233 minutes with a mean of 161 ± 7.6 minutes. Robotic console operating time ranged from 64 to 147 minutes with a mean of 87 ± 7.5 minutes. Avoidable operating room delays occurred (0 - 35 minutes) due to assistant laparoscopic instrument malfunction, staffing or anaesthetic issues, but none were attributable to robot-related or technical reasons. Intravenous opiate analgesia was required in 20.8% of children and 8.3% required oral opiate analgesia. Patients were surgically fit for discharge at 20 - 57 hours post-operatively (median 24 hours) with 66.7% discharged on the first post-operative day and 94.6% by the second post-operative day. One patient developed a small cystic lesion at the site of the renal transection, which has remained stable in size on repeat renal ultrasound studies over a period of 3 years. There were no other post-operative complications.

DISCUSSION

Paediatric laparoscopic heminephroureterectomy is a safe and feasible clinical application for a robot-assisted approach. Our operative times compare favourably to other series [2,3] and appear similar to both open and conventional laparoscopic nephrectomy [5]. In our experience, patients require minimal analgesia and have a short post-operative hospital stay. Our results suggest that both intra-operative and post-operative complications are rare, even during the learning curve phase. Using the available robotic instruments, we find that no more than 3 instruments are required for this procedure. This instrument usage is less than typical requirements for a conventional laparoscopic approach in which up to 5 instruments are used. Given that contemporary conventional laparoscopic instruments are often relatively expensive disposable single-use devices, direct costs for a robotic approach may indeed be lower. This requires further investigation by formal comparative cost-analysis as well as prospective studies to evaluate comparative clinical outcomes.

REFERENCES

[1] Cundy TP, Shetty K, Clark J, Chang TP, Sriskandarajah K, Gattas NE, Najmaldin A, Yang GZ, Darzi A. The first decade of robotic surgery in children. J Pediatr Surg. 2013 Apr;48(4):858-65.

[2] Lee RS, Sethi AS, Passerotti CC, Retik AB, Borer JG, Nguyen HT, Peters CA. Robot assisted laparoscopic partial nephrectomy: a viable and safe option in children. J Urol. 2009 Feb;181(2):823-8.

[3] Mason MD, Herndon CDA, Smith-Harrison LI, Peters CA, Corbett ST. Robotic-assisted patial nephrectomy in duplicated collecting systems in the pediatric population: Techniques and outcomes. J Paedr Urol. 2013 (In Press)

[4] Leclair MD, Vidal I, Suply E, Podevin G, Héloury Y. Retroperitoneal laparoscopic heminephrectomy in duplex kidney in infants and children: a 15-year experience. Eur Urol. 2009 Aug;56(2):385-9.

Real-Time Modelling of Intra-operative Brain Shift Based on Video Tracking

I. Rasin[1], Z. Pekar[1], O. Sadowsky[2], A. E. Forte[3], S. Galvan[3], D. Dini[3], M. Shoham[4], L. Joskowicz[2]

[1]*Avtech Scientific, Modiin Illit, Israel*
[2]*School of Engineering and Computer Science, The Hebrew Univ. of Jerusalem, Israel*
[3]*Department of Mechanical Engineering, Imperial College London, UK*
[4]*Faculty of Mechanical Eng. Technion - Israel Institute of Technology, Haifa, Israel*
igal.rasin@avtechscientific.com

INTRODUCTION

This paper addresses the problem of real-time guidance of a robot operating on an open brain as the brain undergoes a deformation (brain shift) due to the loss of cerebrospinal fluid (CSF) and the reduction of intracranial pressure. Commonly, neurosurgical navigation loses its accuracy due to the deformation, as it is based on static pre-operative brain images. We aim to improve this accuracy by providing a real-time "image" of the deforming brain, which is computed from tracking features on the exposed cortex and models the physical behavior of brain tissue.

We extend our previous work on tracking cortical features in video images [1] with a numerical model of the volumetric deformation which is computed simultaneously with the tracking and is guided by the video-based data. The ultimate goal of this numerical model is to update motion constraints for the surgical robot in treatment of epilepsy. The reconstruction of the 3D deformation from the observed cortex is critical because the constraints are defined within the volume of a pre-operative MRI of the brain, not just on the surface. Real-time performance of the model is also critical since the robot acts in real time.

Previous works on brain-shift modeling [2], propose the creation of "atlases" – databases containing many (e.g. 1000) numerical simulations of the deformations. Given a surface shape obtained, for example, from a laser scan, the 3D brain deformations are synthesized from this database by interpolation of its records and fitted to the observed surface.

MATERIALS AND METHODS

We have developed a model that is based on an actual real-time estimation of the deformation. Fig. 1 outlines our method. The model assumes a poroelastic brain material and constrains the brain shift motion near the skull to be only tangent to the skull surface. It uses a finite difference scheme for discretization of spatial derivatives with D3Q15 template and the explicit first order time integration. The equations are solved on a regular cubic grid.

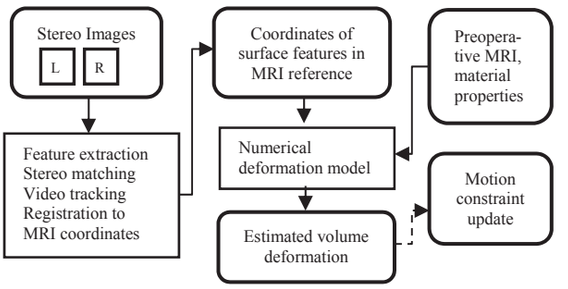

Fig. 1. Data flow in the brain shift model from video acquisition to robot motion constraints.

The inputs to the deformation model are: (1) pre-operative models of the brain volume and skull surface extracted from an MRI scan; (2) material properties of the brain soft tissue, including: bulk modulus, Poisson's ratio, hydraulic conductivity and density, which typically are based on data in the literature [2]; (3) the direction and magnitude of the gravity relative to the MRI brain; (4) an estimated level of the CSF within the intra-cranial cavity; and (5) a set of brain surface points which are located and tracked over time in stereo video and mapped to the MRI reference frame. The tracked points are updated periodically, for example every 1 second.

Given these parameters, the numerical model estimates the evolution of brain shift over time at a high rate, e.g. 100 times faster than real time. This allows it to be run multiple times between the updates and re-evaluate the CSF level parameter to achieve a best fit to the observed surface. The computation involves searching for the least squares fitting error between the observed displacements of the tracked points and their expected displacement based on the deformation model.

To test our system, we designed and built a custom deformable phantom developed for this task. The phantom consists of a solid "skull" in which a deformable "brain" is submerged in water. The brain material consists of a new hydrogel that can accurately mimic the organic tissue response in a rate-dependent manner, varying the velocity over two orders of magnitude. The shapes of the skull and the brain are based on an MRI image of an actual brain. As water is drained from the skull, the brain phantom undergoes a deformation similar in nature to brain shift. Poppy seeds were sprinkled and fixated on the surface of the brain to

create visual features that can be tracked in video images. In live surgery, the tracked features would be parts of cortical blood vessels. The phantom and an example of live brain features are shown in Fig. 2.

RESULTS

Calibration and registration: The stereo camera system was calibrated by imaging a CALTag checkerboard pattern [3]. The spatial relationship between the cameras and the MRI reference was established by imaging a custom fiducial with visual and contact features in a known geometry, then touching the contact features with a robot probe. An example of the registration is shown in Fig. 3 (top left).

Tracking: A stereo video file was recorded of the phantom over a 25 minute period at 1 fps while water was gradually drained from the skull. The video was analyzed to detect and track the motion of 59 feature points over time. Several steps of the deformation, at 0, 500 and 1000 seconds, are shown in Fig. 3.

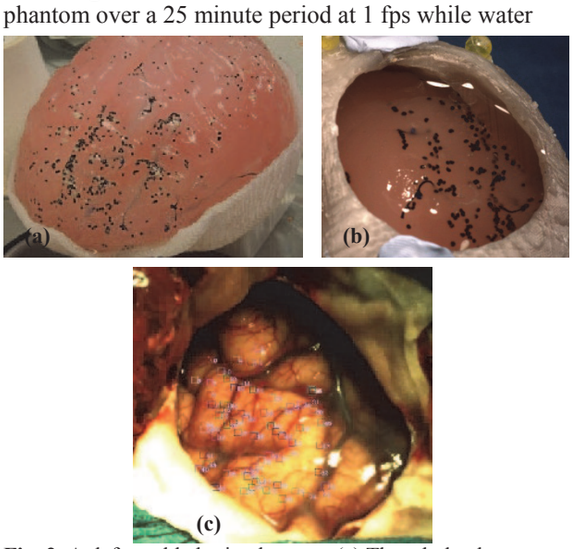

Fig. 2. A deformable brain phantom. (a) The whole phantom; (b) view through a mock craniotomoy; (c) tracked features on a live brain.

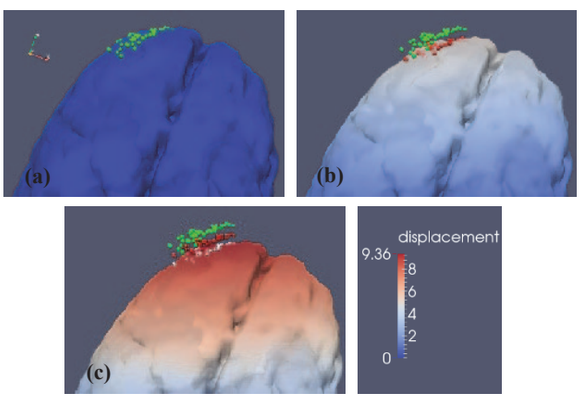

Fig. 3. Tracked feature points and the corresponding deformation of the 4×4×4 mm^3 brain model. (a) green points: initially registered to the surface of a brain phantom. (b) red points: after 500 seconds of deformation tracking. (c) white points: after 1000 seconds of deformation tracking.

Of the 59 tracked points, 48 remained visible after 1197 seconds, and their travel distance from the original positions, reconstructed from the stereo images, ranged from 10.3 mm (min.) to 11.8 mm (max.) with the mean at 11.1 mm.

Deformation model: The numerical model was run with input from the video tracking above and produced an estimated brain shift on a brain model of resolution 4×4×4 mm^3. The simulator can run at 100x real time; that is, simulate 100 seconds of brain shift in 1 second of computation. An example of the resulting outcome is shown (as the outer surface) in Fig. 3. We observe that the direction and the magnitude of the simulated deformation closely match the tracking experiment: at 1000 seconds, the fitting error between the brain surface and the points had RMS of about 1.5 mm. Notice that the displacement magnitude varies in space, which characterizes a physical deformation basis.

CONCLUSION

We demonstrated an integrated system in which a computational deformation model of the brain is fitted to surface features tracked with a stereo camera during a brain shift process. The efficiency of the method fits well to real-time performance, and its current fitting accuracy is about 1.5 mm. The system is demonstrated for a custom brain phantom that resembles real brain tissue properties.

Further tests of the method are planned to perform a quantitative comparison of its outcome with established finite element modeling techniques and with physical measurements of the deformed phantom. The translation to *in-vivo* tests lies farther ahead, due to the complexity of carrying out such experiments.

ACKNOWLEDGMENT

This work is part of the ACTIVE consortium, sponsored by the EU-FP7 programme.

REFERENCES

[1] Vivanti R, Sadowsky O, Shoham M and Joskowicz L. Brain surface tissue deformation tracking in craniotomies. Proc. Hamlyn Symposium on Medical Robotics 2013.

[2] Dumpuri P, Thompson RC, Dawant BM, Cao A and Miga MI. An atlas-based method to compensate for brain shift: Preliminary results. Medial Image Analysis, vol. 11, no. 2, pp. 128-145, 2007.

[3] Atcheson B, Heide F and Heidrich W. CALTag: High Precision Fiducial Markers for Camera Calibration. 15th International Workshop on Vision, Modeling and Visualization. Siegen, Germany. November, 2010.

da Vinci Robot-Assisted Keyhole Neurosurgery: A Cadaver Study

H. J. Marcus[1,2], A. Hughes-Hallett[1], T. P. Cundy[1], G.-Z. Yang[1], D. Nandi[2], A. Darzi[1]

[1]*The Hamlyn Centre, Institute of Global Health Innovation, Imperial College London, UK*

[2]*Department of Neurosurgery, Imperial College NHS Healthcare Trust, London, UK*

INTRODUCTION

Despite advances in image guidance, endoscopy and tube-shaft instruments, keyhole neurosurgical approaches still represent a considerable challenge to neurosurgeons, particularly those unfamiliar with these procedures [1]. Robotic platforms that further enhance surgical skills have the potential to improve the safety and efficacy of keyhole neurosurgery.

At present, the most widely used surgical robot worldwide is the da Vinci system (Intuitive Surgical, California, USA), a master-slave system designed for minimally invasive surgery in which the surgeon remotely controls the robots actions. Although the da Vinci system has been successfully used in a broad range of surgical procedures, it is not yet approved for use in neurosurgery. Recently a group has reported the application of the da Vinci surgical system to assist with the supraorbital subfrontal approach through an eyebrow skin incision in a cadaver study [2]. The goal of the present cadaver study was therefore to confirm and extend these preliminary findings by applying the da Vinci surgical system to a range of keyhole neurosurgical approaches.

MATERIALS AND METHODS

Ethical approval was obtained from the Proportionate Review Sub-committee of the National Research Ethics Service. A formalin-fixed cadaver head was obtained from the Department of Anatomy, Imperial College London. The cadaver head was secured in a Mayfield clamp and a Budde-halo retractor system attached (Integra, New Jersey, USA). An Albert Wetzlar operating microscope (Albert Wetzlar GmbH, Wetzlar, Germany) and high-speed drill (B. Braun, Melsungen, Germany) were used to fashion several previously described keyhole craniotomies, approximately 20-30mm in diameter [3]: supraorbital subfrontal; retrosigmoid; and supracerebellar infratentorial. In each approach a simple durotomy was performed, and the flap retracted.

The standard da Vinci robotic system was used intradurally, and arachnoid dissection performed towards the deep-seated cisterns. The surgeon remained non-sterile at the robot console, while an assistant was available throughout the procedure to exchange robotic instruments. Both 0° and 30° upwards facing 12mm endoscopes were introduced into the keyhole craniotomy for visualisation. Standard 8mm and smaller 5mm instruments were used for tissue manipulation. Throughout each procedure detailed feedback was obtained, including images of the operating room arrangement, and of the endoscope feed.

RESULTS

It was not possible to simultaneously pass both the 12mm endoscope and instruments through the keyhole craniotomy in any of the approaches performed, irrespective of whether two standard 8mm instruments or smaller 5mm instruments were used (Figure 1). Instead, the endoscope had to be placed outside the craniotomy, limiting the illumination, magnification, and wide-angle view provided.

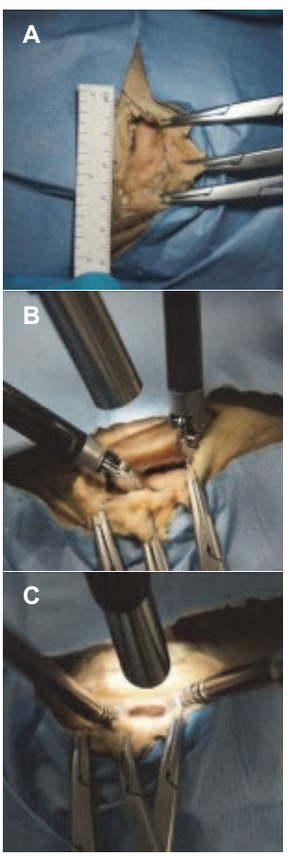

Fig. 1. Left supraorbital subfrontal approach through an eyebrow incision demonstrating (A) keyhole craniotomy approximately 25 x 15mm in size, (B) a 12mm endoscope and two standard 8mm instruments were unable to enter the keyhole simultaneously, and (C) a 12mm endoscope and two smaller 5mm instruments were also unable to enter the keyhole simultaneously.

Dissection with the da Vinci instruments was restricted to superficial structures. The large instrument arms could not be placed in parallel through the keyhole craniotomy, and therefore could not be advanced to the deep cisterns without significant clashing (Figure 2). The smaller 5mm instruments were comparatively easier to pass through the keyhole craniotomy, but utilised tentacle-like continuum tool shafts rather than the articulated wrist-joints that characterise standard 8mm instruments. The result, paradoxically, was that the smaller 5mm instruments had less dexterity than standard 8mm instruments. The range of 5mm instruments was also limited, with no bipolar forceps or suction-irrigation available.

Fig. 2. Arrangement of the da Vinci endoscope and instrument arms in the left supraorbital subfrontal approach, demonstrating the difficulty in parallel insertion through a single keyhole craniotomy

The da Vinci console offered considerable ergonomic advantages over the existing operating room arrangement, allowing the operating surgeon to remain non-sterile and seated comfortably throughout. The visualisation provided by the 3-D endoscope provided an immersive view of the operative field. Control of the instruments was intuitive, and allowed for motion scaling and tremor filtering. However, the lack of haptic feedback was a notable limitation.

DISCUSSION

In this cadaver study, it has been demonstrated that use of the standard da Vinci robotic system in keyhole transcranial endoscope-assisted microsurgery is neither safe nor feasible at present. Arguably the greatest role of surgical robots is as a "great leveller", allowing surgeons to perform keyhole approaches when they would otherwise resort to open surgery. To this end, technically challenging keyhole neurosurgical approaches are ideal targets for such robots. Regrettably, the current da Vinci platform is not well suited to brain surgery given its multiple arms.

The present cadaver study has several inherent limitations. The cadaver brain was formalin-fixed, and was therefore not as a compliant as the living brain, though pathology resulting in cerebral oedema can be similarly tense. The cadaver brain also didn't allow for assessment of haemostasis, which is frequently cited as a limitation of keyhole approaches. Animal studies might better address the issue of haemostasis, but there are very few animal models with brains of a similar size to humans, such studies would be logistically difficult to organise, and also raise ethical concerns.

Only one previous cadaver study has described the use of the da Vinci robot in keyhole brain surgery [2]. Hong *et al* described the application of the da Vinci robot to the keyhole supraorbital approach and, in contrast to the present study, found it was generally feasible, though they did comment on instrument clashes and lack of proper tools. We speculate this discrepancy may be due to their longer incision and larger craniotomy, and their use of brain retractors.

Recently, a group from the University of Washington has proposed new multiport approaches to the anterior cranial fossa that are better suited to the da Vinci robotic platform [4]. In order to overcome the narrow funnel effect generated from arms in close proximity, and the steep angle of approach to the skull base, they suggest transnasal and bilateral medial orbital ports for the camera and instruments respectively. While such novel approaches may be more viable from a technical standpoint, they carry a greater risk of approach-related morbidity than standard uniportal keyhole approaches.

Alongside the clinical challenges to the use of the da Vinci robotic platform in keyhole neurosurgery highlighted here, several other barriers also exist [5]. Arguably the greatest drawback to existing surgical robots is economic. The current da Vinci robot, for example, is priced at over £1m, carries substantial maintenance costs, and requires additional training of the surgeons and nurses involved with its use. The next generation of robotic platforms under development are likely to overcome many of these limitations; with the large and expensive robots of today replaced by smaller and more affordable robots tailored to particular procedures [5].

REFERENCES

[1] Marcus HJ, Cundy TP, Hughes-Hallett A, Yang GZ, Darzi A, Nandi D. Endoscopic and keyhole endoscope-assisted neurosurgical approaches: A qualitative survey on technical challenges and technological solutions. Br J Neurosurg. Feb 17 2014.

[2] Hong WC, Tsai JC, Chang SD, Sorger JM. Robotic skull base surgery via supraorbital keyhole approach: a cadaveric study. Neurosurgery. Jan 2013;72 Suppl 1:33-38.

[3] Perneczky A, Reisch R. Keyhole approaches in neurosurgery. Volume 1: Concept and surgical technique. 1 ed: Springer; 2008.

[4] Bly RA, Su D, Lendvay TS, et al. Multiportal robotic access to the anterior cranial fossa: a surgical and engineering feasibility study. Otolaryngol Head Neck Surg. Dec 2013;149(6):940-946.

[5] Marcus H, Nandi D, Darzi A, Yang GZ. Surgical Robotics Through a Keyhole: From Today's Translational Barriers to Tomorrow's "Disappearing" Robots. IEEE Trans Biomed Eng. Mar 2013;60(3):674-681.

Pre-Operative Planning of Femoral Neck Fractures: A Tool for Accuracy

A. Tsanaka[1], P. Tarassoli[2], S. Dogramadzi[1]

[1]*Bristol Robotics Laboratory, University of the West of England, UK*
[2]*Department for Trauma and Orthopaedics, University Hospital Bristol NHS Trust, UK*
name.surname@uwe.ac.uk

INTRODUCTION

Hip fractures are very common in the elderly population, due to accessional health factors such as osteoporosis, infections and cardiovascular diseases [1]. About 70,000 hip fractures occur each year in UK at the annual cost of about £2 billion. Approximately 50% of these fractures are intertrochanteric, where the patients undergo time-consuming surgery in order for the fracture to be fixed with internal metalwork and thereafter may have a painful recovery [2]. Operations of this type are performed manually and their success depends mainly on the surgeons' skills, therefore accuracy cannot always be guaranteed [3]. Additionally, the risks following such an operation can be damaging or even fatal, since general anaesthesia is required during the process and the recovery time is long enough to often cause further infections. Radiation exposure is also an important issue to be considered for both the patients and the medical team. Therefore, the need for speeding up the surgical procedure whilst providing precision and maintaining safety has emerged. This paper proposes the development of an integrated system, which automates the bone reduction task, by offering accurate and fast fixation of femoral neck fractures. An algorithm has been designed to assist with image processing and pre-planning, which carries out fracture fixation and sends position information of the end-effector to the traction table.

MATERIALS AND METHODS

The proposed solution aims to create an algorithm that takes into consideration the reduction steps in Table 1.

Table 1. Pre-planning of hip joint reduction

Hip joint reduction steps
Retrieve X-ray images (anteroposterior and lateral)
Locate the femoral neck and the femoral shaft by looking at the anteroposterior (AP) image
Propose a fixation by correcting the angle between the neck and the shaft (accepted average value of 135 degrees [4] for healthy hips)
Pull the leg to bring it to the right position (lesser trochanter aligned with lower pelvis)
Rotation of the leg to achieve alignment between the shaft, the neck and the head, by looking at the lateral image

The entire process is replicated by automatically achieving a final, correct position of the end-effector and directly sending the xyz coordinates and the orientation angles to the traction table.

An approach that requires the input from the surgeon in order to calculate the final position of the bones has been designed, utilising fundamental trigonometric concepts and features available within the Matlab Image Processing Toolbox [5]. The X-ray image is loaded in Matlab and the surgeon is required to draw the lines that pass by the middle of the femoral neck and the femoral shaft (shown in Fig. 1 in red). Those two lines are treated as vectors and, by obtaining the edge points of each line, the angle between them can be calculated. When a fracture occurs, the angle between the neck and the shaft is smaller than 135 degrees and therefore a fixation is proposed automatically to place the femoral shaft in such position that the angle is restored. That happens by finding the intersection point between those two lines and, while keeping the neck line constant, the shaft line is moved to achieve the right value for the angle (represented with a green line).

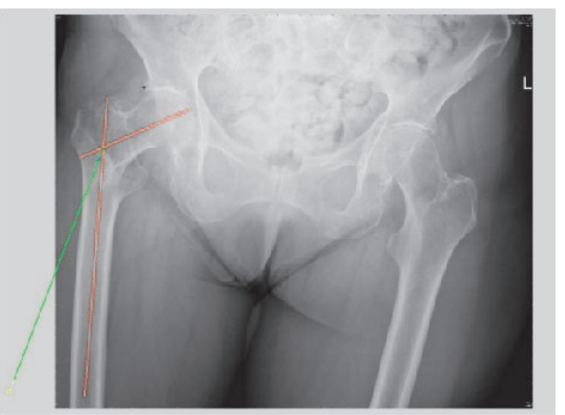

Fig. 1. Fixation of fractured neck

Pulling the leg further downwards can be done by showing a new intersection point between the fixed shaft and the neck lines, which is depicted in with a blue circle. In the same figure and for validation purposes, the shaft line is shown extended in yellow. Of course, in order to obtain the coordinates to be sent to the traction table, this line needs to be extended to match the actual length of the leg and the yellow square point to coincide with the heel of the foot (end-effector). Finally, Fig. 1 also shows the centre of the coordinate system (0,0) used as a reference for all the calculations, which is a constant point on the acetabulum and is highlighted with an asterisk in black. This point is chosen after

consulting the surgeons, for the reason that it is the closest fixed area to the fracture and is not affected by any movement during the reduction.

Note that only AP images are taken into account and, therefore, the algorithm corrects the coronal plane deviation (2D adjustment). Sagittal plane deviation can be ascertained from the lateral radiographs, but when processed, it was impossible to extract any useful information from those (which confirms that, for this exact reason, surgeons do not tend to use lateral images at all for the fixation during the manual process).

RESULTS

Once the pre-planning algorithm was completed and tested on several X-ray images, its functionality and accuracy were validated both numerically and graphically, by comparing the fixation angle before and after the operation. Results have shown that the calculations are extremely accurate with a small deviation of 0.2 mm and no exceptions were present amongst 28 different images of 11 right and 17 left fractured hips (Table 2).

Table 2. Validation results for 28 X-rays

Fixation Accuracy	
Standard deviation	0.2 mm
Max deviation	0.27 mm
Standard error	0.015 mm
Max error	0.03 mm

Pre-operative X-ray images have been processed by the algorithm and a fixation angle is proposed as described previously. Then, the equivalent post-operative image is used to measure the fixed angle of the femoral shaft and neck. Fig. 2 and 3 contain a representative sample verifying the fact that the algorithm produces an accurate fixation, which coincides with the post-operative image and agrees with the manual procedure followed by the surgeons. This shows that the proposed solution here is feasible and can be used effectively, as it reflects reality and actually provides the surgeon with significant assistance concerning the surgical pre-planning.

DISCUSSION

The algorithm presented offers an accurate tool for fixation of femoral neck fractures. Focus was given on reflecting the actual operational steps currently followed during a conventional surgery. The order they are performed and the way the final position is achieved, defines (according to the surgeons) how realistic the solution is. The results show that the concept of having a fixation guide before starting the operation proves extremely useful, as it contributes to significantly reducing the duration of the overall process.

Further work includes the development of a user-friendly version of the algorithm, so that the surgeon can use it to plan the steps of the operation with easiness and simplicity. The software will be designed in a way that, no programming skills are needed at all; just basic computer knowledge. The aim of designing a Graphical User Interface is also for the surgeons to be able to use it without additional training, but only by reading the instructions beforehand.

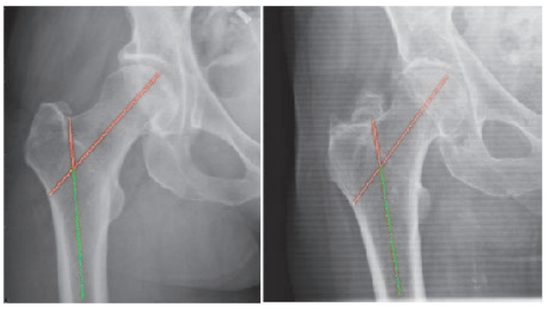

Fig. 2. Post-operative images (left hips)

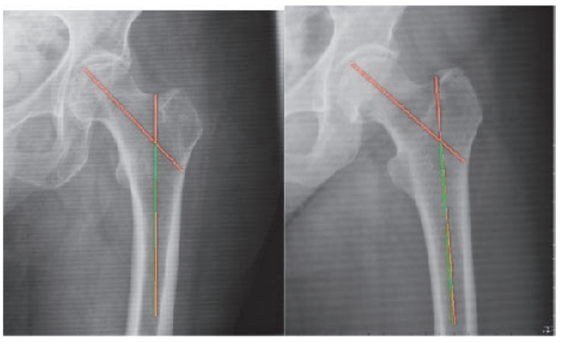

Fig. 3. Post-operative images (right hips)

REFERENCES

[1] National Hip Fracture Database. National Report 2013. Available at: <http://www.nhfd.co.uk>

[2] Hip Fractures. The National Institute for Health and Clinical Excellence, June 2011. Available at: <http://www.nice.org.uk>

[3] Baumgaertner MR, Curtin SL, Lindskog DM, Keggi JM. The value of the tip-apex distance in predicting failure of fixation of peritrochanteric fractures of the hip. J Bone Joint Surg Am. 1995 Jul;77(7):1058-64.

[4] Toogood PA, Skalak A, Cooperman DR. Proximal Femoral Anatomy in the Normal Human Population. Clin Orthop Relat Res. Apr 2009;467(4):876-885.

[5] Matlab. Software version R2009a. Available at: http://www.mathworks.com

Origami-Inspired SMA Actuated Constant Velocity Coupling for Dexterous Telesurgical Robot and Self-Morphing Medical Robots

K. Zhang[1], M. Salerno[2], J. S. Dai[1]

[1]*Centre for Robotics Research, King's College London, UK*

[2]*The BioRobotics Institute of Scuola Superiore Sant'Anna, Pisa, Italy*

ketao.zhang@kcl.ac.uk

INTRODUCTION

Origami has been a long-standing and unique sculptural art varying from simple folds to the more complicated modern origami. The intricate origami is produced by folding a single sheet of paper and combining basic folds in a variety of flexible ways. The underlying principles for geometric design [1] of origami have been investigated, leading to mathematical modelling for various types of origami. The recently emerging development of origami-enabled mechanical systems showed that better understanding of knowledge for origami engineering in artistic disciplines could benefit the study in other areas including architecture design and packaging in food industries. This aroused substantial interests in robotic manipulation of origami-type cartons and led to new challenges and innovation in the mechanical engineering discipline.

The early work which utilized flexible card in mechanism modelling can be dated back to 1950s [2]. The interdisciplinary study on both origami and kinematic structure presented an interesting approach for identifying new mechanical embodiment of intricate origami. Based on study of mechanism and origami folding, a novel 3-DOF parallel mechanism [3] was extracted form an origami with three duplicated waterbomb bases.

In contrast to the conventional mechanisms, the origami-enabled mechanical systems have distinct flexibility and foldability which are expected in practical use. Considering the amazing locomotion in nature which enables movement through unexpected rough terrain and various obstacles, a caterpillar inspired biomimetic inchworm robot was presented by using origami-like structure with capability of turning body motion [4]. As the origami-like structures have the ability not only to fold to a compact form, but also to unfold in deployed form, this kind of mechanisms was adopted for constructing hind wings of dermaptera [5].

Though efforts have been made in identifying new origami-enabled mechanical systems, there are very few work dedicated to the practical use of origami-like structures in medical robots due to primary challenges in design and fabrication. A typical design in this specific filed is the foldable origami stent graft made from a single foldable sheet material with etched origami pattern [6].

One of the crucial challenges for the medical robots is the confined environments. This requires the robots developed for surgical applications to have extra adaptability and flexibility with compact form. Further, the accuracy and precision of the operation carried out by the end-effector of medical robot are expected to be as higher as possible to guarantee the operation safety. A high dexterity snake-like telesurgical robot was developed for minimally invasive surgery of the throat [7]. Flexible joints were then employed in the design of actuation unit for the purpose of in-parallel work by the dual slave arms [8]. However, the flexible joint is a kind of compliant coupling with limited angular misalignment and torsional stiffness. Taking all factors into consideration, the origami-enabled mechanical system on millimetre scale is one promising trend to realize greater performance in medical applications.

MATERIALS AND METHODS

A novel origami-inspired constant velocity coupling is presented in present paper. As illustrated in Fig. 1, an origami structure with three integrated waterbomb-bases can be produced by erecting and closing a flat cardboard with creases pattern. Based on the presented multi-loop origami structure, a miniaturized constant velocity coupling is developed, especially for the practical use of medical robots.

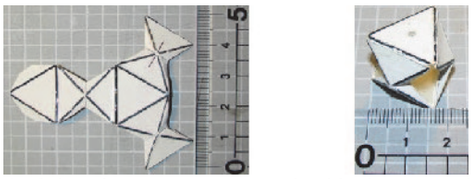

Fig. 1. Origami structure composed with three waterbomb bases and two triangular plates

Taking the creases as revolute joints and the panels as links, the kinematic model mapping from the parallel origami structure in terms of mechanisms is demonstrated in Fig. 2(a). This kinematic model consists of a base and a platform both in triangular shape and three spherical 6R linkages, which are the mapping of three integrated waterbomb bases in Fig. 1. The normal vectors of the base and the platform are denoted by $\boldsymbol{b}$ and $\boldsymbol{p}$, respectively. According to the structure of the kinematic model, the base and the platform in triangular shape are symmetric with respect to the plane formed by the centers B_i (i = 1, 2, 3) of the three spherical 6R linkages. As a result, the platform has three degrees of freedom (DoFs) and implements two rotation and one translation. In other words, the platform is capable of rotating around axes located in

the symmetric plane and translating along the axis passing the geometric centers of the base and platform.

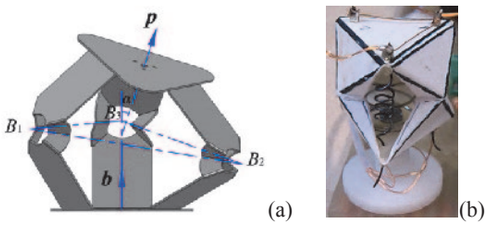

(a) (b)

Fig. 2. Kinematic model of the constant velocity coupling and the prototype with integrated SMA helical spring actuators

Since the kinematic model of the constant velocity coupling is a system with 3 DoFs, the three revolute joints attached to the base are the proper joints that can be selected as input for actuation. However, we propose a equivalent actuation solution for the parallel origami structure by employing three shape memory alloy (SMA) helical spring actuators which directly connect the platform to the base. In order to verify the proposed concept design, an origami model of the constant velocity coupling, made from 0.3mm thick paper, is built as illustrated in Fig. 2(b). Considering the stiffness of the paper sheet used for producing the origami structure, a bias spring is integrated in the origami structure to maintain a desired stiffness of the system before assembling the SMA actuators. The advanced monolithic fabrication method, which imposes limited tolerance, will be considered in the manufacturing process of applicable prototype of the constant velocity coupling to realize greater performance without employing any additional bias spring.

With the three SMA helical spring actuators, the rotation and translation of the platform with respect to the base are demonstrated by the sequential stop pictures of the paper made constant velocity coupling in Fig. 3.

RESULTS

This symmetric structure results in the constant velocity transmission between the base and the platform. The tilt angle α is measured from the normal vector $\boldsymbol{b}$ of the base to the normal vector $\boldsymbol{p}$ of the platform. The maximum yaw and pitch angle of the platform, which is related to the design parameter of the coupling, can be greater than 45°, the extreme value of a universal joint conventionally utilized as coupling for torque and velocity transmission.

Table 1. Prototype testing results

SMA actuator			Coupling prototype	
Wire diameter (μm)	Spring diameter (mm)	Number of turns	Yaw/pitch angle (deg)	Stroke (mm)
375	3.25	5	27~28	5

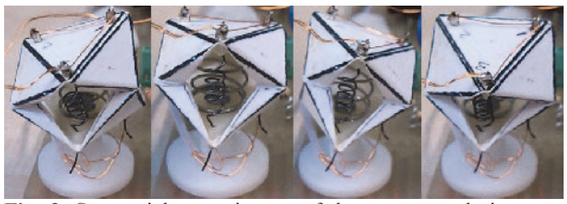

Fig. 3. Sequential stop pictures of the prototype during yaw and pitch motion

DISCUSSION

In contrast to the application as coupling without active joints, the origami-enabled constant velocity coupling in Fig. 2 has the capability to be used as self-morphing module parallel robot by integrating SMA actuators. Only three actuators are necessary for each of the module to drive the platform to expected position. This 3-DOF coupling with improved flexibility and workspace can be integrated in the design of actuation unit for dexterous telesurgical robots. This kind of self-morphing coupling can also be integrated in the snake-like robot as flexible segment. In the future work, the constant velocity coupling in passive motion mode is going to be manufactured and the self-morphing module will be built with proper manufacturing approach and optimal actuation methods.

ACKNOWLEDGMENTS

This work was supported in part by EU FP7 project TOMSY under Grant No. 270436 and NSFC grant No.51205016.

REFERENCES

[1] Lang R. J. Origami design secrets: mathematical methods for an ancient art. CRC Press, NW, 2011.
[2] Cundy HM, Rollett AP. Mathematical Models. Tarquin, Suffolk. 1981.
[3] Zhang K, Fang Y, Fang H, Dai JS. Geometry and Constraint Analysis of the 3-Spherical Kinematic Chain Based Parallel Mechanism. Journal of Mechanism and Robotics. 2010; 2(3):031014.
[4] Koh J-S, Cho K-J. Omegabot: Biomimetic inchworm robot using SMA coil actuator and smart composite microstructures (SCM). IEEE International Conference on Robotics and Biomimetics. 2009; 1154-1159.
[5] Haas F, Gorb S, Wootton RJ. Elastic joints in dermapteran hind wings: materials and wing folding. Arthropod Structure and Development. 2000; 29(2): 137–146.
[6] Kuribayashi, K. A Novel Foldable Stent Graft. PhD diss., University of Oxford. 2004.
[7] Simaan N, Xu K, Wei W, Kapoor A, Kazanzides P, Taylor R, Flint P. Design and Integration of a Telerobotic System for Minimally Invasive Surgery of the Throat. The International Journal of Robotics Research. 2009; 28(9): 1134-53.
[8] Kuo CH, Taylor RH, Dai JS, Iordachita I. Design of a flexural transmission for a dexterous telesurgical robot for throat and upper airway: a preliminary result. Proceedings of The Hamlyn Symposium on Medical Robotics, 2010; 71-72.

MRI-Compatible Needle Positioner for Laser Ablation of the Liver: Preliminary Evaluation in a 3T MRI Scanner

E. Franco, M. Ristic

Department of Mechanical Engineering, Imperial College London, UK
ef1311@imperial.ac.uk

INTRODUCTION

Laser Interstitial Thermoablation (LITT) is used to treat otherwise inoperable liver tumours by delivering thermal energy from a high power laser through a catheter probe directly to the target lesions [1]. The MRI-guided procedure using cylindrical MRI scanners provides better contrast than ultrasound guidance and allows thermal monitoring [2]. However since the patient access is restricted the lesion is targeted with a coaxial puncture needle under ultrasound guidance at a different site in the department after which the catheter probe is inserted and the patient is subsequently moved to the MR scanner [3]. This approach results in a more complex and time consuming workflow and bears the risk of dislodging the catheter probe compromising targeting accuracy. The aim of this research is the development of a remotely actuated needle positioner that will allow accurate alignment of a suitable needle guide while the patient is in the MR scanner and will assist manual needle insertion outside the bore. The expected result is a considerable reduction of the procedure time and an improvement of the targeting accuracy. This paper describes the first prototype of the needle positioner and its user interface. The MRI-compatibility and the targeting accuracy of the prototype have been evaluated with experiments in a 3T closed-bore MRI scanner using a water phantom.

MATERIALS AND METHODS

The prototype was manufactured in plastic to ensure MRI compatibility. The needle guide can translate along the x and z axes (movements q_1, q_2) and can rotate around the z axis (movement q_3) in the base frame $F1$ of the positioner (Fig. 1). The device is designed to be placed inside the MR scanner anchored to the patient bed and is actuated by plastic pneumatic cylinders. The cylinders are supplied through 9 m long pipes by proportional valves located in the control room. The pistons position is measured with optical encoders that are connected to the controller in the control room using a shielded cable grounded to the waveguide. The advantages of keeping the control hardware outside the scanner room are minimum distortions to the MR environment and less space occupied in proximity of the scanner compared to other MRI-compatible devices [4, 5]. The position and orientation of the needle guide in the base frame $F1$ is calculated from encoder readings and kinematic model which was calibrated using an optical tracking system. The base frame $F1$ is automatically registered with respect to the scanner reference frame $F0$ computing the position of wireless micro-coil fiducials [6] mounted on the needle guide with a tracking algorithm that provides sub-millimetre accuracy for marker localization [7]. The inner position control loop and the trajectory generator for the pistons run in real time on a microcontroller. A custom Graphical User Interface (GUI) displays the MR images after each scan. The user can graphically select the position of the target point on the MR image and the pistons align the needle guide with the selected point. The virtual position of the needle tip is displayed on the MR images for verification. After planning the insertion the patient bed is moved out of the MR scanner and the coaxial needle is inserted manually with the aid of the needle guide which lays in the desired orientation.

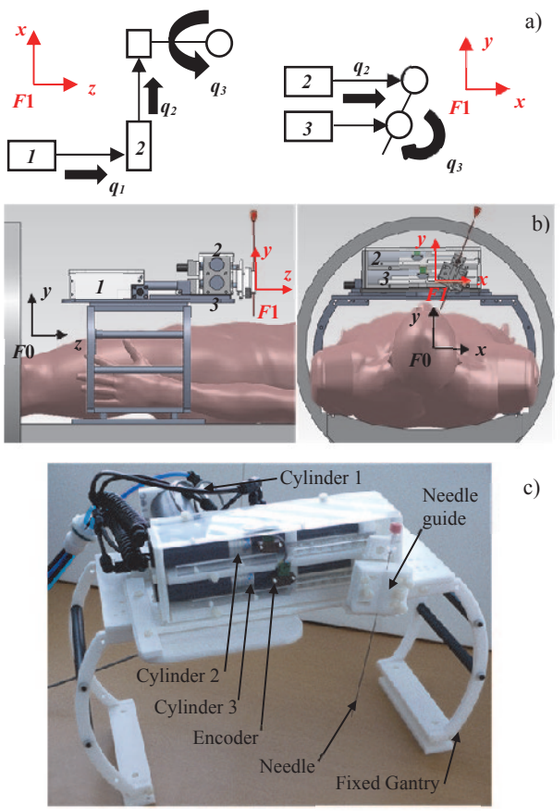

Fig. 1. Kinematic diagram of the needle positioner in top and front views (a); cylinders are numbered from 1 to 3; q_1, q_2, q_3 are the actuated movements of the needle guide. CAD model in side and front views (b); $F1$ and $F0$ are the coordinate frames of positioner and MRI scanner. Prototype of the needle positioner (c).

A functional diagram of the system is shown in Fig. 2.

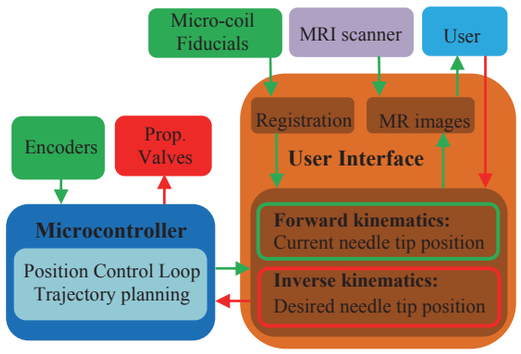

Fig. 2. Functional block-diagram of the system. Red arrows represent commands, green arrows represent feedback. The inner position control loop runs on the microcontroller. The user closes the outer control loop using MR image feedback.

RESULTS

The MRI compatibility of the prototype has been verified in a 3.0T MRI scanner (Siemens Verio). The prototype placed at the scanner isocenter above a Nickel Sulphate phantom was imaged using a GRE sequence (Spoiled Gradient Echo). No visible artifacts appeared (Fig. 3) and the reduction in SNR was below 3%.

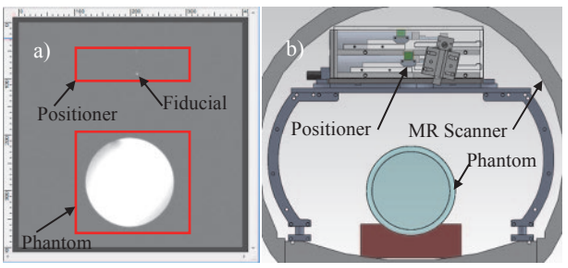

Fig. 3. Axial MR image of the prototype fully powered on in a 3T MRI scanner (a); CAD model of the setup (b).

The targeting accuracy of the prototype has been evaluated in the MR scanner using a water-phantom with MR-visible circular features (diameters from 6 to 12 mm). The phantom was positioned horizontally on the patient bed and aligned with the scanner isocenter. The target point was selected graphically with the GUI and the pistons automatically aligned the needle guide accordingly. Subsequently a plastic needle (20 cm length, 3 mm diameter) was manually inserted in the phantom using the needle guide. Finally the position of the needle tip was verified on a second MR image. The procedure was repeated 10 times for different targets. The targeting error, computed as distance between the center of the circular feature and the center of the needle artifact, varied between 1.2 mm and 3.2 mm with an average of 1.8 mm. A coronal image representative of one test condition is shown in Fig. 4.

DISCUSSION

The experiments in the MRI scanner show that the prototype does not visibly degrade the MR images confirming the validity of the chosen design. The GUI proved intuitive and effective in aligning the needle guide to the target point selected on the MR image. The use of micro-coil fiducials allowed automating the registration of the base frame of the positioner in the MRI scanner which results in further time saving. According to the preliminary tests the targeting accuracy of the device is better than 5 mm. Given that the size of the lesions normally treated by LITT varies between 10 and 50mm in diameter [1], the accuracy achieved appears acceptable at this stage. Further work is being carried out on the control to improve the targeting accuracy of the positioner. An additional actuated movement will be introduced to enhance the dexterity offering clearer advantages over the manual procedure. The possibility of completely automating the needle insertion will also be investigated.

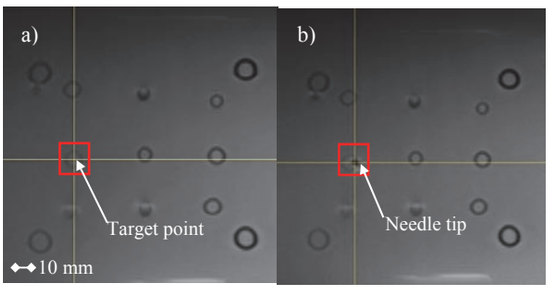

Fig. 4. Desired needle tip position (a) and actual position (b) for one test condition.

ACKNOWLEDGEMENTS

The support of the i4i Grant II-AR-1109-11011 is gratefully acknowledged.

REFERENCES

[1] Gough-Palmer, A.L.; Gedroyc, W.M. “Laser ablation of hepatocellular carcinoma--a review,” World J Gastroenterol. 2008.

[2] Dick, E.A.; Taylor-Robinson ,S.D.; Thomas, H.C.; Gedroyc, W.M..”Ablative therapy for liver tumours,” Gut. May 2002.

[3] Gedroyc, W.M., “Magnetic resonance guidance of thermal ablation,” Top Magn Reson Imaging. Oct 2005.

[4] Fischer, G.S., et al., Pneumatically Operated MRI-Compatible Needle Placement Robot for Prostate Interventions. IEEE Int Conf Robot Autom, 2008. 2008: p. 2489-2495.

[5] Krieger, A.; Sang-Eun Song; Cho, N.B.; Iordachita, I.I.; Guion, P.; Fichtinger, G.; Whitcomb, L.L., "Development and Evaluation of an Actuated MRI-Compatible Robotic System for MRI-Guided Prostate Intervention," Mechatronics, IEEE/ASME Transactions on , vol.18, no.1, pp.273,284, Feb. 2013

[6] Rea, M.; McRobbie, D.; Elhawary, H.; Tse, Z.; Lamperth, M.;Young, I., “Sub-pixel localisation of passive micro-coil fiducial markers in interventional MRI,” Magnetic Resonance Materials in Physics

[7] Brujic, D.; Galassi, F.; Rea, M.; Ristic, M., "A novel algorithm for fast 3D localization of N fiducial markers from 1D projections", ISMRM 2012, Melbourne.

Fluidic Actuators for Minimally Invasive Neurosurgical Instruments

K. Eastwood[1,2], T. Looi[1,2], H. E. Naguib[2], J. M. Drake[1,2]

[1]*Neurosciences and Mental Health, The Hospital for Sick Children, Canada*

[2]*Institute for Biomaterials and Biomedical Engineering, University of Toronto, Canada*
kyle.eastwood@sickkids.ca

INTRODUCTION

Current pediatric neuroendoscopic instruments are limited in their dexterity and reachability for performing complex intraventricular procedures. Presently, the development of higher degree of freedom (DOF) instruments has focused on indirect drive mechanisms, having the actuators located away from the distal instrument tip. Some examples include concentric tube systems or variations of multi-backbone robots [1]. Such systems have demonstrated reliability and cost effectiveness, however there is an upper limit on the number segments (DOF) that can be actuated externally. Moreover, these devices can depend on superelasticity and stiffness for force transmission which are only available in certain metals, posing challenges for MRI compatibility in terms of artifact and induced eddy currents creating unwanted heating and vibration.

The prevalence of indirect drive approaches can be attributed to the high specific power [force output x speed/ size (volume)] that is required at the tip of neurosurgical tools. Based on clinical data, the specific power can be approximated on the order of 200 KW/m^3 considering a 2 mm outer diameter (OD) instrument with segment length of 200mm, 1 N forces and 12 cm/s tip speed [1-2]. This value lies at the performance limit of current miniature actuating technologies applicable to direct drive, where actuators lie along the tool's length.

Recent interest in fluidic based direct drive actuators for natural orifice procedures provides an alternative approach with high specific power translatable to neurosurgery [3]. "McKibben" actuators are elastic tube structures reinforced with an external braid of interwoven wire helicies. An actuator pressurized with saline will expand radially, engage the braid and cause its fibers to twist and accommodate for the change in shape. As the radius increases, the "helical" braid's effective length will decrease, creating a contractile motion. Large scale (>1cm OD) actuators are produced without metal. Three contractile actuators can be combined in parallel with a leaf spring, eliciting bending motions similar to multibackbone segments [6].

The purpose of this study is to investigate the performance of the smallest recorded version of this actuator in literature with reference to applications for possible future neurosurgical instrumentation.

MATERIALS AND METHODS

Miniaturized McKibben actuators (Figure 1) were fabricated with a modified approach to [3]. High purity silicone rubber tubing (0.508mm ID, 0.94 mm OD) was sheathed in silver plated braid mesh (36 AWG, 24 ends; 12.5^o braid angle) to produce ten contractile actuators with OD of 1.52 ± 0.029mm. The ends of the tubes were fitted with 27 AWG luer lock needles and outer stainless steel tubing crimps (1.67mm ID, 2.38mm OD).

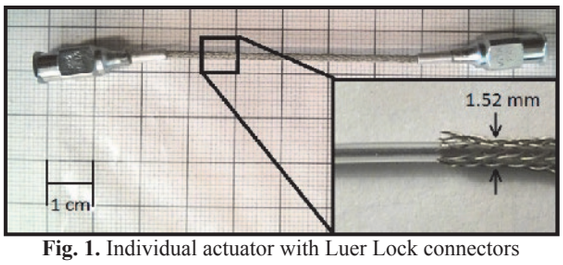

Fig. 1. Individual actuator with Luer Lock connectors

The quality and repeatability of the fabrication procedure was compared to literature by considering the maximal blocking force and unloaded displacement of each actuator. Force measurements were taken with an electronic force transducer (A&D Electronics AN-HE-004; Shenzhen, China) and displacement was measured with ImageJ software (NIH; Bethesda MD, USA). Three McKibben actuators were combined in a bending configuration as depicted in Figure 2.

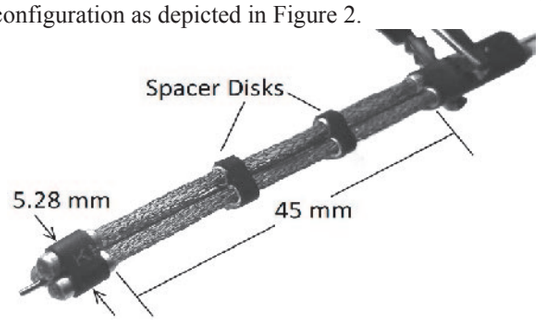

Fig. 2. McKibben bending segment with central leaf spring

A mechanical rig consisting of three actuated syringes with position and pressure feedback was fabricated. The syringes were driven with linear actuators (Firgelli PQ12-100-12-P; Victoria BC, CAN) and pressure data was acquired with pressure sensors (Honeywell SSCDANV150PGAA; Morristown NJ, USA). With this system, the workspace of the bending segment, and the relationship of pressure and volumetric input with the bending angle, was observed.

RESULTS

Preliminary assessment of the 10 individual McKibben actuators demonstrated output contractile

forces of 4.83 ± 0.38N and maximal strain before failure, under no-load conditions, of 8.34 ± 0.23%.

Simulation of the workspace, based on a single multi-backbone unit with assumed piecewise constant curvature, elicited reachable tip positions in the form of a symmetric concave lens surface [6]. This model was approximated by varying the actuator strains between 0-8% as determined experimentally, eliciting bending angles of ±35.5° measured between the tangents of the tip and the fixed based. Actuation pressures varied between 0.1 to a maximum of 1 MPa. A projection of this surface on the XY plane, and the corresponding experimental tip positions are demonstrated in Figure 3.

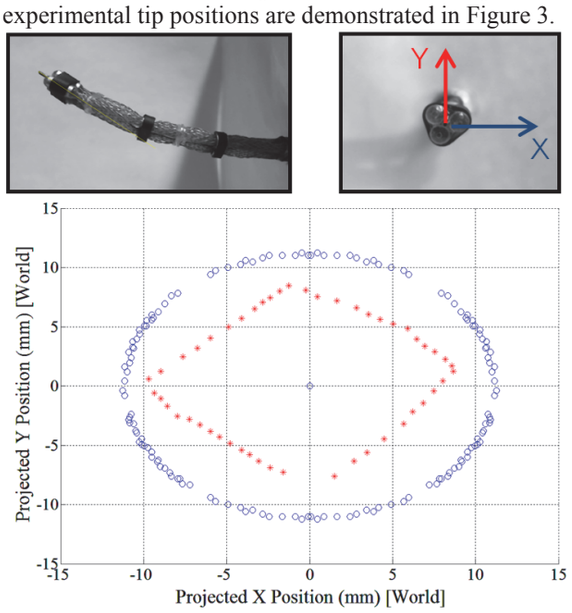

Fig. 3. XY projection of theoretical (blue) and experimental (red) reachable tip positions for McKibben bending segment.

DISCUSSION

The design motivation for this work relates to pediatric endoscopic instruments compatible with trocar channels of 2±0.2mm. Initial design estimates specify McKibben actuators of ≤ 1mm OD to meet this requirement, and custom printed crimps with a narrower profile than those currently used. The actuators explored in this study were selected based upon the smallest geometries currently reported in literature as a basis of comparison [3,4]. The braid selection of a 12.5° weave angle was determined using a force optimization study [5]. The results of 4.83N and 8.34% strain can be compared to 6 N and 12% reported previously for McKibben actuators of similar geometry. The lower performance values seen across the 10 samples, related to the silicone tubing failing at pressures approaching 1 MPa, can be attributed to either the fabrication process or the braiding selected. Presently, the braiding is sheathed around the tubing post fabrication by careful propagation down the length of the tube; an alternative being to wind the braid fibers directly around the tube. Our method involves a guidewire inserted into the lumen of the silicone to provide rigidity while sheathing the braid and may contribute to localized abrasions. Also, use of braiding with smaller gaps between fibers (increased surface area coverage) will better reinforce the tube at high pressure.

The bending prototype has $^1/_3$ the diameter of similar McKibben devices. With non-optimized spacer placement, the net bending achieved meets the required range of motion for neurosurgery of 70° [2]. This result can be compared to a net bending of 90° achieved with a 15mm OD device [3]. Future work in scaling the individual actuators from 1.5 to 1 mm OD will focus on spacer placement to maintain the ±35.5° bending angle.

The theoretical model in Figure 3 was predicted using three 12.5mm constant curvature segments spaced between two 2.5mm linear spacer disks and one 5mm linear tip. Although similar, modifications must be made to achieve closer matching of workspace estimates. Present modeling of individual hydraulic actuators express force and contraction as functions of initial geometrical configurations, operating pressure and the volume of the working fluid added. However, presently no literature models the bending behavior of McKibben actuators for this configuration and scale. Future work will include developing a bending model as a function of pressure and input volume, changing the number and arrangement of spacer disks, sourcing appropriate non-metallic braid and introducing a correction function to better predict the workspace. The next design iteration will be compared to the alternate indirect drive approaches in terms of diameter, curvature, force output and achievable DOF.

In general, fluidic actuators such as the McKibben can prove to be attractive in neurosurgery as they provide additional dexterity, with the required power density, and the potential to remove metal parts, beneficial to imaging. The proposed tool, though larger than the current size constraint, provides sufficient force and workspace for many neuroendoscopic tasks. Future work involves optimizing the design to meet the 2mm size requirement while retaining force and dexterity.

REFERENCES

[1] Mitsuishi M, et al. Force Feedback Manipulating System for Neurosurgery. Procedia CIRP. 2013 Jan; 8:819-829.

[2] Woerdeman PA, et al. The analysis of intraoperative neurosurgical instrument movement using a navigation log file. Int J Med Robot. 2006 Jun; 2(2):139-145.

[3] Moers A, et al. Integrated high pressure microhydraulic actuation and control for surgical instruments. Biomed Microdevices. 2012 Mar; 14:699-708.

[4] Solano B, Rotinat-Libersa C. Compact and lightweight hydraulic actuation system for high performance millimeter scale robotic applications. J. Intell. Mater. Syst. Struct. 2011 Sep; 22(13):1479-1487.

[5] Iwata K, Suzumori K, Wakimoto S. Development of contraction and extension artificial muscles with different braid angles and their applications to stiffness changeable bending rubber mechanism. Journal of Robotics and Mechatronics. 2011 Apr; 23(4):582-588.

[6] Simaan N. Snake-Like Units Using Flexible Back-bones and Actuation redundancy for Enhanced Miniturization. IEEE International Conference on Robotics and Automation. 2005 Apr; 3012-3017.

Preliminary Development of a Novel Amphibious Locomotion System for use in Intra-Luminal Surgical Procedures

W. Mayfield[1], A. Alazmani[1], A. Hood[2], J. Boyle[1], P. Culmer[1], R. Hewson[1], A. Neville[1*], D, Jayne[2]

[1]*School of Mechanical Engineering, University of Leeds, UK*
[2] *Leeds Academic Surgical Unit, St James' University Hospital, Leeds, UK*
a.neville@leeds.ac.uk

INTRODUCTION

The colonoscopy procedure is a means of visually exploring and assessing the colon and is typically performed with a colonoscope- a long, steerable tube with channels for passing air, liquid or tools and a tip-mounted camera and light source. It allows clinicians to visually inspect the inner colon surface and perform various procedures.

Although the colonoscope has been developed and enhanced over many years, it still suffers from several fundamental drawbacks. The human bowel is by no means a straight or simple passageway to navigate. The bowel has many twists, bends and turns as shown in CT data, Fig. 1. The configuration of the bowel varies in size, shape and position within the abdomen from person to person. The organ itself is highly compliant posing a challenging task to navigate during colonoscopy. Furthermore the colonoscopy procedure itself can be very uncomfortable, painful and damaging for the patient [1]. The risk of injuring or perforating the colonic wall is particularly significant in cases of patients with inflammatory disorders of the bowel [2].

Fig. 1. A 3D computer model of a colon reconstructed from CT scan data, showing from left to right: transverse, coronal and sagittal planes. The centre line is shown in red; Scan data courtesy of the Cancer Imaging Archive, accessed 2011 [3].

Several attempts have been made to develop a robotic colonic inspection device as an alternative to the colonoscope. Key systems include those by Menciassi et al. [4], Ikeuchi et al. [5], Zhou et al. [6] and Shikanai et al. [7]. However these approaches have a common drawback; they rely upon contact based locomotion alone. Pure contact based methods risk trauma as they require constant contact with the lumen and impart forces as a means of locomotion.

The Colonic Disease Investigation by Robotic hydro-colonoscopy (CoDIR) project aims to develop a robotic system for colonic inspection that is able to locomote through a fluid filled colon. In hydro-colonoscopy a fluid medium is introduced to help minimise patient discomfort and open the lumen for improved access. This environment provides a unique opportunity for new modes of robotic locomotion. This work details an amphibious locomotion system for CoDIR which aims to help minimise tissue trauma and enable movement through challenging areas of collapsed lumen.

The approach uses two pairs of counter rotating Archimedes screws, allowing both fluid and contact based locomotion from the same drive train, (see Fig. 2). Each of the four screws are attached to an off-centre pivoting arm with all four arms driven by a single internal motor and gearbox allowing for synchronous arm movement. This adjustable geometry allows control over the device's diameter and hence the locomotion strategy. Expanding the arms to the lumen diameter allows for contact-based propulsion while collapsing them enabled fluid based locomotion avoiding contact. Furthermore passage through collapsed sections could be enhanced using the device's adjustable geometry. The rounded front portions of the screws would allow the device the 'burrow' into a collapsed region before expanding the arms to gently open the lumen. The advantaged of such a front driven system is that it reduces pressures on the lumen experienced using a traditional colonoscope. The device is neutrally buoyant allowing it to float freely. Differentially driving the screws allows for changes to its orientation within fluid (e.g. to enable the clinician to control camera angles).

Fig. 2. Device concept CAD model shown in closed position (left) and open position (centre), and assembled rapid prototyped device (right). 1: arm mounted screw section, 2: screw motor housing, 3: central chassis containing arm actuation motor and gears, 4: control electronics capsule.

In order to design, test and analyse the screw system both theoretical and practical experimental evaluations were conducted. This paper details the practical testing of the system in both fluid-based and contact-based modes.

MATERIALS AND METHODS

To evaluate the concept two testing platforms were developed, one each for fluid and contact propulsion. Archimedes screws were rapid prototyped in two pitches, 20 and 40mm, in both right and left handed variations. The same screw pieces were used in both

testing environments with custom motor control software developed in LabVIEW.

The fluid testing rig consists of a partially enclosed screw suspended from a beam load cell with the screw submerged in deionized water. The degree of cowling can be varied to simulate different arm positions.

The contact testing rig consists of two counter rotating screws held at a fixed distance and in contact with a tissue bed which is positioned on a linear bearing slide attached to a load cell such that horizontal forces can be measured. Initial tests used a PVA cyrogel to provide a repeatable model with mechanical properties simulating colonic tissue.

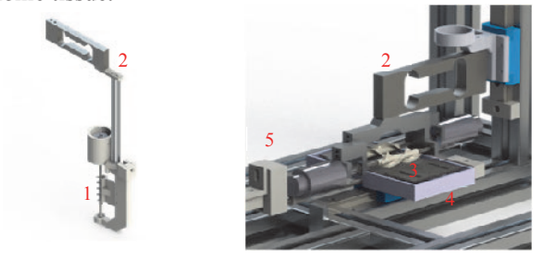

Fig. 3. Experimental test rigs, fluid (left) and contact (right). 1: Partially enclosed screw, 2: beam load cell, 3: counter rotating screw pair, 4: tissue bed, 5: bed load cell.

RESULTS

The results for the fluid propulsion tests are shown in Fig. 4. 20mm pitch screws produce less thrust compared to 40mm with a clear relationship between the thrust generated and cowling coverage being visible.

The results from the contact traction tests can be seen in Fig. 5. Only the results from 20mm pitch screws are shown. The 40mm pitch screws produced less than 0.1N and have not been shown.

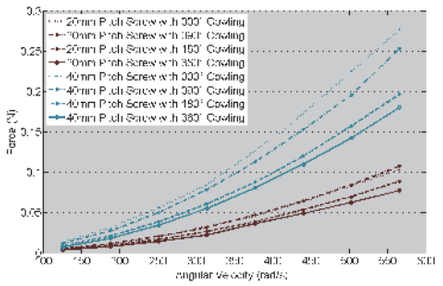

Fig. 4. Angular velocity vs. force produced for 20mm (red) and 40mm pitch (blue) screws in various states of cowling. 360° represents a screw in a pipe, 0° represents open fluid.

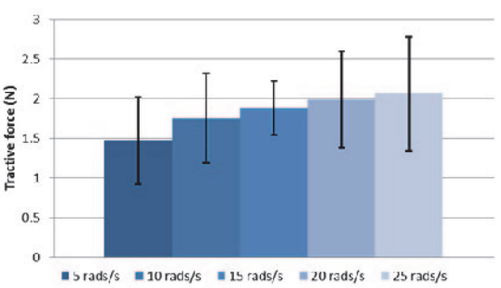

Fig. 5. Screw angular velocity vs. tractive force for 20mm pitch screws. Showing mean tractive force and standard deviation.

DISCUSSION

The results from a single screw in fluid, Fig. 4, show that up to 0.3N of thrust can be produced from a 40mm pitch screw when operating in open fluid at 575 radian s^{-1} (90Hz). Although, as seen in Fig. 4, an increased motor velocity results in greater thrust produced, it is not viable to keep increasing the velocity due to mechanical limits of the motor and gearing. In the full 4 screw concept and assuming perfect scalability, over 1N of thrust should be achievable.

The experimental evaluation used two counter-rotating screws in order to eliminate the force component perpendicular to the intended direction. From Fig. 5 it can be seen that the contact method of locomotion produces significantly greater propulsive thrust, although these values represent the combined effort of two screws while the fluid results are from a single screw. While this greater thrust may be ideal for the complete locomotion system this project aims to minimise trauma due to contact. Further development will see the concept utilize multi-material compliant screws to minimise the potential trauma while allowing hybrid locomotion through a mixed medium. The initial testing shows both forms of locomotion to be viable. Fluid-based locomotion would be the default strategy while contact-based locomotion would serve as backup for tortuous sections of the colon.

Future work will see testing of the dual screw system on ex-vivo colonic tissue as well as testing of a complete quad screw prototype.

REFERENCES

[1] Meinhard, C.T., Guido. Lightdale, Charles., Gastroenterological endoscopy. 2nd ed. 2010: Thieme.

[2] Navaneethan, U., et al., Severe disease on endoscopy and steroid use increase the risk for bowel perforation during colonoscopy in inflammatory bowel disease patients. Journal of Crohns & Colitis, 2012. 6(4): p. 470-475.

[3] NCI. The Cancer Imaging Archive. 2011 [cited 2011; Available from: cancerimagingarchive.net.

[4] Menciassi, A. and P. Dario. Miniaturized robotic devices for endoluminal diagnosis and surgery: A single-module and a multiple-module approach. in Engineering in Medicine and Biology Society, 2009. EMBC 2009. Proc. IEEE. 2009.

[5] Ikeuchi, K., et al., Locomotion of medical micro robot with spiral ribs using mucus. Mhs '96 – Proc. 7th International Symposium on Micro Machine and Human Science: Toward Micro-Mechatronics in 21st Century. 1996, New York: IEEE. 217-222.

[6] Zhou, Y.S., et al., A new medical microrobot for minimal invasive surgery. Proc. IMechE Part H-Journal of Engineering in Medicine, 2001. 215(H2): p. 215-220.

[7] Shikanai, M., et al. Development of a robotic endoscope that locomotes in the colon with flexible helical fins. in Engineering in Medicine and Biology Society, 2009. EMBC 2009. Proc. IEEE. 2009.

3D Motion Planning for Steerable Needles using Path Sets

S. Sanan[1], Y. Chen[1], C. A. Lehocky[2], C. Gong[1], C. N. Riviere[1,2], H. Choset[1]
[1]*The Robotics Institute, Carnegie Mellon University, USA*
[2]*Biomedical Engineering, Carnegie Mellon University, USA*
sanan@cmu.edu

INTRODUCTION

Bevel-tipped flexible needles can be steered in soft tissue to clinical targets along curved paths in 3D while avoiding critical structures. Duty-cycled rotation [1] during insertion allows for control of the curvature of the needle. These capabilities of 3D steerable needles make it potentially suitable for applications such as deep brain stimulation (DBS) and drug delivery to brain tumors [2]. Manually guiding a steerable needle is unintuitive due to the high-dimensional nature of the problem. Planning algorithms can help provide a feasible motion plan for steering the needle between the start and target locations while avoiding critical structures in the tissue. Imaging feedback is incorporated to control the needle along the pre-planned path.

In this paper, we present an algorithm for path planning of steerable needles based on A* graph search on path sets in 3D. Path sets have been utilized extensively, in the past, for motion planning of mobile robots with nonholonomic constraints [3]. The formulation using path sets allows the planner to ouput paths that respect the differential or nonholonomic constraints associated with needle steering. Compared to more commonly used sampling-based approaches such as RRT [4,5,6], an A* search-based approach can guarantee optimality of the path with respect to a pre-defined cost function. Since safety is of paramount importance in our application, we consider two factors in our path cost that influence safety: a) path length and b) curvature. Critical structures are avoided by treating them as obstacles.

MATERIALS AND METHODS

Figure 1 shows the simulation environment used for evaluating our path planning algorithm. To test our path planning algorithm we use the following DBS application scenario in simulation. The needle enters near Kocher's point on the cortical surface (2.5 cm off the midline at the level of the coronal suture) and must reach the subthalamic nucleus. Critical anatomical obstacles that must be avoided include the corticospinal tracts, basal ganglia, and thalamus. These are approximated by combinations of simple geometrical shapes.

Algorithm: The algorithm utilizes the needle steering motion model $\dot{x} = f(x,u)$ to generate a path set P by uniformly sampling a subspace of the control input u. The needle motion model is described in [7]. In this paper we uniformly sample over the axial rotation θ and curvature κ to generate elements of the path set.

Once the path set P is generated, the algorithm proceeds as follows: (1) The initial tip position is added as the first node to the graph and the target position is added as the goal node (2) Starting from the initial configuration the tip position $\mathbf{x} \equiv (x,y,z)^T$ resulting by execution of each path in P is added as a node to the graph. The edge connecting this node to the first node indicates the path set element connecting the two nodes. (3) Each node is evaluated based on the sum of the total cost c to reach the node and the heuristic cost h. The heuristic is the Euclidean distance between the tip position and the goal position:

$$h(\mathbf{x}) = \left\| \mathbf{x} - \mathbf{x}_{\mathbf{goal}} \right\|_2 \quad (1)$$

The algorithm then proceeds using standard A* search on a dynamic graph. The path planner succeeds when a node is reached that is within ε distance of the goal.

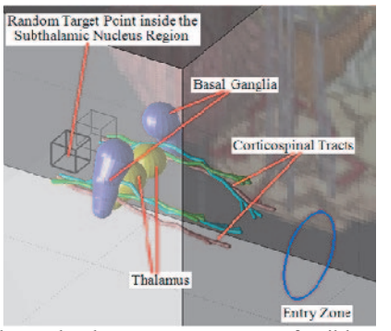

Fig. 1. The path planner pre-computes feasible paths in a human brain environment from entry zone to the target point located in the area of the subthalamic nucleus (indicated by a highlighted black bounding box), while avoiding anatomical obstacles along the paths.

Path safety cost: The cost to reach a node i in the graph is given by:

$$c_i = c_{p(i)} + s(i, p(i)) \quad (2)$$

where, $p(i)$ is the parent of node i, and $s(i,j)$ is the cost to get from node j to node i in the graph. The cost $s(i,j)$ can be based on any characteristic that is desired to be minimized along it. For our application, it is desirable to minimize the damage to the tissue caused by the traversal of the needle through it. We propose two factors that adversely affect safety: (a) path length (b) deviation from maximum needle path curvature. Shorter overall path lengths are preferred as they will traverse through lesser amounts of tissue. Curvature values closer to the maximum curvature for the needle are preferred as these paths require less duty-cycled rotation which can potentially cause tissue damage. We used a weighted combination of these factors as our cost:

$$s(i, j) = w_l l(i, j) + w_r (r(i, j) - r_{\min}) \quad (3)$$

where, l is path length, r is the radius of curvature, and w the respective weights.. The weights sum to 1.

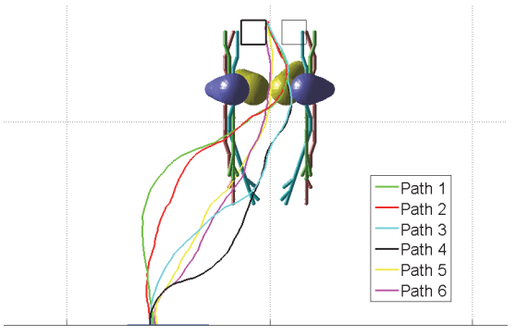

Fig. 2. Planned paths by varying the weighting factors on the two safety cost factors. Path 1 has zero weight associated with path length and Path 6 has zero weight associated with path curvature. The remaining paths interpolate between the two extreme cases. Top view is shown.

RESULTS

We evaluated our algorithm on the environment shown in Figure 1 and varied the weighting between the two safety factors in (3). The paths resulting from this variation are shown in Figure 2.

The path-following controller described in [4] was used to follow the path output by the A* path set planner. The results of the path-following experiments for two paths are shown in Table 1 and indicate that the paths output can be followed fairly accurately for steerable needles under duty-cycled rotation.

DISCUSSION

In this paper, we have demonstrated path planning for steerable needles using the idea of path sets. Path sets allow for natural inclusion of the kinematic constraints of the steerable needle while still allowing for the notion of optimal paths. As a result, paths output from the planner require very little post-processing or smoothing as is often the case with sampling based planners such as RRT. The paths output from the planner can be closely followed by the steerable needle. Further, factors affecting tissue damage along the path can be minimized by choosing an appropriate cost function.

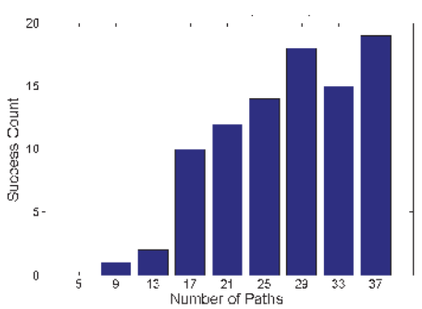

Fig. 3. Success rate of A* on path sets with varying number of paths in the path set. Success rate was computed over 20 trials.

Table 1. Results of path-following on two planned paths from Figure 2.

Path	No. trials	Avg. pos. error along path (true) (mm)	Avg. pos. error along path (mm)	Avg. final target pos. error (mm)
Path1	20	1.2 ± 0.5	1.0 ± 0.2	1.3 ± 0.4
Path2	20	1.6 ± 0.3	1.2 ± 0.3	1.0 ± 0.5

In our approach, the graph is not known *a priori* but is instead dynamically expanded at each iteration of A*. As a result points in 3D that are theoretically reachable from a given starting point may not be present on the search graph. Therefore our method cannot guarantee finding a solution if one exisits. The probability of finding a solution is dependent on the properties of the path set such as number of elements, path diversity, etc. [3]. A formal method to compute the probability of reaching a goal state was introduced in [8] when paths sets result from stochasticity in the motion model. Figure 3 shows empirical results for success-rate variation with increased number of elements in the path sets using our method.

In the future, we plan to extend our approach by using a 3D lattice-based decomposition of the environment. This will improve performance of the planner in terms of computation time and success rate.

REFERENCES

[1] Engh JA, Minhas DS, Kondziolka D, Riviere CN. Percutaneous intracerebral navigation by duty-cycled spinning of flexible bevel-tipped needles. Neurosurgery. 2010 ;67(4):1117–22.

[2] Frasson L, Ko SY, Turner A, Parittotokkaporn T, et al. STING: a soft-tissue intervention and neurosurgical guide to access deep brain lesions through curved trajectories. Proc Inst Mech Eng. 2010; 224(6): 775–88.

[3] Knepper RA, Mason MT. Path diversity is only part of the problem. Proc IEEE Int Conf Robot Autom. 2009;3224-9.

[4] LaValle SM, Kuffner JJ. Randomized kinodynamic planning. Int J Robot Res. 2003;20(5):378-400.

[5] Xu J, Duindam V, Alterovitz R, Goldberg K. Motion planning for steerable needles in 3D environments with obstacles using rapidly-exploring random trees and backchaining. Proc IEEE Int Conf Autom Sci Eng. 2008;41-6

[6] Li X, Lehocky CA, Riviere CN. Efficient 3D control for needle steering using duty-cycled rotation. Int Conf Info Cont Auto Rob. 2013;(2):192-199.

[7] Webster III RJ, Kim JS, Cowan NJ, Chirikjian GS, et al. Nonholonomic modeling of needle steering. Int J Robot Res. 2006;25(5-6):509–525.

[8] Park W, Wang Y, Chirikjian GS. The path-of-probability algorithm for steering and feedback control of flexible needles. Int J Robot Res. 2010;29(7):813-30.

A Bio-inspired Flexible Robot with Hybrid Actuation Mechanisms for Endoscopic Surgery

C. C. Y. Poon[1], H. Yang[1], K. C. Lau[2], W. J. Xu[2], Y. Yam[2], J. Y. W. Lau[1], P. W. Y. Chiu[1]

[1]*Dept. of Surgery, The Chinese University of Hong Kong, China*
[2]*Dept. of Mechanical and Automation Engineering, The Chinese University of Hong Kong, China*
cpoon@surgery.cuhk.edu.hk

INTRODUCTION

Gastric and colorectal cancers are the top leading causes of cancer death worldwide. Survival rates for patients of these cancers can be improved if the tumours are removed en bloc at an early stage. Nevertheless, these cancer types normally grow from the inner mucosa layer of the gastrointestinal tract, which makes them difficult to be dissected with present laparoscopic techniques.

Endoscopic Submucosal Dissection (ESD) is an effective treatment for early gastric and colorectal cancers. Compared to open surgery, ESD is less invasive since the procedure does not perform through an open wound and do not require the resection of the organs involved. Nevertheless, performing ESD with conventional flexible endoscope is challenging due to the lack of dexterity to retract tissues and maintain a good view of the submucosal plane while moving the endoscopic instrument for dissection [1]. Therefore, a surgical robotic system with better ergonomics and high dexterity to assist surgeons in performing this procedure is highly demanded.

A number of endoscopic robots have been developed to perform ESD, e.g. ViaCath System [2], MASTER [3] and STRAS [4]. All these systems used a cable-conduit driven pull-and-pull mechanism to drive the end effectors. The cable-conduit can be 1-2 meters long, connecting the robotic arms to the actuation housing where the motors were located. Since in surgical operation, the force attenuation and elongation of the cables due to friction loss are time-varying functions, the mechanism is difficult to be modelled with precise position and force control.

Therefore, in this paper, we aim to demonstrate the design of a new endoscopic robotic system, which is actuated by hybrid actuation mechanisms using: 1) cable-conduit with a pull-and-pull mechanism and 2) superelastic shape memory alloys (SMAs) with a push-and-pull mechanism. Moreover, a novel multi-section robotic gripper with a continuum structure is fabricated by rapid prototyping technique for illustration of the tissue retraction function for ESD.

MATERIALS AND METHODS

- **Bio-inspired Design**

An ESD surgical robot should have two arms: one with sufficient force to grip and retract tissues while the other with high manoeuvrability for cauterisation of the tissues being lifted. Based on this requirement, we proposed in this study a multi-section robotic arm design, which consists of a upper ball-joint (shoulder) linked with a lower hinge-joint (elbow). The design is inspired by the long claws of Norway lobster (**Fig. 1** *left*), which bears the merits of both excellent manoeuvring ability and force burdening capacity—endowing the animal to forage food in front of its thin body with incredible efficiency. The connection of the two different types of joints provides a 3 degree of freedom (DoF) manoeuvrability without losing force burdening ability when force is applied to the flank of the hinge joint. Moreover, triangulation can be provided by the continuum structure to enhance the cooperation between the two robotic arms. A 2 DoF wrist joint is further added to the robotic gripper. **Fig. 1 (***right)* is the conceptual visualisation of our endoscopic robot.

Fig. 1. Norway lobster (left) the CAD conceptual visualization of our proposed endoscopic robot (right)

- **Mechanical Actuation Mechanisms**

The upper arm of the proposed robot is designed as a continuum bending mechanism with 2 DoF, driven by 2 pairs of antagonized SMAs with a push-and-pull mechanism. Compared with continuum structure driven by pulling cables, the use of SMAs has the advantages of doubling the actuation force since the two antagonised SMAs can be driven simultaneously. The design methodology, kinematics and workspace analysis of continuum robot can be found in [5, 6].

The lower arm is connected to the upper arm through a hinge joint that is driven by 2 antagonised cables that passed through incompressible conduits. Unlike cable actuators which is easy to be elongated, SMA is non-compressed, and therefore the driving backlash can be reduced. Though cables are not as

responsive and efficient as SMAs, they can be bent with a larger angle. Therefore, cables are used to drive the hinge joint in order to achieve a maximum 180 degree rotation. These cables are passed through conduits which allow decoupling of the motions of different sections. The effect is similar to using pulley to divert force direction as in designing grippers with rigid joints, such as those of the Da Vinci surgical robot.

Lengths of each section of the bio-inspired design can be customised according to the workspace required for normal ESD surgery.

Based on the workspace required for normal ESD surgery, the upper and lower arms of the robot was designed to be 40mm and 20mm respectively. Fig. 2 plots the workspace of the two cooperative robotic arms. The workspace is envisaged to provide enough space for lifting tissues in the vertical direction and

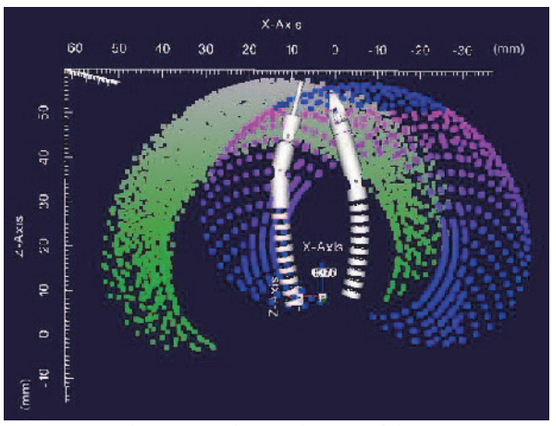

Fig. 2. The cooperative workspace of the two arms.

dissecting tissues in the horizontal submucosal plane.

RESULTS

A prototype for our proposed robotic arm design was implemented via 3-D printing and laser cutting techniques. Micro DC motors (3863A024C, FAULHABER Group) were used to drive the 5 DoF robotic arms (**Fig. 3** *right*). Two rack gears were fixed on each side of the shaft of the motor to move the antagonized actuators in opposite directions. The maximum force accomplishable by the end-effector was around 2N, whereas the control accuracy of the arm was in the order of magnitude of 2 mm.

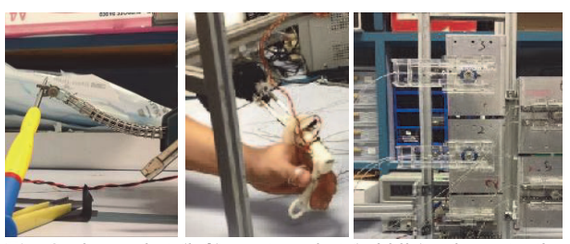

Fig. 3. slave robot (left) master robot (middle) salve actuation mechnisam (right)

To tele-operate the robotic arm ergonomically, a master robot bearing the same configuration with the slave robot was also designed (**Fig. 3** *middle*). A joint control strategy was used to directly map the position of the master to each joint of the slave robot.

DISCUSSION AND CONCLUSION

In this work, a multi-DoF, tele-operated robot is designed to work with the conventional flexible endoscope for ESD surgery. We presented the mechanical design of the slave robot and customised it according to the workspace required for ESD surgery.

Conducting endoluminal surgery requires manipulating surgical tools with the endoscope. Due to the loss of operational triangulation, the performance is difficult when it comes to complex procedures such as ESD. The current state of art endoscopic robotic system only provides limited manoeuvrability, less precise open-loop control, and without haptic feedback. Incorporating sensor in each and every DoF to form close-loop control would be difficult with the present technologies. Therefore, the precision of controlling the slave robotic arms should be improved by modelling the robotic kinematics. On the other hand, haptic feedback can be achieved by estimating contact force on the end-effector of the slave robot or by using image information to assist haptic sensation through virtual fixture. In future, these directions will be further explored and incorporated into the design of the proposed endoscopic robot.

REFERENCES

[1] A. Y. B. Teoh, P. W. Y. Chiu, S. K. H. Wong, J. J. Y. Sung, J. Y. W. Lau, and E. K. W. Ng, "Difficulties and outcomes in starting endoscopic submucosal dissection," *Surgical Endoscopy and Other Interventional Techniques,* vol. 24, pp. 1049-1054, May 2010.

[2] D. J. Abbott, C. Becke, R. I. Rothstein, and W. J. Peine, *Design of an endoluminal NOTES robotic system*. New York: IEEE, 2007.

[3] S. J. Phee, N. Reddy, P. W. Y. Chiu, P. Rebala, G. V. Rao, Z. Wang, Z. Sun, J. Y. Y. Wong, and K. Y. Ho, "Robot-Assisted Endoscopic Submucosal Dissection Is Effective in Treating Patients With Early-Stage Gastric Neoplasia," *Clinical Gastroenterology and Hepatology,* vol. 10, pp. 1117-1121, 2012.

[4] A. De Donno, F. Nageotte, P. Zanne, L. Zorn, and M. de Mathelin, "Master/slave control of flexible instruments for minimally invasive surgery," in *Intelligent Robots and Systems (IROS), 2013 IEEE/RSJ International Conference on*, pp. 483-489, 2013.

[5] I. D. Walker, "Continuous Backbone “Continuum” Robot Manipulators," *ISRN Robotics,* vol. 2013, 2013.

[6] N. Simaan, K. Xu, W. Wei, A. Kapoor, P. Kazanzides, R. Taylor, and P. Flint, "Design and integration of a telerobotic system for minimally invasive surgery of thethroat," The International journal of robotics research, vol. 28, pp. 1134-1153, 2009.

Design of a Bi-Manual End-Effector for an Endoscopic Surgical Robot

C. A. Seneci, J. Shang, G.-Z. Yang

The Hamlyn Centre, Institute of Global Health Innovation, Imperial College London, UK

c.seneci@imperial.ac.uk

INTRODUCTION

Robotics has an increasingly important role in transforming pioneering surgical procedures into every day practice, providing surgeons with adequate instrumentation. Natural Orifice Translumenal Endoscopic Surgery (NOTES) represents a great opportunity for technology to drastically improve surgical outcomes, as nowadays it has not yet widely practiced due to the difficulty raising from using traditional manual instrumentation. Furthermore, the application of such techniques to Gastro-Oesophageal surgical procedures would allow addressing lesions without introducing scars either outside or inside the body. Research carried by companies and universities led to the development of several endoscope-based surgical platforms with either manual or robotic control. An extensive review of emerging surgical robots, for Minimally Invasive Surgery (MIS), reports advantages and disadvantages for many of the platforms in experimentation or use [1]. One of the most common disadvantages introduced in some of these platforms is the large overall size, as per the Anubiscope (Karl Storz Endoskope), which has a diameter of 16mm [2] that could represent a limit while performing operations endolumenally, also due to the presence of side-flaps. Another common drawback in these device is the lack of manoeuvrability of the bi-manual instrumentation, this is well represented by the R-Scope (Olympus), in which the instrument channels have 1 Degree of Freedom (DoF) each that allow the movement of one instrument on the vertical plane for lifting and the other one in the horizontal plane for resection [3]. Furthermore, even when the instrument arms present sufficient manoeuvrability and applicable lateral force, their usage could be difficult for a surgeon if the camera view is almost aligned with the instrument shafts, leading to poor triangulation. An endoscopic platform that is affected by this issue is the Endosamurai (Olympus) with its fixed camera [4]. Finally, a further problem sometimes present in endoscopic platform is the presence of fixed end-effectors that do not allow quick instruments interchange during a procedure. This is the case of the MASTER which present fixed multi-DoF articulated grasper and monopolar cauthery hook as end-effectors [5]. This work addresses the task of designing a compact bi-manual end-effector to enhance the multi-articulated snake-like robot developed in [6]. This preliminary design aims to develop three articulated arm to control the bi-manual instrument channels and the endoscopic camera. The design has referred to the guidelines provided in [7], where it is suggested that a NOTES platform needs at least two instrument working channels.

MATERIALS AND METHODS

The design of the end-effectors relied on the possibility of passing several hollow channels through the main body of the articulated robot. In particular a 3.5mm diameter channel is used to pass an instrument through the right arm and a 2.5mm channel through the left arm. The camera is a flexible 1.8mm diameter endoscope (Shanghai Yanshun Scope Parts & Accessories Co.,Ltd) and provides 62500 pixels image. In addition, a high-intensity white LED is mounted on the robot's tip to provide illumination (Fig. 1).

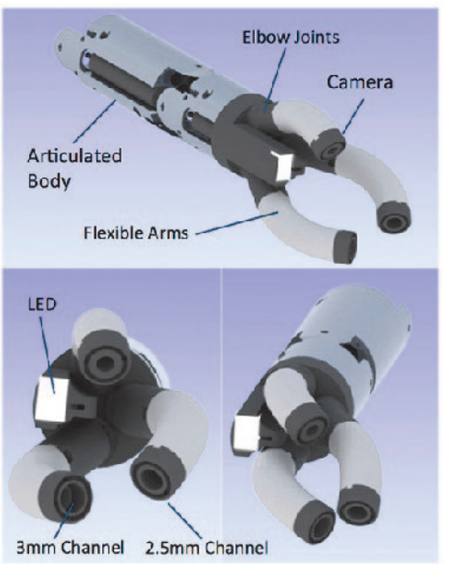

Fig. 1. CAD model of the articulated hollow arms.

The arms have 3 DoF each, the first DoF is used to actuate the elbow-joint to increase the triangulation, while the remaining two DoF are used to actuate the flexible section of the arm. Every DoF is controlled with two 0.3mm Ni-Ti tendons, the tendons are routed to the back of the robot thanks to a low-friction multi-lumen 1.4mm diameter catheter with 0.4mm channels. The elbow joint in all the three cases is able to bend up to 45°, while the bending axis varies from arm to arm. The camera the elbow's axis is horizontal, the left arm one is vertical and the right arm one is tilted 45° with respect to the vertical plane. The elbow links lengths are 5mm

for the camera and 10mm for the arms. The robot body is made with machined aluminium, while the arms-holder cap is rapid prototyped. The arms are made of sintered PA12 and their outer diameter is 5.4mm. The length of the flexible section varies from camera to instruments; in the first case it is 10mm, while in the second is 20mm. The flexible arms present longitudinally 0.5mm recesses on perpendicular planes, to allow two DoF bending. The arms also have 0.5mm channels to allow the passage of two pairs of antagonistic tendons. When the arms are aligned to the body of the robot, the overall diameter is less than 13mm, allowing navigation through small lumens. Also, the possibility of bending the arms together with the camera allows better adaptation to the anatomy of the lumen, as the arms are able also to operate sideways. Given the reduced cost of the materials and components used, sealing has been implemented between the main robot body and the end-effector cap, considering the cap to be disposable.

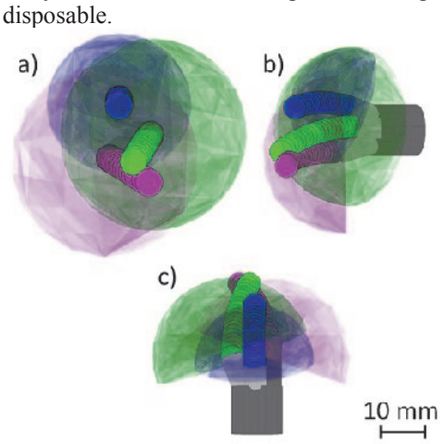

Fig. 2. Workspace simulation: a) frontal view, b) lateral view, c) top view.

As visible from Fig. 2, simulations have been developed to find the adequate design parameters to achieve triangulation and bi-manual coordination with compact size. As visible the left instrument's workspace (WS) (green) and the right instrument's one (pink) has a good overlapping allowing to perform manipulation also on the side of the WS. The camera has a smaller WS that allows the user to keep the instruments centred in the camera view. Finally, since the arms have hollow channels, the instruments can be translated inside the hollow channel, without the need of additional DoF at the end-effectors. This translation has not been considered for the WS simulations.

A prototype of the system has been built; Fig. 3 shows the robot in closed and open configurations, while Fig. 4 shows the camera view of the robot in the same configurations.

DISCUSSION

This work analysed the design challenges of a bi-manual endoscopic robot for gastro-oesophageal NOTES procedures. The work also enumerated some of the limits in the design of research and clinical endoscopic platforms available in literature. Therefore, following a WS study and simulation, the mechanical design of the bi-manual end-effector has been presented, together with photos of the first prototype. The next steps will focus on the experimental evaluation of the platform and on the detailed analysis of the lateral force deliverable with this design.

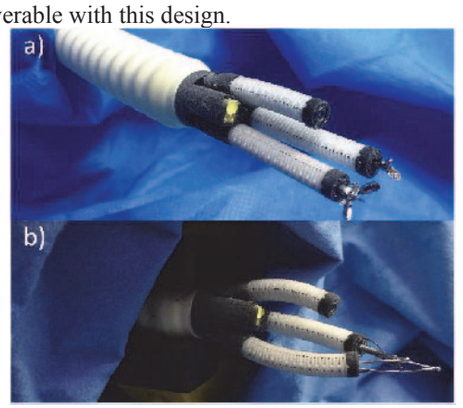

Fig. 3. External view of prototype: a) closed configuration, b) open configuration.

Fig. 4. Camera view: a) close arms view, b) open arms view.

REFERENCES

[1] V. Vitiello, S. Lee, T.P. Cundy, and G.Z. Yang, Emerging Robotic Platforms for Minimally Invasive Surgery, IEEE Review in Biomedical Engineering, Vol. 6, 2013.

[2] B. Dallemagne and J. Marescaux, "The ANUBISTM project," Minimally Invasive Therapy Allied Technol., vol. 19, pp. 257–261, Oct. 2010.

[3] S. J. Bardaro and L. L. Swanstrom, "Development of advanced endoscopes for natural orifice transluminal endoscopic surgery (NOTES)," Minimally Invasive Therapy Allied Technol., vol. 15, pp. 378–383, Jan. 2006.

[4] B. P. M. Yeung and T. Gourlay, "A technical review of flexible endoscopic multitasking platforms," Int. J. Surgery, vol. 10, pp. 345–354, Jun. 2012.

[5] S. J. Phee, A. P. Kencana, V. A. Huynh, Z. L. Sun, S. C. Low, K. Yang, D. Lomanto, and K. Y. Ho, "Design of a master and slave transluminal endoscopic robot for natural orifice transluminal endoscopic surgery," Proc. Inst. Mechanical Engineers, Part C: J. Mechanical Engineering Sci., vol. 224, pp. 1495–1503, Jul. 2010.

[6] Shang J., Noonan DP., Payne C., Clark J., Sodergren M., Darzi A., Yang GZ. An Articulated Universal Joint Based Flexible Access Robot for Minimally Invasive Surgery. International Conference on Robotics and Automation, Shanghai, China. 1147-1152. IEEE (2011).

[7] C.P. Swain, K. Bally, P. O. Park, C.A. Mosse, R.I. Rothstein, "New methods for innovation: the development of a toolbox for natural orifice translumenal endoscopic surgery (NOTES) procedures", Surg Endosc (2012) 26:1010–1020, DOI 10.1007/s00464-011-1987-4.

Ontology-based Modular Architecture for Surgical Autonomous Robots

R. Perrone[1], F. Nessi[1], E. De Momi[1], F. Boriero[2], M. Capiluppi[2], P. Fiorini[2], G. Ferrigno[1]

[1]*Politecnico di Milano, Department of Electronics, Information and Bioengineering (DEIB), Milano, Italy*
-{roberta.perrone, elena.demomi, giancarlo.ferrigno}@polimi.it, federico.nessi@mail.polimi.it
[2]*Dipartimento di Informatica, Università di Verona, Strada le Grazie, Verona, Italy*
-{fabrizio.boriero, marta.capiluppi, paolo.fiorini}@univr.it

INTRODUCTION

Medical robotics is becoming a leading application area in which the surgical assistance provided by robots is rapidly rising such as the Intuitive® Telesurgery System for the Da Vinci Robot, [1] and the NOTES robot for a semi-autonomous surgical task execution, [2]. However, the complexity of the medical environment (which is a dynamic environment) has been a major barrier, preventing a wider use of robotic technology. Providing robots with cognitive architecture for specialized tasks requires a systematic approach in describing the knowledge needed for reaching a goal. At the same time, knowledge processing allows writing of more general and flexible control programs. In this work, we present a workflow for the design and the deployment of an architecture for the execution of a surgical task (i.e. tool positioning on the correct trajectory for needle insertion), where the architecture's components skeleton are automatically derived from ontological description. We formalized basic knowledge in a way that is readable and processable by both man and machine. Ontologies can describe abstract things, like workflows or tasks (e.g. manipulation or grasping [3]) but also real things such as devices [4]. Moreover, the robot control system is able to autonomously perform the initialization of the considered surgical procedure. The system manages also possible failures of software and hardware components.

MATERIALS AND METHODS

We used a 7 degrees of freedom robot (KUKA LWR4+, Germany) in a target approaching task [5], for example the preliminary phase of a surgical needle insertion. The robot movement is followed by two trackers (NDI Optotrack® Certus, NDI Polaris Vicra®) with different characteristics (i.e. accuracy, sampling rate, field of view). Since the operating room is quite crowed during surgery, the field of view of a tracker may be occluded. We considered a second tracker as backup, so that if the best tracker is no more able to provide the position of the robot, we can rely on a second tracker. For the sake of the safety, we set for every tracker two levels of velocity (i.e. *fast* and *slow*), so that when the robot reaches a *Critical Area* (i.e. the sphere around the head of the patient), the robot slows down. The setup is shown in **Fig. 1**. The design of the architecture is made using knowledge stored in an ontology, written in OWL[1], that provides the description of components (e.g. ports, types of data exchanged and priority of sensors). The ontology is built exploiting already existing upper ontology (SUMO[2]) that allows us to append new classes and instances to more general classes like "Device" and "Agent".

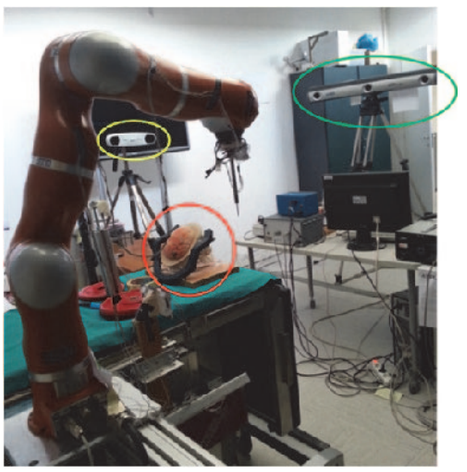

Fig. 1. Scenario of the case study. The end-effector of the 7 dof robot is seen by two optical trackers that are highlighted in the yellow and green circles, respectively. The red circle represents the intra-operative head frame.

The ontology is populated with all devices used at our laboratory. As in the KNOWROB[3] project, we used Prolog to query the ontology and retrieve the knowledge about components (e.g. type of ports, data exchanged, priority), then we processed the results to obtain XML mapping. The XML is the basis for the development of the robotic architecture, achieved using OROCOS[4] running in a ROS environment. A high-level control is implemented, with a Sensor Manager (SM) that reads the data coming from trackers and chooses at each moment the best available tracker according to the performance of the single sensor to track both the robot and the intra-operative reference frame and the sensor accuracy in providing tracking data. This information is

[1] http://www.w3.org/TR/owl-ref/
[2] http://www.ontologyportal.org/
[3] http://www.knowrob.org/
[4] http://www.orocos.org/

sent via OROCOS connection to a Supervisor component, that tells the robot the target to be reached and constantly reads the robot position provided by the tracking system, comparing to the provided target. Besides the high-level control, a simple middle-level control (e.g. a position interpolator) is provided in order to control the robot movement. The deployment of the architecture is accomplished with a Coordinator-Configurator pattern (following what is presented in [6]) using a pure Lua module[5]. The Coordinator component is a hierarchical finite-state machine (see **Fig. 2**) derived from the Task Ontology and written using rFSM Tool[6] with the knowledge about the task to be performed. Events raised from the Supervisor component assert the transition from one state to another, requiring a specific components topology to the Configurator. This allows changing the entire system architecture in reaction to a single event.

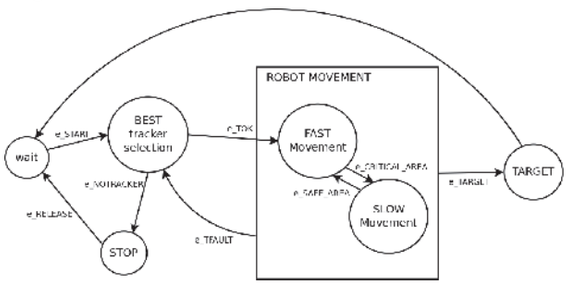

Fig. 2. Coordinator Finite State Machine. It represents the workflow used to drive the robot during target approach.

In order to evaluate the architecture performance, we simulated different emergency situations and measured the latencies of the architecture response through ROS Time Stamps. First, we simulated the fault of a single tracker (*Sensor Swap* test) by occluding the field of view (FOV), in such a way that it is no more able to provide the position of the robot. The latency from the fault recognition and the connection of the best available tracker was measured. Then, we simulated the contemporary fault of all the trackers (*No Sensor To Stop* test) by occluding their FOV. The latency between the recognition of the unavailability of the sensors and the STOP command sent to the robot was measured. Each test was performed 50 times. Mean and standard deviation were computed from the acquired data and used to evaluate the architecture's performance.

RESULTS

The results of performed tests are represented in **Fig. 3**. The *No Sensor To Stop* test resulted to perform better (a mean of 6.6 *ms*), due to less computational time. Considering the worst case of the robot moving at its maximum speed (20 *cm/s*) this leads to a mean of 1.3 *mm* of untracked movement before the STOP assertion. The *Sensor Swap* test had worse performance (a mean of 12 *ms*) because of the need to create a connection with the new best available tracker.

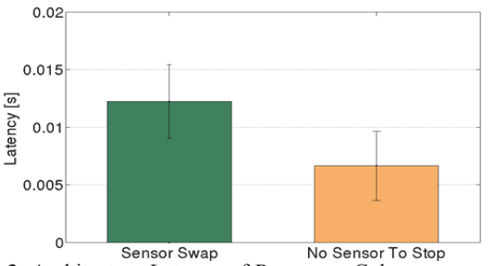

Fig. 3. Architecture Latency of Response. Columns represent mean and standard deviation of the measured latencies (50 repetitions each)

DISCUSSION

In this work we presented an ontology-based approach for the development of an autonomous surgical robotic architecture. The advantages are the standardization of the knowledge on the hardware components and the modularity (in fact it is possible to append every kind of sensor with minimal change on the code). The high-level control provides the possibility to manage possible faults that may happen during the execution. Future works may be related to the fusion of different kinds of knowledge: for example, the information of a Kinect® will be useful to handle security problems related to the presence of too many subjects in the surgical FOV.

ACKNOWLEDGEMENTS

This work is supported within the EuRoSurge European project (FP7-ICT-2011-7-288233).

REFERENCES

[1] Guthart G.S., Salisbury J.K., The Intuitive Telesurgery System: Overview and Application. Proceedings of 2000 IEEE, International Conference on Robotics and Automation. 2000.

[2] Dumpert J., Lehman A.C. et al. Semi-autonomous surgical task using a miniature In vivo Surgical Robot, 31st Annual International Conference of the IEEE EMBS, 2009.

[3] Varadarajan K. M., and Vincze M., Ontological knowledge management framework for grasping and manipulation. IROS Workshop: Knowledge Representation for Autonomous Robots. 2011.

[4] Mudunuri R., Burgert O., and Neumuth T. "Ontological Modelling of Surgical Knowledge." GI Jahrestagung. 2009. pp. 1044-1054.

[5] De Momi E., Perrone R., Capiluppi M., et al., EuRoSurge Workflow: From ontology to surgical task execution, 3rd Workshop on New Technologies for Computer Assisted Surgery. 2013.

[6] Klotzbucher M., Biggs G., Bruyninckx H., "Pure Coordination using the Coordinator–Configurator Pattern". 3rd International Workshop on Domain-Specific Languages and models for ROBotic systems.

[5] https://bitbucket.org/kmarkus/dng
[6] http://people.mech.kuleuven.be/~mklotzbucher/rfsm

Success and Limitations of Robotic Surgery in Infants

T. P. Cundy[1, 2], S. P. Rowland[2], N. K. Alizai[2], A. S. Najmaldin[2]

[1]*The Hamlyn Centre, Institute of Global Health Innovation, Imperial College London, UK*

[2] *Department of Paediatric Surgery, Leeds General Infirmary, Leeds*
azad.najmaldin@leedsth.nhs.uk

INTRODUCTION

Extending the benefits of minimally invasive surgery to infant patient populations is met with technical difficulties imposed by size constraints. Small anatomy results in unavoidable instrument crowding and diminutive endoscopic operative workspaces for which to undertake operations that are typically both complex and reconstructive in nature. Magnified three-dimensional high-definition optics and enhanced dexterity offered by robotic surgical platforms may offer advantages in this setting. This paper critically examines our clinical experience of robot-assisted laparoscopic surgery in infants.

MATERIALS AND METHODS

All infants (< 12 months of age) who underwent robot-assisted laparoscopic surgery between March 2006 and March 2014 were included. The senior author (A.S.N) was primary operator for all cases. All procedures were performed using the da Vinci® Surgical System. Our institution is a large university teaching hospital that serves as a tertiary referral centre. All clinical data was prospectively recorded in an electronic database.

RESULTS

There were 29 patients identified, involving 38 procedures. The primary procedures performed included pyeloplasty (15), fundoplication (7), choledochal cyst excision (3), nephrectomy (1), nephroureterectomy (2), and hepatic cystectomy (1). Concomitant procedures included hiatus hernia repair (5), gastrostomy tube insertion (3), and revision of pre-existing gastrostomy tube (1). Mean patient age was 6 months (range 4 weeks – 11 months). The smallest patient in the series weighed 4.1 kilograms. Overall conversion rate was 6.9% (2/29). The first case that required conversion was for excision of a large inflamed choledochal cyst in a 3 month old child with recurrent cholangitis and a cirrhotic liver. Early decision was made to abandon a laparoscopic approach due to non-technical reasons of considerable adhesions, operative site inflammation, and large dilated bowel loops that limited endoscopic view of the relevant biliary anatomy. The second converted case was a re-do pyeloplasty in a 5 month old child. Conversion to open approach was made for reasons of inadequate access and poor visualisation secondary to both adhesions and distended bowel loops. Only 3 patients required narcotic post-operative analgesia (oral or intravenous morphine). Overall 30-day post-operative complication rate was 13.8% (Table 1).

Table 1 Post-operative complications occurring in the study cohort (n = 29) graded according to the Clavien-Dindo classification [1].

Clavien Grade	n	Description
I	1	Re-presentation with recurrent urinary tract obstruction secondary to renal stones obstruction of distal ureter with spontaneous passage of stones (1)
II	1	Hospital acquired pneumonia with background chronic gastro-oesophageal reflux induced reactive airways disease (1)
IIIa		
IIIb	2	Return to theatre for mini-laparotomy after developing candida peritonitis on post-operative day 9 following fundoplication. This 8-month old 5.9kg child has pre-existing chronic renal failure, massive ascites, and oral candidiasis. At laparotomy, recurrent clear ascites was noted as well gastrostomy tube that had eroded through the gastric wall (1), recurrent pelvi-ureteric junction obstruction requiring re-do robot-assisted pyeloplasty (1)
IVa	0	-
IVb	0	-
V	0	-

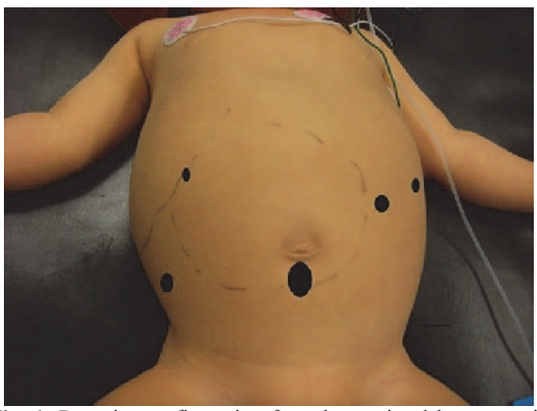

Fig. 1. Port site configuration for robot-assisted laparoscopic excision of choledochal cyst in an infant. Visible skin markings outline anatomical borders of the inferior liver edge and choledochal cyst.

Operating times were variable depending on the relevant procedure, ranging from 107 – 493 minutes for total operating time, and 48 – 343 minutes for console time. Median console operating times for pyeloplasty, fundoplication, and choledochal cyst excision cases were 162 minutes, 85 minutes, and 358 minutes respectively. Median length of post-operative hospital stay was 38 hours (range 18 – 192 hours).

DISCUSSION

This largest published series of robot-assisted laparoscopic surgery in infants demonstrates feasibility for numerous operative indications in selected cases. Our findings are consistent with numerous case reports and small case series (<10 patients) that are emerging in the literature [2-4]. It must be noted however, that specific challenges exist that require important considerations.

Heightened attention to strategic port placement, patient positioning and robot docking is necessary to optimize the functionality of instruments and to avoid robot arm clashing interfering with clinical performance. We have found that elevating patients on soft foam padding and placing ports more laterally and proximal to the operative target site is helpful (Figure 1). Additionally, the remote centre of motion markings on instrument ports (indicated by a solid black line marking) may be placed up to several centimetres above the skin surface to avoid redundant intra-corporeal port length restricting functional instrument length.

There is a technical gap between robotic and non-robotic instruments with respect to size dimensions. The smallest calibre robotic instruments presently available for the da Vinci® system are 5mm. This is in contrast to 2mm or 3mm mini-laparoscopy instruments that are standard for conventional minimally invasive surgery in neonates and infants (Figure 2). Somewhat paradoxically, the larger 8mm robotic instruments tend to be favoured by paediatric surgeons due to a more compact wrist design with shorter articulation length. Without dismissing the technical challenges of scalability, there is clinical need and scope for future instruments that are better suited for spatially constrained operative domains.

As the degree of technical difficulty is considerably higher for pathologies and anthropomorphic features inherent with this patient sub-population, we would advocate that these cases are not well suited for surgeons who might still be progressing through their learning curve for robotic surgery. Case selection is also important with respect to overall suitability and surgeon experience. The two converted cases in this series were both cases of increased complexity in which inadequate operative domain was encountered.

Early comparative assessment literature is encouraging. A recent retrospective cohort study by Bansal *et al* reported significant advantages in operating times, length of hospital stay, and narcotic analgesia use for robot-assisted pyeloplasty in infants compared to open technique [5]. The next iterative step for technology assessment in this niche field will include further feasibility assessment for other indications, as well as prospective comparative efficacy studies.

Fig. 2. Robotic and non-robotic laparoscopic instruments currently available for clinical use.

REFERENCES

[1] Dindo D, Demartines N, Clavien PA. Classification of surgical complications: a new proposal with evaluation in a cohort of 6336 patients and results of a survey. Ann Surg 2004;240:205-13.

[2] Kutikov A, Nguyen M, Guzzo T, Canter D, Casale P. Robot assisted pyeloplasty in the infant – lessons learned. J Urol 2006;176:2237-40.

[3] Meehan JJ. Robotic surgery in children: is there room for this? J Laparoscopsc Adv Surg Tech A 2009;19(5):707-12.

[4] Dangle PP, Kearns J, Anderson B, Gundeti M. Outcomes of infants undergoing robot-assisted laparoscopic pyeloplasty compared to open repair. J Urol 2013;190:2221-27.

[5] Bansal D, Cost NG, DeFoor Jr WR, Reddy PP, Minevich EA, Vanderbrink BA, Alam S, Sheldon CA, Noh PH. Infant robotic pyeloplasty: comparison with an open cohort. J Pediatr Urol 2013 Nov 9 [Epub ahead of print].

Investigation of Performance Log files of Freehand SPECT Acquisitions for Usage Characteristics and Surgical Phase Determination

A. Okur[1,2], R. Voigt[1], R. Stauder[1], N. Navab[1]

[1]*Computer Aided Medical Procedures, Technische Universität München, Germany*

[2]*Department of Nuclear Medicine, Klinikum rechts der Isar, Technische Universität München, Germany*

okur@cs.tum.edu

INTRODUCTION

In Klinikum rechts der Isar, Technische Universität München, there is currently a clinical study where a Freehand SPECT (fhSPECT) [1, 2] system is used intra-operatively in sentinel lymph node biopsy (SLNB) procedures of breast cancer patients. Until now, more than 100 patients are recruited in our university hospital for the study and underwent a SLNB with fhSPECT already.

Fig. 1. fhSPECT system used inside the operating room.

For evaluation of intra-operative imaging devices, an extensible and flexible data gathering and evaluation framework called ORUse [3] has been developed in our institution. The first device modeled in ORUse framework is the Freehand SPECT (fhSPECT) system, which is mentioned above. For each of the acquisitions the fhSPECT system automatically saves all available information into text files, such as tracking, user interaction or activity logs. Even though these files include almost all the information about how the users used the system, they are hard to interpret by the end users due to their sizes, the redundancy in the data and synchronization via numeric timestamps. Until now, only the raw automatic output of the Freehand SPECT system is being saved in the ORUse, with no prior filtering or analysis of the huge amount of the log files. Furthermore, proper analysis of these log files can be useful to approximate the phases of the surgical workflow and the time estimation. Also due to the freehand nature of the device different scan patterns and/or speeds can be identified and investigated for influence in resulting images.

In this work we analyzed SLNB surgeries with fhSPECT for usage characteristics and surgical workflow durations using the abovementioned performance log files in an automated manner.

MATERIALS AND METHODS

For each fhSPECT acquisition, the system generates a folder with the following performance log files, which are synchronized using timestamps.

- *activity.txt*: radiation detected by the gamma probe
- *tracking.txt*: Position and orientation of the reference targets used in surgery in optical camera coordinates
- *userInteraction.txt*: A log file containing information about the user interface elements, button clicks, etc.
- *settings.xml*: An XML file used by the system containing all the settings needed for the fhSPECT acquisition
- *screenshotXXX.jpg*: Screenshots showing the surgical site from the view of the video camera with optional augmented reality information are generated for every 5 seconds
- *screenshots.xml*: Timestamp of each screenshot is saved in an additional XML file for synchronization with other logs.

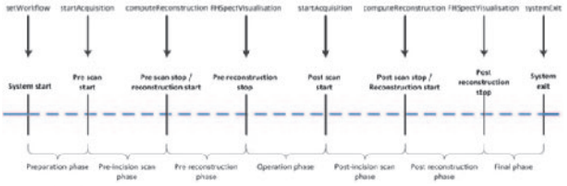

Fig. 2. Based on some specific entries in the user interaction log files the transition between major workflow stages can be determined.

In a previous work, we analyzed fhSPECT acquisitions for usage characteristics of different user groups for augmented reality (AR) and virtual reality (VR) visualization modes of the system, based on the manual analysis of the saved screenshots [4]. However, this is time-consuming and also dependent on the evaluator.
Since some user interface elements may be only available or used in some specific stages in the surgical workflow, the user interaction log can be very helpful to determine the transitions between the stages automatically (Figure 2).

During the whole surgery the tracking information is recorded continuously which results in very large log files. It is not very easy for the study investigators to find the parts, which may be relevant for the resulting end reconstructions or usage characteristics. By an analysis of the tracking log together with the user interaction log, we can limit the tracking log to the parts, which are only related to the aspect we are focusing. Since the scanning phase is the phase which is the most user-dependent part and which affects the reconstructions the most, we focused only on these parts of the logs. This allows us to identify the problems with tracking or speed easily.

RESULTS

By searching automatically for the dedicated entries in the user interaction logs, we determined the duration of the major workflow stages of 19 SLNB surgeries with fhSPECT system (each surgery includes 2 fhSPECT scans, one before the incision, one after the excision of the radioactive lymph node) and looked for variations (Figure 3).

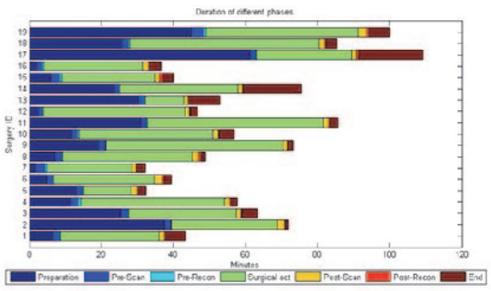

Fig. 3. Duration of workflow stages for 19 different surgeries.

Ideally, since there is a reference tracking target placed on the patient and all the calculations are done in that coordinates, the covered area in both of the scans (pre-incision and post-excision) should overlap. In our analysis, in 18 out of 19 surgeries, this was the case as expected (e.g. Figure 4 left). However, in one case (Figure 4 right) we later found out that between the scans the patient reference target was not taped on the patient properly, therefore moved during surgery and the surgeons reattached it on the body in a different position before the second scan (Figure 5).

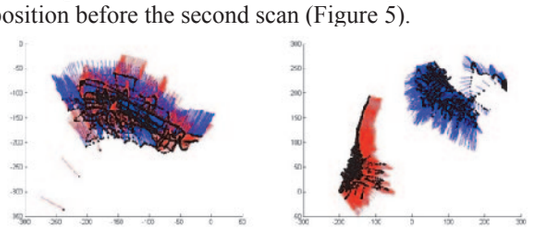

Fig. 4. Covered area during scanning for two different surgeries. Red: Pre-incision fhSPECT acquisition, Blue: Post-excision fhSPECT acquisition.

Fig. 5. AR view of the fhSPECT reconstruction. Left: Pre-incision, Right: Post-excision. White L-shaped optical patient reference target was misplaced in the second scan, which explains the shift in Figure 4 right.

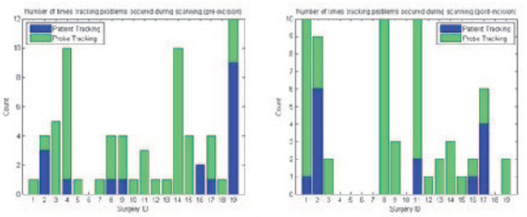

Fig. 6. Lost tracking signals for both optical tracking targets. Left: Pre-incision, Right: Post-excision.

Finally, comparing the two reference targets needed for the optical tracking, the surgeons had experienced tracking problems more related to the probe than the patient reference target (Figure 6).

DISCUSSION

Performance logging can be a very strong tool for identification of usage problems or determination of surgical workflow stages. Retroactive analysis of such performance log files leads to better understanding of the surgical procedures.

REFERENCES

[1] Wendler, T., Hartl, A., Lasser, T., Traub, J., Daghighian, F., Ziegler, S.I., Navab, N.: Towards Intra-operative 3D Nuclear Imaging: Reconstruction of 3D Radioactive Distributions Using Tracked Gamma Probes. In: Ayache, N., Ourselin, S., Maeder, A. (eds.) MICCAI 2007, Part II. LNCS, vol. 4792, pp. 909–917. Springer, Heidelberg (2007)

[2] Wendler, T., Herrmann, K., Schnelzer, A., Lasser, T., Traub, J., Kutter, O., Ehlerding, A., Scheidhauer, K., Schuster, T., Kiechle, M., Schwaiger, M., Navab, N., Ziegler, S.I., Buck, A.K.: First Demonstration of 3-D Lymphatic Mapping in Breast Cancer Using Freehand SPECT. Eur. J. Nucl. Med. 37(8), 1452–1461 (2010)

[3] A. Bigdelou, A. Okur, M.-E. Hoffmann, B. Azizi, and N. Navab, “Towards systematic usability evaluations for the or: An introduction to OR-Use framework”, in Information Processing in Computer-Assisted Interventions, vol. 7330 of Lecture Notes in Computer Science, pp. 146–156, Springer. (2012)

[4] A. Okur, S.-A. Ahmadi, A. Bigdelou, T. Wendler, and N. Navab, “MR in OR: First analysis of AR/VR visualization in 100 intra-operative Freehand SPECT acquisitions,” in Proceedings of the 10th International Symposium on Mixed and Augmented Reality (ISMAR), (Basel, Switzerland), pp. 211–218. (2011)

Detecting and Analyzing the Surgical Workflow to Aid Human and Robotic Scrub Nurses

R. Stauder, A. Okur, N. Navab

Computer Aided Medical Procedures, Technische Universität München, Germany

ralf.stauder@tum.de

INTRODUCTION

Every surgeon and nurse involved in surgery builds a mental model of each type of surgery based on their experiences. This implicit knowledge about the surgical workflow allows them to make decisions based on the current context and predict and prepare future steps. Acquiring this model takes time, therefore experienced scrub nurses are in high demand. Additionally to that, qualified scrub nurses are chronically scarce even in developed countries, which led to the development of robotic surgical assistants. In this paper we give a short introduction to surgical workflow analysis and show, how these methods can be applied to support both the education of human scrub nurses, as well as aid robotic scrub nurses.

The field of surgical workflow analysis or surgical process modelling has developed in recent years with the goal to enable context-awareness in the operating room of the future [1, 2]. Current approaches to recognize the surgical process involve among other methods manual labeling [3], sensor-based instrument detection [4], evaluation of the laparoscopic video [5], and kinematic data from surgical robot systems [6]. The collected data is then usually turned into a specific model through different techniques, like Dynamic Time Warping (DTW), Hidden Markov Models (HMM), or machine learning approaches like Support Vector Machines (SVM) or random forests [4, 5, 7].

The idea for Scrub Nurse Robots (SNR) has also been in development for several years [8]. Most systems rely on voice commands from the surgeon or another nurse to reach for instruments [9, 10], but one could argue that the state models used internally for the robots are already a step towards a surgical model. Enhancing these systems through surgical phase detection and automatic predictions of upcoming instrument requests would further improve the robots performance as it could then also prepare future actions, much like experienced scrub nurses do.

This paper builds on the previous work in [4], so we will apply random forests on instrument detection data in order to recognize workflow phases during a surgery. Based on this information we will deduce for every step in the surgery the most probable instruments to be requested next by the main surgeon in this paper. This allows scrub nurses to prepare these instruments and provide them in time, while robotic scrub nurse systems can use this information also to optimize recognition of commands and actions from the main surgeon.

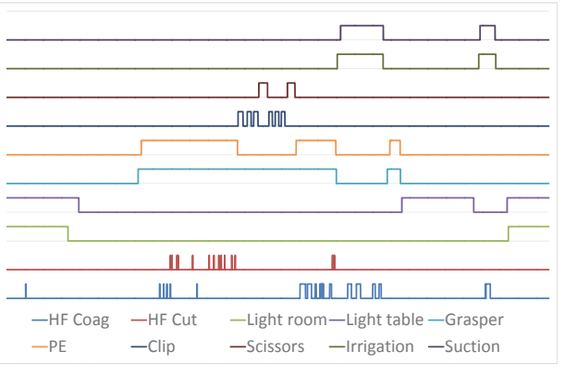

Fig. 1. Binary data collected over the course of a surgery. Each instrument or mode is in use, when the corresponding line is raised.

MATERIALS AND METHODS

Our medical application will be a laparoscopic cholecystectomy. The recorded data consists of measurements of the irrigation and suction bag weights, intra-abdominal CO_2 pressure, the inclination of the surgical table, and binary data for the state of both HF modes, the room and surgical lamps and usage of up to eight RFID-enabled surgical instruments as described in [11]. An exemplary visualization of the binary signals collected over the courses of a single surgery is given in figure 1.

We employ random forests to predict for every step of the surgery in which phase it happens. A random forest is a collection of randomly decorrelated decision trees. Each tree consists of internal nodes that evaluate simple thresholding functions on presented feature vectors. Our feature vectors are the collected measurements for a single timeframe, used directly as elements of the feature vector without further normalization. The hierarchical combination of multiple decision nodes leads to a classification of the given feature vector to one of several possible classes, in our case the a priori known workflow phases. Combining multiple classifications from several trees through majority voting yields the final classification result of the full random forest. A more detailed explanation is given in [12].

RESULTS

Our dataset consists of four fully labeled surgeries with a total of approximately 60,000 measurements. We evaluate our classifier in Leave One Surgery Out (LOSO) fashion by training on three surgeries and validating on the forth, for each surgery. Phases could be detected by our approach with an overall accuracy of

68.78% and an average recall over all classes of 73.41%. Detailed performance measurements per phase are given in table 1. Some phases with typically similar measurements show notably lower recognition rates, as we classify frames without temporal information.
In a different approach we trained the forest in order to detect the expected state of the lights in the OR instead of surgical phases. The training was done after removing the light data from the training set. In this reduced scenario we reach an accuracy of 87.57% with an average recall of 75.44%

Table 1 Recognition rates for all defined workflow phases over four surgeries.

Phase	Precision	Recall
Trocar placement	99,99%	99,52%
Preparation	68,83%	79,36%
Clipping	42,54%	40,50%
Detaching gallbladder	77,89%	11,34%
Retrieving gallbladder	98,06%	99,74%
Stop bleeding	18,52%	83,49%
Drainage and closing	99,85%	99,89%

During training of the random forests it was possible to estimate the relative importance of each individual feature by evaluating the loss in accuracy when measurements for single features are permutated. This yields a perceivable difference between features, though no feature can be discarded without loss of accuracy.

DISCUSSION

Through very simple sensor measurements we are able to detect the current phase in an ongoing surgery. Single phases still have low recognition rates that require further improvements, but as important implication one can argue that the broad application of simple and cheap sensors to the OR can provide the infrastructure for detailed workflow analyses.
For every phase there are usually at most two instruments being changed. By being able to recognize the surgical phases, we can therefor easily predict the two instruments most likely to be exchanged soon. In addition to the prediction of the light state, we can now support both the scrub nurse as well as the circulator by presenting them with their most likely next task. This allows novice nurses to be prepared and reduces the time to switch between instruments, and visualizing the progress of the surgery can improve their learning process and aid them in building their own mental model of the surgery.
In a similar manner scrub nurse robots can be supported. For a two-step system as in [9], where the SNR takes requested instruments from a full tray and delivers them to an interchange tray for a human nurse, the most likely instruments can already be provided solely based on the surgical process. In this scenario the nurse only needs to request special tools in case of emergencies or other deviations from the regular workflow and can otherwise focus on the provided, context-dependent subset of all instruments that is available on the interchange tray. But also the performance of a SNR that interacts directly with the surgeon can be improved by knowledge of the surgical progress. As stated in the conclusion of [10], inclusion of surgical process models can enable context-sensitive devices (such as scrub nurse robots) to predict upcoming steps and react to requests and common situations in smarter ways.

REFERENCES

[1] Lalys, F., Jannin, P.: Surgical process modelling: a review. Int. J. Comput. Assist. Radiol. Surg. (2013).
[2] Cleary, K., Kinsella, A., Mun, S.K.: OR 2020 workshop report: Operating room of the future. Int. Congr. Ser. 1281, 832–838 (2005).
[3] Neumuth, T., Jannin, P., Schlomberg, J., Meixensberger, J., Wiedemann, P., Burgert, O.: Analysis of surgical intervention populations using generic surgical process models. Int. J. Comput. Assist. Radiol. Surg. 6, 59–71 (2011).
[4] Stauder, R., Okur, A., Peter, L., Schneider, A., Kranzfelder, M., Feussner, H., Navab, N.: Random Forests for Phase Detection in Surgical Workflow Analysis. 5th International Conference on Information Processing in Computer-Assisted Interventions (IPCAI) (2014).
[5] Lalys, F., Riffaud, L., Morandi, X., Jannin, P.: Surgical Phases Detection from Microscope Videos by Combining SVM and HMM. In: Menze, B., Langs, G., Tu, Z., and Criminisi, A. (eds.) Medical Computer Vision. Recognition Techniques and Applications in Medical Imaging. pp. 54–62. Springer Berlin Heidelberg, Berlin, Heidelberg (2011).
[6] Padoy, N., Hager, G.D.: Human-Machine Collaborative surgery using learned models. 2011 IEEE International Conference on Robotics and Automation. pp. 5285–5292. IEEE (2011).
[7] Padoy, N., Blum, T., Ahmadi, S.-A., Feußner, H., Berger, M.-O., Navab, N.: Statistical modeling and recognition of surgical workflow. Med. Image Anal. 1–22 (2010).
[8] Miyawaki, F., Masamune, K., Suzuki, S., Yoshimitsu, K., Vain, J.: Scrub Nurse Robot System—Intraoperative Motion Analysis of a Scrub Nurse and Timed-Automata-Based Model for Surgery. IEEE Trans. Ind. Electron. 52, 1227–1235 (2005).
[9] Perez-Vidal, C., Carpintero, E., Garcia-Aracil, N., Sabater-Navarro, J.M., Azorin, J.M., Candela, A., Fernandez, E.: Steps in the development of a robotic scrub nurse. Rob. Auton. Syst. 60, 901–911 (2012).
[10] Yoshimitsu, K., Masamune, K., Iseki, H., Fukui, Y., Hashimoto, D., Miyawaki, F.: Development of Scrub Nurse Robot (SNR) systems for endoscopic and laparoscopic surgery. 2010 International Symposium on Micro-NanoMechatronics and Human Science. pp. 83–88. IEEE (2010).
[11] Kranzfelder, M., Schneider, A., Fiolka, A., Schwan, E., Gillen, S., Wilhelm, D., Schirren, R., Reiser, S., Jensen, B., Feußner, H.: Real-time instrument detection in minimally invasive surgery using radiofrequency identification technology. J. Surg. Res. 1–7 (2013).
[12] Criminisi, A.: Decision Forests: A Unified Framework for Classification, Regression, Density Estimation, Manifold Learning and Semi-Supervised Learning. Found. Trends® Comput. Graph. Vis. 7, 81–227 (2011).

Author Index